A fresh view on carbon radio recombination lines powered by LOFAR

Pedro Salas

Original cover image by Matias Vergara Anguita.

A FRESH VIEW ON CARBON RADIO RECOMBINATION LINES POWERED BY LOFAR

PROEFSCHRIFT

ter verkrijging van
de graad van Doctor aan de Universiteit Leiden,
op gezag van de Rector Magnificus Prof. mr. C. J. J. M. Stolker,
volgens besluit van het College voor Promoties
te verdedigen op Dinsdag 30 april 2019
klokke 15:00 uur

door
Pedro Salas
geboren te Santiago, Chile
in 1988

Promotiecommissie

Promotor:	Prof. dr. A. G. G. M. Tielens
Promotor:	Prof. dr. H. J. A. Röttgering
co-Promotor:	Dr. J. B. R. Oonk
Overige leden:	Prof. dr. C. Heiles *(University of California Berkeley)*
	Prof. dr. K. Menten *(Max Planck Institute Bonn)*
	Prof. dr. G. White *(Open University UK)*
	Prof. dr. H. J. van Langeveld *(Leiden University)*
	Prof. dr. P. P. van der Werf *(Leiden University)*

A mis padres

INDEX

1 INTRODUCTION

1.1. THE INTERSTELLAR MEDIUM

The interstellar medium (ISM) contains the gas, dust, radiation and charged particles that lie between the stars in a galaxy. The gas in the ISM is composed of hydrogen (70.4 % by mass), helium (28.1 % by mass) and heavier elements (1.5 % by mass). In our Galaxy, the Milky Way, gas and dust are $\approx$ 10–15% of the stellar mass (e.g., Ferrière, 2001). Gas, dust and radiation interact with each other. This coupling between gas, dust and radiation gives rise to an ecosystem (e.g., Burton, 2004). In this ecosystem stars are formed out of interstellar gas. Stars process interstellar gas through nucleosynthesis, which is then returned to the Galaxy through stellar winds and supernova explosions. There, it will repeat the process, forming new stars, planets and life. An overly simplified cartoon of this cycle is presented in Figure 1.1. Stars are formed in the densest portions of the ISM, molecular clouds, where gravity compresses the gas to densities high enough that it can form stars (e.g., Blitz & Rosolowsky, 2006). Once stars are formed, these will interact with the surrounding gas. This interaction, through radiation, winds and supernovae explosions, might trigger new rounds of star formation or render the surrounding gas incapable of forming new stars (e.g., Walch, 2014). The exact details of how this cycle develops, how gas transitions from being hot and diffuse to cold and dense, are part of the recipe that determines how galaxies evolve over time, and it is one of the main missing pieces in our understanding of galaxy evolution (e.g., Schaye et al., 2015).

A color composite image of part of the Galactic ecosystem is shown in Figure 1.2. This is Cygnus X (Piddington & Minnett, 1952), a region of massive star formation located at a distance of $\approx$ 1.4 kpc (Rygl et al., 2012; Kiminki et al., 2015). In Cygnus OB2 it is estimated that there are around 2600 OB stars (Knödlseder, 2000), and between DR21 and W75N 40 massive protostars (Beerer et al., 2010). There, the extreme-ultraviolet (EUV) photons (energies $\geq$ 13.6 eV) from massive stars ionize the gas creating HII regions. The free electrons produced in the process heat the gas through collisions to temperatures $\sim 10^4$ K. This results in HII regions having high thermal pressures and

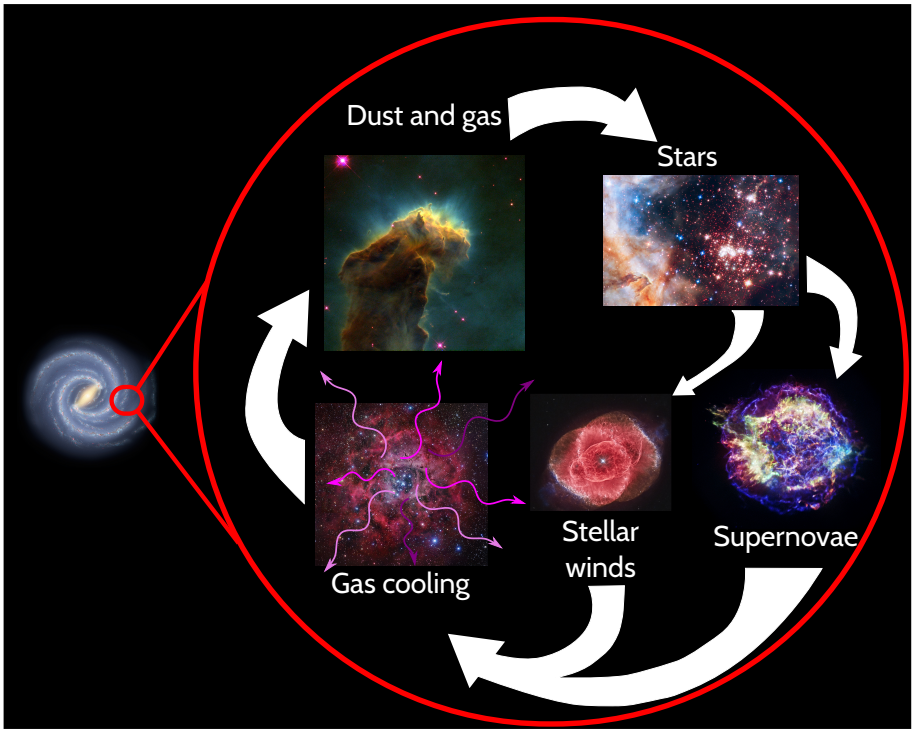

Figure 1.1.: A simplified schematic of the Galactic ecosystem. In a galaxy, like the Milky Way, stars are constantly being born out of dust and gas. These in turn return dust and gas to the galaxy when they go out. Then the hot gas returned by the stars cools down in spectacular displays. Once it has cooled enough it can become the material from which new stars are born. Images credit: NASA/ESA/Hubble/HLA/Robert Gendler/Raul Villaverde.

large thermal velocites, which causes them to expand against the colder material from which the ionizing stars formed. Moreover, the ionizing radiation will drive a ionization front into the surrounding gas. This will cause the gas to compress, forming dense structures which might become gravitationally unstable and hence, new sites of star formation (Elmegreen & Lada, 1977). However, in the long run the ionizing radiation will photoevaporate the parent molecular cloud, shutting down star formation (e.g., Elmegreen, 2007; Murray, 2011). This is one of the ways in which stellar feedback regulates star formation in a galaxy (e.g., McKee & Ostriker, 2007).

The influence of stellar radiation, winds and supernovae explosions gives rise to a turbulent ISM where the gas is found in different states. Depending on its temperature and the dominant form of hydrogen (molecular, atomic or ionized), ISM gas can be grouped into; molecular, cold neutral medium, lukewarm neutral medium, warm neutral medium, warm ionized medium and hot ionized medium (CNM, LNM, WNM, WIM and HIM, respectively). For molecular gas the temperatures are $\sim$ 10 K, and, as it name suggests, hydrogen is molecular. The WNM consists of gas in which hydrogen is atomic

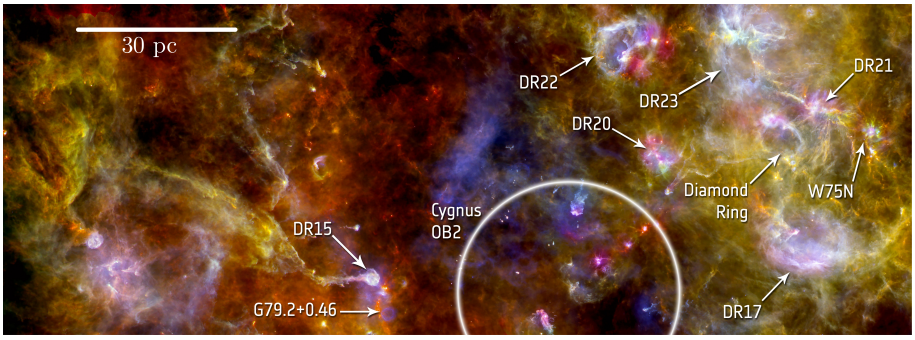

Figure 1.2.: The Cygnus X star forming region in the Milky Way as seen by the Herschel space observatory. In *blue* 70 μm, in *green* 160 μm and in *red* 250 μm. Image credit: ESA/Herschel/PACS/SPIRE/HOBYS Consortium.

with a temperature of $\sim 10^4$ K. In the CNM hydrogen is also atomic, but it has a lower temperature, ~ 100 K (e.g., Wolfire et al., 2003). By mass, most of the gas in the ISM is in the WNM and CNM (e.g., Tielens, 2010). The lukewarm neutral medium is gas where hydrogen is atomic with a temperature between that of the WNM and CNM. In the WIM the temperatures are similar to those in the WNM, $\sim 10^4$ K, but hydrogen is ionized. The density in the WIM is ~ 0.1 cm^{-1} and has a volume filling fraction of 0.4–0.2 (e.g., Haffner et al., 2009). The hot ionized medium comprises gas in which hydrogen is ionized and the temperatures are $\sim 10^6$ K. The high temperatures in the HIM are maintained through shock waves driven by supernovae. As seen in Figure 1.2, all these types of gas coexist and interact with each other. For example, part of the ionizing photons emitted by massive stars are able to leak from HII regions into the neutral ISM. These escaping photons are part of what determines the energy balance of the ISM, and they are responsible for maintaining the ionization of the gas in the WIM (e.g., Haffner et al., 2009). How ionizing photons are able to transverse the large distances required to keep the ionization of the WIM is related to how the CNM is distributed. Thus, to understand the WIM we also need to understand the properties of the CNM.

Observations of different types of gas in our Galaxy are performed using diverse tracers. An example of some of these observations is presented in Figure 1.3. In these maps only regions close to the Galactic plane are shown (Galactic latitudes $|b| < 10°$). The CNM and WNM are traced by the 21 cm line of atomic hydrogen (HI, top panel in Figure 1.3). The distribution of atomic gas peaks close to the Galactic plane and extends over most of the sky (e.g., Kalberla & Kerp, 2009). The CNM has a scale height of ≈ 100 pc, while that of the WNM is ≈ 400 pc (e.g., Kalberla & Kerp, 2009). Molecular gas is usually traced by the first rotational transition of carbon monoxide (CO) at 2.6 mm, the ^{12}CO(1–0) line (second panel, from top to bottom, in Figure 1.3). Most of the molecular gas is concentrated in the Galactic plane, $b \approx 0°$. Molecular gas has higher densities and column densities than atomic gas. For this reason, the radiation field that impinges into molecular gas is softer and less intense than that bathing atomic

gas. Visible light traces the stellar component and the dark regions are produced by absorption and scattering by dust. X-Rays trace regions where the gas is hot and ionized, the HIM. This is mostly in regions of massive star formation, such as Cygnus-X or the Galactic center, or in supernova remnants, like Vela.

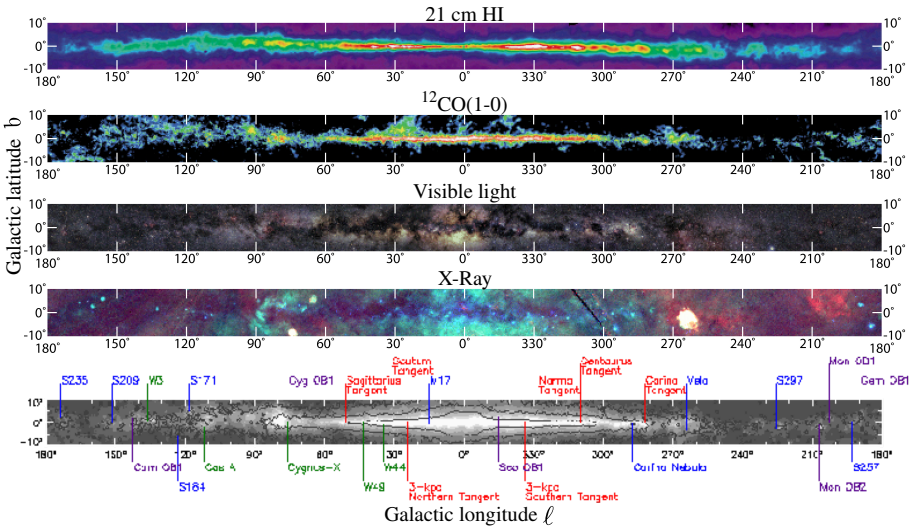

Figure 1.3.: Maps of the Milky Way as seen at different wavelengths. The *top panel* shows the distribution of atomic gas, cold and warm, as seen through the 21 cm line of HI. The next panel shows the distribution of molecular gas as traced by the ^{12}CO(1–0) line at 2.6 mm. The *middle panel* shows the Milky Way as seen in optical light between 0.4–0.6 μm. The next panel shows the X-ray emission from the Milky Way. X-rays trace mostly hot ionized gas. The *bottom panel* is a finder chart showing some regions and their names. The HI-21 cm map is from the Leiden-Argentina-Bonn (LAB) survey (Kalberla et al., 2005). The ^{12}CO(1–0) map is from the Harvard Center for Astrophysics (CfA) survey (Dame et al., 2001). The visible light image was produced by A. Mellinger, and it is an earlier version of the one presented in Mellinger (2009). The X-ray image is from the Position-Sensitive Proportional Counter (PSPC) instrument on the Röntgen Satellite (ROSAT, Snowden et al., 1997). Image credit: NASA.

Observations like the ones presented in Figure 1.3 have helped us describe the Galactic ecosystem. However, it has also become clear that in order to reach a deeper understanding of the physics that drive galaxy evolution we require a quantitative assessment of the gas physical properties (e.g., temperature and density). The distribution of temperature and density of interstellar gas is determined by the effects of different physical mechanisms (e.g., Vázquez-Semadeni, 2012). An extension of this is that it should be possible to determine the relative importance of different physical mechanisms by measuring the temperature and density distribution of the ISM. An example of such analysis is that performed using the 21 cm line of HI. Observations of 21 cm-HI reveal the existence of a broad range of physical conditions for atomic gas (e.g., Kalberla et al., 1985; Heiles, 2001; Heiles & Troland, 2003; Kalberla & Haud, 2018). If the gas is in pressure and thermal equilibrium, then the phase structure is set by the gas

heating and cooling. Under these equilibrium conditions the gas will arrange itself into cold dense clouds (CNM) and a warm diffuse medium (WNM). Gas with conditions between those of the CNM and WNM, e.g., the LNM, is thermally unstable, so it will cool down or heat up to the CNM and WNM, respectively (e.g., Field et al., 1969; Wolfire et al., 1995, 2003). If we consider mechanical energy input by massive stars, then, the constant energy transfer will stir and shock the gas. The pressure fluctuations caused by these shocks and turbulence will drive gas between the CNM and WNM, resulting in the presence of significant quantities of thermally unstable gas (e.g., Kim et al., 2013). Supernovae explosions are one of the main driving mechanism of shocks and turbulence in the ISM (e.g., Mac Low & Klessen, 2004; Gazol et al., 2005; Kim & Ostriker, 2017).

One of the main issues regarding the use of the gas physical conditions to determine the relative importance of different physical mechanisms in setting the phase structure of the ISM is the lack of probes for the physical conditions. The most widely used method to study cold gas in the ISM is through the 21 cm-HI line. When HI is observed in absorption against a continuum source, the absorption feature will be stronger the colder the gas is. This makes the absorption features of the 21 cm-HI line a reliable tracer of cold gas in the ISM. In order to estimate the gas temperature using the 21 cm-HI line observations of both emission and absoprtion profiles are required (e.g., Heiles & Troland, 2003; Murray et al., 2015). However, observations of 21 cm-HI in absorption are only possible against a background source and the line is not sensitive to the gas density.

Another limitation of the bright 21 cm-HI and ^{12}CO(1–0) lines for the study of the cold ISM, is that they do not trace a large fraction of the molecular gas mass. Dust and γ-ray observations have revealed that close to 50% of the molecular gas mass in the Solar neighbourhood is not traced by these lines (e.g., Grenier et al., 2005; Planck Collaboration et al., 2011). This *CO-dark* molecular gas is in regions where hydrogen is mainly molecular, so HI is not detected, and CO has not been formed or it has been destroyed (e.g., van Dishoeck & Black, 1986; Visser et al., 2009; Wolfire et al., 2010). This has led to the use of other lines to determine the gas physical conditions and to probe *CO-dark* molecular gas (e.g., the 18 cm line of OH, Allen et al., 2015; Engelke & Allen, 2019).

For the conditions typical of *CO-dark* molecular gas, most of the hydrogen will be in molecular form, and carbon will be ionized, C^+. This makes the far-infrared (FIR) fine structure line of C^+ at 158 μm ([CII]) a prime tracer of *CO-dark* molecular gas (e.g., Langer et al., 2014; Tang et al., 2016; Goldsmith et al., 2018). However, since the energy difference between the fine structure states of [CII] is 91.2 K, and that [CII] can be easily excited through collisions with electrons, atomic or molecular hydrogen, [CII] emission traces a variety of gas states. Some of these include the WIM, the extended low density WIM (ELDWIM, e.g., Heiles, 1994), extended low density HII regions (e.g., Goldsmith et al., 2015), as well as *CO-dark* molecular gas (e.g., Visser et al., 2009; Wolfire et al., 2010) and photodissociation regions (PDRs). Hence, to study *CO-dark* molecular gas using [CII] we must be able to separate the contribution from different gas states to its excitation (e.g., Pineda et al., 2013; Pabst et al., 2017). An alternative is to use lines from C^+ at radio frequencies, which, as we will see, only trace cold gas.

The radiation from massive stars exposes most of the interstellar gas to ultraviolet (UV) photons creating PDRs in the surfaces of atomic and molecular clouds. PDRs are regions where UV photons (with energies between 6 and 13.6 eV), determine the chemistry, structure and thermal balance (for a review see Hollenbach & Tielens, 1999). Photons with energies less than 13.6 eV are not capable of ionizing hydrogen, but they can ionize other elements, such as carbon (ionization potential 11.2 eV, e.g., Emsley, 1998), and dissociate molecules, such as molecular hydrogen (e.g., Stecher & Williams, 1967). As UV photons penetrate into a PDR, the radiation field will lose energy and hardness due to dust extinction and absorption by molecular hydrogen. This will give rise to a layered structure, where hydrogen is atomic close to the source of photons and molecular far from it (Tielens & Hollenbach, 1985).

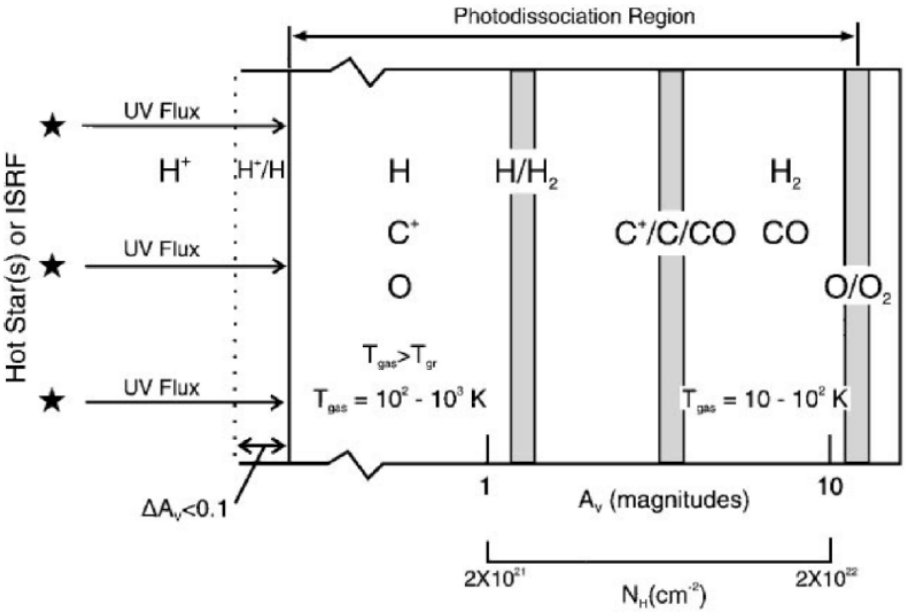

Figure 1.4.: Diagram showing the structure found in a PDR. At the edge of the PDR, on the left, hydrogen is ionized by UV photons with energies above 13.6 eV. As we move to the right, deeper into the PDR, hydrogen becomes atomic and then molecular. Image taken from Hollenbach & Tielens (1999).

An example of the layered structure found in a PDR is presented in Figure 1.4. There the source of radiation is on the left. Close to the source of radiation we have an HII region (labelled H^+ in Figure 1.4). At the interface between the HII region and the neutral gas we have the H^+/H interface (the ionization front). Only photons with energies less than 13.6 eV pass the ionization front. As we move to the right we have two other important regions, these are: the dissociation front, where the transition between atomic and molecular gas takes place (H/H_2 interface) and the C^+/C/CO interface. Between the H^+/H and C^+/C/CO interfaces, the C^+ layer, most of the free electrons are provided

by the ionization of carbon. Because of this, we have that $x_e \approx x_{C^+} \approx 1.6 \times 10^{-4}$ (Sofia et al., 2004), where $x(X)$ is the abundance of X with respect to hydrogen. Also, in the C^+ layer we have that most of the gas heating is through the photoelectric effect (e.g., Spitzer, 1948; Watson, 1972; de Jong, 1977; Draine, 1978; Bakes & Tielens, 1994; Weingartner & Draine, 2001), and the gas cooling is through the FIR lines of oxygen and ionized carbon. In the denser layers of the PDR the gas heating is through collisional de-excitation of UV pumped H_2 (Sternberg & Dalgarno, 1989; Burton et al., 1990; Röllig et al., 2006).

The picture described above represents a *classical* PDR, i.e., the interface between an HII region and a molecular cloud. For the PDRs exposed to the mean interstellar radiation field (ISRF, e.g., Mathis et al., 1983) the relevant physical and chemical processes, as well as the layered structure, are similar to those found in a *classical* PDRs. The PDRs in atomic clouds have been studied using absorption line studies in the UV (e.g., van Dishoeck & Black, 1986). UV absorption studies provide important observational constraints on the physics of the ISM, however, they lack spatial information and only sample local gas, as they can only be performed against a UV bright background source. Given that most of the mass in the ISM is in neutral atomic gas (WNM and CNM), understanding the properties of this gas is a central piece in our understanding of the galactic ecosystem.

1.2. Carbon radio recombination lines

A powerful tool for the study of the cold ISM is through observations of carbon radio recombination lines (CRRLs). The cold gas in the ISM, atomic clouds and the surfaces of molecular clouds, is teeming with ionized carbon. Thanks to the capabilities of new and upgraded telescopes it is now possible to observe these faint lines with unprecedented detail. This was the main motivation for this thesis.

CRRLs, as their name suggests, are spectral lines of ionized carbon observed at radio frequencies. When a carbon ion recombines with an electron to a large principal quantum number n it will result in a Rydberg atom. As the Rydberg atom of carbon transitions between different principal quantum numbers it will produce CRRLs, from GHz to MHz frequencies depending on the n levels involved. For example, a transition from $n' = 31$ to $n = 30$ will produce a line at 232 GHz, and it is called a C30α line. α lines involve a change in principal quantum number $\Delta n = 1$. Transitions involving larger changes in n are called β, γ, δ and so on, for $\Delta n = n' - n = 2, 3, 4$ and larger.

Ionized carbon can also be found in e.g., HII regions, the WNM, the CNM and the surfaces of molecular clouds. However, given the strong dependence of the CRRL optical depth on temperature ($\tau \propto T^{-5/2}$), these lines predominantly arise in cold gas ($\sim$ 100 K, e.g., Gordon & Sorochenko, 2009). This means that they are tracers of the CNM and the surfaces of molecular clouds. Moreover, CRRLs provide independent probes of the gas physical conditions (temperature and density, e.g., Payne et al., 1994). This makes CRRLs particularly interesting tools for the study of cold gas, since the physical conditions of the CNM and *CO-dark* molecular gas are hard to determine by other means.

The first reported detection of CRRLs was that of Palmer, Zuckerman, Penfield, & Lilley (1967). These were quickly followed by the suggestion that departures from local thermodynamical equilibrium (LTE) could help explain the observations (Goldberg & Dupree, 1967). The discovered CRRLs were then interpreted as coming from high density atomic regions surrounding HII regions under LTE (Zuckerman & Palmer, 1968). An alternative explanation was that the lines were stimulated due to the presence of a background source of continuum (Dupree & Goldberg, 1969). The observations of Palmer et al. (1967) and Zuckerman & Palmer (1968) targeted C109α lines at $\approx$ 5 GHz. Observations of the C134α and C166α lines at lower frequencies confirmed that CRRLs were not coming from the HII regions themselves, and that departures from LTE were necessary to explain the observed line strengths (Pedlar, 1970; Zuckerman & Palmer, 1970). Observations of narrow hydrogen RRLs (HRRLs) at the velocity of the corresponding CRRL provided additional evidence supporting that the lines are not produced in the HII region, but in colder gas (Ball et al., 1970; Chaisson, 1971).

Departures in the population of ionized carbon atoms with respect to their LTE values are characterized by the departure coefficients b_n and $\beta_{nn'}$. The factor b_n describes how the number of ions at a particular n deviates from its LTE value, while the factor $\beta_{nn'}$ characterizes the effect of absorption and stimulated emission. The first calculations of departure coefficients for CRRLs were those of Dupree & Goldberg (1969). These calculations were performed for conditions typical of HII regions, as at the time which type of gas the CRRLs were tracing was not clear and the relevant collisional rates were not available at low temperatures. After these rates became available, and observational evidence in favor of a cold gas origin of CRRLs accumulated, Dupree (1972) computed departure coefficients for CNM-like conditions. These calculations were then applied to the interpretation of CRRL observations (e.g., Hoang-Binh & Walmsley, 1974; Dupree, 1974).

The combined use of CRRL observations and calculations of the departure coefficients lead to a picture in which high frequency (frequencies $\gtrsim$ 2 GHz) CRRLs trace the dense interfaces between HII regions and molecular gas (e.g., Zuckerman & Palmer, 1968; Zuckerman & Ball, 1974) –regions now generally recognized as PDRs– while at lower frequencies the lines can be observed thanks to the effect of stimulated emission (e.g., Dupree & Goldberg, 1969; Dupree, 1974).

The first detection of a CRRL in absorption was that of C631α (Konovalenko & Sodin, 1980). This line was first identified as the hyperfine transition of atomic nitrogen (Konovalenko & Sodin, 1980), but it was quickly suggested that the line could be due to a recombination line of carbon (Blake et al., 1980). This was confirmed by the detection of the C630α and C640α lines (Konovalenko & Sodin, 1981). The detection of C631α implied that highly excited states of ionized carbon can be found in our Galaxy. The observations of C631α were performed against Cassiopeia A (Cas A), and led to many more observations of CRRLs towards this source (e.g., Ershov et al., 1982; Konovalenko, 1984; Ershov et al., 1984; Anantharamaiah et al., 1985; Lekht et al., 1989; Payne et al., 1989; Anantharamaiah et al., 1994; Payne et al., 1994; Kantharia et al., 1998; Stepkin et al., 2007; Asgekar et al., 2013; Oonk et al., 2015, 2017; Salas et al., 2017, 2018). There, the largest bound atoms in space have been found ($n = 1009$, corresponding to an atom with a classical diameter of $\approx$ 50 μm, Stepkin et al., 2007), and the lowest

frequency detection of a spectral line at 11 MHz was achieved (Salas et al., 2017). Moreover, these observations showed that low-frequency (frequencies below 1 GHz) CRRLs originate in cold diffuse gas. However, it was not possible to determine whether CRRLs are associated with atomic or molecular gas (e.g., Anantharamaiah et al., 1994).

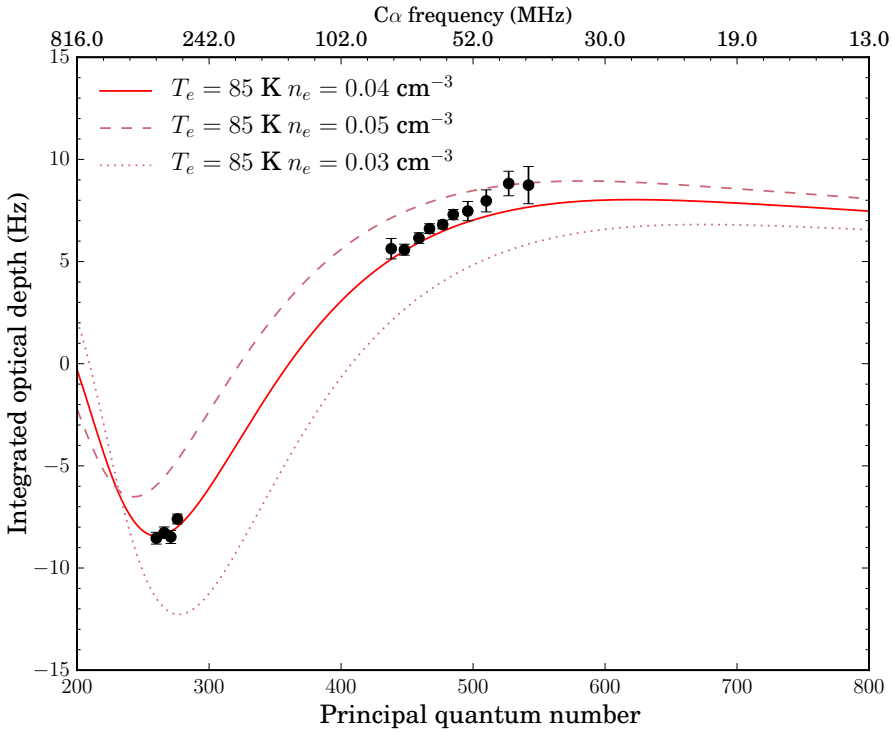

Figure 1.5.: Comparison between the predicted integrated optical depth (*red lines*) and the observed values (*black circles*). The CRRL observations were carried out towards Cas A, one of the brightest low-frequency continuum sources, using LOFAR. The predicted integrated optical depth was computed using the departure coefficient calculations of Salgado et al. (2017). The departure coefficients were evaluated for different values of electron temperature, T_e, and density, n_e. Adapted from Oonk et al. (2017).

A couple of years before the first detection of CRRLs in absorption, it was realized that dielectronic capture plays an important role in setting the level population of ionized carbon (Watson et al., 1980). Dielectronic capture is the process in which a carbon ion recombines with a free electron, exciting the carbon ion core in the process. This led to new calculations of the departure coefficients (e.g., Walmsley & Watson, 1982; Ponomarev & Sorochenko, 1992; Payne et al., 1994; Roshi & Kantharia, 2011). However, with these calculations it was not possible to explain the observed variations in line properties as a function of principal quantum number with one set of physical conditions (e.g., Payne et al., 1994). Recently, Salgado et al. (2017) have updated the calculation of

the departure coefficients. These updated calculations used the semi-classical angular momentum changing collisional rates of Vrinceanu et al. (2012), and solve the level population problem explicitly considering the role of angular momentum, l, in the dielectronic capture process. Previous calculations had to assume some distribution for the departure coefficient b_{nl} as a function of l, largely due to the lack of computing power available. Using the departure coefficient calculations of Salgado et al. (2017) it has been possible to explain the change in CRRL properties as a function of principal quantum number (Oonk et al., 2017). This is illustrated in Figure 1.5, where we show a comparison between predictions for the CRRL integrated optical depth as a function of principal quantum number and the observed values.

Other studies of low-frequency CRRLs have focused on surveying the Galaxy (e.g., Erickson et al., 1995; Kantharia & Anantharamaiah, 2001; Roshi et al., 2002). These surveys studied large portions of the Galaxy using coarse angular resolution observations ($\gtrsim 1^\circ$). This enabled the study of large regions, establishing that low-frequency CRRLs are ubiquitous, but it also limited the interpretation of the results (e.g., Kantharia & Anantharamaiah, 2001). One of the main issues faced in the interpretation was posed by the unknown size of the emitting regions, and the unknown origin of the regions to which the CRRLs were associated with. In the large beams used for these surveys, it was easy to find HII regions, supernova remnants and diffuse regions under the beam. These types of sources have very different continuum spectra, and the gas associated with them can be very different as well. Besides, it was also possible to establish an association between low-frequency CRRLs and HI self absorption (HISA, Roshi & Kantharia, 2011). This association confirmed that low-frequency CRRLs trace cold gas.

With modern radio telescopes, it is now possible to observe low-frequency CRRLs at a much better angular resolution. For example, the Murchison Widefield Array (MWA, Tingay et al., 2013) is able to reach an angular resolution of $2\farcm1$ at 150 MHz and a spectral resolution of 17 km s^{-1}. Additionally, observations of low-frequency CRRLs have benefited from upgrades in receiver technology, particularly the introduction of wideband receivers. Given that the separation between adjacent energy states decreases at large n, the frequency separation between CRRLs decreases at lower frequencies. This means that many CRRLs, corresponding to different values of n, can be observed simultaneously. Since the frequencies at which these lines appear are known, and when they trace the same gas, the lines can be stacked together to increase the signal-to-noise ratio of the observations (e.g., Stepkin et al., 2007; Oonk et al., 2014). These upgrades have motivated a re-flourishing of low-frequency CRRL studies, the main topic of this thesis.

1.2.1. Observations of carbon radio recombination lines powered by the Low Frequency Array

The Low Frequency Array (LOFAR van Haarlem et al., 2013) is an interferometer operating at frequencies between 10 MHz and 250 MHz. This frequency range is covered by two different types of dipoles: low band antennas (LBA, 10–90 MHz) and high band antennas (HBA, 120–250 MHz). The HBA dipoles are combined in a 4×4 tile with

Figure 1.6.: The innermost stations of LOFAR. The stations located in the central circular region, a *terp*, are know as the *superterp* stations. The LBA and HBA dipoles can be identified by their arrangement in the field. The LBA dipoles are distributed in a non-uniform way, while the HBA dipoles are arranged into compact groups.

an analog beamformer. The dipoles and tiles, with no moving parts, are grouped into stations, each one forming an independent phased array. Stations are further combined to form an array, and are distributed all over Europe, resulting in baselines of up to 1900 km. For the core stations of LOFAR (located in the Netherlands), the LBA stations consist of 96 dipoles, while the HBA stations have 48 tiles split into two fields. Of the 96 dipoles in a core LBA station 48 can be actively beamformed (Broekema et al., 2018). There are 24 stations in the core of LOFAR. The core stations are connected via fiber to a central clock, thus their signals can be added coherently to form a telescope with a maximum baseline of 3.5 km. The stations in the innermost 350 m are known as the *superterp*. An aerial view of the innermost stations of LOFAR is presented in Figure 1.6.

The characteristics of LOFAR make it a great instrument for the study of CRRLs at low frequencies. In particular, it has a dense core with baselines of up to 3.5 km and a large fractional bandwidth ($\Delta\nu/\nu \sim 0.5$). Its dense core gives it a good sensitivity to large scale structures (the largest angular scales recoverable by the array are 1.6° at 240 MHz and 2° at 90 MHz), while reaching an angular resolution of $10'$ at 30 MHz. And, its large fractional bandwidth enables observations of hundreds of CRRL transitions simultaneously. These capabilities have been exploited to produce the first detections of low-frequency CRRLs on sub-arcmin scales (Asgekar et al., 2013), in extragalactic sources (Morabito et al., 2014; Emig et al., 2018) and using extragalactic

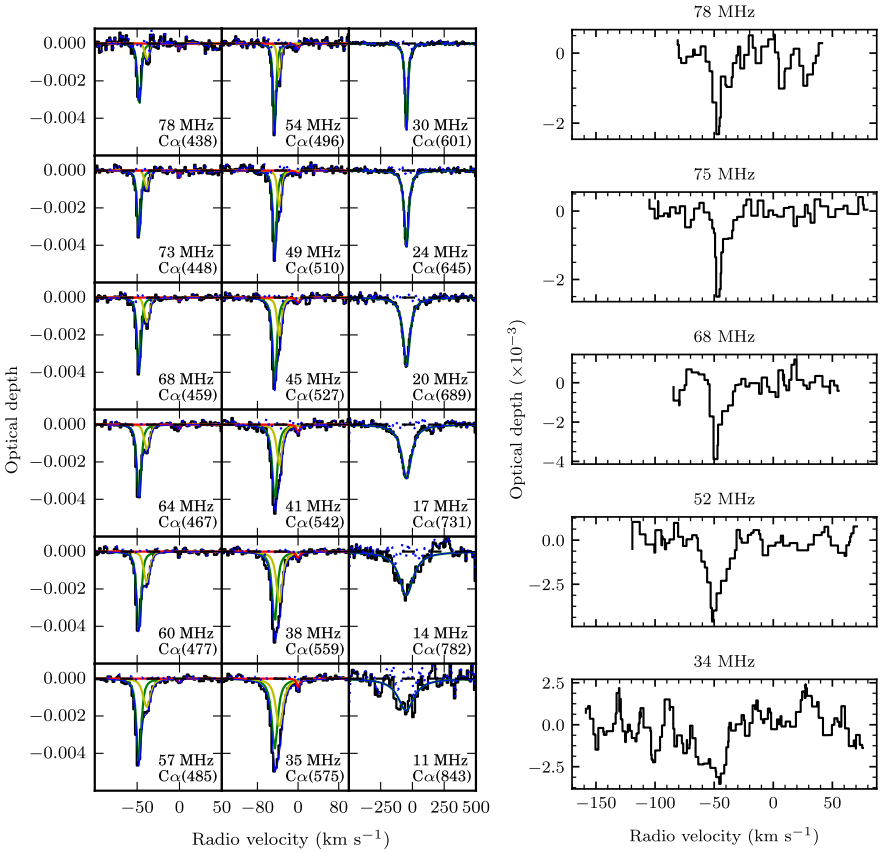

Figure 1.7.: Comparison between low-frequency CRRLs obtained with LOFAR (*left*) and previous telescopes (*right*). Both sets of CRRLs were observed against Cas A. The LOFAR observations were presented in Oonk et al. (2017) and in Chapter II of this thesis. The principal quantum number shown is the effective value for the stack. Previous observations were presented by Payne et al. (1989).

sources as background for Galactic studies (Oonk et al., 2014).

Figure 1.7 shows how LOFAR observations of CRRLs compare with previous observations. In this case the LOFAR observations were performed during three different periods to cover the full bandwidth of the LBA antennas with a spectral resolution of 3.5 km s^{-1} at 33 MHz (Oonk et al., 2017). The increased spectral resolution of these observations with respect to previous ones (e.g., Payne et al., 1989) enables the study of different velocity components along the line of sight. The high signal-to-noise ratio of the CRRLs observed with LOFAR (Figure 1.7) was achieved by stacking multiple transitions (20 per stack on average). This highlights the importance of having a large fractional bandwidth for radio recombination line studies. During the stacking process,

an iterative procedure was used in order to remove the instrumental bandpass response of the telescope (e.g., Stepkin et al., 2007; Salas et al., 2017).

Observations of CRRLs in our Galaxy using LOFAR have focused on a couple of regions so far: Cassiopeia A (Asgekar et al., 2013; Oonk et al., 2017; Salas et al., 2017, 2018), Orion A (Chapter IV, Salas et al. submitted) and the line of sight towards Cygnus A (Oonk et al., 2014). In order to fully exploit the capabilities of LOFAR and the potential of low-frequency CRRLs as tools to study the ISM, observations of larger portions of the Galaxy are required (e.g., Oonk et al., 2015). LOFAR has a field of view (FoV) of 2.4° at 240 MHz (for the core stations) and 90 MHz (using the outer dipole layout in the LBA stations). If we wanted to cover the Galactic plane observable from the northern hemisphere (roughly 180° along the plane) it would require 75 pointings separated by one FoV. For an integration time per pointing of eight hours, sufficient to detect the CNM down to a column density of 3×10^{20} cm^{-2}, it would take 1200 hours to cover the northern Galactic plane using the LBA (between 30 MHz and 90 MHz) and the HBA (between 120 MHz and 170 MHz).

A first attempt at obtaining large scale maps of low-frequency radio recombination lines in our Galaxy targeted the star forming region Cygnus X (Oonk et al. in prep.). In order to avoid the artifacts introduced during the inversion of the observed visibilities, caused by the lack of a zero spacing when observing the Galactic plane, and to limit the data volume, these maps were produced using the tied-array mode of LOFAR. In the tied-array mode the signals from the stations are added together coherently (this is the same as a phased array) instead of cross-correlating the signals (imaging mode). This reduces the amount of data considerably, as only one real valued output is produced for the whole array, instead of one complex-valued quantity for each baseline ($N(N-1)/2$ values for an array with N stations). Additionally, since there is no need to invert visibilities (the products of the cross-correlation between station voltages), the resulting maps do not have a mean flux of zero (as opposed to the imaging case when a baseline of zero length is not measured). This avoids the appearance of large negative bowls around the bright radio continuum of the Galactic plane. Despite these benefits, the use of tied-array observations removes the ability to calibrate the observations, as well as fixing the observed position on the sky (imaging observations are sensitive to the whole FoV of the stations, and more, while in tied-array mode the effective FoV is limited to the beam of the tied-array, $10'$ at 30 MHz for the core stations of LOFAR). Basically, tied-array observations trade flexibility for data volume.

As in synthesis imaging, tied-array observations also have the array beam imprinted on the resulting maps. That is, a map produced from tied-array observations is a dirty map (the convolution of the tied-array beam, dirty beam, with the sky distribution, e.g., Thompson et al., 2017), unless cleaned. Since in tied-array mode the time delays between stations cannot be calibrated, the dirty beam will not only be the Fourier transform of the station positions, but it will also contain any errors on the time delays present during the observations (e.g., the time delays introduced by the ionosphere, Crane, 1977). Thus, if we want to clean tied-array maps, we need a model of the dirty beam which also contains information about the time delays. For this reason we characterized the tied-array beam of the stations using radio holography (e.g., Scott & Ryle, 1977).

1.3. THIS THESIS

To understand the ISM we need to study different gas phases across different scales and that we piece it all together. What we know about these different phases is expanded by the use of different tracers, as they often provide complementary information. Here we focus on diffuse atomic clouds and the surface of molecular clouds as these are main reservoirs of interstellar gas, they feed molecular clouds, the star formation engines of the Galaxy, and they couple radiative and mechanical energy to the ISM. We do this by observing low-frequency CRRLs in our Galaxy using LOFAR. Previous studies of low-frequency CRRLs in our Galaxy have been hampered in their interpretation due to the lack of spatial information (e.g., Kantharia & Anantharamaiah, 2001). The unprecedented frequency coverage, and spatial and spectral resolution afforded by LOFAR, studies of CRRLs are now possible from degree to arcsecond scales. This opens up the low-frequency sky to systematic studies of the cold atomic and diffuse molecular gas. The spatial and velocity resolutions achieved by LOFAR are comparable to those of surveys of the ISM through other tracers, such as 21 cm HI and rotational transitions of CO in the millimeter (e.g., HI4PI Collaboration et al., 2016; Dame et al., 2001), a fundamental requirement for understanding the structure of the ISM.

In **Chapter II** we explore what can be learned from the lowest frequencies observable from Earth. Using LOFAR we observe CRRLs in the frequency range 10–30 MHz towards Cas A. These observations show that the integrated optical depth of the lines is roughly constant, indicating that the population of ionized carbon atoms is close to that in LTE. This result is qualitatively different from previous observations and theory, in which the integrated optical depth seemed to keep increasing towards low frequencies (Konovalenko, 1984; Ponomarev & Sorochenko, 1992). From the observed line widths, and their relative strengths, we were able to constrain the gas physical properties. Moreover, by adding the information provided by the far-infrared line of ionized carbon at 158 μm, we could determine the gas physical properties with an accuracy similar to that obtained by using observations of CRRLs over a larger frequency range (Oonk et al., 2017). In summary, the lowest frequency CRRLs provide a good barometer, while the ratio between radio and FIR carbon lines is a good thermometer.

In **Chapter III** we perform an analysis of the spatial distribution of low-frequency CRRLs towards Cas A. Using observations with a spatial resolution of $\approx 1'$ we explore the relation between CRRLs, the 21 cm line of HI and CO. We find that these tracers are arranged in a layered structure, reminiscent of the structure found in a PDR. Based on the spatial location of the CRRLs, sandwiched between the diffuse atomic gas and the dense molecular gas, we are able to establish that low-frequency CRRLs trace the interface between atomic and molecular gas. Using a set of four CRRLs (C268α, C357α, C494α and C539α) we determine the gas temperature and density over the face of Cas A. We find that the gas properties are comparable to those found from spatially unresolved studies (Oonk et al., 2017). Moreover, using the derived physical conditions, as well as other properties of the region derived independently, as input to a PDR model we predict the strength of the rotational lines of CO available and of the 158 μm-[CII] line. The PDR model predictions match the observed line strengths remarkably well, highlighting that low-frequency CRRLs provide accurate physical conditions.

In **Chapter IV** we use new and archival observations of CRRLs over a wide frequency range (230 GHz to 150 MHz) to study the star forming region Orion A. This is the largest frequency coverage of CRRLs of a single region, including the first two detections of CRRLs in absorption towards this source. We complement the CRRL data with SOFIA observations of the 158 μm-[CII] line. The use of CRRLs over a wide frequency range enables us to study two PDRs found in this region: the foreground Veil and the dense PDR between the HII region and the background molecular cloud. In the Veil we are able to determine the gas temperature and electron density, which we use to measure the ionization parameter and the photoelectric heating efficiency. In the dense PDR, we are able to identify a layered PDR structure at the surface of the molecular cloud to the South of the Trapezium. There we find that the radio lines trace the colder portion of the ionized carbon layer, the C^+/C/CO interface. We explore the ratios of three CRRLs, C30α, C65α and C91α, and find that they alone can be used to constrain the gas temperature and electron density. Our work also highlights the potential of CRRLs as probes of molecular gas formation. By modeling the emission of the 158 μm-[CII] line and CRRLs as arising from a PDR we derive a thermal pressure $\approx 8 \times 10^7$ K cm^{-3} and a radiation field $G_0 \approx 10^4$ close to the Trapezium, and lower values as we move away from it. This work provides additional observational support for the use of CRRLs and the 158 μm-[CII] line as complementary tools to study dense and diffuse PDRs.

Chapter V presents the characterization of the core stations of LOFAR using radio holography. Radio holography is a technique by which the complex-valued beam of a telescope can be measured. Along radio holography, we apply a new calibration method which enables us to obtain a higher signal-to-noise ratio in the observed complex-valued beam maps. From the complex-valued beam of the telescope we infer the time delays of its stations. For short (60 s and 600 s) radio holographic observations of 3C196, 3C147 and 3C48 we are able to derive time delays with errors smaller than one ns, under good ionospheric conditions. We use the derived time delays to update the instrumental time delays in the digital beamformer. For the HBA this leads an improvement of 28% in its sensitivity at 115 MHz, and up to 75% at 165 MHz. For observations with the LBA the sensitivity improves by a factor of six at the center of the frequency band, close to 55 MHz, and larger at higher frequencies. The results from this chapter show that radio holography is a powerful method to calibrate the instrumental time delays applied by the digital beamformer. In the future it should be possible to perform this calibration in real time, providing, for the first time, tied-array observations in which the effects of the ionosphere are accounted for.

1.4. Moving forward

As this thesis shows, observations of low-frequency CRRLs offer a unique perspective to explore the ISM. They trace cold gas, atomic and diffuse molecular, are excellent probes of the gas physical conditions (e.g., temperature and electron density) and kinematics, and they can be mapped over large areas. In the future it should be possible to construct a temperature and density map of the gas in our Galaxy using CRRLs. For this, the next step is a survey of low-frequency CRRLs on the northern hemisphere

using LOFAR.

A survey of low-frequency CRRLs with LOFAR would be a big leap in our understanding of the ISM. This survey would provide cubes of C$n\alpha$ CRRLs with principal quantum numbers between 297 and 869. These observations would map the gas traced by CRRLs over the disk of the Milky Way with a spatial resolution of $10'$ and a spectral resolution of ≈ 1 km s^{-1}, enabling us to determine the temperature and density of the gas and how stellar feedback couples to the ISM. These would be the first spatially and velocity resolved maps of cold atomic and *CO-dark* molecular gas of the galactic disk.

Moreover, CRRL observations would also enable us to measure the strength of the magnetic field. Using Zeeman splitting measurements of CRRLs it would be possible to probe the magnetic field over large regions of the galactic disk. Low-frequency observations of Zeeman splitting are particularly interesting, since the frequency width of the lines, $\Delta\nu$, narrows towards lower frequencies while the Zeeman splitting, $\Delta\nu_Z$, remains constant. In the regime where $\Delta\nu_Z > \Delta\nu$ it is possible to directly measure the strength of the magnetic field (e.g., Heiles et al., 1993).

Another advantage of low-frequency CRRL observations with LOFAR is that with the same observational setup it is also possible to observe HRRLs. With a mass difference of ≈ 12, HRRLs are shifted from CRRLs by a velocity of 149.4 km s^{-1}. The study of low-frequency HRRLs has suffered from the same limitations as that of CRRLs. With LOFAR it is now possible to observe HRRLs with a spatial resolution of $10'$. These observations would shed light on the presence of dense ionized gas in our Galaxy (e.g., Goldsmith et al., 2015).

In the future, the Square Kilometer Array (SKA) will be the world largest radio interferometer, operating between 50 MHz and 14 GHz. It will cover this frequency range with two different arrays, the SKA-low (between 50 MHz and 350 MHz) and the SKA-mid (between 350 MHz and 14 GHz). SKA-low promises to deliver a sensitivity eight times better than that of LOFAR. Both SKA-low and SKA-mid will be commissioned in two phases, the first phase will deliver a fraction of the total collecting area. For SKA-low, during the first phase 476 of the 512 stations will be constructed, with a maximum baseline of 40 km. As of 2017, the brightness sensitivity of SKA-low during phase 1 (SKA-low1) is expected to be roughly 23 mK at 160 MHz, for an integration time of 8 hours, an angular resolution of $4\farcm2$, and a channel width of 4.2 kHz. And 260 mK at 50 MHz, with an angular resolution of $13\farcm4$. This implies that on arcminute scales, it will be possible to detect CRRLs ($\tau \sim 1 \times 10^{-3}$) all over the Galactic plane at longitudes $|b| < 5°$, using the Galactic synchrotron emission as background. This is not considering that we can stack several CRRLs to detect weaker lines (there are 243 C$n\alpha$ lines between 50 MHz and 350 MHz).

At lower frequencies, between 85 MHz and 10 MHz, the new extension in Nançay upgrading LOFAR (NenuFAR) will have a collecting area equivalent to that of 38 LOFAR stations, and it will be able to reach an angular resolution of $23'$ at 15 MHz. This increase in collecting area will enable the detection of low-frequency RRLs from regions where the gas column densities are lower. Moreover, NenuFAR will be sensitive to larger angular scales than LOFAR. This makes NenuFAR a great instrument to study neutral and partially ionized gas outside the disk of the Milky Way, and its properties on large scales.

On the higher frequency end ($>$ 1 GHz) the next generation Very Large Array (ngVLA, 1–116 GHz) and SKA-mid (0.35–14 GHz) will improve over the sensitivity of existing telescopes. Higher frequency RRLs trace denser gas than their low-frequency counterparts. Thus, the combined use of RRLs over the whole radio regime will enable us to study the properties of HII regions, and how the radiation emitted by the massive stars that power them interact with the dense molecular clouds that surround them, how it escapes these regions, and how then it couples to the diffuse ISM. Providing the observational information required to understand stellar feedback.

BIBLIOGRAPHY

Allen, R. J., Hogg, D. E., & Engelke, P. D. 2015, AJ, 149, 123

Anantharamaiah, K. R., Erickson, W. C., Payne, H. E., & Kantharia, N. G. 1994, ApJ, 430, 682

Anantharamaiah, K. R., Erickson, W. C., & Radhakrishnan, V. 1985, Nature, 315, 647

Asgekar, A., Oonk, J. B. R., Yatawatta, S., et al. 2013, A&A, 551, L11

Bakes, E. L. O., & Tielens, A. G. G. M. 1994, ApJ, 427, 822

Ball, J. A., Cesarsky, D., Dupree, A. K., Goldberg, L., & Lilley, A. E. 1970, ApJL, 162, L25

Beerer, I. M., Koenig, X. P., Hora, J. L., et al. 2010, ApJ, 720, 679

Blake, D. H., Crutcher, R. M., & Watson, W. D. 1980, Nature, 287, 707

Blitz, L., & Rosolowsky, E. 2006, ApJ, 650, 933

Broekema, P. C., Mol, J. J. D., Nijboer, R., et al. 2018, Astronomy and Computing, 23, 180

Burton, M. 2004, in IAU Symposium, Vol. 213, Bioastronomy 2002: Life Among the Stars, ed. R. Norris & F. Stootman, 123

Burton, M. G., Hollenbach, D. J., & Tielens, A. G. G. M. 1990, ApJ, 365, 620

Chaisson, E. J. 1971, ApJ, 170, 81

Crane, R. K. 1977, IEEE Proceedings, 65, 180

Dame, T. M., Hartmann, D., & Thaddeus, P. 2001, ApJ, 547, 792

de Jong, T. 1977, A&A, 55, 137

Draine, B. T. 1978, ApJS, 36, 595

Dupree, A. K. 1972, ApJ, 173, 293

—. 1974, ApJ, 187, 25

Dupree, A. K., & Goldberg, L. 1969, ApJL, 158, L49

Elmegreen, B. G. 2007, ApJ, 668, 1064

Elmegreen, B. G., & Lada, C. J. 1977, ApJ, 214, 725

Emig, K. L., Salas, P., de Gasperin, F., et al. 2018, arXiv e-prints

Emsley, J. 1998, The Elements, Oxford chemistry guides (Clarendon Press)
Engelke, P. D., & Allen, R. J. 2019, arXiv e-prints
Erickson, W. C., McConnell, D., & Anantharamaiah, K. R. 1995, ApJ, 454, 125
Ershov, A. A., Ilyashov, Y. P., Lekht, E. E., et al. 1984, Soviet Astronomy Letters, 10, 348
Ershov, A. A., Lekht, E. E., Rudnitskii, G. M., & Sorochenko, R. L. 1982, Soviet Astronomy Letters, 8, 374
Ferrière, K. M. 2001, Reviews of Modern Physics, 73, 1031
Field, G. B., Goldsmith, D. W., & Habing, H. J. 1969, ApJL, 155, L149
Gazol, A., Vázquez-Semadeni, E., & Kim, J. 2005, ApJ, 630, 911
Goldberg, L., & Dupree, A. K. 1967, Nature, 215, 41
Goldsmith, P. F., Pineda, J. L., Neufeld, D. A., et al. 2018, ApJ, 856, 96
Goldsmith, P. F., Yıldız, U. A., Langer, W. D., & Pineda, J. L. 2015, ApJ, 814, 133
Gordon, M. A., & Sorochenko, R. L., eds. 2009, Astrophysics and Space Science Library, Vol. 282, Radio Recombination Lines
Grenier, I. A., Casandjian, J.-M., & Terrier, R. 2005, Science, 307, 1292
Haffner, L. M., Dettmar, R.-J., Beckman, J. E., et al. 2009, Reviews of Modern Physics, 81, 969
Heiles, C. 1994, ApJ, 436, 720
—. 2001, ApJL, 551, L105
Heiles, C., Goodman, A. A., McKee, C. F., & Zweibel, E. G. 1993, in Protostars and Planets III, ed. E. H. Levy & J. I. Lunine, 279–326
Heiles, C., & Troland, T. H. 2003, ApJ, 586, 1067
HI4PI Collaboration, Ben Bekhti, N., Flöer, L., et al. 2016, A&A, 594, A116
Hoang-Binh, D., & Walmsley, C. M. 1974, A&A, 35, 49
Hollenbach, D. J., & Tielens, A. G. G. M. 1999, Reviews of Modern Physics, 71, 173
Kalberla, P. M. W., Burton, W. B., Hartmann, D., et al. 2005, A&A, 440, 775
Kalberla, P. M. W., & Haud, U. 2018, A&A, 619, A58
Kalberla, P. M. W., & Kerp, J. 2009, ARA&A, 47, 27
Kalberla, P. M. W., Schwarz, U. J., & Goss, W. M. 1985, A&A, 144, 27
Kantharia, N. G., & Anantharamaiah, K. R. 2001, Journal of Astrophysics and Astronomy, 22, 51
Kantharia, N. G., Anantharamaiah, K. R., & Payne, H. E. 1998, ApJ, 506, 758
Kim, C.-G., & Ostriker, E. C. 2017, ApJ, 846, 133
Kim, C.-G., Ostriker, E. C., & Kim, W.-T. 2013, ApJ, 776, 1
Kiminki, D. C., Kobulnicky, H. A., Vargas Álvarez, C. A., Alexander, M. J., & Lundquist, M. J. 2015, ApJ, 811, 85
Knödlseder, J. 2000, A&A, 360, 539
Konovalenko, A. A. 1984, Soviet Astronomy Letters, 10, 353
Konovalenko, A. A., & Sodin, L. G. 1980, Nature, 283, 360
—. 1981, Soviet Astronomy Letters, 7, 221
Langer, W. D., Velusamy, T., Pineda, J. L., Willacy, K., & Goldsmith, P. F. 2014, A&A, 561, A122
Lekht, E. E., Smirnov, G. T., & Sorochenko, R. L. 1989, Soviet Astronomy Letters, 15, 171

Mac Low, M.-M., & Klessen, R. S. 2004, Reviews of Modern Physics, 76, 125
Mathis, J. S., Mezger, P. G., & Panagia, N. 1983, A&A, 128, 212
McKee, C. F., & Ostriker, E. C. 2007, ARA&A, 45, 565
Mellinger, A. 2009, PASP, 121, 1180
Morabito, L. K., Oonk, J. B. R., Salgado, F., et al. 2014, ApJL, 795, L33
Murray, C. E., Stanimirović, S., Goss, W. M., et al. 2015, ApJ, 804, 89
Murray, N. 2011, ApJ, 729, 133
Oonk, J. B. R., van Weeren, R. J., Salas, P., et al. 2017, MNRAS, 465, 1066
Oonk, J. B. R., van Weeren, R. J., Salgado, F., et al. 2014, MNRAS, 437, 3506
Oonk, R., Morabito, L., Salgado, F., et al. 2015, Advancing Astrophysics with the Square Kilometre Array (AASKA14), 139
Pabst, C. H. M., Goicoechea, J. R., Teyssier, D., et al. 2017, A&A, 606, A29
Palmer, P., Zuckerman, B., Penfield, H., & Lilley, A. E. 1967, Nature, 215, 40
Payne, H. E., Anantharamaiah, K. R., & Erickson, W. C. 1989, ApJ, 341, 890
—. 1994, ApJ, 430, 690
Pedlar, A. 1970, Nature, 226, 830
Piddington, J. H., & Minnett, H. C. 1952, Australian Journal of Scientific Research A Physical Sciences, 5, 17
Pineda, J. L., Langer, W. D., Velusamy, T., & Goldsmith, P. F. 2013, A&A, 554, A103
Planck Collaboration, Ade, P. A. R., Aghanim, N., et al. 2011, A&A, 536, A19
Ponomarev, V. O., & Sorochenko, R. L. 1992, Soviet Astronomy Letters, 18, 215
Röllig, M., Ossenkopf, V., Jeyakumar, S., Stutzki, J., & Sternberg, A. 2006, A&A, 451, 917
Roshi, D. A., & Kantharia, N. G. 2011, MNRAS, 414, 519
Roshi, D. A., Kantharia, N. G., & Anantharamaiah, K. R. 2002, A&A, 391, 1097
Rygl, K. L. J., Brunthaler, A., Sanna, A., et al. 2012, A&A, 539, A79
Salas, P., Oonk, J. B. R., van Weeren, R. J., et al. 2018, MNRAS, 475, 2496
—. 2017, MNRAS, 467, 2274
Salgado, F., Morabito, L. K., Oonk, J. B. R., et al. 2017, ApJ, 837, 141
Schaye, J., Crain, R. A., Bower, R. G., et al. 2015, MNRAS, 446, 521
Scott, P. F., & Ryle, M. 1977, MNRAS, 178, 539
Snowden, S. L., Egger, R., Freyberg, M. J., et al. 1997, ApJ, 485, 125
Sofia, U. J., Lauroesch, J. T., Meyer, D. M., & Cartledge, S. I. B. 2004, ApJ, 605, 272
Spitzer, Jr., L. 1948, ApJ, 107, 6
Stecher, T. P., & Williams, D. A. 1967, ApJ, 149, L29
Stepkin, S. V., Konovalenko, A. A., Kantharia, N. G., & Udaya Shankar, N. 2007, MNRAS, 374, 852
Sternberg, A., & Dalgarno, A. 1989, ApJ, 338, 197
Tang, N., Li, D., Heiles, C., et al. 2016, A&A, 593, A42
Thompson, A. R., Moran, J. M., & Swenson, Jr., G. W. 2017, Interferometry and Synthesis in Radio Astronomy, 3rd Edition
Tielens, A. G. G. M. 2010, The Physics and Chemistry of the Interstellar Medium
Tielens, A. G. G. M., & Hollenbach, D. 1985, ApJ, 291, 722
Tingay, S. J., Goeke, R., Bowman, J. D., et al. 2013, PASA, 30, e007
van Dishoeck, E. F., & Black, J. H. 1986, ApJS, 62, 109

van Haarlem, M. P., Wise, M. W., Gunst, A. W., et al. 2013, A&A, 556, A2
Vázquez-Semadeni, E. 2012, in EAS Publications Series, Vol. 56, EAS Publications Series, ed. M. A. de Avillez, 39–49
Visser, R., van Dishoeck, E. F., & Black, J. H. 2009, A&A, 503, 323
Vrinceanu, D., Onofrio, R., & Sadeghpour, H. R. 2012, ApJ, 747, 56
Walch, S. K. 2014, in Astrophysics and Space Science Proceedings, Vol. 36, The Labyrinth of Star Formation, ed. D. Stamatellos, S. Goodwin, & D. Ward-Thompson, 173
Walmsley, C. M., & Watson, W. D. 1982, ApJ, 260, 317
Watson, W. D. 1972, ApJ, 176, 103
Watson, W. D., Western, L. R., & Christensen, R. B. 1980, ApJ, 240, 956
Weingartner, J. C., & Draine, B. T. 2001, ApJS, 134, 263
Wolfire, M. G., Hollenbach, D., & McKee, C. F. 2010, ApJ, 716, 1191
Wolfire, M. G., Hollenbach, D., McKee, C. F., Tielens, A. G. G. M., & Bakes, E. L. O. 1995, ApJ, 443, 152
Wolfire, M. G., McKee, C. F., Hollenbach, D., & Tielens, A. G. G. M. 2003, ApJ, 587, 278
Zuckerman, B., & Ball, J. A. 1974, ApJ, 190, 35
Zuckerman, B., & Palmer, P. 1968, ApJL, 153, L145
—. 1970, A&A, 4, 244

II

LOFAR OBSERVATIONS OF DECAMETER CARBON RADIO RECOMBINATION LINES TOWARDS CASSIOPEIA A

2.1. INTRODUCTION

Radio recombination lines (RRLs) are an important diagnostic tool to study the properties of the interstellar medium (ISM) in galaxies (e.g., Gordon & Sorochenko, 2009). The population of carbon ions in a given n level is determined by the gas density, temperature and radiation field, as well as the atomic physics involved (e.g., Shaver, 1975; Watson et al., 1980; Salgado et al., 2017a). By comparing the optical depth of carbon radio recombination lines (CRRLs) for a set of levels the gas properties can be determined.

Low frequency CRRLs have been observed towards a number of galactic sources (Konovalenko, 1984; Erickson et al., 1995; Roshi & Anantharamaiah, 2000; Kantharia & Anantharamaiah, 2001) and in particular against the bright radio source Cassiopeia A (Cas A, e.g. Konovalenko & Sodin, 1981; Ershov et al., 1982; Konovalenko, 1984; Anantharamaiah et al., 1985; Lekht et al., 1989; Payne et al., 1989; Anantharamaiah et al., 1994; Payne et al., 1994; Stepkin et al., 2007; Asgekar et al., 2013; Oonk et al., 2017). Towards Cas A three velocity components have been identified in CRRL emission and absorption (e.g., Payne et al., 1989), which correspond to gas located in the Perseus arm of the Galaxy and the Orion spur. Recent analysis by Oonk et al. (2017) has shown that the Perseus arm gas traced by low frequency CRRLs has a temperature of ~ 85 K, an electron density of ~ 0.04 cm^{-3} and large column densities ($N_{\rm H} \sim 10^{22}$ cm^{-2}). These properties suggest that the gas traced by CRRLs is in the interface between atomic (e.g., Shuter & Verschuur, 1964; Davies & Cummings, 1975; Bieging et al., 1991; Schwarz et al., 1997) and molecular gas (e.g., Liszt & Lucas, 1999; Mookerjea et al., 2006; Kilpatrick et al., 2014). The data used by Oonk et al. (2017) consisted of observations between 300–390 MHz and 33–78 MHz obtained with the Westerbork radio telescope (WSRT) and the low frequency array (LOFAR) respectively.

Previous low frequency CRRL observations and models have suggested that at lower frequencies ($\nu < 33$ MHz) the integrated optical depth of the CRRLs increases with increasing principal quantum number (e.g., Payne et al., 1994). This would make observations below 33 MHz particularly interesting, since (i) given the large integrated optical depths involved the lines should be easily detected, and (ii) at these low frequencies, collisional and radiation broadening of RRLs provide insight into the physical conditions of the emitting gas (Shaver, 1975; Salgado et al., 2017a,b).

Low-frequency observations are hindered by ionospheric phase distortions, scintillation, and strong radio frequency interference (RFI). Below 20 MHz these observations are very difficult due to the plasma frequency cutoff which is typically located around 10 MHz, but varies depending on the ionospheric conditions (e.g., Budden, 1985; Fields et al., 2013). Nevertheless, CRRLs have been detected at frequencies as low as 12 MHz (Konovalenko et al., 2002).

Previous $\nu < 33$ MHz studies have been carried out with the UTR-2 telescope in Ukraine (Braude et al., 1978). Using this telescope Konovalenko & Sodin (1980) reported the detection of a spectral line at 26 MHz towards Cas A, which was later identified as a CRRL with principal quantum number $n = 631$ (Blake et al., 1980; Konovalenko & Sodin, 1981). They also reported the detection of six Cα lines between 16.7 and 29.9 MHz (Konovalenko, 1984), and more recently showed a spectrum of five Cα lines around 20 MHz and a number of Cβ lines (Konovalenko, 2002). These studies showed that the line peak optical depth decreases while the line width increases when the frequency decreases. Stepkin et al. (2007) reported the detection of Cα, Cβ, Cγ and Cδ lines towards Cas A at 26 MHz. Their detection of a Cδ line sets the record for the largest bound atom ever detected with a principal quantum number $n \sim 1000$.

LOFAR, operating at 10–240 MHz (van Haarlem et al., 2013) provides a new opportunity to study RRLs at frequencies down to 10 MHz. Due to its large bandwidth, hundreds of lines can be detected in a single observation. This opens up the possibility to study a broad range in principal quantum number with the same telescope. The LOFAR low band antenna (LBA) operates in the frequency range 10–90 MHz. Previous LOFAR studies have focused on the higher frequency range (33–70 MHz) of the LBA (Asgekar et al., 2013; Oonk et al., 2014; Morabito et al., 2014; Oonk et al., 2017) as the sensitivity of the LBA peaks in this frequency range (van Haarlem et al., 2013).

In this paper we report on LOFAR LBA observations of Cas A between 10 and 33 MHz, the lowest frequency range LOFAR can reach. Our aim is to (i) determine if observations with LOFAR in this frequency range can yield CRRL detections, (ii) test if the integrated optical depth of the lines at high principal quantum number increases as suggested by previous observations, (iii) determine how low frequency CRRL observations can be used to constrain the physical conditions of the cold ISM.

The observations and data reduction are described in Sect. 2.2. The results are presented in Sect. 2.3 and then compared with models and previous results in 2.4. This is followed by our conclusions in Sect. 2.5.

Table 2.1.: LBA low observations

Observations ID	L69891, L69893
Integration time per visibility	1 s
Observation dates	20, 21 October 2012 (15:00-01:00 UT)
Total on-source time	10 hr, 10 hr
Correlations	XX, XY, YX, YY
Frequency setup	10–33 MHz full coverage
Bandwidth per subband	195.3125 kHz
Channels per subband	512
Channel width	4–12 km s^{-1}

2.2. Observations & data reduction

2.2.1. LOFAR observations

Cas A was observed with the LOFAR LBA for two separate runs on October 20 and 21, 2012 for a total integration time of 20 hr. This data were taken as part of the Lofar Cassiopeia A Spectral Survey (LCASS, PI, J. B. R. Oonk). An overview of the observations is given in Table 2.1. During the time of the observations 34 Dutch LOFAR stations were available. For the L69891 observation 26 stations recorded good data, while for L69893 this number was reduced to 21 due to ongoing upgrades. The entire 10–33 MHz range was covered with 195.3125 kHz wide subbands. Each subband had a total of 512 channels, providing a channel width of $\sim$ 380 Hz or $\sim$ 4–12 km s^{-1}.

The first and last 25 channels of each subband were flagged due to the bandpass roll-off. To mitigate the effect of RFI, we flagged the data using *AOFlagger* (Offringa et al., 2010, 2012). The percentage of data flagged due to RFI varied drastically across the band from about 20% at 30 MHz to 40% at 20 MHz and 70% at 15 MHz, see Figure 2.1. We also removed the last three hours of both datasets due to severe scintillation, although this part of the data was less affected by RFI by a factor of two to three. We note that especially the first part of the observations were heavily affected by RFI, while the situation improved considerably after 23:00 UT for both datasets. Although the data were affected by scintillation after 22:00 UT, it suggests that night time observations are required to avoid severe RFI below 30 MHz.

The data were then calibrated against a $11\farcs2 \times 9\farcs8$ resolution 69 MHz model of Cas A (Oonk et al., 2017). The calibration was performed with the New Default Processing Pipeline (*NDPPP*) package which is part of the standard LOFAR software. Below 16 MHz we could not obtain good gain solutions for several time ranges during the observations. These time ranges were also flagged and thus increase the percentage of flagged data (Figure 2.1). Most likely, these periods correspond to severe ionospheric distortions. These are expected at low frequencies since the observations are carried out not far from the plasma cutoff frequency. However, signal from Cas A was observed all the way down to 10 MHz for certain time ranges. The LOFAR bandpass is very smooth

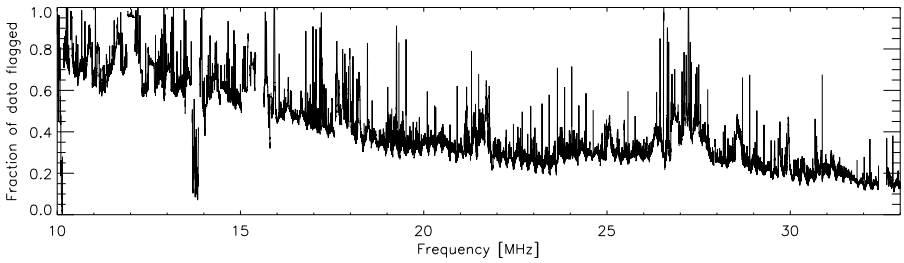

Figure 2.1.: Fraction of data flagged due to RFI or bad calibration solutions as function of frequency for the L69891 dataset (results for L69893 are very similar). The frequency width is the same as the one used in the observations, i.e., 380 Hz.

and, except for the bandpass roll-off regions (about 5 to 10 percent on either side of a subband) is well fit by a low order polynomial. To estimate how well a polynomial corrects the subband bandpass we also derived a bandpass calibration using Cygnus A. We find that the results obtained from a polynomial are equivalent to those obtained with Cygnus A. However, given that brightness of Cygnus A is comparable to that Cas A at these frequencies, using Cygnus A leads to a slightly higher spectral noise (by about a factor $\sqrt{2}$). We therefore use a low order polynomial to correct our subband spectra for the bandpass shape.

Image cubes were made with *AWImager* (Tasse et al., 2013) by splitting and imaging one channel at a time. The images were convolved with a Gaussian beam with a size ranging between $23'$ at 10 MHz and $5'$ at 30 MHz. Given the size of the convolving beam the background source is unresolved (Cassiopeia A has a radius of $\sim 2.5'$ at 74 MHz, e.g., DeLaney et al., 2014; Oonk et al., 2017). Spectra were then extracted from a tight box around the source at each channel. We combined the spectra from the two different runs by weighting with the fraction of usable data at the corresponding frequency. Channels whose amplitude deviated more than 1σ from the median were removed. To determine the median we used a running median window filter with a box size of five channels. σ was determined using Tukey's biweight (e.g. Equation (9) in Beers et al., 1990). This typically resulted in less than 10% of the data being flagged. We also discard any channels where the percentage of flagged data deviated more than 5% from the median amount of flagged data in the subband (see the bottom panel of Figure 2.2).

In each subband we estimate the continuum level by fitting a linear function to line free channels. Then the spectra are converted to optical depth units using (e.g., Oonk et al., 2014)

$$\tau_\nu = I_\nu / I_\nu^{\mathrm{cont}} - 1. \tag{2.1}$$

Here I_ν is the spectrum extracted from the data cubes and I_ν^{cont} is the continuum determined from line free channels. Of the 286 Cα lines observable in the 10–33 MHz range, 219 were observed. Missing lines lie in the subband gaps or close to flagged edge channels.

2.2.2. Herschel PACS archival data

Cas A was observed with the Photoconductor Array Camera and Spectrometer (PACS, Poglitsch et al., 2010) instrument onboard the Herschel space observatory (Pilbratt et al., 2010) during January 2011 (observation IDs: 1342212243–1342212260). These observations consist of nine footprints, each with 5×5 spaxels of $9\farcs4 \times 9\farcs4$. These nine PACS footprints cover $\sim$ 20% of Cas A. The observations were made using range spectrography scans between 140–210 μm with a 30 km/s sampling near the 158 μm line. To remove the instrument response, the chopping/nodding mode was used. However, the off source scans show significant line emission at the same velocity as the on source spectra. Because of this we used the on source spectra without removing the off source spectra. To separate on and off-source scans *HIPE* version 14.0.0 was used (Ott, 2010).

2.2.3. CRRL Stacking

Since the 10–33 MHz range is heavily populated by CRRLs we used a procedure similar to that of Stepkin et al. (2007) to stack individual lines and obtain robust line profiles. This stacking procedure also helps in removing residual bandpass structure. First we searched the spectra for Cα and Cβ lines that were not blended with other lines, were not heavily affected by RFI and were far from the subband bandpass roll-off. We stacked these lines in the frequency ranges indicated in Figures 2.3 and 2.4. The stacking was performed by interpolating to a regular grid in velocity, with a bin size equal to the coarsest velocity resolution of the spectra included in the stack. Each individual spectrum was weighted by the inverse of its channel to channel variance.

The stacked spectra were then fitted with a Voigt profile centred at -47 km s^{-1}. Using the results of the fit to the stacked Cα and Cβ lines we then subtracted the best fit Voigt profile from each spectrum. In the Cα and Cβ subtracted spectrum we searched for Cγ lines that were far from the roll-off of the subband bandpass, not blended with Cδ lines and not heavily affected by RFI. These Cγ lines were stacked in 4 frequency ranges. Of these ranges, only one yields a detection, see Figure 2.5. In the remaining frequency ranges the signal-to-noise is below 3σ. The Cγ stacks were fitted with a Voigt profile. The best fit Cγ Voigt profile was also removed from the Cα and Cβ free spectra. In the residual spectra we then searched for Cδ lines by stacking all the available transitions in 2 frequency ranges. These yielded non detections with 3σ upper limits on the peak optical depth of 10^{-4} for $n = 1020$ and 2×10^{-4} for $n = 1248$. The Cδ stack was also removed from the spectra. After this we performed a baseline correction on the line removed spectra using a polynomial of order 0. Using the baseline corrected spectra we repeated the stacking of the lines. This was repeated 5 times increasing the polynomial order by 1 in each step. Finally, spectra with only one kind of transition were obtained by removing the corresponding best fit Voigt profiles from the spectra. The final Cα, Cβ and Cγ spectra are shown in Figures 2.3, 2.4 and 2.5 respectively. In the final spectra, lines which were partially flagged due to RFI were also included.

Payne et al. (1994) showed that a finite bandwidth combined with a baseline removal process can cause systematic biases in the observed line profiles. To test whether the

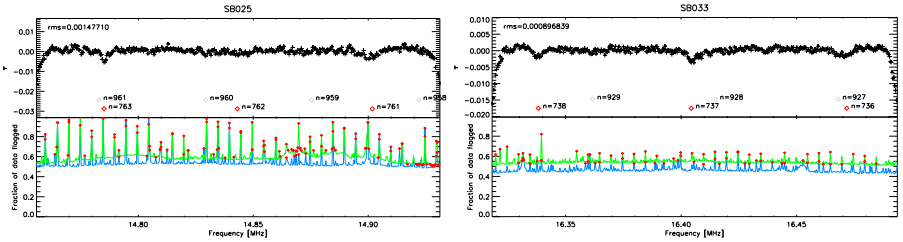

Figure 2.2.: Spectra of two individual subbands, 25 and 33. The *top* panels show the optical depth τ as function of frequency. The *red diamonds* show the location of Cα lines, while the empty labels those of Cβ. The *bottom* panels show the percentage of data flagged for the L69891 and L69893 datasets in blue and green respectively. *Red diamonds* mark channels which were removed because their flagging percentage is larger than 5% that of the subband mean.

stacking and baseline removal procedure combined with the correlator setup used introduces any biases in the measured line properties we performed a test using synthesised spectra. The synthetic spectra are generated with known line properties. These synthetic spectra are stacked in the same way as the observed data, including the baseline and line removal (e.g., removing the Cβ, Cγ and Cδ lines from the Cα stack) steps. Then, by comparing the known input model properties with the measured line properties after stacking we can determine if the measured line properties are distorted by the stacking procedure. The tests show that without baseline and line removal the line properties are up to 40% different from those of the input model. If we apply the baseline and line removal during stacking the difference is less than 15%, where the highest n data is the hardest to recover. From this we conclude that baseline corrections on scales larger than the line width and line removal help recover the line profiles. These tests also show that we can recover the line properties of the dominant velocity component at -47 km s^{-1}. To do so we need to fit three velocity components up to $n \approx 650$ and two components from $n = 650$ to 700. The details of these simulations can be found in the Appendix.

2.3. Results

We display examples of individual subband spectra in Figure 2.2. Individual Cα lines are visible above 16 MHz. The peak optical depth ranges from 4.6×10^{-3} at 30 MHz to 2×10^{-3} at 11 MHz. Individual Cβ lines are visible above $\nu \gtrsim 28$ MHz.

The line profiles obtained after stacking are shown in Figures 2.3, 2.4 and 2.5. These Figures show how the line width increases while the peak optical depth decreases towards lower frequencies. The Cα stacks show detections down to the lowest frequency of 10.96 MHz, with a signal-to-noise ratio of 3.7σ. To our knowledge this is the lowest frequency detection of a Cα line to date.

The line centroid is found to be offset by -47 km s^{-1} with respect to the local standard of rest, $v_{\rm LSR}$, as expected from all previous CRRL observations in the direction of Cas A. This velocity is coincident with the strongest HI absorption component observed against

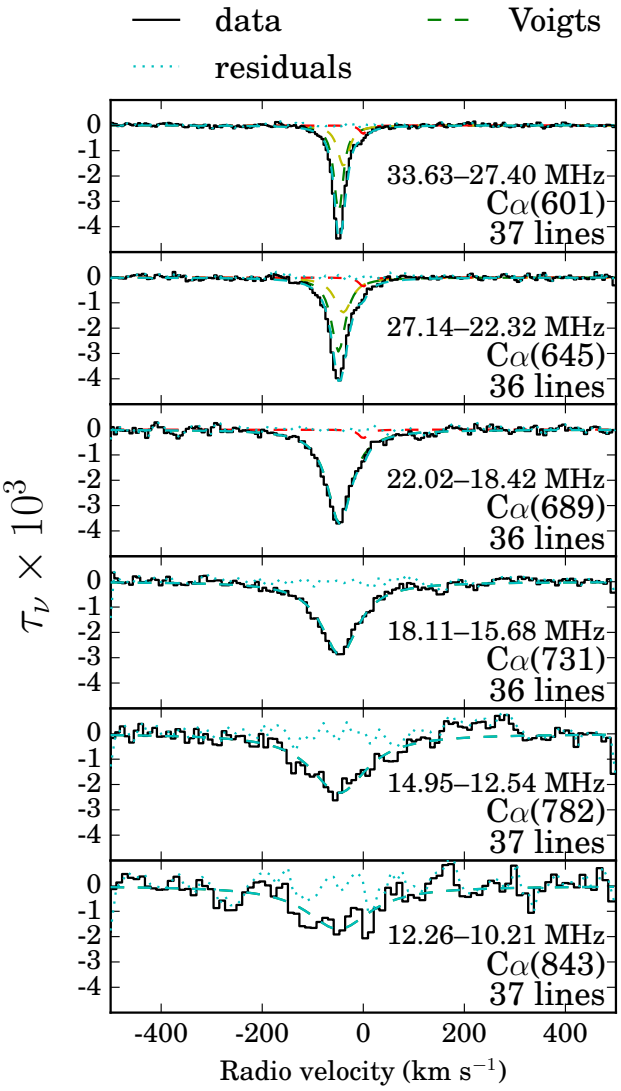

Figure 2.3.: Stacked Cα spectra. The *black steps* show the stacked spectra after processing, the *green*, *yellow* and *red dashed lines* show the best fitting Voigt profiles for the different components, the *cyan dashed line* shows the combined best fit Voigt profile and the *cyan dotted line* shows the residuals. The spectra are shown in optical depth units.

Cas A and it is associated with gas in the Perseus arm of our Galaxy (e.g., Davies & Cummings, 1975). Spectra of CRRLs at higher frequencies, where the line broadening is not as severe and the velocity resolution is better, show that along this line of sight 2 additional velocity components can be identified. One is at -38 km s^{-1}, also associated with the Perseus arm of the Galaxy, and the other is at 0 km s^{-1}, associated with the Orion spur (e.g., Payne et al., 1989).

2.3.1. Line fitting

CRRLs

Based on the results of the fits to the simulated line profiles we use a different number of Voigt profiles to fit the stacked lines. The number of profiles is determined by requiring that the residuals are reduced by more than a factor of two while still recovering reasonable line parameters. For $n < 650$ using three profiles, two for the Perseus arm and one for the Orion spur components, results in the lowest residuals. The Doppler widths of the -47, -38 and 0 km s^{-1} components are fixed at 3.4, 6.8 and 2.5 km s^{-1} respectively (Oonk et al., 2017). For $650 < n < 700$, we fit two Voigt profiles, one for the Perseus component and one for the Orion component. For $n > 700$ a single component is used to fit the line profile. The best fit parameters are given in Table 2.2. Here we see that even when we fit a single component the observed Cα line centre is close to -47 km s^{-1}. This indicates that this velocity component still dominates at the lower frequencies. While the observations clearly reveal the presence of CRRLs up to $n = 843$ (see Figure 2.3), corresponding to $\nu = 10$–12 MHz, quantitative analysis of this data is limited by recovery of the line wings (see Appendix 2.A). We have ignored the Cα(843) data in further analysis.

To test the fit results we varied the noise properties of the stacked spectra and repeated the fit. To do this we subtract the best fit Voigt profiles from the stacked spectra. The best fit Voigt profiles are then added to a spectra with a different noise level. The noise level was randomly drawn from a Gaussian distribution with a standard deviation equal to the rms in the stack. The stacks with the different noise levels were then fit again. We repeated this 1000 times for every stacked spectrum. The measured line properties varied little between different realisations of the noise. For each stack we made histograms of the measured line properties. The distribution of the line parameters showed Gaussian distributions for the line width and integrated optical depth. The standard deviation of these distributions are comparable to the errors given for the line parameters in Table 2.2.

158 μm [CII] line

From each of the nine PACS footprints we extracted an average spectrum. We fitted the [CII] 158 μm line in this average spectrum with a Gaussian. To account for the continuum emission we fit a linear function to line free channels. The source averaged spectra with the continuum subtracted is shown in Figure 2.6. The line centroid is -16 ± 19 km s^{-1}, its full width at half maximum 218 ± 3 km s^{-1} and its amplitude 0.096 ± 0.003 Jy arcsec^{-2}. The average line intensity integrated over frequency over

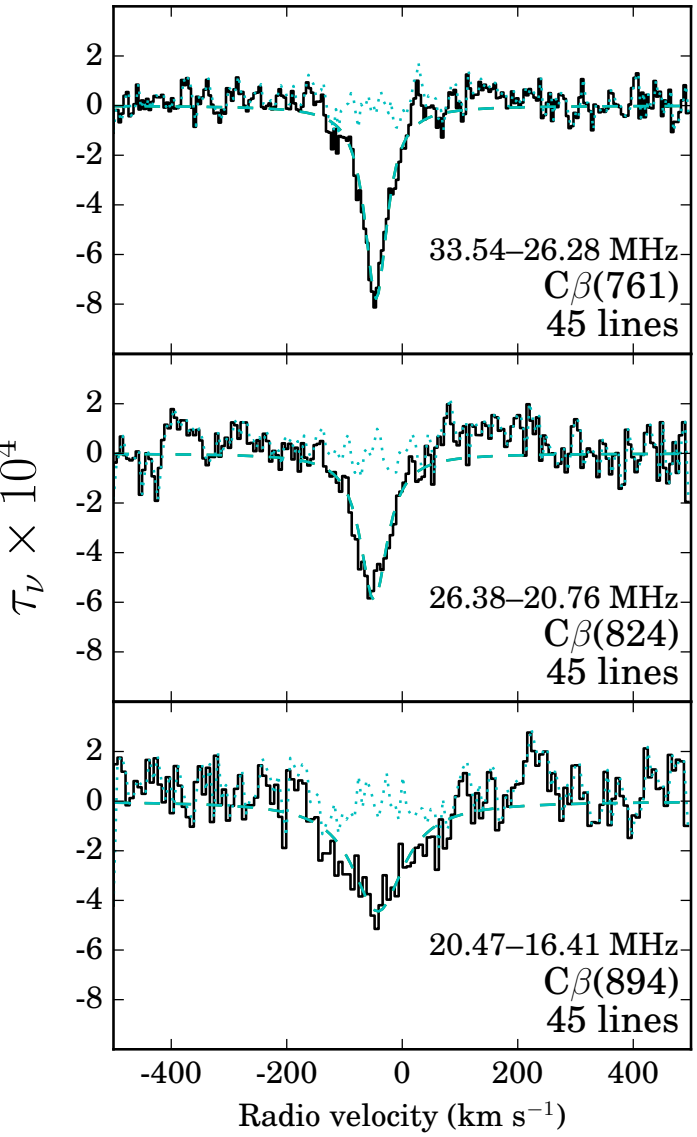

Figure 2.4.: Stacked Cβ spectra. The *black steps* show the stacked spectra after processing, the *cyan dashed line* shows the best fit Voigt profile and the *cyan dotted line* shows the residuals. This is the same as in Figure 2.3.

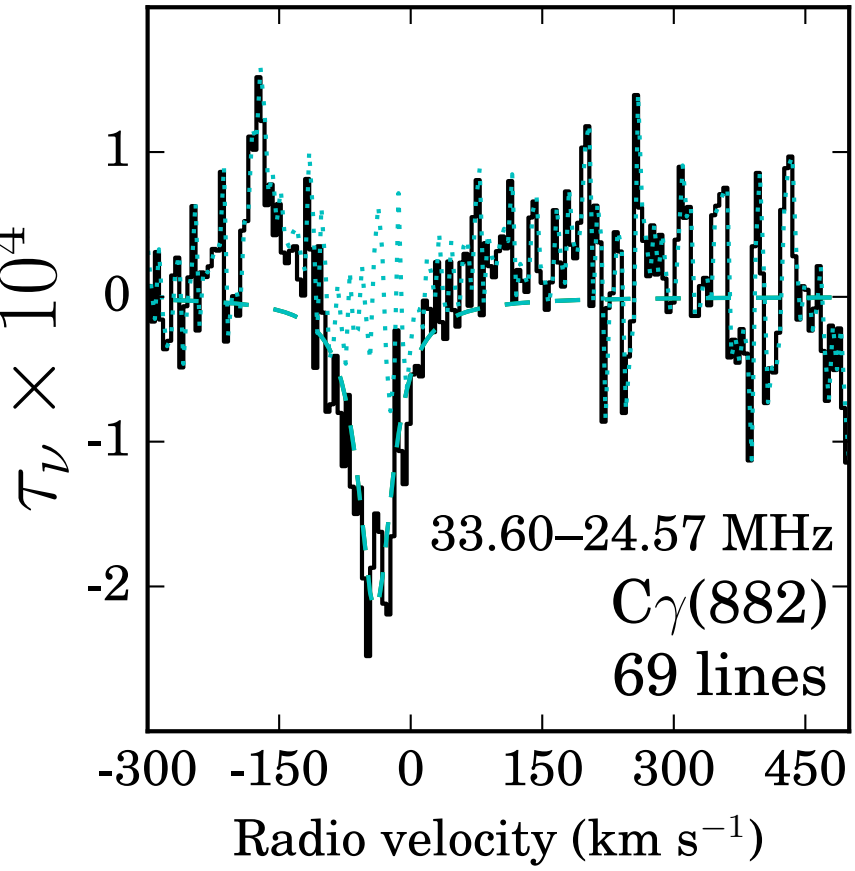

Figure 2.5.: Stacked Cγ spectrum. The *black steps* show the stacked spectra after processing, the *cyan dashed line* shows the best fit Voigt profile and the *cyan dotted line* shows the residuals. This is the same as in Figure 2.3.

Table 2.2.: Line parameters

n	n range	Frequency (MHz)	I_l/I_c $\times 10^{-3}$	Line centre (km s^{-1})	Lorentz line width (km s^{-1})	Integrated optical depth (Hz)	Spectral rms $\times 10^{-4}$
				Cα			
			3.44±0.05	-48±3	17±2	11.9±0.1	0.4
601	580–621	30.23	1.59±0.04	-39±3	22±2	6.8±0.1	0.4
			0.33±0.06	0±3	13±3	0.9±0.1	0.4
			2.92±0.07	-49±4	29±2	12.7±0.3	0.5
645	623–665	24.46	1.38±0.06	-39±4	35±2	7.3±0.3	0.5
			0.3±0.1	0±4	23±4	1.1±0.2	0.5
689	668–709	20.07	3.6±0.1	-46±5	58±1	22.8±0.4	0.8
			0.3±0.1	0±5	20±8	0.7±0.4	0.8
731	713–748	16.80	2.88±0.07	-46±6	89±3	22.7±0.5	1.4
782	760–806	13.73	2.3±0.1	-47±8	132±12	22±1	3.0
843	812–863	10.96	1.7±0.1	-48±10	153±26	15±1	4.0
				Cβ			
761	731–793	29.74	-0.78±0.02	-45±4	45±2	5.6±0.1	0.5
824	792–858	23.43	-0.58±0.04	-48±5	54±5	3.9±0.2	0.8
894	862–928	18.35	-0.44±0.04	-41±6	103±14	4.4±0.4	1.0
				Cγ			
882	836–928	28.62	0.21±0.01	-39±4	44±7	1.5±0.1	0.5

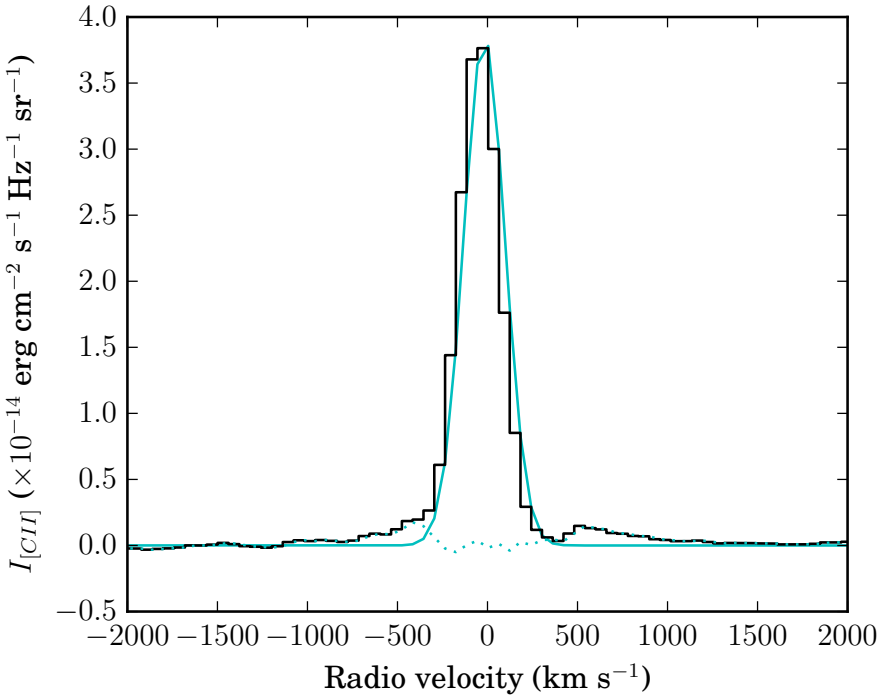

Figure 2.6.: [CII] 158 μm line spectra obtained with PACS. The line was averaged over the face of Cas A after removing the continuum. The *black steps* show the data, the *cyan solid line* shows the best fit Gaussian profile and the *dotted cyan line* shows the fit residuals. This is similar to Figure 2.3.

the face of Cas A is $(7.0 \pm 0.2) \times 10^{-5}$ erg cm^{-2} s^{-1} sr^{-1}. Because the PACS footprints cover only $\sim 20\%$ of the supernova remnant the uncertainty on the line intensity can be larger. Given the velocity resolution of the PACS observations the line is not resolved. This implies that the Perseus, Orion and any other velocity components present in [CII] appear as a single component. Even background [CII] emission could contaminate our spectra. Observations of other tracers, with higher spectral resolution, such as the 21 cm spin-flip transition of HI (Bieging et al., 1991) and CO (Kilpatrick et al., 2014), show that the most prominent component is at -47 km s^{-1}. Since we do expect a correlation between [CII], CO and HI (e.g., Pineda et al., 2013), the 158 μm line intensity should be dominated by the contribution from the -47 km s^{-1} component.

2.3.2. CRRL OBSERVED PROPERTIES

In the frequency range 10–33 MHz two properties of the observed CRRL profiles can be used to determine the gas physical conditions, the line width and its integrated

optical depth. Here we present the change in line properties, which will be later used to determine the gas physical conditions.

The line widths determined from fitting Voigt profiles to the CRRL stacks are shown in Figure 2.7. Here we see how the lines get broader as the principal quantum number increases. The increase in line width causes the lines to become blended as frequency decreases. In the top panels of Figure 2.3 it is possible to see the asymmetry in the line profile towards positive velocities due to the presence of additional gas. This is washed away as the dominant component gets broader. Our data in combination with the LCASS data (Oonk et al., 2017) at higher frequencies clearly reveals the transition from Doppler dominated to Lorentz dominated line widths in the range $n = 500$–600.

The integrated optical depths are shown in Figure 2.8. Since for part of the low frequency spectra presented here ($n > 700$) it is not possible to find a unique solution to separate the different velocity components we show the sum of the optical depths from the Perseus arm gas at -47 and -38 km s^{-1}. This is done by adding the two components together when more than two Voigt profiles are fit, or by subtracting a 5% contribution, corresponding to the Orion component, when one Voigt profile is fit. The LCASS points at $n > 600$ show a fairly constant integrated optical depth as n increases up to 800. In Figure 2.8 we also show the LCASS data (Oonk et al., 2017) at higher frequencies, the latest compilation of integrated optical depths (Kantharia et al., 1998) as well as the more recent Cα data from Stepkin et al. (2007) and Sorochenko & Smirnov (2010). The line width and integrated optical depth are used in the following section to constrain the gas properties.

2.4. Analysis

In this section we analyse CRRLs below 33 MHz in combination with the 158 μm [CII] line. For the analysis we exclude the Cα(843) line for the reasons given in Sect. 2.3.1.

2.4.1. Line width

Two effects dominate the broadening of low frequency CRRLs. These are, pressure broadening, which depends on the electron temperature and density, and radiation broadening, which depends on the radiation field in which the atoms are immersed (Shaver, 1975; Salgado et al., 2017a). Both effects affect the Lorentzian wings of the line profile. As mentioned in Sect. 2.2.3 the line width at the low frequencies, where the lines are heavily blended, will be dominated by the most prominent component. In this case this is the -47 km s^{-1} component. For principal quantum numbers below ~ 700 the line profiles of the -47 and -38 km s^{-1} components can be decomposed. For $n > 700$, the line profile shows no deviations from a single Voigt, but at this point the -47 km s^{-1} is so broad that it dominates the line width. In Figure 2.7 we present the line width for the -47 km s^{-1} velocity component as a function of principal quantum number over the full LBA frequency range. The higher frequency data for the -47 km s^{-1} component is

taken from (Oonk et al., 2017). In Figure 2.7 we see that the line width increases with principal quantum number.

The coloured curves in Figure 2.7 show the contribution from pressure and radiation broadening on the lines. The line width due to pressure broadening is (e.g., Salgado et al., 2017b),

$$\Delta\nu_p = \frac{1}{\pi} 10^a n_e n^{\gamma_c} \text{ Hz}. \tag{2.2}$$

Here, n_e is the electron density, n the principal quantum number, a and γ_c are constants that depend on the electron temperature of the gas, T_e. The values of a and γ_c are tabulated in Salgado et al. (2017b). Using this model the maximum electron density of the gas is 0.3 cm^{-3} for the lowest temperature in our grid of models, i.e. $T_e = 10$ K. The maximum allowed electron density decreases for higher temperatures.

Radiation broadening produces a line width given by (Salgado et al., 2017b),

$$\Delta\nu_r = \frac{1}{\pi} \sum_{n \neq n'} B_{n'n} I_\nu \text{ Hz}. \tag{2.3}$$

Here, $B_{n'n}$ is the Einstein coefficient for stimulated emission and I_ν the intensity of the radiation field. At low frequencies the background radiation field is generally due to synchrotron emission and can be described by a power law $T_r \propto \nu^\alpha$. Using the available low frequency surveys Zheng et al. (2016) find that the spectral index of synchrotron emission below 408 MHz is $\alpha_{\rm MW} = -2.52 \pm 0.02$. Studies of low frequency CRRLs in the Milky Way usually assume that $\alpha = -2.6$ (e.g., Payne et al., 1989; Kantharia et al., 1998; Oonk et al., 2017). The difference in $\Delta\nu_r$ between using a power law index of -2.52 and -2.6 is less than 20% for $n = 400$–1000. Here we will adopt the value of $\alpha_{\rm MW} = -2.6$ to be consistent with previous work. In this case the line width due to radiation broadening becomes

$$\Delta\nu_r \approx 0.8 \left(\frac{T_{r,100}}{1000 \text{ K}}\right) \left(\frac{n}{600}\right)^{5.8} \text{ kHz}. \tag{2.4}$$

Where, $T_{r,100}$ is the brightness temperature of the radiation field at 100 MHz in units of K.

Using Eq. 2.4 and the line widths for $n < 750$ (see Sect. 2.3.1) we constrain $T_{r,100}$ to < 2000 K. This is a strict upper limit, since pressure broadening is not considered. An approximate lower limit can be obtained from the lowest brightness temperature of the Milky Way in a region of similar galactic latitude to Cas A. Using the global sky model of de Oliveira-Costa et al. (2008) we have a value of $T_{r,100} \gtrsim 800$ K. However, the exact value is highly uncertain. Fitting a power law to the change in line width with principal quantum number in the range $n = 601$–731 we find that we can not discriminate between collisional or radiation broadening. This because both effects have a similar dependence on n. Oonk et al. (2017) find a gas electron density of 0.04 cm^{-3}, a temperature of 85 K and a radiation field intensity at 100 MHz of 1350 K, for the -47 km s^{-1} velocity component. If we use these results for the gas conditions then the relative contributions from pressure and radiation broadening are similar. This suggests

that both pressure and radiation broadening are of importance in setting the behaviour of the line width along this line of sight.

If we combine the Doppler, pressure and radiation induced broadening terms and fit it to the data with frequencies greater than 30 MHz, then we arrive at the following relation for T_e, n_e and $T_{r,100}$;

$$\left(\frac{n_e}{\mathrm{cm}^{-3}}\right) = \left(0.8 - 0.38\left(\frac{T_{r,100}}{1000\ \mathrm{K}}\right)\right)\left(\frac{T_e}{\mathrm{K}}\right)^{-0.46}. \tag{2.5}$$

This expression is valid for this line of sight when $T_{r,100} \lesssim 1600$ K and accurate to within 10%. In Sect. 2.4.5 we adopt this relation to constrain the gas properties. In Sect. 2.4.5 we also assume that this relation is valid for both the -47 and -38 km s^{-1} velocity components. This assumption is based on the similitude between the derived gas physical properties from both velocity components (Oonk et al., 2017). The physical conditions in this case are derived using higher frequency data, where the line profile can be more reliably decomposed.

Stepkin et al. (2007) showed that using a power law radiation field with $T_{r,100} = 3200$ K overestimated the line widths for $n > 600$. To solve this issue they argued that the contribution from Cas A to the radiation field has to be taken into account when modelling the line widths. The spectrum of Cas A has a turnover point close to 30 MHz (e.g., Braude et al., 1978; Vinyaikin, 2014), which causes its flux density to decrease for frequencies lower than the turnover frequency. This solved the apparent discrepancy between the observed line widths and the model predictions. Here we make use of the broadening expressions derived by Salgado et al. (2017b). These result in a $\sim 30\%$ lower Lorentz line width with respect to the Shaver (1975) expressions used by Stepkin et al. (2007). For $n \lesssim 650$, the use of expressions which predict a smaller line width combined with our attempt to fit three velocity components results in line widths which are consistent at the 3σ level with a power law line broadening. However, as our simulations show, recovering the correct line width for $n \lesssim 700$ depends on the number of components fit to the blended line profiles, which has no unique solution. Additionally, for $n \geq 800$ the line profiles are likely to be underestimated due to the severe line broadening. At some point the width of the lines within a single subband is such that it is no longer possible to find line-free channels. We believe that the combination of these effects could mimic a deviation from a power law line broadening (e.g., a broken power law).

In Figure 2.7 we also show the line width when the contribution from Cas A is taken into account. To include the contribution from Cas A to the radiation field (I_ν in Eq. 2.3) we add it to the radiation field from the Milky Way. To model the intensity of the radiation field due to Cas A at frequencies lower than 100 MHz we use two different models. One is the model by Stepkin et al. (2007), in which a broken power law is used. This broken power law has a turnover at $\nu = 26$ MHz, for frequencies below this point the spectral index is $\alpha = -1$. Above the turnover the spectral index is the same as that from the Milky Way radiation field, i.e. $\alpha = -2.6$. In this model the contribution from Cas A to the radiation field at the cloud is $T_{r,100} \approx 360$ K. The second model we use is based on the observed flux density from Cas A (Vinyaikin, 2014). In this case

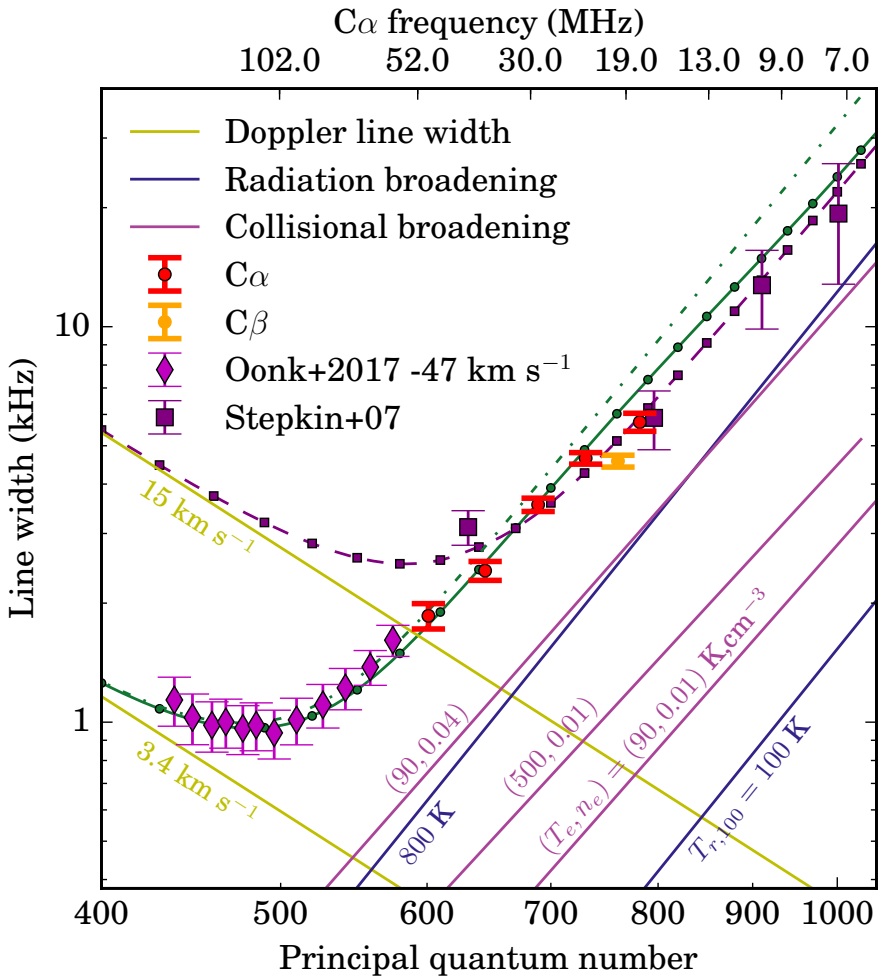

Figure 2.7.: Line width for the −47 km s^{-1} velocity component as a function of principal quantum number. The *red* and *orange points* show the measured line widths from this work (Table 2.2). The *purple diamonds* the line widths from Oonk et al. (2017) and the *purple squares* the Cα, Cβ, Cγ and Cδ data from Stepkin et al. (2007). The *coloured solid lines* show the contribution from Doppler broadening (*yellow lines*), pressure broadening (*purple lines*) and radiation broadening (*blue lines*). The *purple line with squares* shows the line width produced by the Stepkin et al. (2007) model. The *green dot dashed line shows the line width for a model with a Doppler line width of* 3.4 *km s*$^{-1}$, $T_e = 85$ *K*, $n_e = 0.04$ *cm*$^{-3}$, *and a power law radiation field with* $\alpha = -2.6$ *and* $T_{r,100} = 1400$ *K (Oonk et al., 2017).* The *green line with circles* shows the line width for a model with the same physical conditions as the green dot dashed line, but in this case the radiation field is a combination of a power law with $T_{r,100} = 800$ K and $\alpha = -2.6$ plus a contribution to the radiation field from Cas A. To model the contribution from Cas A we use its observed flux density (Vinyaikin, 2014). We can see that the line width due to the radiation field from the observed flux density of Cas A (Vinyaikin, 2014) decreases faster than that of a power law with $\alpha = -1$ (Stepkin et al., 2007, line with squares versus line with circles).

the contribution from Cas A is $T_{r,100} \approx 360$ K, which is determined from a fit to the observed line widths.

2.4.2. Integrated optical depth

The observed change in integrated optical depth with principal quantum number, n, can be used to constrain the properties of the CRRL emitting gas (e.g., Dupree, 1971; Shaver, 1975; Walmsley & Watson, 1982; Ershov et al., 1984; Payne et al., 1989; Ponomarev & Sorochenko, 1992; Kantharia et al., 1998; Salgado et al., 2017a,b; Oonk et al., 2017). Here we compare the observed integrated optical depth to those predicted by the updated models of Salgado et al. (2017a,b). In these models the level populations are fully determined by the atomic physics involved, including the effect of dielectronic capture (Watson et al., 1980). The level populations are obtained by self consistently solving the statistical equilibrium equations. Deviations from LTE in the level population are characterised by the departure coefficient b_n, while the contribution from stimulated emission to the line intensity is characterised by $\beta_{n'n}$ (Shaver, 1975; Salgado et al., 2017a).

To model the line optical depth we assume that the absorbing gas is a plane parallel slab which completely covers the face of Cas A. We assume a constant electron temperature and density. The assumption of constant temperature and density is justified since we are studying a small frequency range (10–33 MHz) and density filter effects should be small. The assumption of a unity beam filling factor seems reasonable given the spatially resolved observations of Anantharamaiah et al. (1994), which show emission all over the face of Cas A (Oonk et al., 2017). When we compare the integrated optical depth to the models, we use the combined optical depth of the -47 and -38 km s^{-1} velocity components. We do this based on the detailed analysis at higher frequencies (Payne et al., 1994; Oonk et al., 2017), which suggests that both velocity components trace gas with similar temperature and density. In this case, the combined integrated optical depth of both velocity components will show the same behaviour with n scaled by the total emission measure. These assumptions will be used in the rest of the analysis.

When solving the statistical level population problem using the models of Salgado et al. (2017a,b) we use atomic hydrogen and electrons as collisional partners and we chose to ignore collisions with molecular hydrogen since we expect their importance to be relatively small given the gas physical conditions (Oonk et al., 2017). We evaluate the models in a grid in n_e–T_e–$T_{r,100}$ space. For the electron density the grid spans the range $n_e = 0.01$–1.1 cm^{-3} in steps of 0.005 cm^{-3}. The electron temperature is evaluated between 10–150 K in steps of 5 K. $T_{r,100}$ is evaluated at 800, 1200, 1400, 1600 and 2000 K.

The integrated optical depth as a function of n is shown in Figure 2.8. In this Figure we also show the latest compilation of CRRL observations towards Cas A presented in Kantharia et al. (1998), the Cα data points from Stepkin et al. (2007) and Sorochenko & Smirnov (2010), and the LCASS data (Oonk et al., 2017). The LOFAR points at $n > 600$ show a fairly constant integrated optical depth as n increases up to 800. The observed shape of the change in integrated optical depth is similar to the one predicted by the models of CRRL emission (Salgado et al., 2017a). In these models a

constant optical depth is reached faster than in previous ones (e.g., Payne et al., 1994). A constant integrated optical depth is expected if the population of carbon atoms is close to LTE ($b_n \sim 1$). When b_n gets close to unity, $\beta_{n'n}$ has an almost constant value. This is reflected in a constant integrated optical depth as a function of n. The models of Salgado et al. (2017a) show that this happens for $n > 600$ in regions that satisfy $n_e > 0.015\ \mathrm{cm}^{-3}(T_e/60\ \mathrm{K})^{-2}$. Under these conditions, the highest n levels are close to collisional equilibrium while the lower n levels decay rapidly radiatively. As density or temperature increases, a larger fraction of the levels is close to collisional equilibrium and hence the total population of the collisionally dominated levels increases. This translates into an increment in the optical depth of the high n transitions.

The LCASS data shows a similar trend when compared with previous results, but with a smaller scatter. LOFAR, with its large fractional bandwidth and high spectral resolution, is an ideal instrument for low frequency CRRL observations. Additionally, systematic differences arising from different calibration and data reduction strategies are minimised when using the same instrument. The trend in line width and integrated optical depths shows a smooth change with n. This suggests that there are no major systematic differences between the different LCASS LBA data sets. This is not the case for the literature data, for which a larger point to point scatter is observed.

Another advantage of LOFAR for CRRL observations is given by the frequency coverage of its subbands. The frequency coverage of the LOFAR subbands results in sufficient velocity coverage to measure the Lorentzian wings of the line profiles for $n \lesssim 800$. This was not the case for older receivers. As noted by Payne et al. (1994) some of the previous decametric observations could have underestimated the line profiles. This because in previous observations the velocity coverage of the spectrometers was comparable to the line width. In this case, there are no line-free channels from which to determine the continuum. This led Payne et al. (1994) to estimate how much the line profiles could have been underestimated and derive a correction based on this. However, such a correction depends on the model used for its derivation and the physical conditions assumed. Models which predict larger line widths will require larger correction factors for a fixed velocity coverage. Given that the gas conditions are not know a priori, this kind of correction can lead to erroneous determination of the gas properties.

2.4.3. Carbon lines ratio

A way of breaking the degeneracy between different gas properties of the observed CRRL properties is to compare the CRRLs with the 158 μm [CII] line (Natta et al., 1994; Salgado et al., 2017b). Both lines are emitted by ionised carbon, but the line strengths have different temperature dependencies. This makes the CRRL/[CII] line ratio a good thermostat. Though, this also means that emission from both tracers can have different contributions from different phases of the ISM. The contribution from different phases of the ISM to the [CII] line intensity is still poorly constrained (e.g., Pineda et al., 2013). In the case of CRRLs this is still an open question (see e.g., Anantharamaiah et al., 1994; Sorochenko, 1996). Since the derived temperature for the CRRL gas is 85 K (Oonk et al., 2017), which is close to the temperature required to excite the carbon

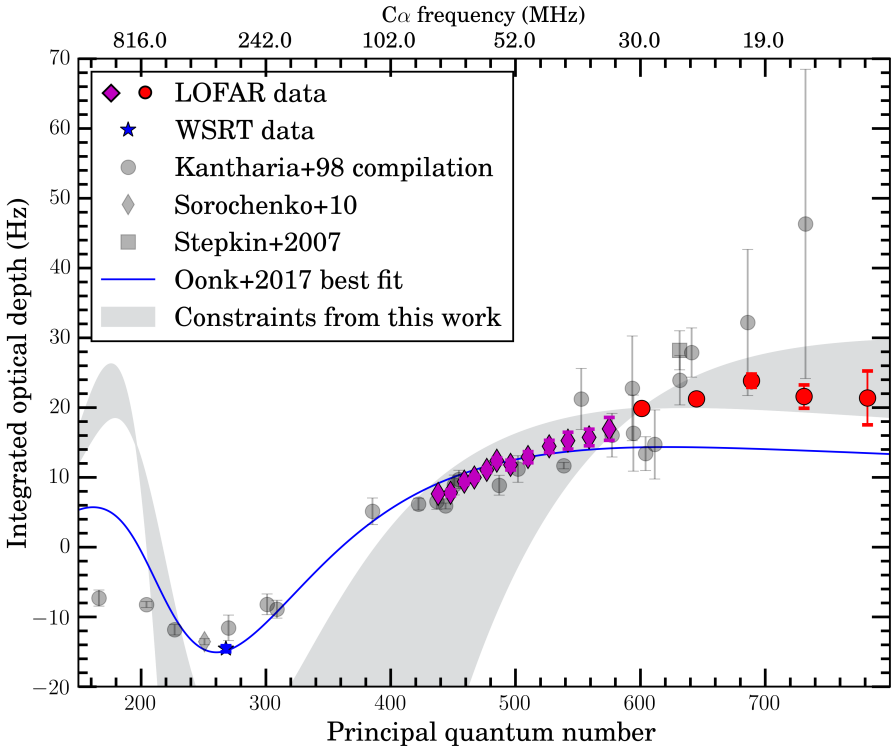

Figure 2.8.: Integrated optical depth as a function of principal quantum number for the sum of the Perseus arm components at −47 and −38 km s^{-1}. The LCASS data is shown with *red circles* for the data presented in this work and *purple diamonds* for the higher frequency data (Oonk et al., 2017). The LCASS WSRT data is shown with a *blue star*. Data from the literature is shown in *grey*. The best fit model from Oonk et al. (2017) for the sum of the −47 and −38 km s^{-1} components is shown with a *blue line*. The models which correspond to the physical constraints from this work are shown in a *gray shaded region*. In some cases the error bars are smaller than the symbols.

$^2P_{3/2}$-$^2P_{1/2}$ core, here we will assume that both lines have equal contributions from different ISM phases.

To model the line intensity of the [CII] line we use the equations of Salgado et al. (2017b). Given the gas conditions (Oonk et al., 2017) and the atomic hydrogen column density (Mebold & Hills, 1975) the [CII] line will be optically thick. We assume that the [CII] emission in the PACS spectra comes from the two velocity components at -47 and -38 km s^{-1}. For the line widths we use 3.4 and 6.8 km s^{-1} respectively (Oonk et al., 2017). Additionally, we assume that the path length of the -38 km s^{-1} velocity component is half that of the -47 km s^{-1}, as determined from higher frequency CRRL observations (Oonk et al., 2017). Under these assumptions we evaluate the intensity of the [CII] line in a n_e-T_e grid which is the same as for the CRRLs.

Towards Cas A, the ratio between the integrated optical depth of the C(731)α line and the [CII] line is $(-3.7 \pm 0.1) \times 10^5$ Hz/(erg s^{-1} cm^{-2} sr^{-1}). The region of parameter space consistent with this ratio to within 3σ is shown in Figure 2.9 with red lines. The gas electron temperature is constrained to the range T_e = 70–100 K for the lowest densities in our grid ($n_e < 0.02$ cm^{-3}). For higher densities the allowed temperature range narrows considerably, decreasing to 60–70 K for the highest density in our grid ($n_e = 0.11$ cm^{-3}). As the temperature increases the number of carbon atoms in the $^2P_{3/2}$ state is larger. This translates into an increase of the [CII] line intensity. In practice this means that for a smaller CRRL/[CII] ratio the allowed temperature would be higher.

We do recognise that the [CII] 158 μm intensity used only refers to $\sim$ 20% of the Cas A supernova remnant and is unresolved in velocity. As shown by Gerin et al. (2015), observations of [CII] unresolved in velocity can hide absorption features. This has the effect of lowering the observed [CII] intensity when absorption and emission features are convolved with the spectrometer response. Further high spectral resolution observations with SOFIA are necessary to determine this ratio well.

2.4.4. CRRL RATIO

A way in which the emission measure dependence is eliminated is by considering the ratio between the integrated optical depth of CRRLs. The ratio between CRRLs has a weaker dependence on calibration uncertainties. The measured Cα(731)/Cα(601) integrated optical depth ratio has a value of 1.12 ± 0.07. The region of parameter space which produces a line ratio consistent with the observations to within 3σ is shown in Figure 2.9 as the hatched region between yellow lines. Even if the range of pressures allowed by the 3σ values is large, it does pose a strict lower limit on the electron pressure of $P_e \geq 0.9$ K cm^{-3}, for $T_{r,100} = 800$ K and $T_e \geq 20$ K. For higher values of $T_{r,100}$ the lower limit will be larger. We can turn this in to a lower limit on the gas pressure by adopting an electron fraction. If we use an electron fraction equal to the gas phase carbon abundance (1.5×10^{-4}, Cardelli et al., 1996; Sofia et al., 1997), i.e. all the electrons come from ionized carbon, this is $P \geq 6 \times 10^3$ cm^{-3} K. This gas pressure is comparable to that measured using UV absorption lines of neutral carbon (Jenkins & Tripp, 2001).

2.4.5. Piecing it all together

Using the measured temperature from the CRRL–[CII] ratio, and the constraints from the Cα(731)/Cα(601) ratio and line width we can break the degeneracy between T_e, n_e and $T_{r,100}$. We can combine these constraints since the line width traces the most prominent velocity component at -47 km s^{-1} and we assume that the -38 km s^{-1} velocity component traces gas with similar physical properties. An example of this is shown in Figure 2.9. In this Figure we can see how the line width relation (Eq. (2.5)) and the pressure derived from the Cα(731)/Cα(601) ratio intersect only at the correct value of $T_{r,100}$, when we adopt the 1σ value for the Cα(731)/Cα(601) ratio. Then, from the allowed range of pressure and temperature the density can be determined. However, if we consider the 3σ range for the Cα(731)/Cα(601) ratio, then we are in a situation were $T_{r,100}$ and the pressure are degenerate. This shows the importance of having high signal-to-noise data to determine the gas conditions.

Using the ranges allowed by our data we note that a value of $T_{r,100}$ lies between 1500 and 1650 K, T_e between 68–98 K and P_e between 1.5–2.9 K cm^{-3}. The density range allowed by the intersection of these constraints is 0.02–0.035 cm^{-3}. These results are in line with those published by Oonk et al. (2017), but here we have made use only of CRRLs below 33 MHz and the 158 μm [CII] line.

In Figure 2.8 we also show how the derived range of physical conditions translate into integrated optical depth. We can see how the LOFAR data falls within the range of allowed physical conditions. However, the integrated optical depth is underestimated for the WSRT data point. When performing a spatial average, such as that done inside the synthesized beam of the observations presented here, the observed line optical depth will be a weighted average of the line optical depth. The weight is proportional to the brightness temperature of the background source. If the background source shows spectral index variations on scales smaller than the synthesized beam, then the line profiles will sample different spatial structures with frequency. The continuum from Cas A shows variation in its optical depth on scales of arcseconds, with a flatter spectral index in its inner $50''$ (DeLaney et al., 2014). The spatial structure of the gas at -47 km s^{-1} shows variations on arcminute scales with the gas concentrated towards the south and west of Cas A (Anantharamaiah et al., 1994; Asgekar et al., 2013). The integrated optical depth towards the western hotspot of Cas A can be a factor of two larger than that extracted over the whole face of Cas A (Asgekar et al., 2013). This implies that at frequencies below 30 MHz the line profiles will be weighted towards the gas in the south and west of Cas A. Similarly, gas outside the supernova remnant could be sampled by the lower frequency observations. However, we estimate that the surface brightness of Cas A relative to the surrounding Milky Way at these frequencies is larger by a factor of $\gtrsim 10$. Then, the effect of gas outside the face of Cas A should be small unless its integrated optical depth is ten times larger than that of the gas which covers the face of Cas A. Another reason for underestimating the WSRT integrated optical depth is related to the change of physical conditions traced by CRRLs at different frequencies. This can be caused because the CRRL optical depth acts as a density filter (e.g. Mohan et al., 2005), or because some components can be absorbed by free electrons at lower frequencies (e.g. Pankonin, 1980). CRRLs act as a density

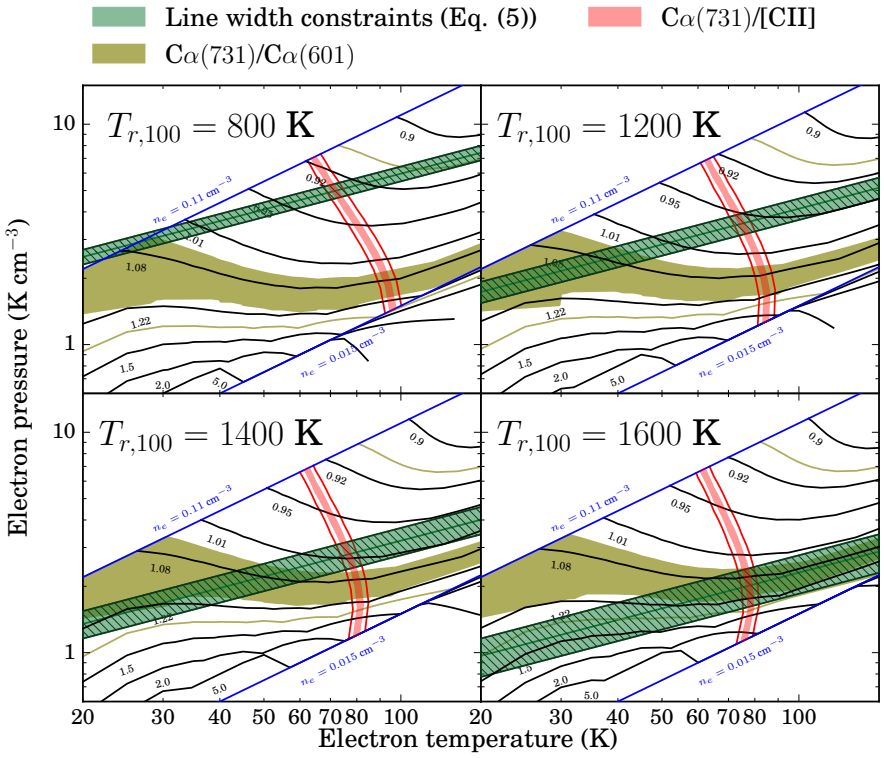

Figure 2.9.: Pressure temperature diagrams for CRRLs below 33 MHz and the 158 μm [CII] line. These can be used to constrain the gas properties given measurements of decametric CRRLs and [CII]. The *black lines* show the pressure for constant values of the Cα(731)/Cα(601) ratio. The *red region* shows the allowed temperature range derived from the Cα(731)/[CII] ratio with a 1σ error. The *red lines* show the allowed temperature range when considering a 3σ error bar. The *green region* shows the allowed range of pressures given Eq. (2.5) for $T_{r,100} \pm 100$ K. The *yellow region* shows the measured value of the Cα(731)/Cα(601) ratio with a 1σ error, while the *densely hatched region* shows the same value with a 3σ error. The difference between the 1σ and 3σ curves reflects the importance of having high signal-to-noise detections. The *blue lines* show constant electron density curves for $n_e = 0.015$ and 0.11 cm^{-3}. For values of $T_{r,100} > 1650$ K, the green region goes outside the allowed range of parameters.

filter because gas with different physical conditions will emit/absorb preferentially at different frequencies. A model with a single slab of gas does not take into account this. However, the good fit of Oonk et al. (2017) to the integrated optical depth of the -47 km s^{-1} velocity component using a single slab of gas suggests that along this line of sight low frequency ($\nu \lesssim 1$ GHz) CRRLs trace gas with a narrow range of physical conditions. The last possibility we consider is that the physical conditions of the -47 and -38 km s^{-1} gas are not the same. The work of Oonk et al. (2017) at higher frequencies shows that the -38 km s^{-1} velocity component is less well fit than the -47 km s^{-1} one. However, with the current data we do not find a significant difference between the two components. Data at higher frequencies, e.g., obtained with the LOFAR HBA (120–240 MHz), would help narrow down the physical conditions of the -38 km s^{-1} velocity component.

2.4.6. The Perseus arm Cas A distance

In the previous subsections we have obtained a range of allowed values for $T_{r,100}$. Even if we can not accurately determine the contribution from Cas A to the radiation field it is interesting to use the constraints on $T_{r,100}$ to try and determine the distance between the Perseus arm gas and the background source. Figure 2.9 shows that $T_{r,100}$ can take values between 1500 and 1650 K if we consider the 1σ ranges. The brightness of the source at 100 MHz extrapolated from the Vinyaikin (2014) model is 1.8×10^7 K. If we adopt a contribution from the Milky Way to $T_{r,100}$ of 800 K and a radius of 3 pc for Cas A, then the distance between the Perseus arm gas at -47 km s^{-1} and Cas A can be between 262 and 220 pc. This distance would increase if the contribution from the Milky Way to $T_{r,100}$ is larger.

We can compare this with estimates of the distance to the Perseus arm gas based on the Galactic rotation curve. We use a flat rotation curve outside the solar circle ($R_\odot = 8.5$ kpc) with a constant velocity of 220 km s^{-1} (Dickey et al., 2009). For the -47 km s^{-1} component, the distance of the Perseus arm gas to Earth is 4.5 kpc. This distance is larger than the Earth-Cas A distance (3.4 kpc Reed et al., 1995), but this cannot be the case as the lines appear in absorption. Parallax measurements of star forming regions in the Perseus arm show that kinematic distances are in disagreement with parallax determined distances (e.g., Xu et al., 2006; Choi et al., 2014). Based on these measurements the distance from Earth to the gas in the Perseus arm towards Cas A is ≈ 3.3 kpc.

2.5. Conclusions

We have observed Cas A in the 10–33 MHz LBA band of LOFAR. Our results show that, while observations are hampered by ionospheric effects and RFI noise, Cα lines can be readily detected over this frequency range up to principal quantum numbers in excess of ~ 800 and Cβ and Cγ lines to even higher quantum numbers. At the lowest frequencies, analysis of this data is hindered because of severe line broadening, which

leaves a dearth of line free channels. This limits the effective analysis of Cα lines to $n \lesssim 800$. Nevertheless, this still gives access to hundreds of transitions.

As line frequencies are accurately known, stacking procedures can be used to increase the signal to noise and very weak lines ($\sim 10^{-3}$ in peak optical depth) can still be reliably detected ($S/N > 10$) after stacking. These lines are caused by absorption associated with the Perseus spiral arm along the line of sight towards this supernova remnant. The observed lines show a pronounced broadening with principal quantum number while the peak optical depth decreases. The integrated optical depth stays quite constant over the full n-range (600–800). This contrasts with previous observations which suggested a continuous increase in integrated optical depth with principal quantum number. The line broadening at high n reflects the importance of radiation and/or pressure broadening and provides insight into the physical conditions of the emitting gas. We find that the change in line width with frequency can be described by a model in which the radiation field is due to Galactic synchrotron emission, without the necessity to invoke additional contributions. However, deviations from a power law in the radiation broadening term are difficult to measure given the biases in the line recovery process at these low frequencies. Higher signal-to-noise observations would help to determine if the apparent flattening in the line width at the highest principal quantum numbers is significant.

The high-n lines presented in this work are close to collisional equilibrium and a constant integrated optical depth is expected. As they are close to LTE, the ratio of the CRRLs is not very sensitive to the physical conditions but they do put a firm constraint on the minimum gas electron pressure of $P_e \geq 0.9$ K cm^{-3}, which corresponds to 6×10^3 K cm^{-3} for an electron fraction of 1.5×10^{-4}.

By using the CRRL-[CII] line ratio as a thermostat, the ratio between CRRLs as a barometer and the line widths we are able to obtain physical conditions for the gas. Based on the data in the range 10–33 MHz and its 1σ errors we derive $T_e = 60$–98 K, $T_{r,100} = 1500$–1650 K and $n_e = 0.02$–0.035 cm^{-3}. This highlights the power of combining low frequency CRRLs with the 158 μm [CII] line. However, we caution that these results are uncertain due to the blend of at least two velocity components along this line of sight. Adding to this uncertainty is the unknown relation between [CII] and low frequency CRRLs. Also, due to the limited spatial coverage and spectral resolution of the Herschel PACS observations, the [CII] intensity is not very well known. High spectral and spatial resolution observations with SOFIA would greatly help to determine the [CII] intensity over the face of Cas A.

Our study demonstrates that the lowest frequency window available with LOFAR can provide important insights into the physical conditions of the gas traced by CRRLs.

2.A. Simulated line profiles

We generate synthetic spectra using the same number of channels and bandwidth as the LOFAR observations. To each synthesised spectrum we add Gaussian noise that mimics the noise properties of the LOFAR data. Ripples that simulate the effect of the bandpass response of LOFAR (Romein, 2008) are also added. Then we add Cα, Cβ, Cγ and Cδ lines to the spectra using Voigt profiles and generating the line

properties based on the Salgado et al. (2017a) models. For each transition and for each velocity component we add one Voigt profile. The code used can be found in `https://github.com/astrofle/CRRLpy` (Salas et al., 2016). The velocity components are centred at -47, -38 and 0 km s^{-1}. The synthesised spectra with the line profiles are then converted to antenna temperatures by inverting Eq. 2.1 to add the continuum back. In all cases we used a cloud covering factor of unity and a Doppler line width of 3.4 km s^{-1}. We use 3 different temperatures for the line properties, 30 K, 90 K and 200 K. The emission measure is adjusted to match the observed integrated optical depths. For the 30 K model the emission measure of the -47, -38 and 0 km s^{-1} components is 0.03, 0.02 and 0.0045 pc cm^{-6} respectively. For the 90 K model these are 0.08, 0.04 and 0.009 pc cm^{-6}, for the 200 K model 0.25, 0.1 and 0.05 pc cm^{-6}. The synthetic spectra are processed in the same way as the LOFAR spectra. First we remove the continuum by estimating it from line free channels and then the stacking and baseline removal process is performed. This was repeated 60 times. Each time the noise in the synthetic spectra was recomputed. A comparison between the input models and the measured values from the stacks is shown in Figure 2.10. Here we also compare with stacks that were not processed, i.e., Cα, Cβ, Cγ and Cδ lines are present in the spectrum while stacking and no bandpass correction was applied.

In the top panel of Figure 2.10 we compare the integrated optical depth. This comparison shows that before processing the integrated optical depth is underestimated for $n > 710$. We have investigated the cause of this bias and have concluded that it arises because the number of lines per frequency unit increases with n. At $n \approx 710$ the Lorentzian wings of adjacent CRRLs begin to overlap and correctly estimating the continuum becomes difficult. To test this we generated the same line profiles with a constant noise level of 10^{-5}, in optical depth units, and added only Cα lines. No processing other than continuum removal and stacking was applied. The results are very similar, indicating that the underestimation is due to the presence of Cα lines in the spectra. After processing, the measured values are closer to those of the input model. The difference between the integrated optical depth of the input model and the measured value after processing can be up to 16%, in the worst case.

The middle row of Figure 2.10 shows a comparison between the measured line width and the line width of the dominant component, at -47 km s^{-1}. The measured line full width at half maximum (FWHM) is overestimated for $n < 710$. This is partially because for $n < 710$ the Orion component is still not completely blended with the Perseus components, so that fitting a single Voigt profile will result in a larger line FWHM. In the middle and bottom panels of Figure 2.10 we also show the measured value when fitting up to 3 Voigt profiles. The number of profiles used is such that the fit residuals are minimised. For $n > 710$ the profiles are blended enough that fitting a single Voigt profile is enough. Also, the results of the simulations show that after processing the line width is underestimated by no more than $\sim 16\%$ for $n > 710$. These results also show that even if the different velocity components are blended, the measured line width will resemble the line width of the most prominent velocity component.

We also analysed the results for Cβ and Cγ lines. After our processing, Sect. 2.2.3, the integrated optical depth and line width of Cβ lines can be recovered to within 3% and 10% respectively for $n < 800$. For Cγ lines the measured values can be recovered

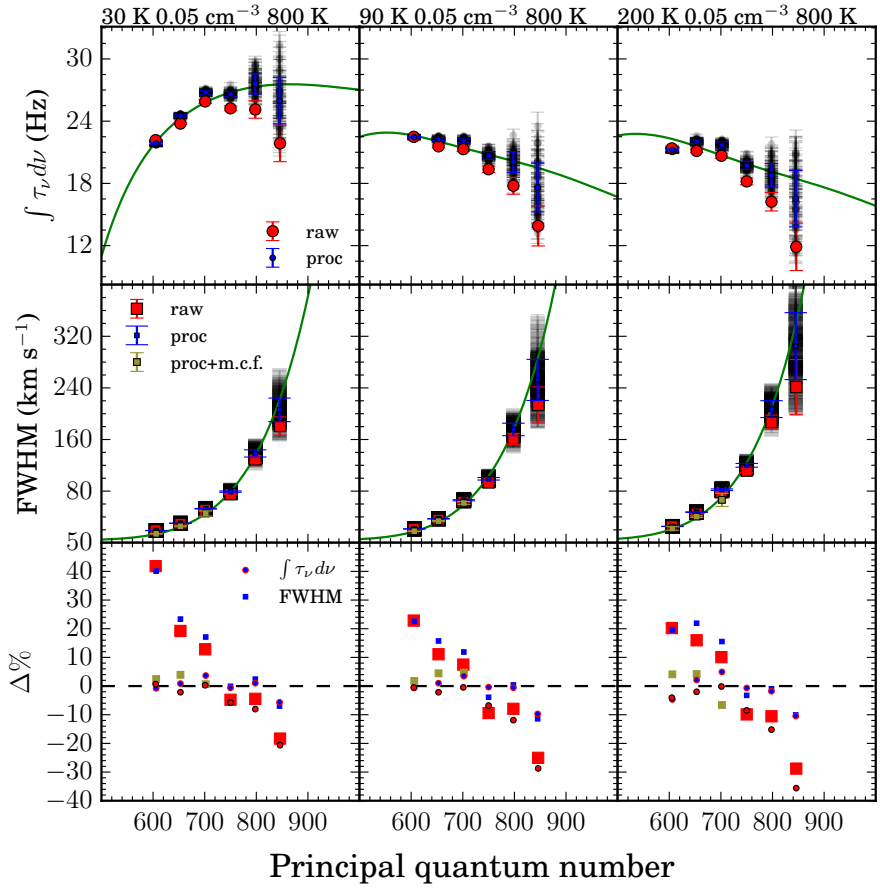

Figure 2.10.: Comparison between the input line properties and the measured line properties of synthetic spectra. The *top* row shows the integrated optical depth as a function of principal quantum number. The *grey points* show the results of individual simulations after continuum subtraction, stacking and baseline removal, the *blue points* show the mean of the grey points and the *red points* show the mean of the stacks with no baseline removal. The input line property is shown with a *green line*. The *middle* row shows the line FWHM. The symbols have the same meaning as in the top row, but the points are now *squares*. The *yellow squares* show the line width of the dominant component when multiple velocity components are fitted (m.c.f.) to the line profiles. The *bottom* panel shows the difference between the input value and the measured one. The comparison with processed data is shown by the *blue symbols*, while for the unprocessed data we use *red symbols*. The *yellow squares* show the difference between the input model for the dominant component and the measured line width for the dominant component after processing.

to within 50% and 30% for the integrated optical depth and line width respectively. In both cases using a single Voigt profile when fitting provides the best results. Based on these results we choose to consider only the Cβ(761) detection in the analysis.

These simulations do not include an effect which affects the data. This is contamination and loss of channels due to RFI. In some cases strong RFI is present on top of the lines, and the affected channels have to be flagged resulting in an incomplete line profile. This is partially alleviated by the fact that the stack contains multiple lines which suffer from RFI differently. Even though we have not investigated the effect of RFI in the final stacks, we believe this will have a minor effect on the derived line properties.

BIBLIOGRAPHY

Anantharamaiah, K. R., Erickson, W. C., Payne, H. E., & Kantharia, N. G. 1994, ApJ, 430, 682

Anantharamaiah, K. R., Erickson, W. C., & Radhakrishnan, V. 1985, Nature, 315, 647

Asgekar, A., Oonk, J. B. R., Yatawatta, S., et al. 2013, A&A, 551, L11

Beers, T. C., Flynn, K., & Gebhardt, K. 1990, AJ, 100, 32

Bieging, J. H., Goss, W. M., & Wilcots, E. M. 1991, ApJS, 75, 999

Blake, D. H., Crutcher, R. M., & Watson, W. D. 1980, Nature, 287, 707

Braude, S. I., Megn, A. V., Riabov, B. P., Sharykin, N. K., & Zhuk, I. N. 1978, Ap&SS, 54, 3

Budden, K. G. 1985, The propagation of radio waves: The theory of radio waves of low power in the ionosphere and magnetosphere

Cardelli, J. A., Meyer, D. M., Jura, M., & Savage, B. D. 1996, ApJ, 467, 334

Choi, Y. K., Hachisuka, K., Reid, M. J., et al. 2014, ApJ, 790, 99

Davies, R. D., & Cummings, E. R. 1975, MNRAS, 170, 95

de Oliveira-Costa, A., Tegmark, M., Gaensler, B. M., et al. 2008, MNRAS, 388, 247

DeLaney, T., Kassim, N. E., Rudnick, L., & Perley, R. A. 2014, ApJ, 785, 7

Dickey, J. M., Strasser, S., Gaensler, B. M., et al. 2009, ApJ, 693, 1250

Dupree, A. K. 1971, ApJL, 170, L119

Erickson, W. C., McConnell, D., & Anantharamaiah, K. R. 1995, ApJ, 454, 125

Ershov, A. A., Ilyashov, Y. P., Lekht, E. E., et al. 1984, Soviet Astronomy Letters, 10, 348

Ershov, A. A., Lekht, E. E., Rudnitskii, G. M., & Sorochenko, R. L. 1982, Soviet Astronomy Letters, 8, 374

Fields, D. E., Kennedy, R. G., Roy, K. I., & Vacaliuc, B. 2013, Acta Astronautica, 82, 251

Gerin, M., Ruaud, M., Goicoechea, J. R., et al. 2015, A&A, 573, A30

Gordon, M. A., & Sorochenko, R. L., eds. 2009, Astrophysics and Space Science Library, Vol. 282, Radio Recombination Lines
Jenkins, E. B., & Tripp, T. M. 2001, ApJS, 137, 297
Kantharia, N. G., & Anantharamaiah, K. R. 2001, Journal of Astrophysics and Astronomy, 22, 51
Kantharia, N. G., Anantharamaiah, K. R., & Payne, H. E. 1998, ApJ, 506, 758
Kilpatrick, C. D., Bieging, J. H., & Rieke, G. H. 2014, ApJ, 796, 144
Konovalenko, A. A. 1984, Soviet Astronomy Letters, 10, 353
Konovalenko, A. A. 2002, in IAU Symposium, Vol. 199, The Universe at Low Radio Frequencies, ed. A. Pramesh Rao, G. Swarup, & Gopal-Krishna, 327
Konovalenko, A. A., & Sodin, L. G. 1980, Nature, 283, 360
—. 1981, Nature, 294, 135
Konovalenko, A. A., Stepkin, S. V., & Shalunov, D. V. 2002, in IAU Symposium, Vol. 199, The Universe at Low Radio Frequencies, ed. A. Pramesh Rao, G. Swarup, & Gopal-Krishna, 349
Lekht, E. E., Smirnov, G. T., & Sorochenko, R. L. 1989, Soviet Astronomy Letters, 15, 171
Liszt, H., & Lucas, R. 1999, A&A, 347, 258
Mebold, U., & Hills, D. L. 1975, A&A, 42, 187
Mohan, N. R., Goss, W. M., & Anantharamaiah, K. R. 2005, A&A, 432, 1
Mookerjea, B., Kantharia, N. G., Roshi, D. A., & Masur, M. 2006, MNRAS, 371, 761
Morabito, L. K., Oonk, J. B. R., Salgado, F., et al. 2014, ApJL, 795, L33
Natta, A., Walmsley, C. M., & Tielens, A. G. G. M. 1994, ApJ, 428, 209
Offringa, A. R., de Bruyn, A. G., Biehl, M., et al. 2010, MNRAS, 405, 155
Offringa, A. R., van de Gronde, J. J., & Roerdink, J. B. T. M. 2012, A&A, 539, A95
Oonk, J. B. R., van Weeren, R. J., Salas, P., et al. 2017, MNRAS, 465, 1066
Oonk, J. B. R., van Weeren, R. J., Salgado, F., et al. 2014, MNRAS, 437, 3506
Ott, S. 2010, in Astronomical Society of the Pacific Conference Series, Vol. 434, Astronomical Data Analysis Software and Systems XIX, ed. Y. Mizumoto, K.-I. Morita, & M. Ohishi, 139
Pankonin, V. 1980, in Astrophysics and Space Science Library, Vol. 80, Radio Recombination Lines, ed. P. A. Shaver, 111–125
Payne, H. E., Anantharamaiah, K. R., & Erickson, W. C. 1989, ApJ, 341, 890
—. 1994, ApJ, 430, 690
Pilbratt, G. L., Riedinger, J. R., Passvogel, T., et al. 2010, A&A, 518, L1
Pineda, J. L., Langer, W. D., Velusamy, T., & Goldsmith, P. F. 2013, A&A, 554, A103
Poglitsch, A., Waelkens, C., Geis, N., et al. 2010, A&A, 518, L2
Ponomarev, V. O., & Sorochenko, R. L. 1992, Soviet Astronomy Letters, 18, 215
Reed, J. E., Hester, J. J., Fabian, A. C., & Winkler, P. F. 1995, ApJ, 440, 706
Romein, J. W. 2008, LOFAR, Tech. rep., ASTRON
Roshi, D. A., & Anantharamaiah, K. R. 2000, ApJ, 535, 231
Salas, P., Morabito, L., Salgado, F., Oonk, R., & Tielens, A. 2016, CRRLpy: First pre-release
Salgado, F., Morabito, L. K., Oonk, J. B. R., et al. 2017a, ApJ, 837, 141
—. 2017b, ApJ, 837, 142

Schwarz, U. J., Goss, W. M., & Kalberla, P. M. W. 1997, A&AS, 123
Shaver, P. A. 1975, Pramana, 5, 1
Shuter, W. L. H., & Verschuur, G. L. 1964, MNRAS, 127, 387
Sofia, U. J., Cardelli, J. A., Guerin, K. P., & Meyer, D. M. 1997, ApJL, 482, L105
Sorochenko, R. L. 1996, Astronomical and Astrophysical Transactions, 11, 199
Sorochenko, R. L., & Smirnov, G. T. 2010, Astronomy Reports, 54, 776
Stepkin, S. V., Konovalenko, A. A., Kantharia, N. G., & Udaya Shankar, N. 2007, MNRAS, 374, 852
Tasse, C., van der Tol, S., van Zwieten, J., van Diepen, G., & Bhatnagar, S. 2013, A&A, 553, A105
van Haarlem, M. P., Wise, M. W., Gunst, A. W., et al. 2013, A&A, 556, A2
Vinyaikin, E. N. 2014, Astronomy Reports, 58, 626
Walmsley, C. M., & Watson, W. D. 1982, ApJ, 260, 317
Watson, W. D., Western, L. R., & Christensen, R. B. 1980, ApJ, 240, 956
Xu, Y., Reid, M. J., Zheng, X. W., & Menten, K. M. 2006, Science, 311, 54
Zheng, H., Tegmark, M., Dillon, J., et al. 2016, ArXiv e-prints

III

Mapping low frequency carbon radio recombination lines towards Cassiopeia A at 340, 148, 54 and 43 MHz

3.1. Introduction

Molecular hydrogen, the material that fuels star formation, is formed out of atomic hydrogen (e.g., Cazaux & Tielens, 2004). This is clear in the interstellar medium (ISM), where we observe that molecular gas is embedded in atomic hydrogen (e.g., Andersson et al., 1991; Williams & Maddalena, 1996; Moriarty-Schieven et al., 1997; Fukui et al., 2009; Pascucci et al., 2015). Despite the clear association between these two gas compositions, the exact details of what is this atomic envelope are not clear (e.g., Blitz & Williams, 1999; Hollenbach & Tielens, 1999). In order to understand better the relation between mostly molecular dense gas and mostly atomic diffuse gas a larger sample of gas in this transition regime is required, along accurate estimates of its temperature and density.

A way in which we can study the cold atomic gas in the envelopes of molecular clouds is through observations of low frequency ($\nu \lesssim 1$ GHz) carbon radio recombination lines (CRRLs, e.g., Gordon & Sorochenko, 2009). The population of carbon ions recombining to a given principal quantum number, n, is determined by the gas density, temperature and radiation field, as well as the atomic physics involved (e.g., Shaver, 1975; Watson et al., 1980; Salgado et al., 2017a). Thus, we can determine the gas physical conditions by comparing the observed properties of CRRLs at different frequencies with model predictions (e.g., Payne et al., 1989; Kantharia et al., 1998; Oonk et al., 2017). Using this method it has been determined that CRRLs trace cold ($T \sim 100$ K) diffuse gas ($n_{\rm H} \sim 100$ cm^{-3}, e.g., Konovalenko, 1984; Ershov et al., 1987; Sorochenko & Walmsley, 1991; Payne et al., 1994; Kantharia et al., 1998; Roshi & Kantharia, 2011; Oonk et al., 2017) in the Galaxy. These physical conditions are similar to those found from observations of atomic hydrogen associated with molecular clouds, either using self absorption features (HISA e.g., Gibson, 2002; Kavars et al., 2003; Kerton,

2005; Kavars et al., 2005; Moss et al., 2012) or absorption measurements against bright background continuum sources (HICA e.g, Dickey et al., 2009; Stanimirović et al., 2014; Bihr et al., 2015).

Most of our understanding of low frequency CRRLs in the Galaxy comes from studies where the spatial resolution is coarse (e.g., $\theta_{\rm HPBW} \gtrsim 30'$ Anantharamaiah et al., 1988; Erickson et al., 1995; Kantharia & Anantharamaiah, 2001; Roshi et al., 2002). This has hindered a spatially resolved identification of which components of the ISM do low frequency CRRLs preferentially trace, such as the outskirts of HII regions, diffuse CII clouds and/or the envelopes of molecular clouds. A notable exception to this limitation is the line of sight towards the supernova remnant Cassiopeia A (Cas A). Along this line of sight, the bright background continuum (relative to the diffuse synchrotron emission from the Milky Way) enables RRL studies with an effective resolution comparable to the size of Cas A (diameter of $6'$ at 64 MHz, e.g., Oonk et al., 2017). Additionally, the large gas column density in the intervening ISM has allowed a direct detection of CRRLs with a spatial resolution smaller than the size of Cas A (Anantharamaiah et al., 1994; Kantharia et al., 1998; Asgekar et al., 2013). From these observations we know that the optical depth of the CRRLs associated with gas in the Perseus arm increases towards the South of Cas A (Anantharamaiah et al., 1994; Kantharia et al., 1998), peaking against its western hotspot (Asgekar et al., 2013).

Besides low frequency CRRLs, the line of sight towards Cas A has been the target of numerous studies of the ISM (e.g., Davies & Matthews, 1972; Mebold & Hills, 1975; Troland et al., 1985; Bieging & Crutcher, 1986; Wilson et al., 1993; Liszt & Lucas, 1999; De Looze et al., 2017). Given that Cas A is located on the far side of the Perseus arm of the Galaxy (at a distance of 3.4 kpc from the observer Reed et al., 1995), most of the Perseus arm gas lies between the observed and the background source (e.g., Troland et al., 1985). Additionally, the distance between Cas A and the gas in the Perseus arms is large enough that they should be unrelated (Xu et al., 2006; Sorochenko & Smirnov, 2010; Choi et al., 2014; Salas et al., 2017). The spatial distribution of the atomic gas towards Cas A shows that it completely covers the face of Cas A, as revealed by observations of the 21 cm line of HI in absorption against Cas A (e.g., Bieging et al., 1991; Schwarz et al., 1997). However, the saturation of the 21 cm-HI line profiles makes it difficult to identify small scale structure. Observations of other tracers have revealed the presence of gas with a large column density over the southern half of Cas A, with a visual extinction in the range $A_{\rm V} \sim 4$–10 (e.g., Troland et al., 1985; Hwang & Laming, 2012; De Looze et al., 2017). A cartoon illustrating the distribution of the gas relative to Cas A and the observer is shown in Figure 3.1.

The larger optical depth of CRRLs towards the south of Cas A (Anantharamaiah et al., 1994; Kantharia et al., 1998), where CO emission is readily detected, provides evidence, for the association of low frequency CRRLs with cold atomic or diffuse molecular envelopes of molecular clouds (e.g., Andersson et al., 1991). Another argument in favor of this association comes from the gas temperature and density as traced by low frequency CRRLs. Using spatially unresolved observations of CRRLs Oonk et al. (2017) derived a gas electron temperature of 85 K and a density of ~ 280 cm^{-3}, in between those of cold molecular and diffuse atomic gas. A step forward in this direction would be to extend this spatial comparison to the gas physical conditions, which was

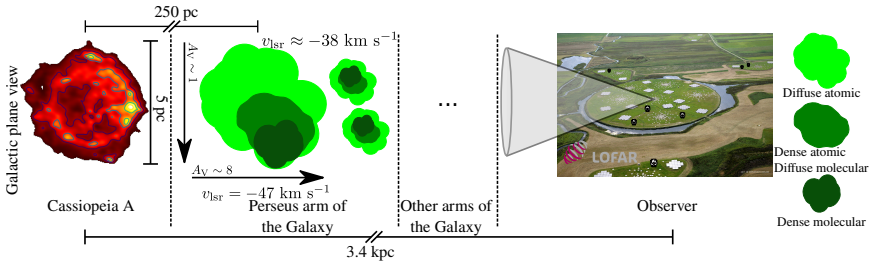

Figure 3.1.: Cartoon depicting the geometry of the studied gas relative to Cassiopeia A and the observer. The gas studied in this work is part of the Perseus arm of the Galaxy and does not show signs of being related to the supernova remnant. The dense molecular gas peaks to the south of Cas A, as shown by continuum observations in the far infrared (De Looze et al., 2017) and CO lines (e.g., Liszt & Lucas, 1999; Kilpatrick et al., 2014). Here we only illustrate the gas over the face of Cas A as our RRL observations do not trace gas outside the face of Cas A.

not possible previously due to the lack of frequency coverage.

In this work we present CRRL emission and absorption cubes centred around the C268α, C357α C494α and C539α lines with a resolution of 70$''$ (1.2 pc at the distance of Cas A). With these cubes we aim to study the relation between the gas traced by low frequency CRRLs and other tracers of cold gas such as cold atomic gas traced by the 21 cm line of HI in absorption and molecular gas as traced by CO lines in the millimetre. We perform this comparison both spatially and in terms of the physical conditions as derived from two sets of lines; one containing the CRRLs and the second the molecular lines.

3.2. Observations & data reduction

Here we describe the data reduction of the low frequency array (LOFAR, van Haarlem et al., 2013) high band antenna (HBA) observations presented in this work, as well as further processing steps applied to the previously published observations used. For the details about the observations collected from the literature we refer the reader to the original works (Table 3.1).

3.2.1. WSRT data

The WSRT data used in this work is the same presented in Oonk et al. (2017). The data reduction steps are the same up to the imaging part. Before imaging, we subtracted the continuum from the calibrated visibilities using *CASA*'s (McMullin et al., 2007) *uvcontsub* (see e.g., van Gorkom & Ekers, 1989; van Langevelde & Cotton, 1990). We use a first order polynomial which is fit to line free channels at both sides of the α lines when possible. After this we imaged the continuum subtracted data using Briggs weighting (Briggs, 1995). We tested using different robust parameters to determine the

Table 3.1.: Selected observations towards Cas A

Line or band	Telescope	Velocity resolution (km s^{-1})	Spatial resolution[c]	Reference
C268α	WSRT	0.6	$70'' \times 70''$ 0°	This work.
C357α	LOFAR HBA	0.7	$18'' \times 18''$ 0°	This work.
C494α	LOFAR LBA	2	$65'' \times 45''$ 100°	Oonk et al. (2017)
C539α	LOFAR LBA	2	$65'' \times 45''$ 100°	Oonk et al. (2017)
HI–21 cm	VLA	0.65	$7'' \times 7''$ 0°	Bieging et al. (1991)
1667 MHz–OH	VLA	1.3	$7'' \times 7''$ 0°	Bieging & Crutcher (1986)
^{13}CO(1–0)[a]	NRAO 12 m	0.13	$56'' \times 56''$ 0°	Liszt & Lucas (1999)
CO(2–1)[b]	SMT	0.3	$33'' \times 33''$ 0°	Kilpatrick et al. (2014)
[CI] $^3P_1$–$^3P_0$	KOSMA	0.63	$54'' \times 54''$ 0°	Mookerjea et al. (2006)
[CII]	Herschel PACS[d]	250	$12'' \times 12''$ 0°	Salas et al. (2017)
A_V			$35'' \times 35''$ 0°	De Looze et al. (2017)

[a] ^{12}CO(2–1) is also available from the same observations.
[b] ^{12}CO and ^{13}CO.
[c] Observing beam major axis, minor axis and position angle.
[d] Herschel is an ESA space observatory with science instruments provided by European-led Principal Investigator consortia and with important participation from NASA.

best trade-off between sensitivity and resolution. Using a robust factor of -1 provided the best angular resolution $\theta \leq 70''$ for most subbands (40 out of the 6×8 subbands). A robust factor of 1 provides a factor of two lower spectral noise with a synthesised beam size of $\theta \leq 100''$ (47/48 subbands). We use the cubes generated with a robust of -1 since we are interested in the spatial structure of the line. After imaging we stack the cubes and apply a bandpass correction in the image plane. The stacked cube has a spatial resolution of $70''$ and contains 40 α RRL transitions[1]. The stacked line profile corresponds to RRLs with an average n of 268. After this we compared the stacked line profile extracted from over the face of Cas A with those presented by Oonk et al. (2017). This comparison showed that the spectra agree within errors.

To study the distribution of the weaker C268α -38 km s^{-1} velocity components we convolve the spectral axis of the cube to increase the signal-to-noise. As convolution kernel we use a boxcar four channels wide. This also produces a cube with a similar velocity resolution as that of the C539α cube (see Table 3.1). In order to allow for a better comparison between the C268α and C539α lines we regrid the spectral axis of the C268α cube to match that of the C539α cube.

Of the CRRL data used in this work, the one coming from the WSRT observations is the one with the coarsest spatial resolution.

3.2.2. LOFAR HBA DATA

Cas A was observed with the LOFAR HBA on December 13, 2015 for four hours (obsid: L415239). This data was taken as part of the LOFAR Cassiopeia A spectral survey (LCASS, PI, J. B. R. Oonk). During the observation all 23 + 14 Dutch stations were used. These observations cover the 132.6–152.3 MHz range with 195.3125 kHz wide spectral windows. The correlator was set up to deliver spectral windows with 512 spectral channels. This results in a channel width of 0.75–0.87 km s^{-1}.

Cygnus A was used as amplitude calibrator at the beginning of the observations (obsid: L415237). Phase and amplitude solutions were derived against Cygnus A and then applied to the Cas A data. After transferring the amplitude and phase from Cygnus A, we self calibrated the Cas A data. We started the self-calibration cycle using a small number of clean iterations and short baselines, then in each repetition of the cycle a larger number of clean iterations, as well as longer baselines, were used. The cut-off in the baseline length started at 2000 lambdas and increased to 12000 lambdas. LOFAR has baselines longer than 12000 lambdas, but we decided to stop at this cut-off because the signal-to-noise ratio drops for higher resolution. After imaging, the cubes were convolved to a common resolution of $18''$. The cubes were then converted to optical depth using $\tau_\nu = I_\nu / I_\nu^{\rm cont} - 1$, where I_ν is the spectrum extracted from the data cubes and $I_\nu^{\rm cont}$ is the continuum determined from a linear fit to line free channels (e.g., Oonk et al., 2014; Salas et al., 2017). Any residual bandpass in the optical depth cubes was corrected in the image plane using an order two polynomial.

After this, the RRL optical depth cubes were stacked. In the frequency range between 132.6 and 152.3 MHz there are 16 α RRLs. From these, we selected four lines which

[1] A line involving a change in principal quantum number of $\Delta n = 1$ is called an α line.

were in spectral windows with low radio frequency interference during the observations. The stacked cube has α RRLs with an averaged principal quantum number $n = 357$.

3.2.3. LOFAR LBA DATA

The data reduction of the LOFAR LBA data is described in Oonk et al. (2017, obsid 40787). For this work we have split the ~ 75 CRRLs present in the 33–57 MHz range into two groups; one group uses the first six CRRLs, which have principal quantum numbers $n = 491, 492, 493, 495, 496, 497$, and another group with the remaining CRRLs (see Table 2 of Oonk et al., 2017 for the complete list). This division is made in order to study the CRRL profile at a lower n number, where the effects of pressure and radiation broadening are less severe and it is easier to differentiate velocity components (e.g., Oonk et al., 2017). The stacked cubes have α RRLs with averaged principal quantum numbers of 494 and 539.

3.2.4. LITERATURE DATA

We complement the spatially resolved LOFAR and WSRT cubes presented in this work with observations from the literature. A summary of the literature observations is presented in Table 3.1. From the literature we have selected the following maps; HI–21 cm (Bieging et al., 1991), the 1667 MHz line of OH (Bieging & Crutcher, 1986), ^{12}CO(2–1) and ^{13}CO(2–1) (Kilpatrick et al., 2014), 492 GHz [CI] Mookerjea et al. (2006), and 158 μm [CII] (Salas et al., 2017). Additionally we include the dust-derived interstellar extinction A_V map of De Looze et al. (2017).

To compare observations with different angular resolutions we convolve the maps to a common resolution of $70''$. We use $70''$ to match the resolution of the WSRT cubes. Two exceptions are the 158 μm [CII] cube and A_V map. We do not convolve the 158 μm [CII] cube since the area covered by each PACS observation is smaller ($45'' \times 45''$) than the target resolution. As for the dust-derived A_V map, we do not convolve because the images used to model the dust emission were analysed at $35''$ resolution (De Looze et al., 2017).

3.3. RESULTS

3.3.1. GLOBAL VELOCITY STRUCTURE

In terms of the line of sight structure, the gas towards Cas A is observed in various ISM tracers in at least four velocity components. One component corresponds to gas in the local Orion spur at velocities close to 0 km s^{-1} (all velocities are referenced with respect to the local standard of rest). The remaining velocity components, and main focus of this work, are associated with the Perseus arm of the Galaxy at velocities of -47, -41 and -36 km s^{-1}. These last two velocity components have been treated as a single velocity component at -38 km s^{-1} in previous CRRL studies because they are difficult to separate (e.g., Payne et al., 1994; Kantharia et al., 1998; Oonk et al.,

2017). Here we use this nomenclature when we are not able to separate the −41 and −36 km s^{-1} velocity components.

To compare the line profiles we averaged the pixels covering the face of Cas A. We define the face of Cas A as a circle of radius 2′.5 centred on $(\alpha, \delta)_{\rm J2000} = (23^{\rm h}23^{\rm m}24^{\rm s}, +58°48'54'')$. The spectra are shown in Figure 3.2. In this Figure we highlight the position of three velocity components, at −47, −41 and −36.5 km s^{-1}. When the spectra shows the presence of these three velocity components, we notice that the velocity of the line peak agrees between different tracers. For the −38 km s^{-1} velocity component we can see that the line profile is a blend of two or more velocity components. This is more readily seen in the line profiles of C268α, ^{12}CO and 1667 MHz–OH, where two velocity components are observed, one close to −41 km s^{-1} and other at −36.5 km s^{-1}.

3.3.2. Channel maps

Here we present spatially resolved C268α and C539α optical depth cubes. The C357α and C494α maps will be shown later (in § 3.3.3), as these show a spatial distribution very similar to that of the C268α and C539α lines (Figures 3.3 and 3.4).

C268α channel maps at velocities around that of the −47 km s^{-1} velocity component are shown in Figure 3.3. These maps show that the gas is predominantly concentrated to the southwest of Cas A. At around −47 km s^{-1} there is emission in an elongated structure running from Cas A's western hotspot to its south. This has been labelled with a white line between the W and S (Figure 3.3). Higher resolution OH observations show that there are three OH clumps over this W-S structure at a velocity $\sim$ −47 km s^{-1} (clumps B, D and E, Bieging & Crutcher, 1986). However, since OH and CRRLs do not trace exactly the same gas, we cannot use this as evidence that the W-S structure is a collection of clumps. With the resolution of the cubes presented in this work it is not possible to distinguish if this is a filament or unresolved clumps.

Channel maps showing velocities corresponding to the Perseus arm features of the C268α and C539α lines are presented in Figure 3.4. Here we use the velocity averaged C268α cube to emphasise features close to −38 km s^{-1}. Emission from the C268α −38 km s^{-1} velocity component is located in the western side of Cas A as well as in the northeast, with a clump close to the centre of Cas A between −43 and −41 km s^{-1}. This central clump is also identified in OH and CO (Bieging & Crutcher, 1986; Wilson et al., 1993).

In the C539α maps we can see similar structures to those seen in the C268α maps, albeit with more detail due to the higher signal-to-noise ratio of the LOFAR data. The W-S structure is visible between −49 and −37 km s^{-1}. The larger extent in velocity is partially due to (radiation or pressure) broadening of the lines at high n (e.g., Salgado et al., 2017b). The spatial distribution of the C539α −38 km s^{-1} velocity component is harder to interpret due to the blending of the Perseus arm velocity components. If we assume that absorption at the more positive velocities is mainly due to the −38 km s^{-1} velocity component, then the absorption close to −33 km s^{-1} should be representative. At this velocity we see that the absorption comes primarily from the east and west of Cas A, like the C268α emission from this velocity component.

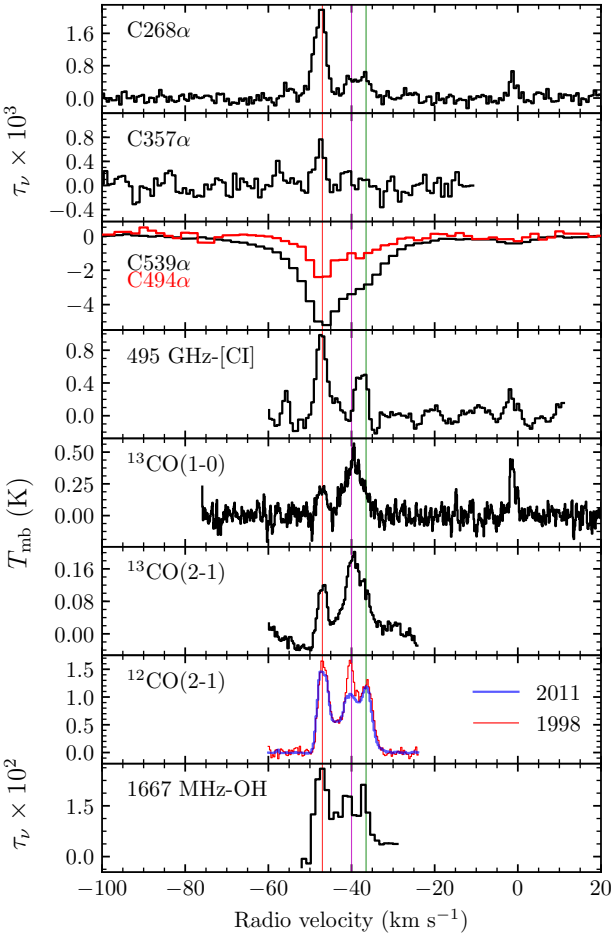

Figure 3.2.: Comparison between the spectra of C268α, C357α, C539α, 492 GHz–[CI], ^{13}CO(1–0), ^{13}CO(2–1), ^{12}CO(2–1) and 1667 MHz–OH. The three CRRLs and the OH line are shown in optical depth units while the [CI] and CO lines in brightness temperature units. The spectra where extracted from an aperture defined by the extent of the 1667 MHz–OH line map. The Perseus arm velocity components at −47, −41 and −36.5 km s^{-1} are shown with *red*, *magenta* and *green* lines respectively. The difference in the 1998 and 2011 ^{12}CO(2–1) line profiles is due to the different choice of off-source position.

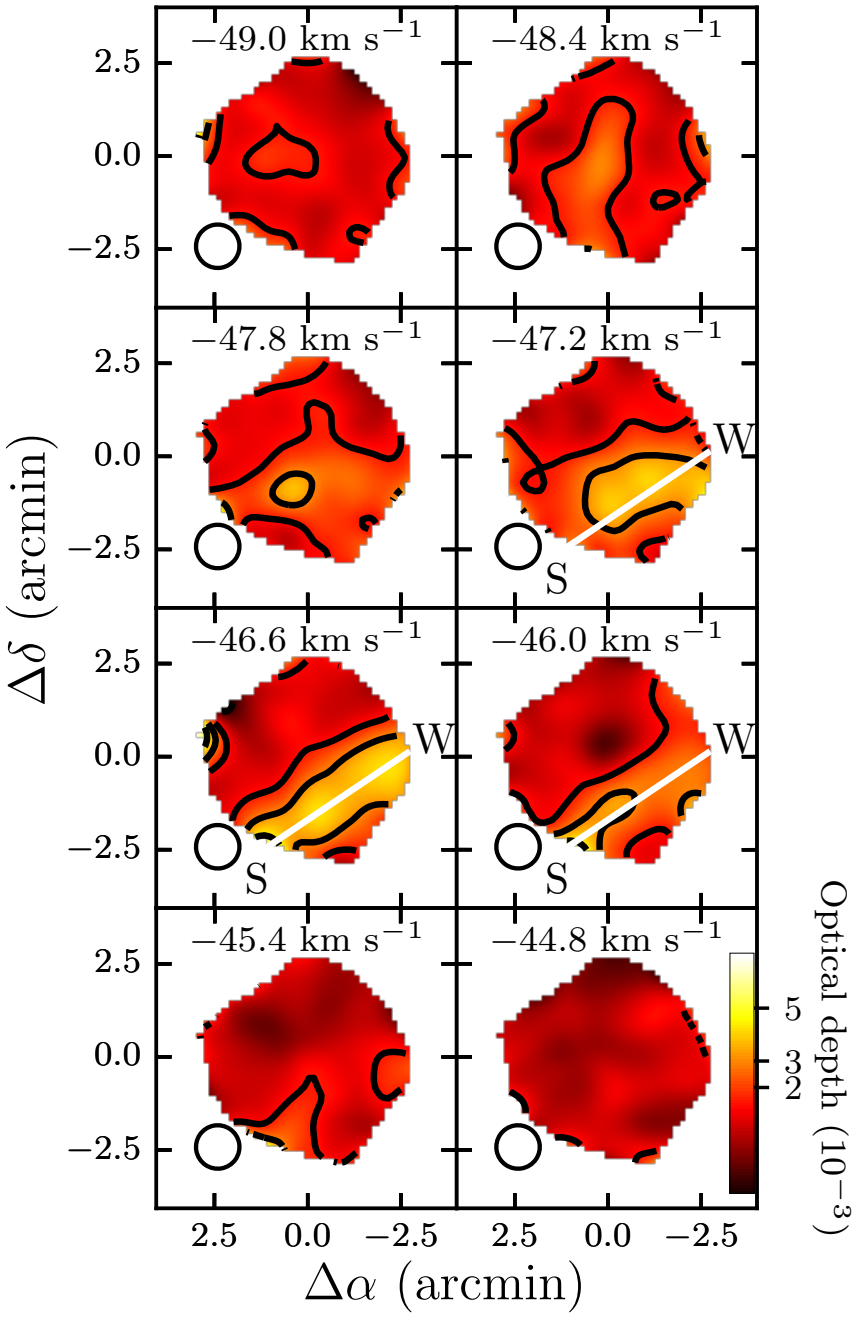

Figure 3.3.: C268α emission around -47 km s^{-1} channel maps. These maps have a spatial resolution of 70″, shown in the lower left corner of each panel. The contours start at 3σ, with $\sigma = 6 \times 10^{-4}$, and continue at values of 4σ, 5σ and 6σ. The white line marks the location of an elongated structure with a W-S orientation.

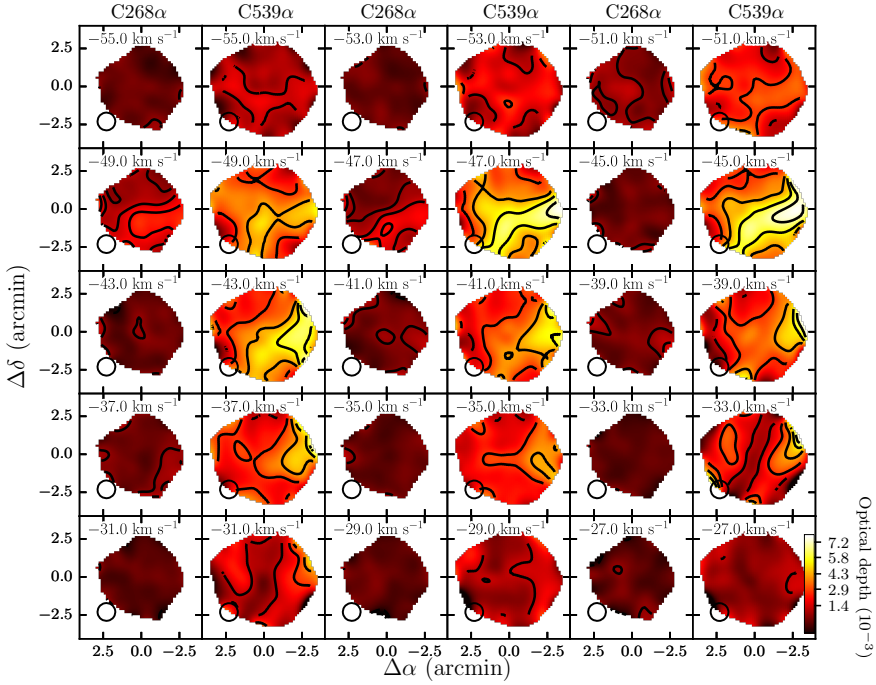

Figure 3.4.: C268α emission and C539α absorption channel maps. The spectral axis of the C268α cube was convolved to a 2.4 km s^{-1} velocity resolution and reggrided to match the spectral axis of the C539α cube. The colour scale is the same for both C268α emission and C539α absorption. The contours start at 3σ with $\sigma = 2.5 \times 10^{-4}$ for C268α and $\sigma = 4.8 \times 10^{-4}$ for C539α. The 70″ resolution of the channel maps is shown in the bottom left corner of each map.

3.3.3. CRRL PROPERTIES

The properties of low frequency CRRLs can be used to determine the gas electron density, temperature and pressure. These properties imprint their signature in the line integrated optical depth as a function of principal quantum number n (e.g. Shaver, 1975; Salgado et al., 2017a). Additionally, the change in line width with n, caused by radiation and pressure broadening, also provides information about the gas properties (e.g. Shaver, 1975; Salgado et al., 2017a).

To determine the line properties over the face of Cas A on a pixel-by-pixel basis we fit the line profiles and construct moment maps. In order to fit the line profiles we first determine where the lines are detected by using the moment masking method as refined by Dame (2011). In this method the data cube is smoothed to a resolution which is two times the original cube resolution in the spatial and spectral directions. Using the smoothed cube we search for significant detections by requiring that the signal-to-noise ratio is above some threshold level. For each pixel/channel which shows a significant detection we also set the neighbouring pixels which are inside the convolution kernel as detections. Then we fit the line profile only in those regions where there are significant detections.

To determine an optimum threshold level we tested using synthetic data cubes. In this test we varied the threshold level between one and ten times the noise in the synthetic data cube and compared the recovered moment 0 with the known input. This test shows that if we use a threshold of three times the noise in the smoothed cube, then the line properties can be recovered with no significant deviation from the input data. For these observations this means that for the higher signal-to-noise line at -47 km s^{-1} we should recover most of the line structure. However, for the weaker velocity component at -38 km s^{-1}, we are likely to recover only the brightest regions.

To fit the RRLs with principal quantum number 268 we use Gaussian line profiles. We fit up to three CRRLs close to -47 km s^{-1}, -38 km s^{-1} and 0 km s^{-1}. Once we have the line properties from the $n = 268$ CRRLs, we use their second and third moments to guide the fit for the higher n lines. In the case of the $n = 357$ lines this is necessary given the lower signal-to-noise ratio. For the $n = 494$ and 539 lines this is done to guide the separation of the blended line profiles. This relies on the assumption that the CRRLs at different frequencies will trace gas with similar properties. Studies which cover a larger frequency range than the one studied here show that the line properties can be accurately modelled by a single set of gas properties (Oonk et al., 2017). With this the line centroid should be the same for different n lines, and for $n \leq 500$ the line profile is dominated by the gas thermal motion (Salas et al., 2017), which does not depend on frequency.

To fit the C357α lines we use two Gaussian profiles, one for the -47 km s^{-1} velocity component and one for -38 km s^{-1}. When fitting we fix the line centroid and line width to those of the C268α line. This leaves the line amplitude as the only free parameter.

To fit the C494α and C539α lines we use two Voigt profiles, one for the -47 km s^{-1} velocity component and one for -38 km s^{-1}. When fitting we fix the line centroid and the Doppler core of the line profiles to those of the C268α lines. This leaves the amplitude and Lorentz width as free parameters. When there is no significant C268α

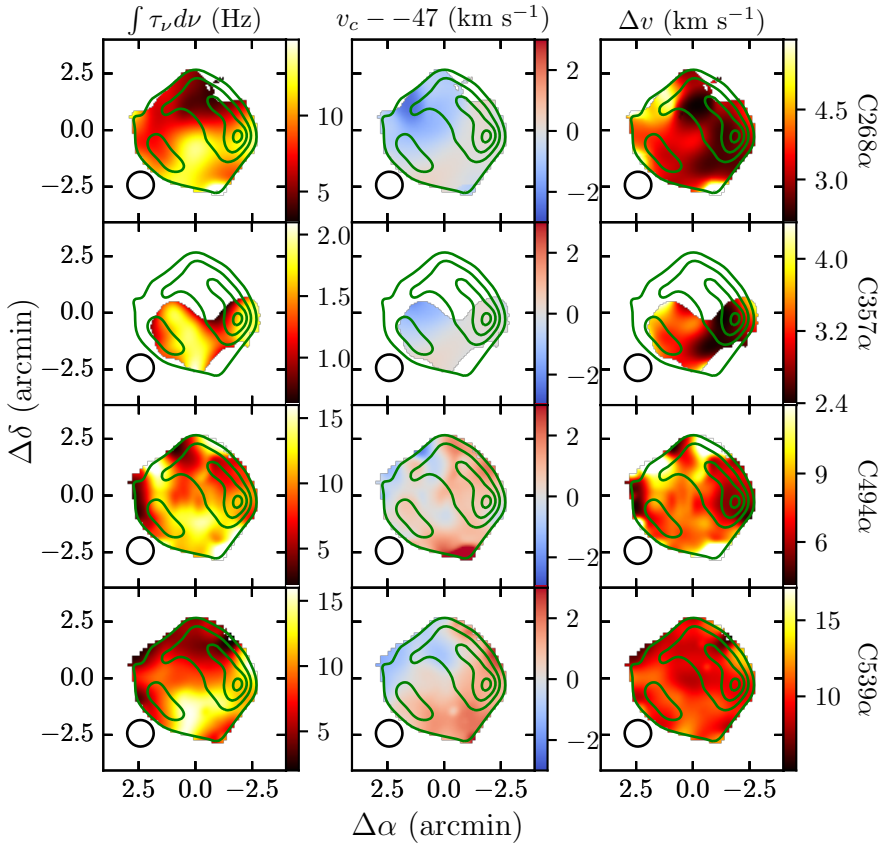

Figure 3.5.: Moment maps for the CRRLs at −47 km s^{-1}. The *top row* shows the moment maps for the C268α line, the *upper middle row* for the C357α line, the *lower middle row* for the C494α line and the *bottom row* for the C539α line. The *left column* shows the integrated optical depth, the *middle column* the velocity centroid of the line with respect to −47 km s^{-1} and the *right column* the full width at half maximum of the line. The *green contours* show the 345 MHz continuum from Cas A at 51″ × 45″ resolution. The 70″ resolution of the moment maps is shown in the bottom left corner of each map. At the edges of Cas A the signal-to-noise ratios are lower due to the fainter continuum.

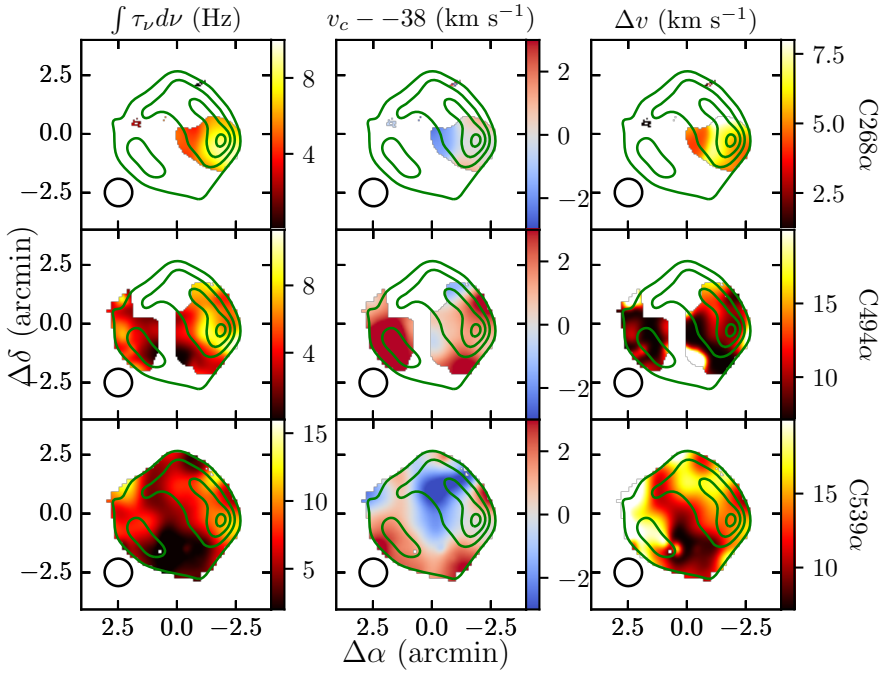

Figure 3.6.: Moment maps for the CRRLs at -38 km s^{-1}. The *top row* shows the moment maps for the C268α line, the *middle row* for the C494α line and the *bottom row* for the C539α line. The *left column* shows the integrated optical depth, the *middle column* the velocity centroid of the line with respect to -38 km s^{-1} and the *right column* the full width at half maximum of the line. Here we do not show the C357α line moments as they are similar to those of the C268α line. The *green contours* show the 345 MHz continuum from Cas A at $51'' \times 45''$ resolution. The $70''$ resolution of the moment maps is shown in the bottom left corner of each map. At the edges of Cas A the signal-to-noise ratios are lower due to the fainter continuum.

line emission we adopt the median values from the C268α moments as initial guesses for the line parameters, but we allow them to vary. This is mostly the case for the line at -38 km s^{-1}.

The moment maps for the $n = 268$ RRL at -47 km s^{-1} are shown in the top row of Figure 3.5. Here we see that emission from the -47 km s^{-1} velocity component extends almost all over the face of Cas A, with a lower integrated optical depth to the north of the remnant. The moment 0, or velocity integrated optical depth, map for the -47 km s^{-1} velocity component shows that most of the emission comes from the W-S structure. The moment 1, or optical depth weighted velocity centroid, map shows that over the W-S structure the velocity remains constant. The moment 2, or full width at half maximum, map shows that the line is narrow in the West and broadens to the East of Cas A. Towards the North-east of Cas A the -47 km s^{-1} C268α line is broader by a factor of ~ 2 with respect to the W-S structure. The CRRL at 0 km s^{-1} is not displayed because at $70''$ resolution the signal-to-noise ratio is lower than three in individual pixels.

The moment maps for the C357α -47 km s^{-1} velocity component are shown in the middle panels of Figure 3.5. These show that the velocity integrated optical depth of the -47 km s^{-1} velocity component is larger in the W-S structure, similar to that observed in the C268α line.

The moment maps for the C539α line at -47 km s^{-1} are shown in the bottom panels of Figure 3.5. These show that most of the C539α absorption from the -47 km s^{-1} velocity component comes from the W-S structure, in accordance with the lower n lines. The moment 2 maps suggests that the -47 km s^{-1} velocity component is broader towards the south-east of Cas A, however the line width is consistent with a constant value over the face of Cas A.

The moment maps for the C268α and C539α -38 km s^{-1} velocity component are shown in Figure 3.6. The C268α line is only detected towards the western hotspot of Cas A. In contrast, the C539α line is detected almost all over the face of Cas A. Both maps show that the peak integrated optical depth is located towards the western hotspot of Cas A. For the C357α line at -38 km s^{-1} the spatial distribution is similar to that of the C268α at the same velocity, a patch $\sim 0.4'$ towards the south of the western hotspot of Cas A.

The moment 2 maps for the -38 km s^{-1} component shows that the line is broader towards the northern half of Cas A, with the broadest line towards the east. The minimum line broadening is observed towards the centre and south of Cas A. This resembles the ridge of CRRL absorption that passes through the centre of Cas A between -33 and -31 km s^{-1} (Figure 3.4).

3.3.4. Physical conditions from CRRLs

The change in the CRRL profile as a function of principal quantum number has the signature of the gas physical conditions imprinted on it (Shaver, 1975; Salgado et al., 2017a). The gas properties which can be determined using CRRLs are its electron density $n_{\rm e}$, electron temperature $T_{\rm e}$ and the intensity at 100 MHz of the radiation field the carbon atoms are immersed in, $T_{r,100}$.

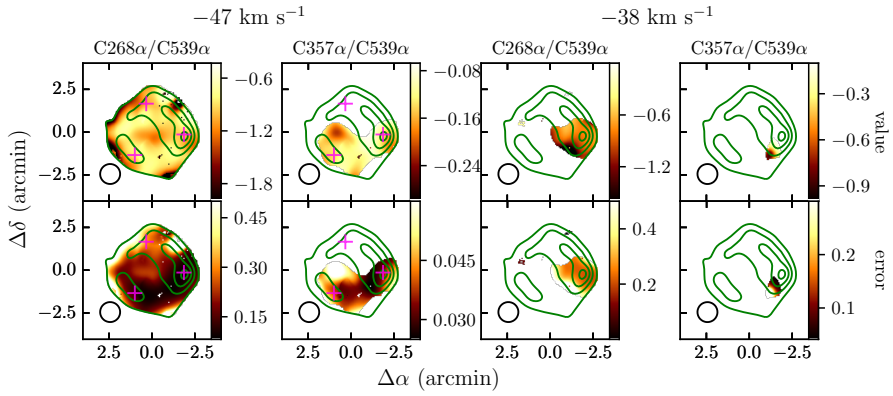

Figure 3.7.: Ratios between different CRRLs at different velocities. The ratios shown are the R_{539}^{268} =C268α/C539α and R_{539}^{357} =C357α/C539α line ratios. The *top panels* show the ratio value and the *bottom panels* the error on the ratio. The *text on top of each column* indicates which ratio is shown in the corresponding column, and a *text label* on the top of the Figure shows the velocity component. The ratios show only regions where both lines involved have been detected with a signal-to-noise ratio larger than three. The *pink crosses* in the top panel show the regions used in Figure 3.8. The 70″ resolution of these maps is shown in the bottom left corner of each map.

To determine the CRRL properties we use the models of Salgado et al. (2017a). To solve the level population problem we assume that collisions with atomic hydrogen and electrons set the relative population of carbon ions in the $^2P_{1/2}$ and $^2P_{3/2}$ states. For the collisional rates we adopt the values of Tielens & Hollenbach (1985) for collisions with hydrogen and those of Hayes & Nussbaumer (1984) for collisions with electrons. We adopt electron and carbon abundances of 3×10^{-4} while solving the level population problem. However, when converting to per hydrogen atom quantities, we adopt electron and carbon abundances of 1.5×10^{-4}. The effect of these assumptions is small ($\sim$ 10%), and will be discussed later. For the ℓ-changing collisional rates we use the semi-classical formulation of Vrinceanu et al. (2012) incorporated into the Salgado et al. (2017a) models. Additionally, when solving the level population problem, a radiation field with a power law shape is included. This radiation field has a spectral index of −2.6, similar to the observed spectral index of Galactic synchrotron emission (e.g., de Oliveira-Costa et al., 2008; Zheng et al., 2016), and its intensity is defined at 100 MHz by $T_{r,100}$ (Shaver, 1975; Salgado et al., 2017a).

In order to model the gas properties we assume that the radiation field the gas is immersed in is constant. Since we are studying gas on scales of $\lesssim$ 1 pc and the gas is at a distance of $\gtrsim$ 220 pc from Cas A (e.g., Kantharia et al., 1998; Salas et al., 2017), the possible contribution of Cas A to the radiation field (Stepkin et al., 2007) will change by a negligible amount over the observed structure. Additionally, there are no other known strong, low-frequency, discrete radiation sources in the field. Considering this, it seems reasonable to assume that the gas is immersed in a constant radiation field.

Table 3.2.: Grid of CRRL models

Parameter	Notation	Value	Step
Electron density	$n_{\rm e}$	0.01–0.1 cm^{-3}	0.005 cm^{-3}
Electron temperature	$T_{\rm e}$	10–400 K	5 K
Radiation field at 100 MHz	$T_{\rm r,100}$	800–2000 K and 1400 K	400 K

Following the results of Oonk et al. (2017) we adopt $T_{r,100} = 1400$ K.

Given the C268α, C357α, C494α and C539α velocity integrated optical depths we explore how these can be used to constrain the gas properties. We do not attempt to model the change in integrated optical depth as a function of n, like Oonk et al. (2017) did, given that the number of free parameters is similar to the number of data points. Instead, we use the ratios between these lines. We will use the notation $R^{n}_{n'}$ to denominate the C$n\alpha$/C$n'\alpha$ line ratio, e.g., C357α/C539α line ratio will be R^{357}_{539}.

To generate R^{268}_{539}, R^{268}_{494} and R^{357}_{539} from the observations we use the respective velocity integrated optical depth maps (Figures 3.5 and 3.6). These line ratios are shown in Figure 3.7. In the case that one of the lines is not detected in one of the pixels we adopt the 3σ upper/lower limit on the integrated optical depth for the non detection. If two lines are not detected on a pixel we do not attempt to constrain the gas physical conditions. This limits our analysis for the -38 km s^{-1} velocity component to the western hotspot of Cas A, where the C268α line is detected (Figure 3.6).

The line ratios as a function of gas properties in the $n_{\rm e}$–$T_{\rm e}$ plane are shown in Figure 3.8 for three different locations in the map (see Figures 3.7 and 3.9). As a result of the C268α line being in emission and the C539α line in absorption R^{268}_{539} produces contours which have a similar shape to the constraint imposed by the transition from emission to absorption (Salgado et al., 2017b). The situation is similar for R^{268}_{494}. However intersecting the R^{357}_{539} constraint with either R^{268}_{539} or R^{268}_{494} restricts the range of allowed $n_{\rm e}$ and $T_{\rm e}$ values. The left panel of Figure 3.8 shows that the CRRL ratios used can constrain the gas properties in regions with high signal-to-noise ratio detections. Yet it also reveals that when one of the lines is not detected it is not possible to constrain the gas properties (e.g., right panel in Figure 3.8). In this case the line ratios constrain the gas electron density, and place a lower limit on the gas temperature. An upper limit on the gas temperature can be obtained if we consider the implied gas path length. If we restrict the models to path lengths smaller than 200 pc, this effectively puts an upper limit on the electron temperature of ≈ 160 K (Figure 3.8). We adopt an upper limit of 200 pc since we do not expect the gas structures to be larger than this in the line of sight direction.

Maps with the electron density, temperature and pressure constraints derived from the line ratio analysis for the -47 km s^{-1} velocity component are shown in Figure 3.9. The electron density shows almost no variation over the face of Cas A, while the electron temperature and pressure show a slight decrease towards the South. The electron density

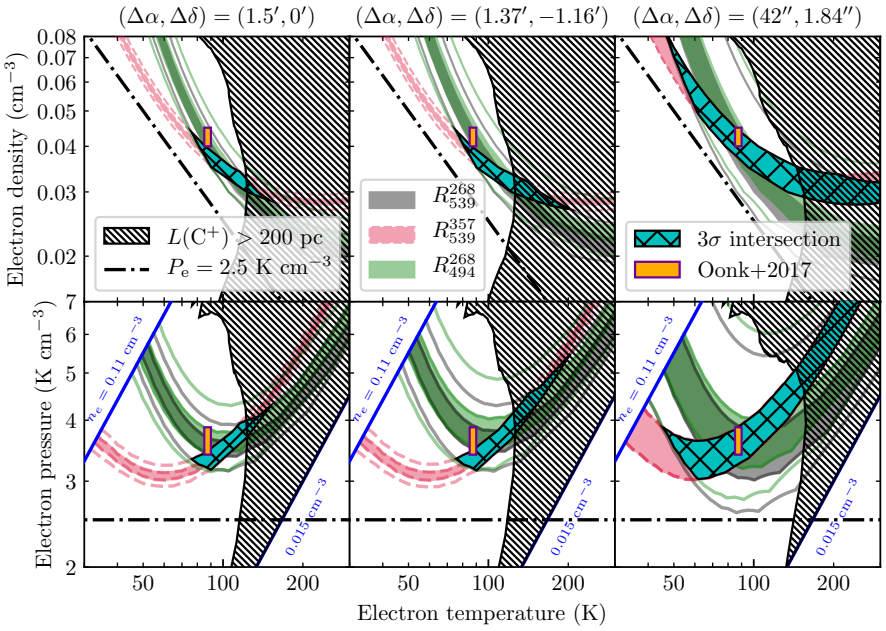

Figure 3.8.: Constraints imposed by the R^{268}_{539} =C268α/C539α, R^{357}_{539} =C357α/C539α and R^{268}_{494} =C268α/C494α line ratios in the n_e–T_e plane (*top panels*) and in the P_e–T_e plane (*bottom panels*). The constraints are shown for the −47 km s^{-1} velocity component at three different positions in the map. The positions, relative to the map centre, are shown on the top of the corresponding column. These positions are shown in Figures 3.7 and 3.9 as green crosses. The *orange rectangle with purple borders* shows the gas physical conditions derived by Oonk et al. (2017). The *dot-dashed line* shows a curve of constant electronic pressure. The *cyan region hatched with black lines* shows the intersection of the constraints imposed by the R^{268}_{539}, R^{357}_{539} and R^{268}_{494} line ratios if we consider their 3σ ranges. The *densely hatched region* shows where the required ionized carbon path length is larger than 200 pc. *Blue lines* in the bottom row show the limits of the grid of CRRL models.

has an almost constant value over the face of Cas A, however this largely due to the resolution of the model grid. In the density axis we have 18 resolution elements, while on the temperature axis we have 78 (Table 3.2). The discrete nature of the grid of models used to determine the electron temperature and density also results in abrupt changes in the gas properties. Additionally, this discreteness can produce patches which have sizes smaller than the spatial resolution of the data. This effect is particularly notorious in the T_e map (Figure 3.9).

As it is evident in Figure 3.8, we are constraining the gas properties to a given range. The size of this range will depend on the error bars of each pixel. For pixels with high signal-to-noise (left and centre panels in Figure 3.8) the uncertainty in electron density is about $\sim 30\%$ and in electron temperature $\sim 25\%$. While on pixels with lower signal to noise (right panel in Figure 3.8), the uncertainty can be of a factor of three or more. A change of about 25% in electron temperature translates into a 65% change in emission measure. In Table 3.3 we present the gas properties averaged over the face of Cas A. In this Table we provide the parameter ranges if we consider the 1σ uncertainties in the observed line ratios. In terms of the spatial distribution, this shows little change when we consider the uncertainties. The biggest change is on the mean value.

To estimate the hydrogen density from the electron density we assume that 94% and 100% of free electrons come from carbon for the -47 and -38 km s^{-1} velocity components respectively (Oonk et al., 2017). Additionally, we adopt a carbon abundance relative to hydrogen of 1.5×10^{-4} (Sofia et al., 1997). With this, the hydrogen density is 210–360 and 200–470 cm^{-3} for the -47 and -38 km s^{-1} velocity components respectively.

The largest uncertainty in the derived gas properties comes from the separation between the -47 and -38 km s^{-1} velocity components for the $n > 400$ lines. We test this effect by varying the integrated optical depth of the C539α line and comparing the derived values of n_e and T_e. We find that the electron temperature has an almost linear relation with the integrated optical depth of the C539α line, i.e. if we decrease the C539α line integrated optical depth by 30%, then the derived electron temperature decreases by 30%. For the electron density the change is less pronounced. A change of 30% in the integrated optical depth of the C539α line results in a change of less than 15% in the electron density.

Using the electron density and temperature maps and the C268α integrated optical depth we compute the ionized carbon emission measure, $EM_{\rm CII}$, column density, N(CII), and its path length along the line of sight, $L_{\rm CII}$. To determine the column density and $L_{\rm CII}$ we assume that 94% of the free electrons come from ionized carbon (Oonk et al., 2017). Maps with $EM_{\rm CII}$, N(CII) and $L_{\rm CII}$ for the -47 km s^{-1} velocity component are shown in Figure 3.10. These show a similar structure to the C268α integrated optical depth map, with larger values towards the South and West of Cas A. The structures smaller than the beam size are due to the strong dependence of the integrated optical depth on the electron temperature ($\propto T_e^{-5/2}$), and the discrete nature of the model grid used. For a constant electron and carbon density the only variation in the emission measure comes from variations in the path length of the gas along the line of sight. This will also be reflected in the column density $N(\mathrm{CII}) = L_{\rm CII} n_{\rm CII}$.

We compare the derived gas physical conditions against the spatially unresolved work

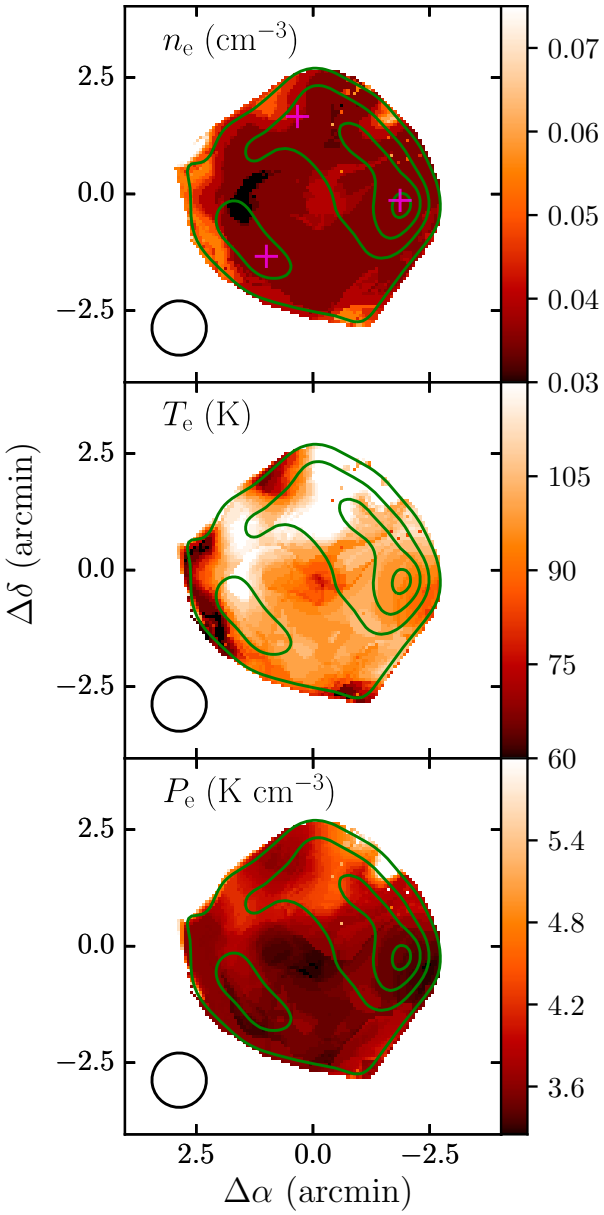

Figure 3.9.: Gas properties derived from the CRRL ratios for the Perseus arm component at −47 km s^{-1}. The *top panel* shows the electron density, the *middle panel* the electron temperature and the *bottom panel* the electron pressure. These are derived under the assumption of a constant radiation field of 1400 K at 100 MHz. The *pink crosses* in the top panel show the regions used in Figure 3.8. The 70″ resolution of these maps is shown in the bottom left corner of each map.

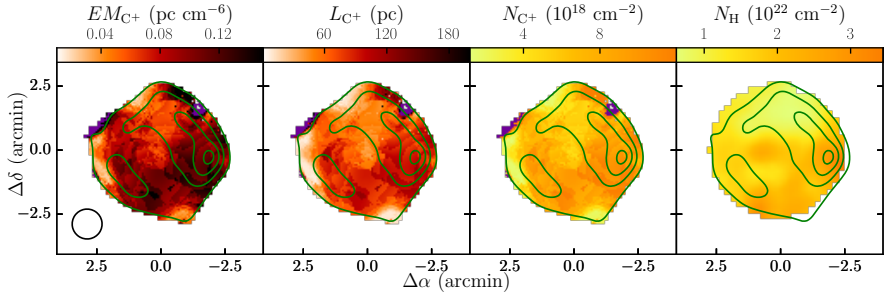

Figure 3.10.: C^+ emission measure EM_{CII}, path length L_{CII} and column density of ionized carbon N(CII) derived from the CRRL analysis for the Perseus arm component at −47 km s^{-1}, and the hydrogen column density map derived from the dust analysis by De Looze et al. (2017). The *leftmost column* shows the emission measure, the *middle left column* the path length, the *middle right column* the column density of ionized carbon and the *rightmost column* the hydrogen column density derived from analysis of the dust emission towards Cas A (De Looze et al., 2017). Regions where we cannot constrain the gas properties given the parameter space explored and observational uncertainties are shown with a colour not present in the colour bar. The 70″ resolution of these maps is shown in the bottom left corner of each map. The *green contours* show the 345 MHz continuum from Cas A at 51″ × 45″ resolution.

Table 3.3.: Ranges of the mean gas properties over the face of Cas A

Gas property	Velocity component	
	−47 km s^{-1}	−38 km s^{-1}
T_e (K)	71–137	50–145
n_e (cm^{-3})	0.03–0.055	0.03–0.07
P_e (K cm^{-3})	3.1–4.95	2.7–4.8
EM_{CII} (pc cm^{-6})	0.046–0.26	0.02–0.21
N_{CII} (10^{18} cm^{-2})	3.4–25.9	1.6–18.1
L_{CII} (pc)	27–182	10–180
n_H[a] (cm^{-3})	210–360	200–470
N_H[a] (10^{22} cm^{-2})	2.3–17.3	1–12
A_V[b]	11.5–360	200–470

[a] Assuming a carbon abundance relative to hydrogen of 1.5×10^{-4} (Sofia et al., 1997) and that 94% and 100% of the free electrons come from ionized carbon for the −47 and −38 km s^{-1} velocity components respectively (Oonk et al., 2017).

[b] Adopting $N_H = (2.08 \pm 0.02) \times 10^{21} A_V$ cm^{-2} (Zhu et al., 2017).

Table 3.4.: 158 μm-[CII] Line properties

Region	v_c (km s^{-1})	$\int I_\nu d\nu$ (10^{-5} erg cm^{-2} s^{-1} sr^{-1})	$L_{[CII]}$ ($L_\odot$)
1	-19 ± 15	6.70 ± 0.11	1.14 ± 0.02
2	-20 ± 15	5.99 ± 0.11	1.02 ± 0.02
3	-18 ± 15	6.15 ± 0.09	1.05 ± 0.01
4	-20 ± 15	6.76 ± 0.12	1.15 ± 0.02
5	-19 ± 15	4.65 ± 0.22	0.79 ± 0.04
6	-23 ± 15	5.10 ± 0.19	0.87 ± 0.03
7	-19 ± 15	6.92 ± 0.08	1.18 ± 0.01
8	-19 ± 15	6.74 ± 0.15	1.15 ± 0.02
9	-15 ± 15	7.14 ± 0.11	1.22 ± 0.02

of Oonk et al. (2017) towards the same background source to check for any differences. We focus on their study as it was the first one which was able to simultaneously explain the line width and integrated optical depth change with *n*. Additionally, this work and that of Oonk et al. (2017) use the same models, which reduces the need to account for different assumptions in the modelling. If we compare Table 3.3 with Table 7 of Oonk et al. (2017) we see that our results, averaged over the face of Cas A, are consistent.

3.3.5. 158 μm-[CII] LINE PROPERTIES

The 158 μm-[CII] line is the main coolant of the neutral diffuse ISM (e.g. Wolfire et al., 1995, 2003). Here we present the properties of the spatially resolved, velocity unresolved, 158 μm [CII] line.

To determine the properties of the 158 μm-[CII] line we fit a Gaussian profile to each of the nine PACS footprints. We only fit one Gaussian component since the line is unresolved in velocity. The best fit parameters of the Gaussian profile are presented in Table 3.4. These show little variation in the line frequency integrated intensity, but we do note that the lowest values are found in the northern footprints (5 and 6, see Figure 3.11). This could be due to the lower column densities found towards the north of Cas A (see Figure 3.10).

If we take the observed luminosity of the 158 μm-[CII] line and compare it to the CRRL derived gas column density we obtain values of the order of $(1.4 \pm 0.1) \times 10^{-26}$ erg s^{-1} (H-atom)$^{-1}$. This cooling [CII] rate is is somewhat less than the cooling rate derived from ultraviolet absorption line studies originating from the upper fine structure level in sighlines through nearby diffuse clouds ($(3–10) \times 10^{-26}$ erg s^{-1} (H-atom)$^{-1}$ Pottasch et al., 1979; Gry et al., 1992) but comparable to the average cooling rate of the Galaxy, $(2.65 \pm 0.15) \times 10^{-26}$ erg s^{-1} (H-atom)$^{-1}$ (Bennett et al., 1994). For the CRRL derived column densities (Table 3.3), the 158 μm-[CII] line will be optically thick (e.g., Tielens & Hollenbach, 1985). If the [CII] line is optically thick, then the observed line does not account for the total line of sight ionized carbon column which

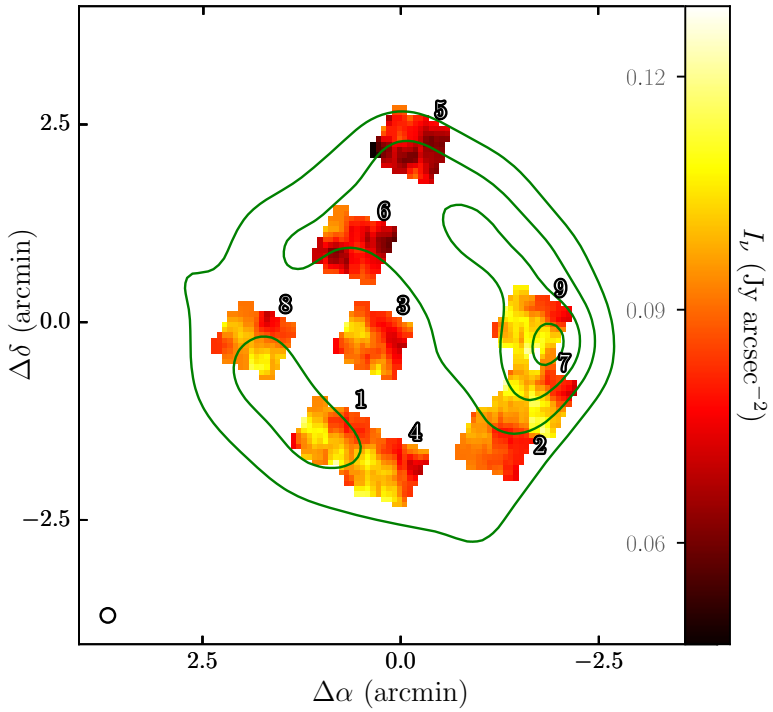

Figure 3.11.: Map of 158 μm-[CII] line emission obtained with Herschel PACS. In these the [CII] line is unresolved in velocity, and only $\sim$ 20% of the surface of Cas A is covered. This map is shown at its native resolution of 12″.

in turn results in a lower [CII] cooling rate.

3.4. Discussion

3.4.1. Comparison with other tracers

We compare the CRRL optical depth with lines which trace different components of the ISM. These include diffuse atomic gas (21 cm-HI, Bieging et al., 1991), diffuse molecular gas (18 cm-OH, Bieging & Crutcher, 1986), translucent gas (492 GHz–[CI], Mookerjea et al., 2006) and dense molecular gas (CO, Wilson et al., 1993; Liszt & Lucas, 1999; Kilpatrick et al., 2014).

Spatial distribution

A comparison between the optical depths of 21 cm-HI, C268α and the ^{12}CO(2–1) line is presented in Figure 3.12. This shows that most of the C268α emission comes from regions where HI is saturated (cyan pixels in the HI maps). The ^{12}CO(2–1) line also shows structures which are well correlated with the ones seen in C268α and 21 cm-HI. However, the peaks of CO emission are generally located outside the face of Cas A, which does not allow for a direct comparison. One exception is at a velocity of -47.8 km s^{-1}, where a peak of ^{12}CO(2–1) emission is located over the face of Cas A. In this case the distance between the peaks of ^{12}CO(2–1) and C268α is $87''$.

The spatial distribution of ^{12}CO(2–1) shows that most of the gas at -41 km s^{-1} is located to the West of Cas A, while the gas at -36.5 km s^{-1} extends from the west to the south east of Cas A (Kilpatrick et al., 2014). Both velocity components overlap towards the West of Cas A. This makes the distinction of these velocity components more difficult in this region.

To explore the relation between CO emission and CRRL emission we draw a slice joining the peaks of ^{12}CO(2–1) and C268α emission at a velocity of -47.8 km s^{-1}. The slice is shown as a green line in Figure 3.12 in the panels with a velocity of -47.8 km s^{-1}. The normalised intensity or optical depth of different tracers along this slice is shown in Figure 3.13. Here we notice how the optical depth of C268α and Cα(537) peaks at the same location, and the molecular lines peak towards the left of the CRRLs, which corresponds to the South-East direction in the sky. The difference between the peaks of the CRRLs and the molecular lines is similar to that expected in a photo-dissociation region (PDR, e.g., Hollenbach & Tielens, 1999). As we move towards the South-East of Cas A the gas shows a CII/CI/CO layered structure, which suggests that we are observing the photodissociation region associated with the edge of a molecular cloud.

The distance at which the gas becomes CO bright will depend on the average PDR density. The projected distance on the plane of the sky between the peak of the C268α optical depth and the peak of the ^{12}CO(2–1) emission is $1.3 \pm 0.6'$. If we assume that the Perseus arm gas is at a distance of 3.16 ± 0.02 kpc from Earth in the direction of Cas A (Choi et al., 2014; Salas et al., 2017), then this corresponds to $\sim 1.2 \pm 0.5$ pc in the plane of the sky. CO will be sufficiently shielded from photo-dissociating photons when $A_{\rm FUV} \sim 1$. We adopt a conversion factor between extinction in the V band

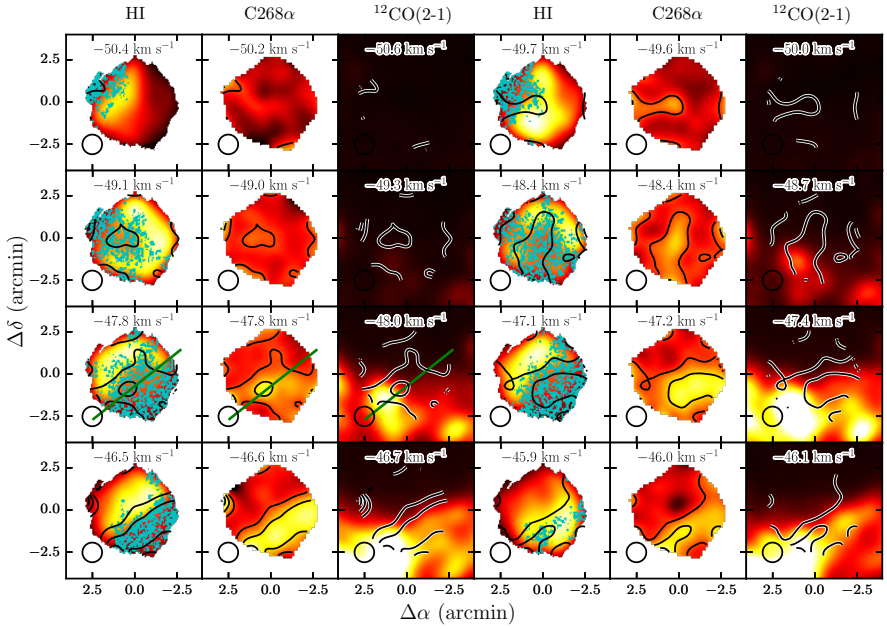

Figure 3.12.: Comparison between the optical depths of 21 cm-HI, C268α and the ^{12}CO(2–1) line brightness. Masked pixels in the 21 cm-HI optical depth maps are shown in cyan. The *green line* in the −47.8 km s^{-1} map shows the slice used to study the gas between the peaks of the ^{12}CO(2–1) and C268α lines. The 70″ resolution of these maps is shown in the bottom left corner of each map.

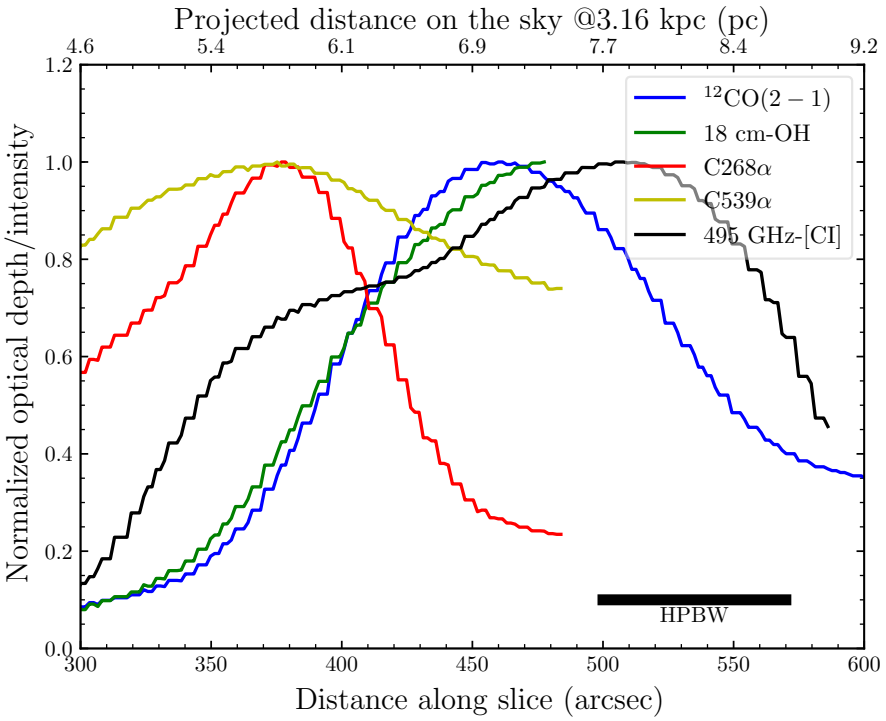

Figure 3.13.: Comparison between different ISM tracers along a slice joining the C268α optical depth peak and ^{12}CO(2–1) line peak at a velocity of −47.8 km s^{-1}. The *black bar* at the bottom shows the half power beam width (70″) of the images. The *top axis* shows the plane of the sky distance along the slice assuming that the gas is at a distance of 3.16 kpc from the observer (Salas et al., 2017). Given that the gas could be closer to the observer this distance is an upper limit.

and hydrogen column density of $N_{\rm H} = (2.08 \pm 0.02) \times 10^{21} A_{\rm V}$ cm^{-2} (Zhu et al., 2017). Then, to convert between optical opacity and far-ultra violet (FUV) opacity we adopt $\kappa_{\rm d}({\rm FUV}) \approx 1.8\kappa_{\rm d}({\rm V})$. With this, for an $A_{\rm FUV}$ of one magnitude we have $N_{\rm H} = (1.15 \pm 0.01) \times 10^{21}$ cm^{-2}. This implies that the mean density in this PDR is $n_{\rm H} = 310 \pm 28$ cm^{-3}. This density is consistent with the hydrogen density derived from the CRRL analysis (Table 3.3).

Motivated by the observed layered structure we compare the CO emission to that of an edge-on PDR model. This model is an extension of the Tielens & Hollenbach (1985) PDR model which includes the updates of Wolfire et al. (2010) and Hollenbach et al. (2012). The calculation of line intensities and source parameters for edge-on models are discussed in Pabst et al. (2017). We use a total hydrogen density of 300 cm^{-3}, an $A_{\rm V}$ of eight along the line of sight and of eight in the transverse direction. The gas in the PDR is illuminated on one side by an interstellar radiation field with $G_0 = 4.2$, measured in Habing (1968) units, and primary cosmic ray ionisation rate per hydrogen

of 7×10^{-17} s^{-1}. The carbon and hydrogen RRLs observed towards Cas A (Oonk et al., 2017) have been reanalysed by Neufeld et al. (subm) taking into account the relevant chemical recombination routes and we have adopted values of the radiation field and cosmic-ray ionisation rate consistent with their results. We adopt an abundance ^{12}CO/^{13}CO of 60, appropriate for gas in the Perseus arm in this direction (Langer & Penzias, 1990; Milam et al., 2005).

The comparison between observations and the output from the PDR model is presented in Figure 3.14. The adopted density ensures that the calculated distance on the sky between the CO peak and the surface of the PDR, as defined by the CRRL peak, agrees with the observations. For $A_V \geq 0.5$ the increase in the line intensity is well described by the model. For $A_V \sim 0.9$ the proximity to the edge of the mapped region causes the velocity integrated line intensity to decrease. This decrease close to the map edge is caused by the convolution with a $70''$ beam.

Additionally, we use the same model to predict the velocity integrated line intensity of the 492 GHz-[CI] and 158 μm-[CII] lines, and the optical depth of the 18 cm-OH line. The model does a good job in reproducing the observed optical depth of the OH line. In the region where the slice intersects footprint 1 of the PACS 158 μm-[CII] cube (Figure 3.11), the model predicts a value of 4.3×10^{-5} erg cm^{-2} s^{-1} sr^{-1}. The observed value is 56% larger, which can be accounted for by the prescence of gas at higher velocities not present in the model (e.g., the -38 and 0 km s^{-1} velocity components present in the velocity unresolved PACS observations). However, in the case of atomic carbon, the model overestimates the observed values by a factor of five. This is similar to that found in other lines of sight, where the predicted atomic carbon column density is larger than the observed one (e.g., Gong et al., 2017).

De Looze et al. (2017) find an interstellar radiation field (ISRF) with a strength $G_0 \sim 0.6$. This value is lower than the one adopted here, but we do note that against Cas A it is not possible to use the dust spectral energy distribution to estimate the strength of the ISRF. Outside the area covered by Cas A De Looze et al. (2017) find strengths for the ISRF of the order of unity. However, the derived strength of the ISRF will depend on the adopted model with a variation of up to 1.6 depending on the model details (e.g., Fanciullo et al., 2015; Planck Collaboration et al., 2016). In their work De Looze et al. (2017) also use line ratios and the PDR toolbox models (Pound & Wolfire, 2008) to estimate the strength of the ISRF in the ISM between Cas A and Earth. They find that the line ratios are consistent with their dust derived value of $G_0 \sim 0.6$, but the line ratio is also consistent with a lower density and stronger ISRF (see Figure C1 in De Looze et al., 2017). Based on the current data we infer that the adopted value is in reasonable agreement with all observations.

GAS COLUMN DENSITY

For the -47 km s^{-1} feature most of the 21 cm-HI optical depth maps show that the line is saturated with values of $\tau \gtrsim 5$ (Bieging et al., 1991). Nonetheless, this lower limit on the optical depth can be used to place a lower limit on the atomic hydrogen column density. If we assume that the width of the 21 cm-HI line profile at -47 km s^{-1} is the same as that of the CRRL at the same velocity, and that the spin temperature is

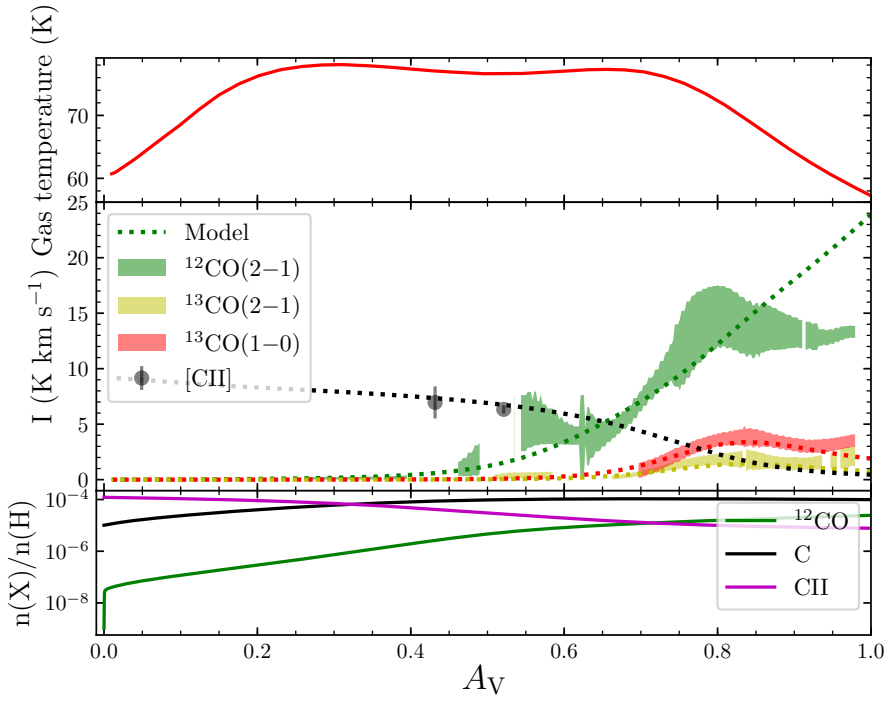

Figure 3.14.: Comparison between the ^{12}CO(2–1), ^{13}CO(1–0), ^{13}CO(2–1) and 158 μm [CII] velocity integrated line intensity along the slice shown in Figure 3.13. The observed quantities (*shaded regions*) are compared with a PDR model (*dashed lines*). The *shaded regions* show the observed values and their 3σ error range. The 158 μm [CII] points have been rescaled to be visible in this Figure. The PDR model is that of a region with a constant hydrogen density of 300 cm^{-3}, an incident radiation field of $G_0 = 4.2$ on one side of the cloud, and a line of sight optical interstellar extinction of eight. For more details on the PDR model see the text and Pabst et al. (2017).

greater than 50 K, then we have that $N(\mathrm{HI}) > 1.5 \times 10^{21}$ cm^{-2}. This limit is consistent with the column density derived from the CRRL and edge-on PDR analysis and it implies a fraction $N(\mathrm{HI})/N(\mathrm{H_2}) \gtrsim 0.1$.

Additional estimates of the gas column density can be obtained from measurements of X-ray absorption and from the dust optical depth. In the case of X-ray absorption Hwang & Laming (2012) determined values of 2×10^{22} cm^{-2} over the South portion of Cas A, with higher values ($\sim 3 \times 10^{22}$ cm^{-2}) towards its western hotspot. These values are slightly smaller than the ones found using the CRRLs lines. We consider that this difference is not significant given the uncertainties associated with X-ray column density measurements (e.g., Predehl & Schmitt, 1995; Zhu et al., 2017). Recently, De Looze et al. (2017) modelled the dust emission towards Cas A and used it to determine the mass of dust in the ISM along the line of sight. They adopted a dust-to-gas ratio of 0.0056 and found column densities of 1.5×10^{22} cm^{-2} towards the south of Cas A, and 2.2×10^{22} cm^{-2} towards the western hotspot. A map showing the spatial distribution of column density derived from the dust analysis is shown in the rightmost panel of Figure 3.10. A comparison between the column densities derived from the dust and CRRL analysis (right panels in Figure 3.10) shows good agreement, with larger values towards the South of Cas A and a peak against its western hotspot. To compare their magnitudes we focus on regions towards the South of the centre of Cas A, where we see less emission from gas at -38 km s^{-1} which would create confusion. Here the magnitude of the CRRL derived gas column density, (2.4–11.3 $\times 10^{22}$ cm^{-2}, is comparable to that derived from the dust analysis. The major uncertainty in the determination of the ISM dust content along this line of sight comes from the separation between the foreground ISM dust component and the contribution from dust associated with the supernova remnant. This introduces a factor of a few uncertainty in the derived dust mass and column density.

The CRRL derived gas column density averaged over the face of Cas A, (3.4–25.9) $\times$ 10^{18} cm^{-2}, on its own implies an hydrogen column density of (2.3–17.3) $\times 10^{22}$ cm^{-2}. Given that not all of the carbon is ionized, we also need to account for carbon in atomic and molecular forms. We focus on a region to the South of the center of Cas A, following the slice in Figure 3.12, where there is CO emission. Here, with an adopted A_V of eight, our PDR model is able to reproduce the CO observations. However, for an A_V of eight and an excitation temperature $\sim$ 20 K, the CO lines used here are optically thick. This points towards the presence of denser CO-rich clumps embedded in a lower density CO-dark halo. This situation is similar to that observed towards the W43 star forming region, where large column densities are derived from atomic hydrogen observations at 21 cm ($N_\mathrm{H} \approx 2 \times 10^{22}$ cm^{-2}, Bihr et al., 2015; Bialy et al., 2017). Gamma-ray and dust observations in our Galaxy have revealed the prescence of large reservoirs of CO-dark molecular gas (with a mass fraction comparable to that of the CO molecular gas Grenier et al., 2005; Planck Collaboration et al., 2011). Likely, much of this gas is in extended atomic hydrogen halos around giant molecular cloud complexes in spiral arms such as the ones probed in this study in the Perseus arm.

3.4.2. Envelopes of molecular clouds

The gas properties derived from the CRRL analysis seem to bridge the gap between the atomic gas traced by the 21 cm line of HI and the molecular gas traced by the CO lines in the millimimeter (Oonk et al., 2017; Salas et al., 2017). From spatially unresolved observations of the 21 cm-HI line in this direction Davies & Matthews (1972) derived a temperature of 140 ± 40 K for the two most prominent Perseus arm absorption features at -47 and -38 km s^{-1}. It has not been possible to estimate this value on smaller scales due to the saturation of the 21 cm-HI line at these velocities (e.g., Bieging et al., 1991), but it is likely to be slightly colder. On the molecular side of things we have temperatures of $\sim$ 20 K (Batrla et al., 1984). This would put the gas traced by low frequency CRRLs, with an electron temperature of $\sim$ 80 K, in between atomic and molecular gas. A place where this transition takes place is the envelope of molecular clouds (e.g., Moriarty-Schieven et al., 1997; Krumholz et al., 2009; Sternberg et al., 2014).

Studies of molecular clouds in the solar vicinity show that their atomic envelopes have temperatures of the order $\sim$ 100 K (Andersson et al., 1991). A comparisson between gas traced by the 21 cm HI and the ^{13}CO lines shows that the atomic component is more extended than the molecular one and their velocity fields are not necessarily aligned (Imara & Blitz, 2011). The properties of the envelope will depend on the environment. Here we compare against two giant molecular clouds, both show large fractions of atomic gas, but one shows little star formation, with an infrared luminosity of $\approx$ 5000 L$_\odot$; G216–2.5 (the Maddalena-Thaddeus cloud, Maddalena & Thaddeus, 1985; Williams & Maddalena, 1996; Megeath et al., 2009; Imara, 2015) and the other a mini-starburst with an infrared luminosity of 3.5×10^6 L$_\odot$ (Motte et al., 2003; Nguyen Luong et al., 2011; Bihr et al., 2015; Bialy et al., 2017). The atomic envelope around G216–2.5 has a thickness of $\sim$ 50 pc and the atomic gas column density inferred from observations of the 21 cm line of HI is $\approx 2.21 \times 10^{21}$ cm^{-2} (Williams & Maddalena, 1996). Around W43, the atomic envelope has a thickness of 140 pc (Motte et al., 2014), and the atomic gas column density is $\approx 2 \times 10^{22}$ cm^{-2} (Bihr et al., 2015; Bialy et al., 2017). The later column density is consistent with the lower end of the ranges found here (Table 3.3).

Another way in which we can study the envelopes of giant molecular clouds is with observations of the 158 μm-[CII] line. In cases where it is possible to isolate an ionized carbon layer around a molecular cloud it is found that the gas temperature and density are close to those found here. In the Magellanic clouds Pineda et al. (2017) find densities of 700–2000 cm^{-3} and temperatures of $\sim$ 50 K.

3.4.3. Uncertainties in the CRRL modelling

The change in line properties as a function of physical properties is quite sensitive to the gas physical conditions. During the modelling of the CRRL line properties as a function of principal quantum number a series of assumptions are made which have an effect on the derived gas properties. Some of these have been explored previously, like the use of different angular momentum changing collisional rates (Salgado et al., 2017a),

or including collisions with hydrogen when solving the level population problem (Oonk et al., 2017). Additionally, two assumptions have not been explored before, those are; the use of different collisional rates for the excitation of ionized Carbon and changing the carbon and electron abundances relative to hydrogen. Having different collisional rates and abundances will change the dielectronic capture rate. This will be reflected as a change in the departure coefficient b_n, which determines how the integrated optical depth will behave as a function of n.

Given that it is computationally expensive to recompute the grid of models for each set of assumptions, we focus on a particular point in the $n_{\rm e} - T_{\rm e}$ plane. The change in the $b_n\beta_{n,n'}$ coefficients as a function of n is shown in Figure 3.15 for different assumptions. These show that the change in the integrated optical depth will be $\sim 10\%$ for the models computed using the different collisional rates and lower carbon and electron abundances. For other assumptions the difference will be lower.

Recently, Guzmán et al. (2017) and Vrinceanu et al. (2017) have investigated the effect of using different formulations (semi-classical versus quantum mechanical) when computing the ℓ-changing collisional rates. As shown by Salgado et al. (2017a, See their Figure 14) this will affect the departure coefficients, mainly their absolute values. However, as Guzmán et al. (2017) and Vrinceanu et al. (2017) point out, there is no physical reason to prefer one formulation over the other. A more detailed comparison of the effect different formulations will have on the predicted CRRL properties will be investigated in the future.

3.5. SUMMARY

We have presented $70''$ resolution CRRL maps at 340, 148, 54 and 43 MHz. The distribution of the C268α line in emission reveals a good correlation with regions where the 21 cm-HI line is saturated and regions of faint ^{12}CO(2–1) emission. We interpret this as as a diffuse PDR, in which low frequency CRRLs trace the less dense, warmer envelope of molecular gas.

Using the ratios between CRRLs we have constrained the gas electron temperature and density along the line of sight on scales of $\lesssim 1.2$ pc. With the line ratios used here, the constraints result in a range of allowed electron temperatures and densities. Averaged over the face of Cas A the constraints on the electron density are $n_{\rm e} = (0.03\text{–}0.055)$ cm^{-3} and $T_{\rm e} =$ (70–140 K for gas in the Perseus arm of the Galaxy at -47 km s^{-1}. The pressure shows variations of less than a factor of two on $\lesssim 1.2$ pc scales.

From the constraints on the electron temperature and density we derived lower limits for the ionized carbon emission measure, column density and its line of sight path length. The lower limit on the column density is 3.4×10^{18} cm^{-2}, which corresponds to an hydrogen column density of 2.2×10^{22} cm^{-2} if all carbon is ionized and [C/H]= 1.5×10^{-4}. The hydrogen density derived from analysis of the CRRLs integrated optical depths is 210–360 cm^{-3}.

A PDR model with an average hydrogen density of 300 cm^{-3}, and conditions similar to those inferred for the clouds in this region, is able to reproduce the observed distribution of ^{12}CO(2–1), ^{13}CO(2–1), ^{13}CO(1–0) and 1667 MHz OH.

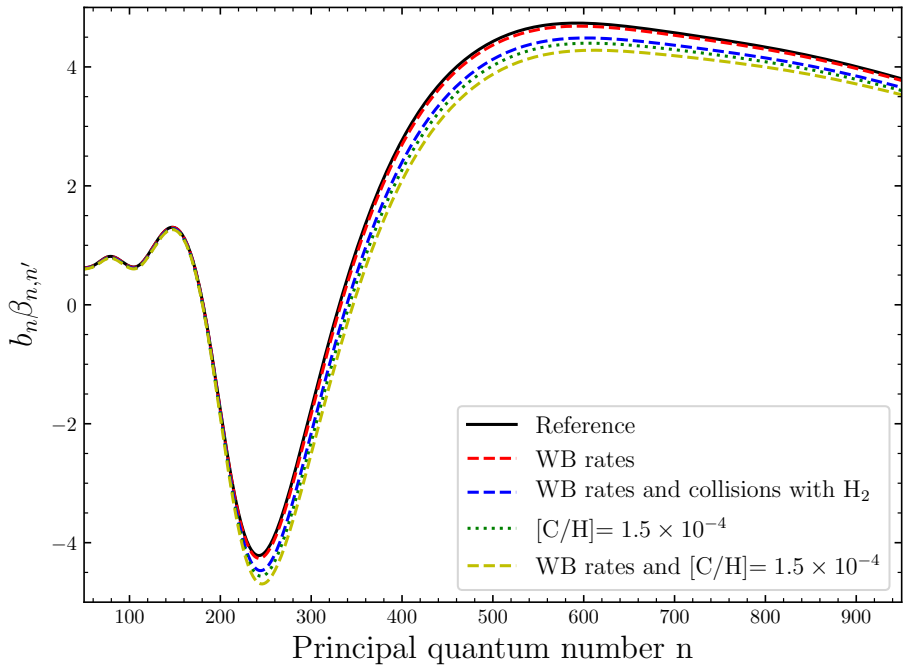

Figure 3.15.: Comparison between CRRL models under different assumptions regarding the carbon ion collisional excitation rates, carbon and electron abundances. All models were computed for an electron density of 0.05 cm^{-3} and temperature 80 K. The reference model is one computed assuming $[C/H] = [e/H] = 3 \times 10^{-4}$ and using the Tielens & Hollenbach (1985) and Hayes & Nussbaumer (1984) collisional rates. The models labelled with WB rates use the Wilson & Bell (2002) rates for collisions with electrons and those of Barinovs et al. (2005) for collisions with atomic hydrogen. The model which includes collisions with molecular hydrogen, H_2, uses the rate for collisions with molecular hydrogen presented in Goldsmith et al. (2012). The models labelled with $[C/H] = 1.5 \times 10^{-4}$ use this abundance for carbon and electrons. The largest difference for and individual change is produced when the electron and carbon abundances are modified.

The relatively high spatial resolution of the present observations enables us to study the relation between CRRLs and other tracers of the ISM on scales where it is possible to observe the PDR like structure in the surface of a molecular cloud. This also highlights the importance of CRRLs as tracers of the diffuse ISM, as they allow us to determine the gas physical conditions in regions which are not readily traced by 21 cm-HI and/or CO. These observations highlight the utility of CRRLs as tracers of low density extended HI and CO-dark gas halo's around molecular clouds. Future surveys of CRRLs with the low frequency array (LOFAR) are promising as they could reveal important new clues about the physics of the ISM, particularly about the transition from atomic-to-molecular gas and the properties of CO-dark gas.

BIBLIOGRAPHY

Anantharamaiah, K. R., Erickson, W. C., Payne, H. E., & Kantharia, N. G. 1994, ApJ, 430, 682

Anantharamaiah, K. R., Payne, H. E., & Erickson, W. C. 1988, MNRAS, 235, 151

Andersson, B.-G., Wannier, P. G., & Morris, M. 1991, ApJ, 366, 464

Asgekar, A., Oonk, J. B. R., Yatawatta, S., et al. 2013, A&A, 551, L11

Astropy Collaboration, Robitaille, T. P., Tollerud, E. J., et al. 2013, A&A, 558, A33

Barinovs, Ğ., van Hemert, M. C., Krems, R., & Dalgarno, A. 2005, ApJ, 620, 537

Batrla, W., Walmsley, C. M., & Wilson, T. L. 1984, A&A, 136, 127

Bennett, C. L., Fixsen, D. J., Hinshaw, G., et al. 1994, ApJ, 434, 587

Bialy, S., Bihr, S., Beuther, H., Henning, T., & Sternberg, A. 2017, ApJ, 835, 126

Bieging, J. H., & Crutcher, R. M. 1986, ApJ, 310, 853

Bieging, J. H., Goss, W. M., & Wilcots, E. M. 1991, ApJS, 75, 999

Bihr, S., Beuther, H., Ott, J., et al. 2015, A&A, 580, A112

Blitz, L., & Williams, J. P. 1999, in NATO Advanced Science Institutes (ASI) Series C, Vol. 540, NATO Advanced Science Institutes (ASI) Series C, ed. C. J. Lada & N. D. Kylafis, 3

Briggs, D. S. 1995, in Bulletin of the American Astronomical Society, Vol. 27, American Astronomical Society Meeting Abstracts, 1444

Cazaux, S., & Tielens, A. G. G. M. 2004, ApJ, 604, 222

Choi, Y. K., Hachisuka, K., Reid, M. J., et al. 2014, ApJ, 790, 99

Dame, T. M. 2011, ArXiv e-prints

Davies, R. D., & Matthews, H. E. 1972, MNRAS, 156, 253

De Looze, I., Barlow, M. J., Swinyard, B. M., et al. 2017, MNRAS, 465, 3309

de Oliveira-Costa, A., Tegmark, M., Gaensler, B. M., et al. 2008, MNRAS, 388, 247

Dickey, J. M., Strasser, S., Gaensler, B. M., et al. 2009, ApJ, 693, 1250

Erickson, W. C., McConnell, D., & Anantharamaiah, K. R. 1995, ApJ, 454, 125

Ershov, A. A., Lekht, E. E., Smirnov, G. T., & Sorochenko, R. L. 1987, Soviet Astronomy Letters, 13, 8
Fanciullo, L., Guillet, V., Aniano, G., et al. 2015, A&A, 580, A136
Fukui, Y., Kawamura, A., Wong, T., et al. 2009, ApJ, 705, 144
Gibson, S. J. 2002, in Astronomical Society of the Pacific Conference Series, Vol. 276, Seeing Through the Dust: The Detection of HI and the Exploration of the ISM in Galaxies, ed. A. R. Taylor, T. L. Landecker, & A. G. Willis, 235
Goldsmith, P. F., Langer, W. D., Pineda, J. L., & Velusamy, T. 2012, ApJS, 203, 13
Gong, M., Ostriker, E. C., & Wolfire, M. G. 2017, ApJ, 843, 38
Gordon, M. A., & Sorochenko, R. L., eds. 2009, Astrophysics and Space Science Library, Vol. 282, Radio Recombination Lines
Grenier, I. A., Casandjian, J.-M., & Terrier, R. 2005, Science, 307, 1292
Gry, C., Lequeux, J., & Boulanger, F. 1992, A&A, 266, 457
Guzmán, F., Badnell, N. R., Williams, R. J. R., et al. 2017, MNRAS, 464, 312
Habing, H. J. 1968, BAN, 19, 421
Hayes, M. A., & Nussbaumer, H. 1984, A&A, 134, 193
Hollenbach, D., Kaufman, M. J., Neufeld, D., Wolfire, M., & Goicoechea, J. R. 2012, ApJ, 754, 105
Hollenbach, D. J., & Tielens, A. G. G. M. 1999, Reviews of Modern Physics, 71, 173
Hwang, U., & Laming, J. M. 2012, ApJ, 746, 130
Imara, N. 2015, ApJ, 803, 38
Imara, N., & Blitz, L. 2011, ApJ, 732, 78
Kantharia, N. G., & Anantharamaiah, K. R. 2001, Journal of Astrophysics and Astronomy, 22, 51
Kantharia, N. G., Anantharamaiah, K. R., & Payne, H. E. 1998, ApJ, 506, 758
Kavars, D. W., Dickey, J. M., McClure-Griffiths, N. M., Gaensler, B. M., & Green, A. J. 2003, ApJ, 598, 1048
—. 2005, ApJ, 626, 887
Kerton, C. R. 2005, ApJ, 623, 235
Kilpatrick, C. D., Bieging, J. H., & Rieke, G. H. 2014, ApJ, 796, 144
Konovalenko, A. A. 1984, Soviet Astronomy Letters, 10, 353
Krumholz, M. R., McKee, C. F., & Tumlinson, J. 2009, ApJ, 693, 216
Langer, W. D., & Penzias, A. A. 1990, ApJ, 357, 477
Liszt, H., & Lucas, R. 1999, A&A, 347, 258
Maddalena, R. J., & Thaddeus, P. 1985, ApJ, 294, 231
McMullin, J. P., Waters, B., Schiebel, D., Young, W., & Golap, K. 2007, in Astronomical Society of the Pacific Conference Series, Vol. 376, Astronomical Data Analysis Software and Systems XVI, ed. R. A. Shaw, F. Hill, & D. J. Bell, 127
Mebold, U., & Hills, D. L. 1975, A&A, 42, 187
Megeath, S. T., Allgaier, E., Young, E., et al. 2009, AJ, 137, 4072
Milam, S. N., Savage, C., Brewster, M. A., Ziurys, L. M., & Wyckoff, S. 2005, ApJ, 634, 1126
Mookerjea, B., Kantharia, N. G., Roshi, D. A., & Masur, M. 2006, MNRAS, 371, 761
Moriarty-Schieven, G. H., Wannier, & P. G. 1997, ApJ, 475, 642

Moss, V. A., McClure-Griffiths, N. M., Braun, R., Hill, A. S., & Madsen, G. J. 2012, MNRAS, 421, 3159
Motte, F., Schilke, P., & Lis, D. C. 2003, ApJ, 582, 277
Motte, F., Nguyên Luong, Q., Schneider, N., et al. 2014, A&A, 571, A32
Neufeld, D. A., Wolfire, M. G., Oonk, J. B. R., Tielens, A. G. G. M., & Salas, P. subm, submitted
Nguyen Luong, Q., Motte, F., Schuller, F., et al. 2011, A&A, 529, A41
Oonk, J. B. R., van Weeren, R. J., Salas, P., et al. 2017, MNRAS, 465, 1066
Oonk, J. B. R., van Weeren, R. J., Salgado, F., et al. 2014, MNRAS, 437, 3506
Pabst, C. H. M., Goicoechea, J. R., Teyssier, D., et al. 2017, A&A, 606, A29
Pascucci, I., Edwards, S., Heyer, M., et al. 2015, ApJ, 814, 14
Payne, H. E., Anantharamaiah, K. R., & Erickson, W. C. 1989, ApJ, 341, 890
—. 1994, ApJ, 430, 690
Pineda, J. L., Langer, W. D., Goldsmith, P. F., et al. 2017, ApJ, 839, 107
Planck Collaboration, Ade, P. A. R., Aghanim, N., et al. 2011, A&A, 536, A19
—. 2016, A&A, 586, A132
Pottasch, S. R., Wesselius, P. R., & van Duinen, R. J. 1979, A&A, 74, L15
Pound, M. W., & Wolfire, M. G. 2008, in Astronomical Society of the Pacific Conference Series, Vol. 394, Astronomical Data Analysis Software and Systems XVII, ed. R. W. Argyle, P. S. Bunclark, & J. R. Lewis, 654
Predehl, P., & Schmitt, J. H. M. M. 1995, A&A, 293, 889
Reed, J. E., Hester, J. J., Fabian, A. C., & Winkler, P. F. 1995, ApJ, 440, 706
Roshi, D. A., & Kantharia, N. G. 2011, MNRAS, 414, 519
Roshi, D. A., Kantharia, N. G., & Anantharamaiah, K. R. 2002, A&A, 391, 1097
Salas, P., Oonk, J. B. R., van Weeren, R. J., et al. 2017, MNRAS, 467, 2274
Salgado, F., Morabito, L. K., Oonk, J. B. R., et al. 2017a, ApJ, 837, 141
—. 2017b, ApJ, 837, 142
Schwarz, U. J., Goss, W. M., & Kalberla, P. M. W. 1997, A&AS, 123
Shaver, P. A. 1975, Pramana, 5, 1
Sofia, U. J., Cardelli, J. A., Guerin, K. P., & Meyer, D. M. 1997, ApJL, 482, L105
Sorochenko, R. L., & Smirnov, G. T. 2010, Astronomy Reports, 54, 776
Sorochenko, R. L., & Walmsley, C. M. 1991, Astronomical and Astrophysical Transactions, 1, 31
Stanimirović, S., Murray, C. E., Lee, M.-Y., Heiles, C., & Miller, J. 2014, ApJ, 793, 132
Stepkin, S. V., Konovalenko, A. A., Kantharia, N. G., & Udaya Shankar, N. 2007, MNRAS, 374, 852
Sternberg, A., Le Petit, F., Roueff, E., & Le Bourlot, J. 2014, ApJ, 790, 10
Tielens, A. G. G. M., & Hollenbach, D. 1985, ApJ, 291, 722
Troland, T. H., Crutcher, R. M., & Heiles, C. 1985, ApJ, 298, 808
van Gorkom, J. H., & Ekers, R. D. 1989, in Astronomical Society of the Pacific Conference Series, Vol. 6, Synthesis Imaging in Radio Astronomy, ed. R. A. Perley, F. R. Schwab, & A. H. Bridle, 341
van Haarlem, M. P., Wise, M. W., Gunst, A. W., et al. 2013, A&A, 556, A2
van Langevelde, H. J., & Cotton, W. D. 1990, A&A, 239, L5
Vrinceanu, D., Onofrio, R., & Sadeghpour, H. R. 2012, ApJ, 747, 56

—. 2017, MNRAS, 471, 3051
Watson, W. D., Western, L. R., & Christensen, R. B. 1980, ApJ, 240, 956
Williams, J. P., & Maddalena, R. J. 1996, ApJ, 464, 247
Wilson, N. J., & Bell, K. L. 2002, MNRAS, 337, 1027
Wilson, T. L., Mauersberger, R., Muders, D., Przewodnik, A., & Olano, C. A. 1993, A&A, 280, 221
Wolfire, M. G., Hollenbach, D., & McKee, C. F. 2010, ApJ, 716, 1191
Wolfire, M. G., Hollenbach, D., McKee, C. F., Tielens, A. G. G. M., & Bakes, E. L. O. 1995, ApJ, 443, 152
Wolfire, M. G., McKee, C. F., Hollenbach, D., & Tielens, A. G. G. M. 2003, ApJ, 587, 278
Xu, Y., Reid, M. J., Zheng, X. W., & Menten, K. M. 2006, Science, 311, 54
Zheng, H., Tegmark, M., Dillon, J., et al. 2016, ArXiv e-prints
Zhu, H., Tian, W., Li, A., & Zhang, M. 2017, MNRAS, 471, 3494

IV

CARBON RADIO RECOMBINATION LINES FROM GIGAHERTZ TO MEGAHERTZ FREQUENCIES TOWARDS ORION A

4.1. INTRODUCTION

The transfer of material from the massive reservoirs of the cold neutral medium (CNM, $T \sim 80$ K) into cold molecular clouds partially regulates the star formation cycle in a galaxy (e.g., Klessen & Glover, 2016). This conversion of atomic to molecular gas is intimately related to the heating and cooling processes the gas experiences.

The heating and cooling of atomic gas can be studied in photodissociation regions (PDRs e.g., Hollenbach & Tielens, 1999). These are regions where the influence of far-ultraviolet (FUV) photons shape the interstellar medium (ISM) into a layered structure with hydrogen ionized or neutral close to the source of radiation and molecular farther from it. PDRs can be found in dense and diffuse regions, the former happen close to sites of star formation, where the FUV radiation from young stars impinges on the surface of their natal molecular cloud, while the later can be found throughout most of the CNM, powered by the interstellar radiation field (ISRF). For the CNM and in PDRs, one of the main cooling mechanisms is through the FIR fine-structure line of ionized carbon ([CII]) at 158 μm (e.g., Field et al., 1969; Dalgarno & McCray, 1972; Pottasch et al., 1979; Wolfire et al., 1995, 2003). Since carbon has a lower ionization potential than hydrogen, it is ionized throughout the diffuse ISM and in PDR surfaces, and with an energy difference between its fine structure states of 91.2 K, it is easily excited. However, this implies that the 158 μm-[CII] line will also trace other phases of the ISM. These phases include the warm ionized medium (WIM, $T \sim 8000$ K), extended low density WIM (ELDWIM, e.g., Heiles, 1994), extended low density HII regions (e.g., Goldsmith et al., 2015) and also the surfaces of molecular clouds (e.g., Visser et al., 2009; Wolfire et al., 2010). It has been estimated that $\sim 21\%$ of the 158 μm-[CII] line in our Galaxy is produced in the CNM and $\sim 47\%$ in dense PDRs (Pineda et al.,

2013). In order to measure the cooling rate of the CNM, we must be able to isolate its contribution to the excitation of the 158 μm-[CII] line (e.g., Pabst et al., 2017).

The separation between cold and warm gas can be done using carbon radio recombination lines (CRRLs e.g., Gordon & Sorochenko, 2009). These are lines produced when a carbon ion recombines with an electron to a large principal quantum number n resulting in a Rydberg atom. When a Rydberg atom of carbon transitions between different principal quantum numbers it will produce CRRLs, from GHz to MHz frequencies depending on the n levels involved. The optical depth of the produced CRRL has a strong dependence on the gas temperature ($\tau \propto T^{-5/2}$), so CRRLs have little contamination from warm gas or HII regions. Thus, one can use CRRLs to isolate emission from the CNM and the surfaces of molecular clouds and their contribution to the 158 μm-[CII] line excitation.

Another property of CRRLs is that the population of carbon atoms in each energy state is determined by the gas density, temperature and radiation field, as well as the atomic physics involved (e.g., Shaver, 1975; Watson et al., 1980; Salgado et al., 2017a). Therefore, it is possible to determine the gas physical conditions by observing CRRLs at a range of frequencies and comparing this to the predicted line properties (e.g., Dupree, 1974; Payne et al., 1989; Roshi & Kantharia, 2011; Salgado et al., 2017b; Oonk et al., 2017; Salas et al., 2018).

Moreover, given that CRRLs have a different temperature dependency than the 158 μm-[CII] line, one can combine both types of lines to determine the gas temperature and/or density (e.g., Natta et al., 1994; Smirnov et al., 1995; Salgado et al., 2017b; Salas et al., 2017). This approach is particularly useful as it requires observations of a few of the faint CRRLs ($\tau \sim 10^{-3}$–10^{-4}) instead of a large set of them to reach a similar accuracy on the derived gas properties. However, the combined use of the 158 μm-[CII] line and CRRLs has been performed only towards a handful of sources and using observations which do not resolve the lines in velocity and/or do not have the same angular resolution.

One of the sources which has been studied in both CRRLs and the 158 μm-[CII] line is the Orion star forming region. Orion A is a nearby giant molecular cloud which covers ≈ 29 deg^2 (Maddalena et al., 1986). In the northern part of this cloud we can find the Orion nebula cluster (ONC, e.g., Pickering, 1917; Sharpless, 1952; O'Dell, 2001), the region of massive star formation that is closest to Earth. The brightest stars in the ONC are the Trapezium stars (M42, $(\alpha, \delta)_{\rm J2000} = (5^{\rm h}35^{\rm m}17.3^{\rm s}, -5°23^{\rm m}28^{\rm s})$, e.g., Large et al., 1981). The ionizing radiation from the Trapezium stars has created an HII region. M42 lies in front of Orion A, which makes it easier for the ionizing radiation to escape towards the observer (Zuckerman, 1973; Balick et al., 1974a,b). Behind the Trapezium stars and the HII region, Orion A is arranged in an S shaped structure known as the integral shaped filament (ISF, Bally et al., 1987). In front of the Trapezium stars and the HII region, there are layers of neutral gas collectively known as the Veil (e.g., van der Werf & Goss, 1989; Abel et al., 2004; O'Dell et al., 2009; van der Werf et al., 2013; Troland et al., 2016). Observations of the 21 cm-HI line at high spatial resolution ($\approx 7''$) show that the gas in the Veil is composed of two spatially distinct velocity components; component A at 5.3 km s^{-1} and component B at 1.3 km s^{-1} (van der Werf & Goss, 1989). The proximity and geometry of M42, sandwiched between a high

density molecular cloud and the diffuse gas in the Veil, makes it an ideal target to study how the gas cooling rate changes between dense and diffuse gas.

The goal of this work is to re-evaluate the relation between the 158 μm-[CII] line and CRRLs at radio frequencies in the light of new models and observations of Orion A. We take advantage of new large scale maps (≈ 1 deg^2) of the 158 μm-[CII] line in the FIR (Pabst et al., 2019). This improves on previous comparisons which used velocity unresolved observations of the 158 μm-[CII] line (Natta et al., 1994). The velocity resolution of the 158 μm-[CII] line observations in this study was of ≈ 50 km s^{-1}, while in the observations of Pabst et al. (2019) this is 0.2 km s^{-1}. Additionally, we use models that describe the level population of carbon atoms including the effect of dielectronic capture (Salgado et al., 2017a). Incorporating this effect can change the predicted CRRL intensities by a factor of two (e.g., Wyrowski et al., 1997).

In this work, all velocities are given in the local standard of rest unless otherwise specified. To convert to heliocentric velocities 18.1 km s^{-1} should be added. We adopt a distance of 414 pc to Orion A (e.g., Menten et al., 2007; Zari et al., 2017).

4.2. Observations & data reduction

We start by describing previously unpublished CRRL observations. These include: an L-band (1 GHz to 2 GHz) map of CRRLs; pointings towards M42 which include CRRLs at frequencies between 2.8 GHz and 275 MHz; and a cube of CRRL absorption at 150 MHz. We also briefly describe CRRL observations taken from the literature, as well as observations of other tracers relevant for this work.

4.2.1. GBT observations

L-band CRRL maps

We observed Orion A with the National Radio Astronomy Observatory (NRAO) Robert C. Byrd Green Bank Telescope[1] (GBT) during seven nights on November 2016 (project: AGBT16B_225). We mapped a $\approx 0.4° \times 1°$ region centered on $(\alpha, \delta)_{\rm J2000} = 5^{\rm h}35^{\rm m}14.5^{\rm s}, -5°22^{\rm m}29.3^{\rm s}$ using the on-the-fly imaging technique (e.g., Mangum et al., 2007). The observations were performed using the L-band (1.1–1.8 GHz) receiver and the versatile GBT astronomical spectrometer (VEGAS, Bussa & VEGAS Development Team, 2012). VEGAS was setup to process 27 spectral windows 23.44 MHz wide. Each spectral window was split into 65536 channels 0.357 kHz wide. The spectral windows were centered on the 21 cm-HI line, the four 18 cm-OH lines and the remaining on RRLs within the GBT L-band range. As an absolute flux calibrator we observed 3C123 (Baars et al., 1977) with the Perley & Butler (2013) flux scale to convert from raw counts to temperature. We adopted the methods described in Winkel et al. (2012) to convert the raw units to temperature when possible. As will be discussed later, in some

[1]The Green Bank Observatory is a facility of the National Science Foundation operated under cooperative agreement by Associated Universities, Inc.

Table 4.1.: GBT mapping observation parameters

Project code	AGBT16B_225
Observation dates	5, 6, 8, 9, 10, 15 and 17 of November 2016 and 2 of December 2016.
Polarizations	XX,YY
Spectral windows	27
Spectral window frequencies (MHz)	1156, 1176, 1196, 1217, 1240, 1259, 1281, 1304, 1327, 1351, 1375, 1400, 1420.4, 1425, 1451, 1478, 1505, 1533, 1561, 1591, 1608, 1621, 1652, 1665.4, 1684, 1716, 1720.53
Spectral window bandwidth (MHz)	23.44
Channels per spectral window	65536
Integration time per spectral dump (s)	10.57
Absolute flux calibrator	3C123
Total observing time	15 hours
Principal quantum numbers[a]	156–178

[a] For C$n\alpha$ lines.

steps this was not possible due to the high continuum brightness of Orion A. A summary of the observational setup is presented in Table 4.1.

The mapped region was subdivided into smaller maps in order to keep the variations in antenna temperature within the three dB dynamical range of VEGAS. At the beginning of each session, the pointing and focus solutions were updated on 3C161. The pointing corrections were less than 10% of the beam width.

Given the high continuum brightness of Orion A ($\sim$ 375 Jy or 600 K at 1.4 GHz, e.g., Goudis, 1975), the telescope amplifiers were saturated over the brightest portions of the source. The saturation produced a compression of the amplifier gain. In order to correct for the non-linearity in the conversion from raw counts to brightness temperature in the affected portions of the map we followed a procedure similar to that used by the GBT intermediate frequency non-linearity project[2] and briefly outlined in Appendix 4.A. To quantitatively determine the deviation from a linear gain we compared the raw counts against the 21 cm continuum maps of van der Werf et al. (2013). To scale the the temperature of the van der Werf et al. (2013) map across the 700 MHz wide

[2] http://www.gb.nrao.edu/~tminter/1A4/nonlinear/nonlinear.pdf

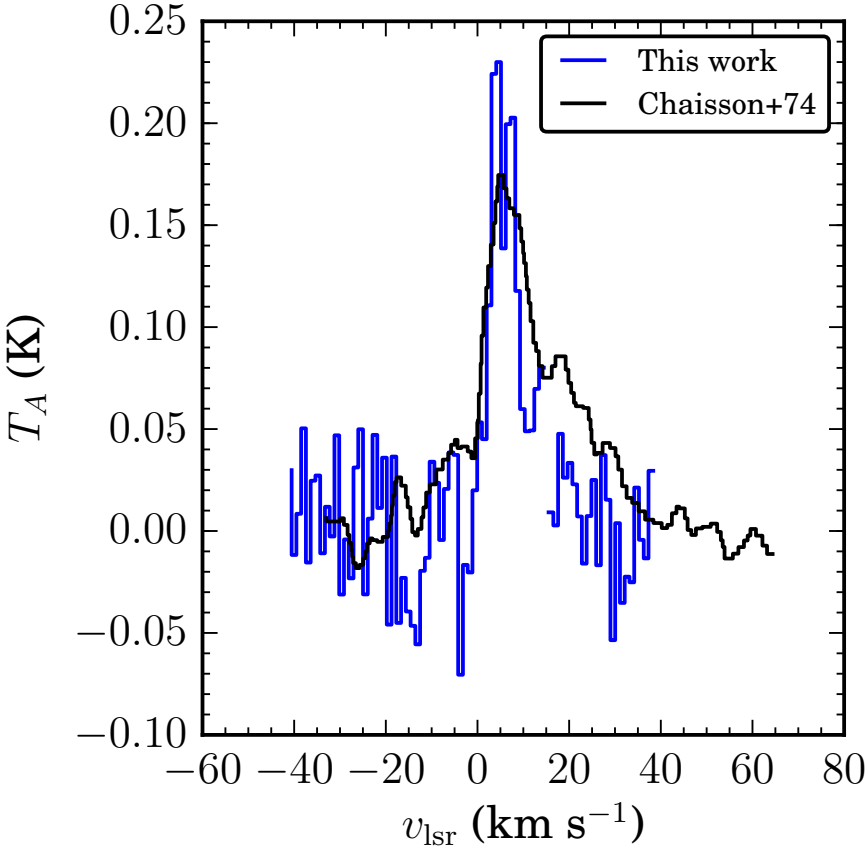

Figure 4.1.: Comparison between the temperature calibrated GBT C157α line and the C158α observation of Chaisson (1974). The temperature scale of the two spectra agrees over the brightest portion of M42, the most affected by a non-linearity in the signal path (see text for details). Both spectra were extracted from an aperture of diameter 18′ centered on $(\alpha, \delta)_{\rm J2000} = (5^{\rm h}35^{\rm m}17.45^{\rm s}, -5°23^{\rm m}46.8^{\rm s})$. The on-source time of the C157α observations is roughly seven minutes, while that of the C158α observations is 1200 minutes. The spectral resolution of the C158α spectrum is 1.9 km s^{-1} (Chaisson, 1974) and that of the C157α spectrum is 1 km s^{-1}.

Table 4.2.: GBT single pointing observation parameters

Project code	Frequency ranges MHz	Aperture efficiency	HPBW ′	Principal quantum numbers[a]
	275–912	0.7	41–14	193–287
AGBT02A_028	1100–1800	0.7	11–7	154–181
	1800–2800	0.68	7–4.4	133–153
AGBT12A_484	827–837	0.7	12	199
AGBT14B_233	691–761	0.7	14	204–211

[a] For C$n\alpha$ lines.

frequency range used in the GBT observations we use the results of Lockman & Brown (1975). Lockman & Brown (1975) present a compilation of continuum measurements of Orion A. According to these, the brightness temperature of the source scales as $T_{\rm M42} \propto \nu^{-1.7}$ between 1.1 GHz and 1.8 GHz. After converting the data to temperature units we compared the resulting spectra against previously published values. An example of this comparison is shown in Figure 4.1, where we compare the C158α spectrum against that observed by Chaisson (1974) using the 42.7 m antenna of the NRAO. The uncertainty in the absolute flux calibration is of $\approx 20\%$, considering the non-linear gain correction.

Before gridding all maps together, we checked that the line profiles on overlapping regions agreed. We found no significant differences among the maps. Then all the data was gridded together using the standalone *GBTGRIDDER*[3]. With this we produced a CRRL cube for each line observed.

To obtain the best spatial resolution possible from these observations, we stacked the first three CRRLs observed (156, 157 and 158) in one cube. This produced a cube with a half power beam width (HPBW) of $\approx 8\farcm1$ and an average principal quantum number of 157. To increase the signal-to-noise ratio of the cube we averaged in velocity to a channel width of ≈ 1 km s^{-1} (Figure 4.1).

Pointings towards M42

We searched the NRAO archive for observations of M42. From the available observations we used projects AGBT02A_028, AGBT12A_484 and AGBT14B_233. These correspond to single pointings of M42 with the GBT which have a spectral resolution adequate for spectral line analysis (≈ 1 km s^{-1} spectral resolution). A summary of these observations is provided in Table 4.2.

The data was exported to SDfits format from the NRAO archive. The observations were calibrated to a temperature scale using the hot load on the GBT and its temperature as listed in the SDfits header. To remove the continuum and any large scale ripples in the spectra we fitted a polynomial to line free channels. For 97.5% of the spectra an

[3] https://github.com/nrao/gbtgridder

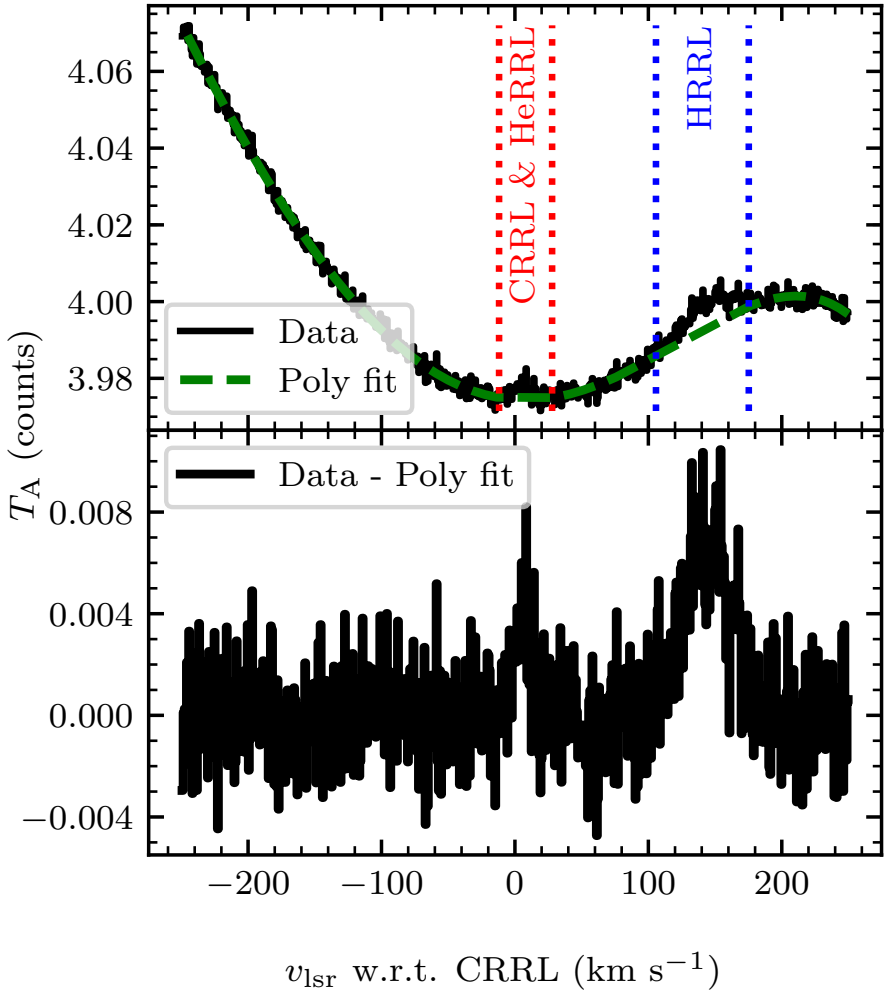

Figure 4.2.: Example of the baseline removal process for the GBT observations. The *upper panel* shows the raw data (*black steps*) and the polynomial (*green dashed line*) used to remove the bandpass shape from the data. The *red* and *blue dotted lines* show the ranges where we expect the RRLs. These ranges are not considered while fitting the polynomial. The *bottom panel* shows the data after subtraction of the polynomial used to capture the bandpass shape. The velocity axis is referenced with respect to the rest frequency of the corresponding CRRL. This data is part of project AGBT12A_484.

order five polynomial was used, for 2% an order nine polynomial, and for the remaining an order 11 polynomial. If a polynomial with an order greater than 11 was required, the data was flagged as bad and not used. The line free channels are defined as those that have velocities less than -5 km s^{-1} and greater than 180 km s^{-1}, and those between 25 km s^{-1} and 100 km s^{-1}, where the velocities quoted are with respect to the rest frequency of the corresponding CRRL. An example of the polynomial fitting is shown in Figure 4.2. In this example a polynomial of order five was used to remove the continuum and the large scale ripples. In some cases the spectral window was flagged and marked as bad because of strong RFI. The remaining spectra which showed no obvious artifacts were then stacked to improve the signal-to-noise ratio.

In the pointing observations present in the archive, we found no corresponding observations of a reference region. For this reason we did not try to estimate the continuum temperature of the source from these observations.

4.2.2. LOFAR OBSERVATIONS

We observed Orion A with the low frequency array (LOFAR, van Haarlem et al., 2013) during two separate projects, two years apart. The observations were carried-out on February 2, 2014 and October 27, 2016. Both observations used the high band antennas (HBA) in their low (110–190 MHz) frequency range. The number of Dutch stations available was 34 for both observations.

Complex gain solutions were derived on 3C147 and then transferred to the target field, following a first generation calibration scheme (e.g., Noordam & Smirnov, 2010). We adopted the Scaife & Heald (2012) flux scale. The calibrated visibilities were then imaged and cleaned. During the inversion a Briggs weighting was used, with a robust parameter of 0 (Briggs, 1995). The cubes have a synthesized beam of $3\farcm65 \times 2'$ at a position angle of 166°. Given the shortest baseline present in the visibilities, 130 m, the LOFAR observations are sensitive to emission on angular scales smaller than $53'$.

From the cubes we extracted a spectrum from a $9' \times 9'$ region centered on M42. For the 2014 observations, 20 spectral windows were stacked resulting in a spectrum with a spectral resolution of 7 km s^{-1}. This resulted in a detection of the C351α line in absorption with a signal-to-noise ratio of 4.5 for the 2014 observations. For the 2016 observations, 22 spectral windows were stacked. In general, the data quality for the 2016 observations was worse than in the 2014 ones by a factor 2–4. In the 2016 observations we found an absorption feature with a signal-to-noise ratio of 2.5. A comparison of the observed line profile for both observations is presented in Figure 4.3. The line properties are consistent between the two observations. Based on this, we are confident that the detected absorption feature, which we associate with the C351α line, is of astronomical origin.

4.2.3. LITERATURE DATA

We also use observations of CRRLs and other tracers of the ISM from the literature. The CRRL observations include: the C65α map of a $5' \times 5'$ region close to M42 at a spatial resolution of $40''$; the intensity of the C91α line towards a region to the North

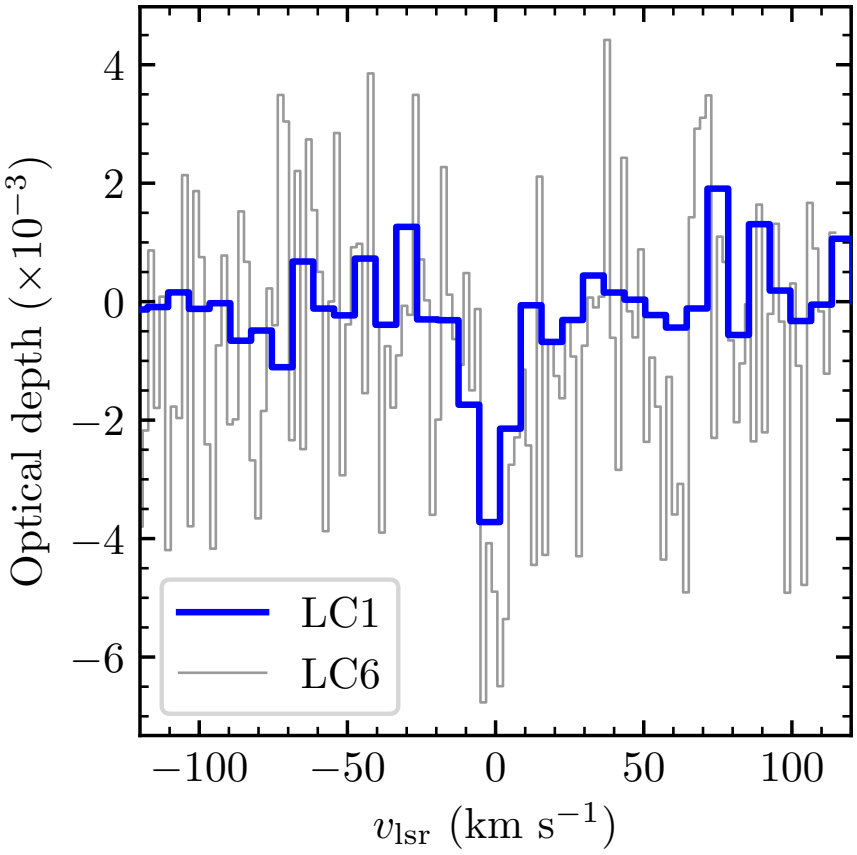

Figure 4.3.: LOFAR spectra of C351α observed on two different nights. The *blue steps* show the spectra obtained from observations performed during February 2014 and the *black steps* for observations taken during October 2016. The 2014 detection, with a signal-to-noise ratio of 4.5, is confirmed by the 2016 observations (with a signal-to-noise ratio of 2.5).

of Orion-KL (Wyrowski et al., 1997); and observations of the C30α line using the Atacama Large Millimeter Array (ALMA) total power array plus ALMA compact array (ACA) at a spatial resolution of 28″ (Bally et al., 2017). Throughout this work we compare the CRRL observations with the 158 μm-[CII] line cube observed with the Stratospheric Observatory for Infrared Astronomy (SOFIA Young et al., 2012) upGREAT receiver (Heyminck et al., 2012; Risacher et al., 2016). This cube has a spatial resolution of 18″, a velocity resolution of 0.2 km s^{-1} and covers a region of roughly 1° × 1°. The observations and reduction used to produce the 158 μm-[CII] line cube are described in detail in Pabst et al. (2019). Additionally, we compare with observations of ^{12}CO(2–1) and ^{13}CO(2–1) (Berné et al., 2014), and with the dust properties as derived from Herschel and Planck observations (Lombardi et al., 2014).

4.3. Results

In this section we start by describing the RRL spectra towards M42, focusing on the CRRLs. Then, we present maps of CRRL emission which we use to study the spatial distribution of the lines and to compare with other tracers of the ISM, particularly the 158 μm-[CII] line.

4.3.1. RRLs from M42

Some of the RRL stacks obtained from the pointed observations towards M42 are presented in Figure 4.4. In these stacks the strongest features are hydrogen RRLs (HRRLs), followed by a blend of CRRLs and helium RRLs (HeRRLs). The velocity difference between HeRRLs and CRRLs is of 27.4 km s^{-1}, and between HRRLs and CRRLs is 149.4 km s^{-1}. HRRLs and HeRRLs trace the ionized gas in the HII region, for which the line FWHM due to Doppler broadening is $\approx$ 20 km s^{-1}. In M42 the ionized gas is blueshifted with respect to the bulk of the molecular and neutral gas (e.g., Zuckerman, 1973; Balick et al., 1974a,b). This brings the HeRRL and CRRL closer, resulting in the observed blending. Fortuitously, we can use the fact that the HeRRLs are broader to distinguish them from the CRRLs.

Before focusing on the CRRLs we use the strength of the HRRLs to estimate the accuracy of the temperature scale. We use the fact that HRRLs of similar principal quantum number have similar properties. Then we can quantify the accuracy of the temperature scale by comparing the temperature of H$n\alpha$ lines of similar principal quantum number. The peak temperatures of the HRRLs presented in Figure 4.4 show variations of up to 25% between adjacent stacks (see Table 4.4). For example, the peak temperature of the H155α line should be almost the same as that of the H156α line, however they differ by 22%. Based on this we conclude that the calibration using the noise diode has an accuracy of about 25%.

CRRLs

As pointed out above, the CRRLs can be identified as a narrow feature on top of the broader HeRRLs in Figure 4.4. A zoom-in of the CRRLs is presented in Figure 4.5.

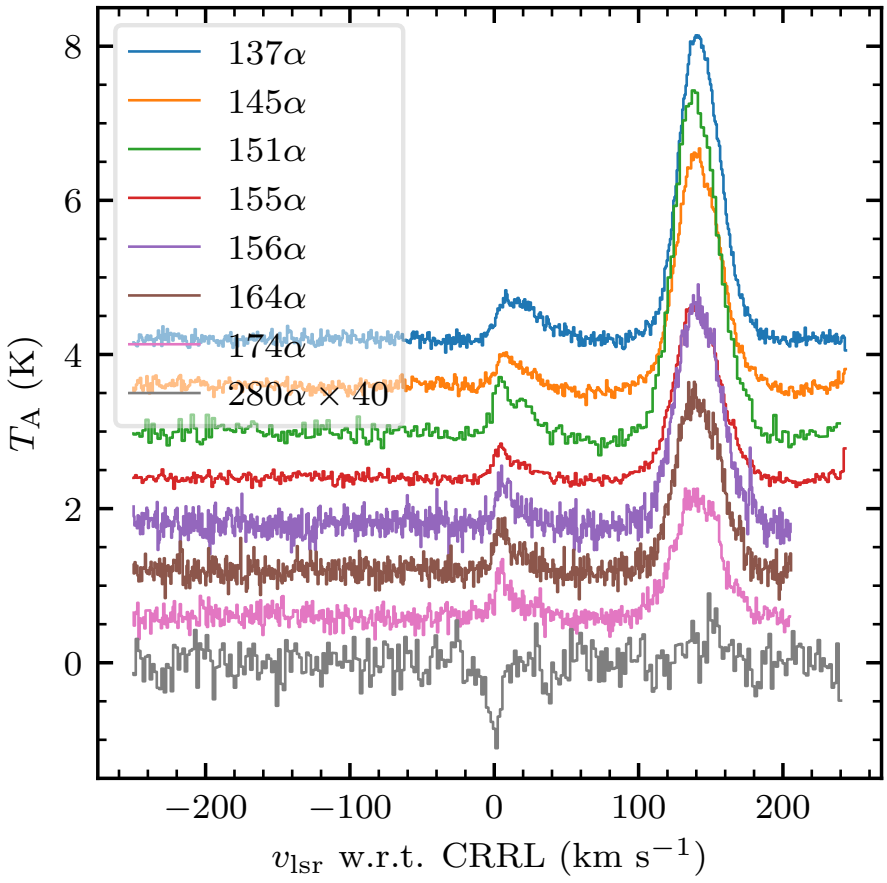

Figure 4.4.: Hydrogen, helium and carbon radio recombination lines observed with the GBT for α lines (the change in principal quantum number is $\Delta n = 1$) with principal quantum numbers 137, 145, 151, 155, 156, 164, 174 and 280. The velocity is given with respect to the CRRL. To reference the velocity with respect to helium or hydrogen subtract 27.4 km s^{-1} or 149.4 km s^{-1} respectively. The spectra are offset by a constant 0.7 K, and the 280α spectrum is scaled by a factor of 40. This data is part of project AGBT02A_028. Since the observations are obtained using the same telescope, the GBT, their spatial resolution ranges from 4′.4 to 36′.

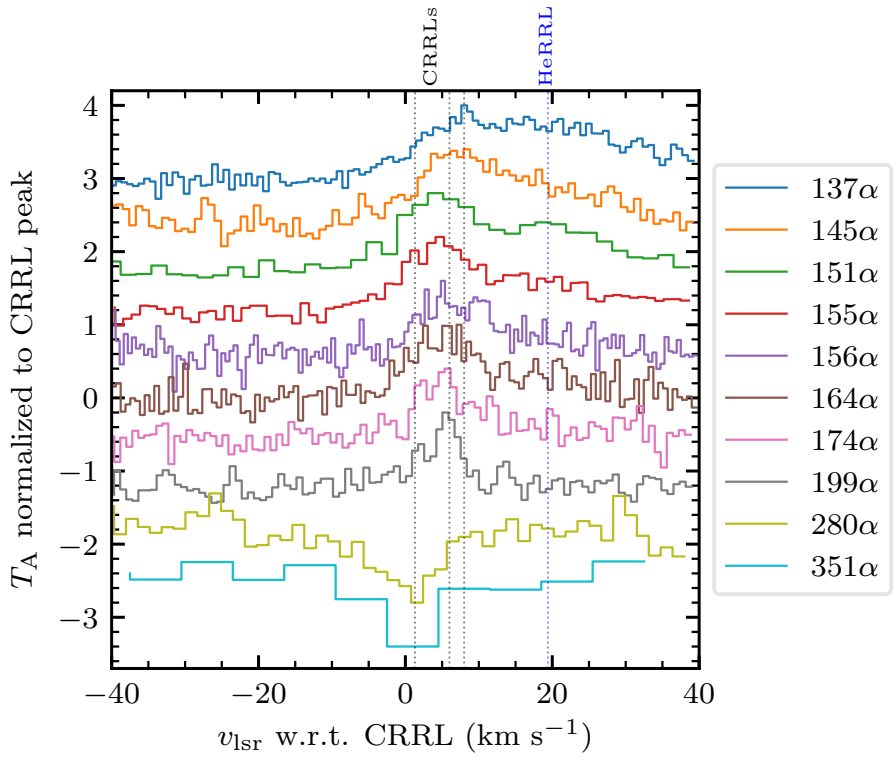

Figure 4.5.: Zoom in of RRL spectra towards M42 around the carbon feature. The RRLs correspond to α lines with principal quantum numbers 137, 145, 155, 156, 164, 174, 199, 280 and 351. CRRLs with $n \leq 199$ appear in emission while those with $n \geq 280$ appear in absorption. The velocity is given with respect to the CRRL and the intensity axis is normalized to the peak of the CRRL. To reference the velocity with respect to helium subtract 27.4 km s^{-1}. The spectra are offset by a constant 0.6 and are normalized using peak of the brightest CRRL in each spectra. The *dotted lines* indicate the position of the CRRLs at $\approx$ 1.3 km s^{-1}, $\approx$ 6 km s^{-1} and $\approx$ 8 km s^{-1} (*black*) and the HeRRL (*blue*). The C351α spectrum is the spatial average over a circle 36′ in diameter centered on M42.

One of the most notable features in the spectra of Figure 4.5 is the transition of the lines from emission to absorption between the C199α and C280α lines. Towards M42, this is the first time that CRRLs have been observed in absorption.

In terms of the velocity structure of the CRRLs, we can identify at least two velocity components in emission at 6 and 8 km s^{-1}. The $\approx$ 8 km s^{-1} velocity component can be observed in the C137α RRL, while the $\approx$ 6 km s^{-1} velocity component can be observed in the CRRLs with n = 145–199. Gas with a velocity of $\approx$ 8 km s^{-1} is associated with the background molecular cloud, while that with lower velocities is associated with foreground gas (e.g., Dupree, 1974; Ahmad, 1976; Boughton, 1978). In the case of this line of sight the foreground gas corresponds to the Veil, which is less dense ($n_{\rm H} \sim 10^3$ cm^{-3} Abel et al., 2016) and irradiated by a weaker radiation field (e.g., Abel et al., 2016) than the PDR that forms between the HII region and Orion A ($n_{\rm H} \sim 10^5$ cm^{-3}; e.g., Natta et al., 1994).

For the C174α and C199α lines there are hints of emission at $\approx$ 2 km s^{-1}. CRRL emission at this velocity has not been reported previously, though some authors reported the detection of unidentified RRLs at velocities of ≈ -3 km s^{-1} (Chaisson & Lada, 1974) and ≈ -0.6 (Pedlar & Hart, 1974). Given that the $\approx$ 2 km s^{-1} velocity component is detected in two independent observations (the C174α stack is part of project AGBT02A_028 while the C199α stack is part of AGBT12A_484) consider the features to be CRRLs. The C174α and C199α lines at $\approx$ 2 km s^{-1} trace gas in component B of the Veil.

To compare the lines in absorption we use an aperture of 36′, similar to the resolution of the observations used to produce the C280α detection (40′, Table 4.2). The inverted spectra are presented in Figure 4.6. The C280α line has a velocity centroid of 0.7 $\pm$ 1.0 km s^{-1} (Table 4.4), while the C351α line has a velocity centroid of 2.3 $\pm$ 0.8 km s^{-1}. These lines trace the expanding Veil.

The 158 μm-[CII] line spectrum extracted from the 36′ aperture used to study the C280α and C351α lines is also shown in Figure 4.6. There we see that the Veil ($v \approx$ 3 km s^{-1}) has a peak antenna temperature of $\approx$ 1.8 K, while that from the background PDR ($v \approx$ 9 km s^{-1}) is a factor of ten stronger. The Veil is weaker in the 158 μm-[CII] line because it is farther from the Trapezium ($\approx$ 2 pc; Abel et al., 2016) and hence colder.

4.3.2. Spatial distribution of CRRLs

C157α

The spatial distribution of a stack of CRRLs with n = 156–158 (with an effective n = 157) is presented in Figure 4.7 in the form of channel maps. In Figure 4.7 we also include channel maps of 158 μm-[CII] and ^{12}CO(2–1) at the same resolution. The channel maps show that the C157α emission avoids the regions where the 18 cm continuum is brightest. At the frequency of the C157α line ($\approx$ 1.6 GHz) the brightest portions of the HII region are optically thick (e.g., Wilson et al., 2015). This means that radiation coming from the interface between the background cloud and the HII region is heavily attenuated at these frequencies. Moreover, the noise is larger towards the HII

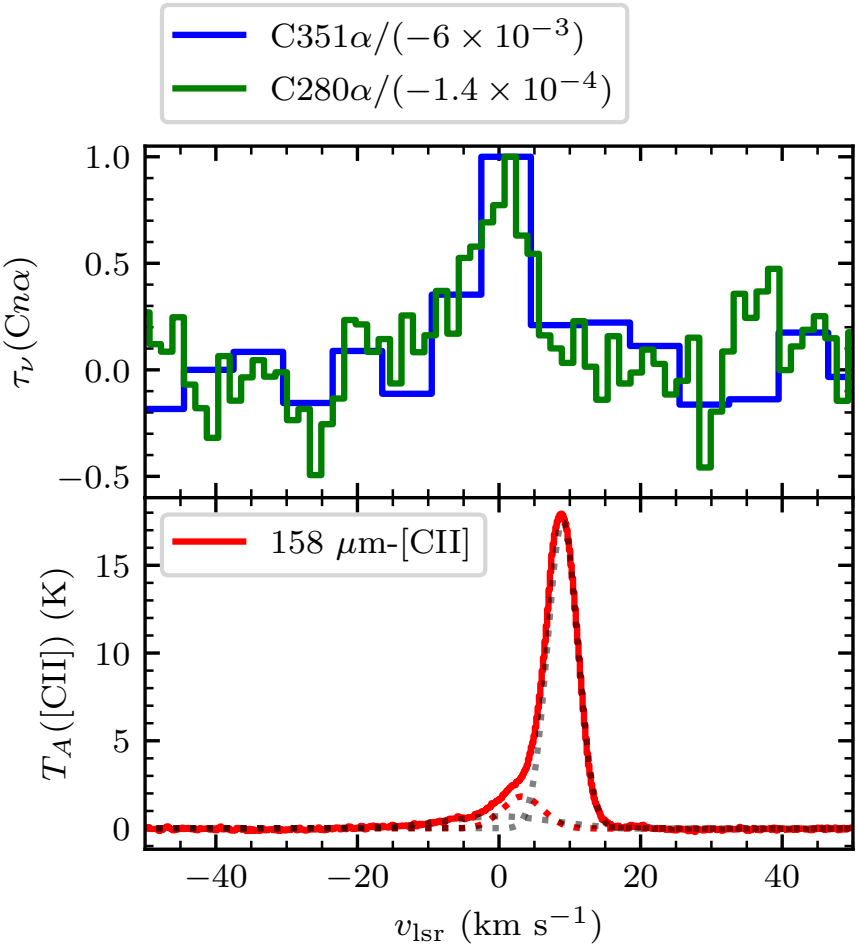

Figure 4.6.: Comparison between the CRRLs observed in absorption and the 158 μm-[CII] line. The *blue steps* show the C351α line profile inverted (from the LOFAR observations in 2014), the *green steps* the C280α line inverted (from the GBT observations AGBT02A_028) and the *red steps* show the 158 μm-[CII] line (from the SOFIA observations of Pabst et al. 2019). The CRRLs trace a fainter velocity component in the 158 μm-[CII] line due to the effect of stimulated emission. The *dotted lines* in the lower panel show the best fit Gaussian line profiles used to decompose the 158 μm-[CII] line (the properties of these component are given in Table 4.3). The spectra are the spatial average over a circle 36′ in diameter centered on M42.

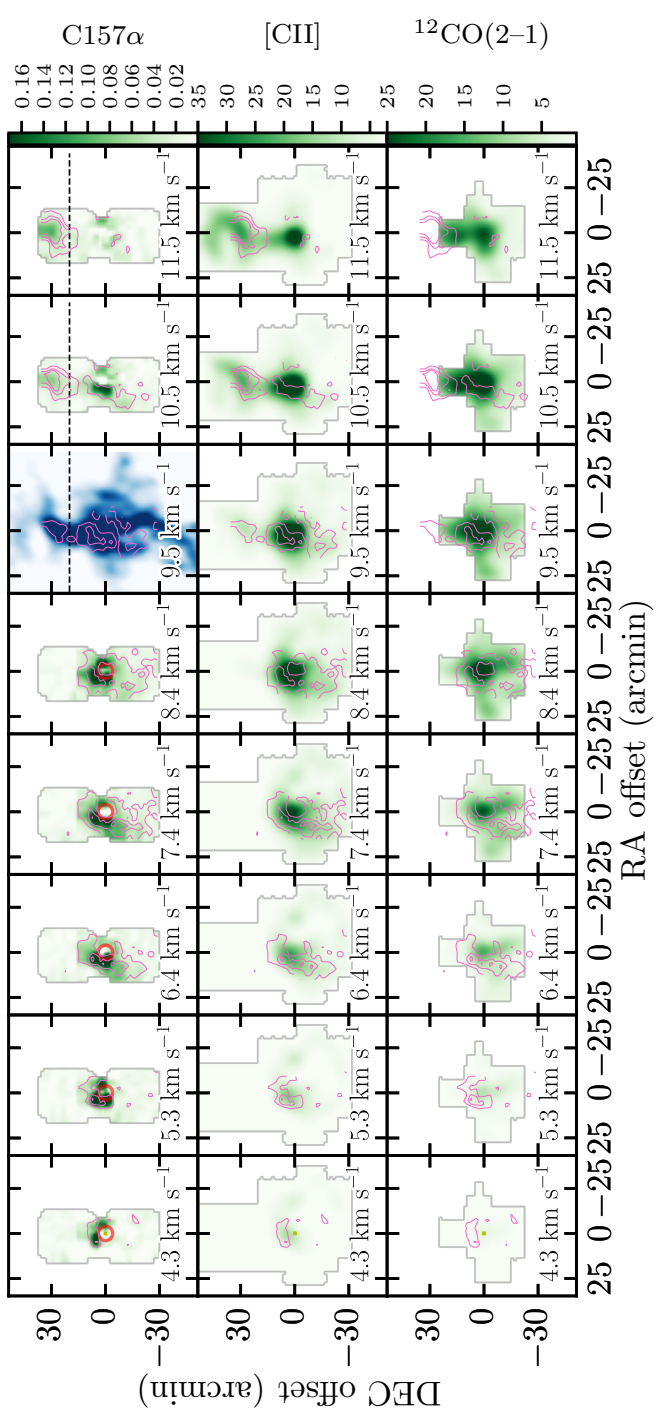

Figure 4.7.: Channel maps of C157α (*top row*), 158 μm-[CII] (*middle row*) and ^{12}CO(2–1) (*bottom row*) line emission. The *pink contours* show C157α emission above 3σ in steps of 3σ, with σ being the standard deviation of the spectra ($\sigma \approx 10$ mK). The velocity is indicated at the bottom of each panel. All cubes have been convolved to a spatial resolution of 8′.1. The velocity axes were averaged to match the velocity resolution of the C157α cube. The spatial axes are given in offsets with respect to M42. The *red circle* shows the extent of M42 in the 21 cm continuum map of van der Werf et al. (2013). In the top panel with a velocity of 9.5 km s^{-1} the background image *in blue* is the 857 GHz emission as observed with Planck at 4′.6 resolution (Planck Collaboration et al., 2016a). In the top row panels with a velocity $\geq$ 9.5 km s^{-1} the *dashed line* shows a Declination of −5.0583° (J2000), used to separate S279 from Orion A. The color scales in the rightmost panel are in units of K.

region due to its contribution to the antenna temperature.

At velocities less than 6 km s^{-1} the C157α emission comes from regions close to the Northern Dark Lane and the Dark Bay. The Northern Dark Lane is a dark structure which separates M42 from M43 in optical images (see Figure 12 of O'Dell & Harris, 2010). The Dark Bay is a region of high optical extinction which seems to start in the Northern Dark Lane and extends to the Southwest in the direction of the Trapezium stars. These structures are also seen in the lines of 158 μm-[CII] and ^{12}CO(2–1). At velocities in the range 6 km s^{-1} to 7.4 km s^{-1} the C157α emission extends to the South of M42, following the limb brightened edge of the Veil (Pabst et al., 2019). Then at 8.4 km s^{-1} the C157α emission seems to trace the Orion molecular cloud 4 (OMC4, e.g., Berné et al., 2014). At velocities larger than 9 km s^{-1} we see C157α emission extending to the North of M42. At 10 km s^{-1} we see part of the HII region S279 in the northernmost portion of the map (at an offset of 30′ to the North), containing the reflection nebulae NGC 1973, 1975, and 1977. In general, the spatial distribution of the C157α emission follows that of 158 μm-[CII] and to a lesser extent that of ^{12}CO(2–1). Then, C157α emission predominantly traces the northern part of the ISF (see the top panel in Figure 4.7 for $\upsilon_{\rm lsr} = 9.8$ km s^{-1}).

To further explore the relation between the FIR [CII] line and the C157α line we compare their intensities at each position in the map. We select pixels which show C157α emission with a signal-to-noise ratio ≥ 5 in the velocity range 4–12 km s^{-1}. We split the selected pixels into three groups that separate different components in Orion A. The first group aims to trace gas along the ISF. For this group we select pixels with line emission in the velocity range $7.5 \leq \upsilon_{\rm lsr} < 12$ km s^{-1} and with a Declination below $-5.0583°$ (J2000). The second group targets gas that is associated with the Veil. Pixels with line emission in the velocity range $4 \leq \upsilon_{\rm lsr} < 7.5$ km s^{-1} and a Declination below $-5.0583°$ (J2000) are selected in this group. The third and last group targets gas associated with S279. In this group, pixels with a declination above $-5.0583°$ (J2000) are selected.

The 158 μm-[CII] and C157α line intensities for the different groups are presented in Figure 4.8. Here we can see that there is a relation between the intensities of both lines, and that the shape of their relation depends on which velocity structure is selected. Gas associated with the ISF reaches a higher 158 μm-[CII] line brightness than that in the other groups (the Veil or S279). The shape of the relation for the gas associated with S279 looks like a scaled down version of that in the ISF. For the gas in the Veil the C157α line is brighter than in the ISF or S279 at similar 158 μm-[CII] brightness temperature, which reflects that the Veil is in front of the continuum source.

In Figure 4.8 we have also color coded the data as a function of their projected distance from the ionizing star. For the gas in the ISF and the Veil Θ^1 Ori C (HD 37022) is the ionizing star, while for gas in S279 it is 42 Ori (HD 37018, c Ori). Θ^1 Ori C is a O7 star, while 42 Ori is a B1 star (Hoffleit & Warren, 1995). There is a trend in the line brightness as a function of distance from the ionizing star; closer to the ionizing source the lines are brighter.

In the CRRL spectra of Figure 4.5 we can see that as the frequency decreases (increasing n), the velocity centroid of the emission lines shifts from ≈ 9 km s^{-1} to ≈ 6 km s^{-1} and additional velocity components are more easily observed at lower frequencies (e.g.,

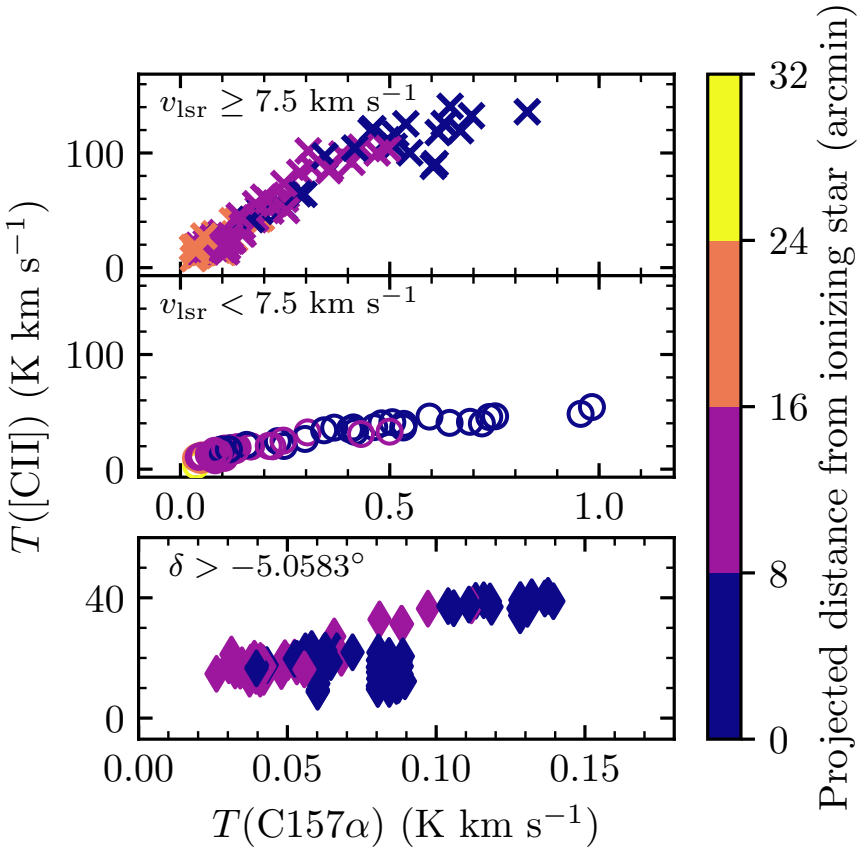

Figure 4.8.: 158 μm-[CII] line intensity as a function of the C157α line intensity. The line emission is separated into different groups based on known features in the maps. The *top panel* shows line emission with a velocity in the range [4, 7.5) km s^{-1} and a declination below −5.0583°, associated with the Veil, the *middle panel* shows line emission with a velocity in the range [7.5, 12) km s^{-1} and a declination below −5.0583°, associated with the ISF, and the *bottom panel* shows line emission at a declination above −5.0583°, associated with S279.

at 2 km s^{-1}). This is due to the combination of effects. First, the dominant emission mechanism changes as a function of frequency. At higher frequencies spontaneous emission dominates, while at lower frequencies stimulated transitions become dominant (Sect. 4.4.1). Spontaneous emission lines are brighter from denser regions (i.e. the background PDR), while to get stimulated transitions a bright background continuum is required. Second, all the observations were obtained using the same telescope, hence the observing beam becomes larger with decreasing frequency and therefore different gas structures are included in the beam. As Figure 4.7 shows, the velocity distribution of the gas is such that gas with lower velocities has a higher emission measure around M42 than towards M42 itself. This implies that at higher frequencies we mainly see CRRLs from the background PDR since this is the densest component along the line of sight, while at lower frequencies we observe the gas around and in front of M42.

C30α

We searched for CRRLs in the ALMA cubes presented by Bally et al. (2017). These cubes contain α RRLs with $n = 30$ within the observed frequency range. H30α, He30α and C30α lines are detected in the cube which covers the South-East region of the Orion Molecular Core 1. We confirm that the observed line is C30α by comparing its velocity integrated intensity (moment 0) with that of the C65α line at a similar angular resolution (40″, Wyrowski et al., 1997). The comparisson is presented in Figure 4.9, where we can see the C30α emission overlapping with the C65α emission over the region mapped. This confirms that the emission corresponds to C30α and not to a molecular line at a similar velocity.

Next we turn our attention to how the C30α emission is distributed with respect to the 158 μm-[CII] and ^{12}CO(2–1) lines. This comparison is presented in Figure 4.10. The distribution of C30α resembles that of the other two lines, but there are differences between them. For example, at 12.1 km s^{-1} there is C30α emission to the North of the map, but there is little 158 μm-[CII] and ^{12}CO(2–1) is more compact.

To illustrate the above point we extract the line intensity from a slice that joins Θ^1 Ori C with the peak of C30α emission in the South of the map (purple line in Figure 4.10). To produce the intensity profiles the cubes are integrated over the velocity range 8 km s^{-1} to 12 km s^{-1}, and the result is presented in Figure 4.11. There we can see that the 158 μm-[CII] line peaks closer to Θ^1 Ori C than the ^{12}CO(2–1) line and the CRRLs. This arrangement is similar to the layered structure found in a PDR (e.g., Wyrowski et al., 2000).

4.3.3. PDR MODELS

To understand the relation between the gas traced by the 158 μm-[CII] line and that traced by the CRRLs we use a PDR model. In this case we use the *Meudon* PDR code (Le Petit et al., 2006) to generate temperature and density profiles. To model the PDR we adopt a total extinction of $A_V = 20$ along the line of sight and a constant thermal pressure throughout the gas slab. How far does the UV radiation penetrate into the PDR is largely determined by the extinction curve, which towards Θ^1 C Ori is almost flat

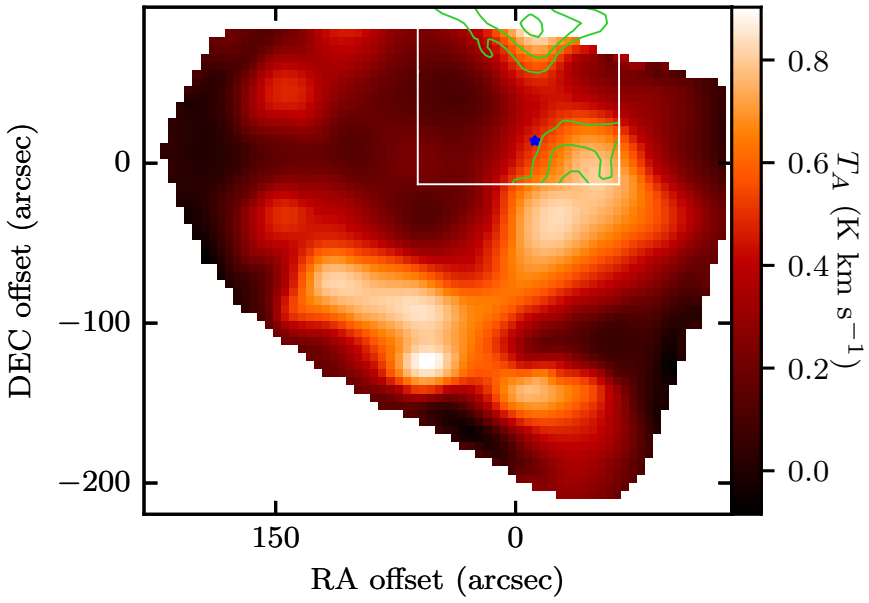

Figure 4.9.: Moment 0 maps of C30α emission and C65α emission. The *green contours* show the C30α emission at values of 40, 60 and 80 mK km s^{-1}. The *colormap* shows the C65α emission (Wyrowski et al., 1997). The spatial resolution of the C30α map is 28″ while that of the C65α map is 40″. A *white box* shows the extent of the region mapped by ALMA where C30α is detected (South-East map of Bally et al., 2017). The spatial axes are given in offsets with respect to M42, and a *blue star* marks the position of Θ^1 Ori C.

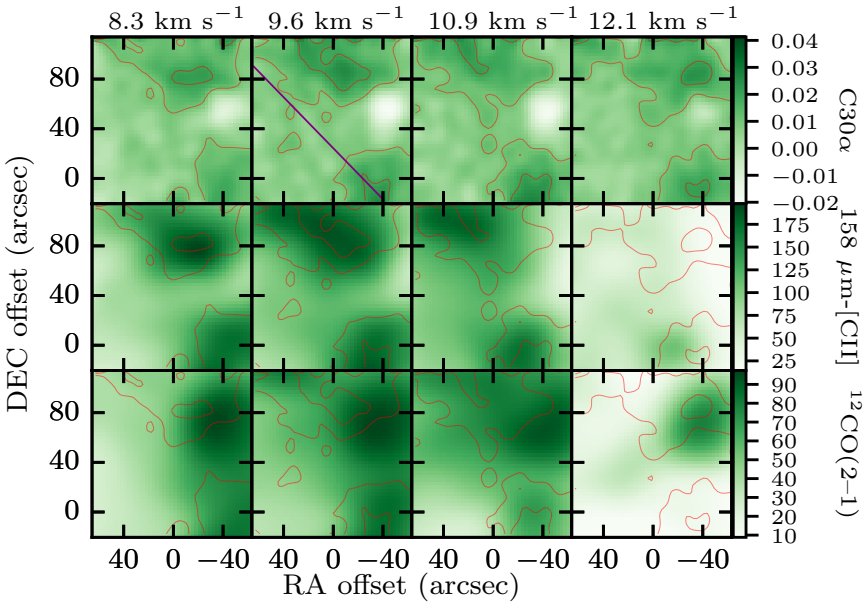

Figure 4.10.: Channel maps of C30α (*top row*), 158 μm-[CII] (*middle row*) and ^{12}CO(2–1) (*bottom row*) line emission. The *red contours* show C30α emission above 10 mK, in steps of 10 mK. The velocity with respect to the local standard of rest is indicated at the top of each row. All cubes have been convolved to a spatial resolution of 28″. The velocity axes were averaged and then linearly interpolated to match the velocity axis of the C30α cube. The spatial axes are given in offsets with respect to M42. In the C30α panel with a velocity of 9.6 km s^{-1} a *solid purple line* shows the slice used to extract the brightness profile presented in Figure 4.11.

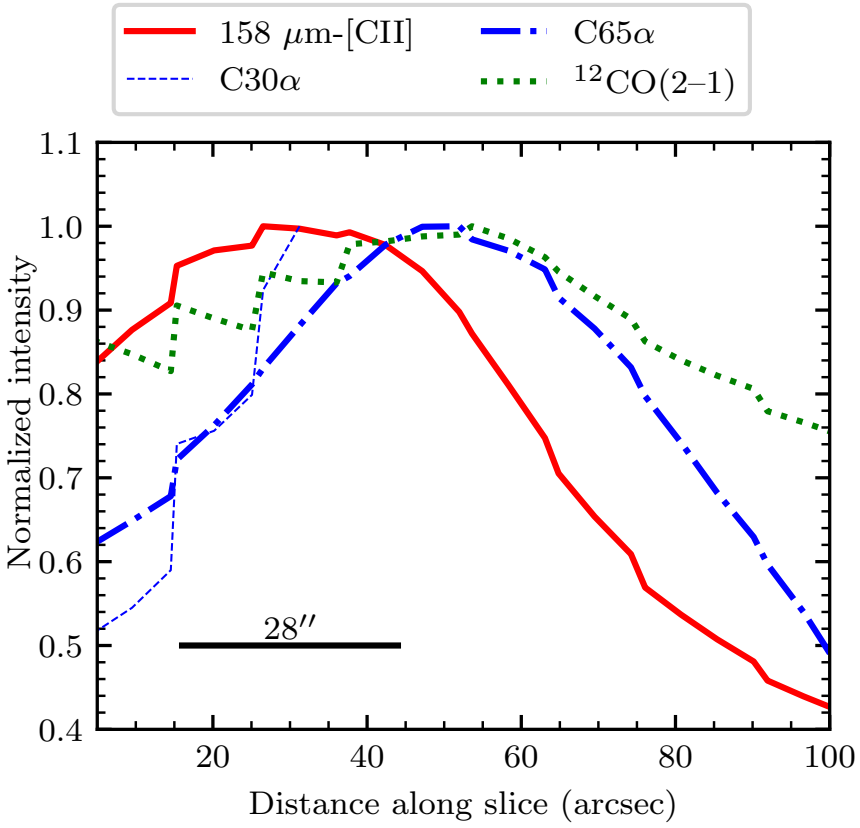

Figure 4.11.: Comparison between the velocity integrated brightness of the C30α, 158 μm-[CII] (Pabst et al., 2019) and ^{12}CO(2–1) (Berné et al., 2014) lines. The *thin dashed blue line* shows the C30α line profile, the *blue dash dotted line* that of the C65α line, the *red solid line* the one for the 158 μm-[CII] line and the *green dotted line* the ^{12}CO(2–1) line. The slice from where the velocity integrated brightness profiles was extracted is shown in Figure 4.10. The position of Θ^1 Ori C marks the origin of the distance scale.

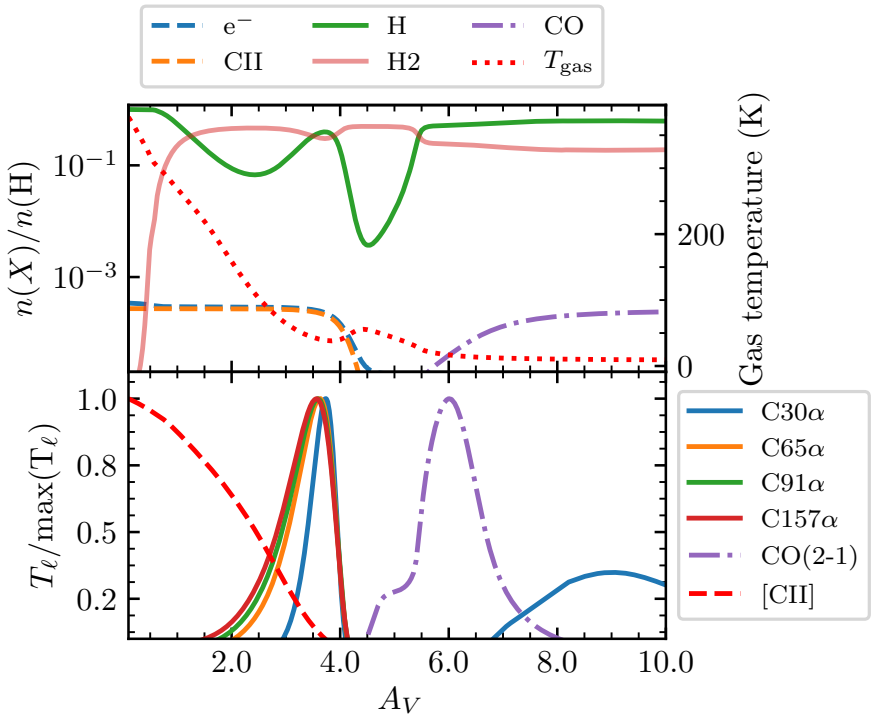

Figure 4.12.: Example of temperature and abundance profiles obtained with the *Meudon PDR code*. The *top panel* shows the gas temperature and abundances, while the *bottom panel* shows the line brightness temperature of C$n\alpha$ lines with principal quantum numbers $n = 30$, 65, 91 and 157, and of the 158 μm-[CII] line. The input conditions for the model are a radiation field of $G_0 = 1 \times 10^4$, in Mathis units, and a total gas density of $n_{\rm H} = 1 \times 10^4$ cm^{-3}. The difference between the abundance of free electrons and the abundance of ionized carbon is produced by the ionization of species such as sulfur or hydrogen.

with an extinction to color index $R_V = 5.5$ (Fitzpatrick & Massa, 1988; Cardelli et al., 1989). The extinction to column density ratio $A_V / N_{\rm H}$ is determined from the extinction observed towards the Trapezium stars, $A_V = 2.13 \pm 0.52$ (Ducati et al., 2003), and the hydrogen column density towards Θ^1 Ori C and B of $N_{\rm H} = 4.4 \times 10^{21}$ cm^{-2} (Shuping & Snow, 1997; Cartledge et al., 2001). We adopt a carbon abundance of [C/H]= 1.4×10^{-4}, measured against Θ^1 Ori B (Sofia et al., 2004). The models are illuminated by the ISRF on the far side ($A_V = 20$) scaled to $G_0 = 1$ using the parametrization of Mathis et al. (1983). On the observer side ($A_V = 0$) we vary the strength of the ISRF to explore its effect on the gas properties.

Once we have computed the temperature and density in the PDR, we process the output to determine how much of the 158 μm-[CII] and CRRL brightness comes from different layers in the PDR. The different layers represent different depths into the

molecular cloud and are expressed in terms of the visual extinction A_V. An example of the temperature and density profiles, as well as the line brightness contributed from each layer in the PDR, are presented in Figure 4.12. For this model we used an incident radiation field of $G_0 = 1 \times 10^4$, in Mathis units, and a total gas density of $n_{\rm H} = 1 \times 10^4$ cm^{-3}. The layered structure in the models is in good agreement with observations of CRRLs and the 158 μm-[CII] line for the PDRs associated with the Orion Bar and NGC 2023 (Wyrowski et al., 1997, 2000; Bernard-Salas et al., 2012; Sandell et al., 2015).

Here we use the models of Salgado et al. (2017a) to compute the properties of the CRRLs. These models solve the level population equations taking into account deviations from local thermodynamical equilibrium (LTE). The deviation from LTE in the population of carbon atoms is characterized by the factor b_n and the effect of stimulated emission by the factor $\beta_{nn'}$ (e.g., Shaver, 1975; Salgado et al., 2017a). These are known as departure coefficients. The models of Salgado et al. (2017a) include the effect of dielectronic capture (Watson et al., 1980; Walmsley & Watson, 1982). This effect will produce an overpopulation at n levels in the range 30–500 with respect to a system which does not undergo dielectronic capture. For conditions like those found towards Orion A ($n_{\rm H} \sim 10^5$ and $T \sim 100$ K, e.g., Natta et al., 1994), dielectronic capture will produce twice as many atoms with an electron at $n = 91$ than if we ignore its effect. The effect of dielectronic capture has not been considered explicitly before when studying the Orion A region, but it has been noted that it could help explain the observed line ratios (Wyrowski et al., 1997). We note that when solving the level population problem we do not include the presence of a free-free radiation field. For hydrogen atoms, the departure coefficients will change by less than 12% for n between 10 and 60 (e.g., Prozesky & Smits, 2018). The effect is smaller for $n > 60$.

For a homogeneous slab of gas in front of a continuum source, the velocity integrated brightness temperature of a CRRL, $T_\ell \Delta v$, is given by (e.g., Dupree, 1974)

$$T_\ell \Delta v = \tau^*_\ell \Delta v (b_{n'} T_{\rm e} - b_n \beta_{nn'} T_{\rm cont}), \tag{4.1}$$

where τ^*_ℓ is the line optical depth in LTE, $T_{\rm e}$ the electron temperature of the gas and $T_{\rm cont}$ the temperature of the background continuum. In this equation, the first term in parenthesis corresponds to the contribution to the line brightness temperature from spontaneous emission, while the second term represents the contribution from stimulated emission. The line optical depth in LTE is given by (e.g., Salgado et al., 2017b),

$$\tau^*_\ell \Delta v = 1.069 \times 10^7 \Delta n M T_{\rm e}^{-2.5} e^{\chi_n} EM_{\rm C^+} \text{ Hz}, \tag{4.2}$$

here $\Delta n = n' - n$, M is the oscillator strength of the transition (Menzel, 1968), $\chi_n = 157800 n^{-2} T_{\rm e}^{-1}$ and $EM_{\rm C^+} = n_{\rm e} n_{\rm C^+} L$ the ionized carbon emission measure in pc cm^{-6} with L the thickness of the slab.

To compute the CRRL brightness temperature from the PDR we assume that the emission is due to spontaneous emission with no background continuum (Natta et al., 1994). In each layer the temperature and electron density determine the value of b_n. For the CRRLs the b_n values are < 1 over the range of physical properties explored here. The line brightness in the LTE case is, on average, a 50% larger than in the non-LTE

case. The difference between the LTE and non-LTE cases is larger for lower pressures and higher radiation fields. In an extreme case the LTE value is 70% larger than the non-LTE value.

To compute the 158 μm-[CII] line brightness temperature we use the equations provided in Appendix B of **?** and the collisional excitation rates provided in Goldsmith et al. (2012). The equations in **?** provide the line intensity with a correction for the finite optical depth of the line.

In Figure 4.12 we can see that most of the 158 μm-[CII] line comes from the surface layers of the PDR ($A_V < 3.5$), while the CRRL emission comes from a deeper layer ($A_V = 3.5$). The gas temperature can be a factor of 10 lower at $A_V = 3.5$ with respect to $A_V < 3.5$. This reflects the fact that the CRRL optical depth has a stronger dependence on the temperature ($\propto T^{-5/2}$) than that of the 158 μm-[CII] line. Therefore, when we constrain the gas physical properties using CRRLs and the 158 μm-[CII] line using a uniform gas slab model, the temperature and density will be an average between the properties of the layers traced by both lines. We also note that the studied CRRLs trace an almost identical layer in the PDR, which justifies using their line ratios regardless of geometry. The situation is similar for PDRs with $10^2 < G_0 \leq 10^5$ and 5×10^4 K cm^{-3} $< P \leq 10^8$ K cm^{-3}.

The structure observed in Figure 4.12 is similar to that found in Figure 4.11. There, we observe that the separation between the peak of the 158 μm-[CII] line is offset by $\approx 10''$ with respect to the peak of ^{12}CO(2–1). For a distance of 417 pc, this translates to a projected separation of 0.02 pc. Using the result of Figure 4.12, we have that the separation between these tracers corresponds to roughly $A_{\rm V} = 6$ or $N_{\rm H} = 1.2 \times 10^{22}$ cm^{-2}. This corresponds to an hydrogen density of 2×10^5 cm^{-3}, similar to that found in the interclump medium in the Orion Bar (5×10^4 cm^{-3} Young Owl et al. 2000 or 2×10^5 cm^{-3} Simon et al. 1997). This hydrogen density is also consistent with the value found towards a nearby region using CRRL and [CII] ratios (Sect. 4.4.2).

4.4. Physical conditions

In this section we use CRRLs and the 158 μm-[CII] line to determine the physical conditions of the gas, e.g., its temperature and density. We do this by modeling the change in the properties of the CRRLs as a function of principal quantum number (e.g., Ahmad, 1976; Boughton, 1978; Jaffe & Pankonin, 1978; Payne et al., 1994; Oonk et al., 2017; Salas et al., 2018), and by comparing the CRRLs with different principal quantum numbers to the 158 μm-[CII] line.

4.4.1. The Veil towards M42

To study the Veil of Orion we focus on the information provided by the CRRLs observed in absorption and the C157α emission at velocities $\lesssim 7$ km s^{-1}.

Transition from emission to absorption

For the CRRLs associated with the Veil the largest principal quantum number for which the line is observed in emission is $n = 199$ (Figure 4.5). Then, at $n = 280$ the line is observed in absorption. This sets a lower limit to the electron density of the gas of $n_e \geq 0.03$ cm^{-3}, and for the electron temperature 35 K $\leq T_e \leq$ 130 K. The constraint on the gas properties set by the transition from emission to absorption is shown in Figure 4.13 as a purple dashed line.

CRRL ratio

The ratio between two CRRLs in absorption provides an additional constraint to determine the gas properties (e.g., Salgado et al., 2017b; Salas et al., 2017, 2018). Here we use the ratio between the integrated optical depths of the C280α and C351α lines to constrain the gas temperature and electron density.

In order to convert the observed C280α line temperature to optical depth, we need to estimate the continuum adjacent to the line. As mentioned in Section 4.2.1, we chose not to directly estimate the continuum from the observations used to produce the C280α spectrum as we do not have a reference position where to estimate the contribution from non-astronomical sources to the antenna temperature. Instead, we use the low frequency spectrum of M42 to estimate the contribution to the continuum in the C280α spectrum. Using the Very Large Array (VLA, Napier et al., 1983) in its D configuration (minimum baseline 35 m), Subrahmanyan et al. (2001) observed M42 at 330 MHz. They measured a total combined flux for M42 and M43 (which is only $\sim 5'$ away from M42) of 167 ± 5 Jy. This flux density is similar to that measured using single dish telescopes (e.g., Lockman & Brown, 1975), so it should not have missing flux. We assume that the combined flux density from M42 and M43 scales as $S_\nu \propto \nu^{0.92\pm0.08}$ between 240 and 400 MHz (based on the continuum measurements presented in Lockman & Brown, 1975). We estimate the effect of beam dilution on the measured antenna temperature for the continuum using the 330 MHz continuum maps (Subrahmanyan et al., 2001). In these maps, M42 and M43 cover a circular area with a radius of $18'$ centered at $(\alpha, \delta)_{J2000} = (5^h35^m00^s, -5°25^m22^s)$. The 330 MHz continuum shows a structure which is similar to that of the LOFAR 149 MHz continuum map. The beam of the C280α observations covers most of this region, and leaves out less than 0.4% of the continuum flux. Therefore, we estimate that at 298 MHz the continuum temperature of the C280α spectra will be 195 ± 6 K. Ultimately, we find the integrated optical depth of the C280α line is 1.4 ± 0.2 Hz.

The ratio between the integrated optical depths of the C280α and C351α lines is $(4 \pm 1) \times 10^{-2}$.. The constraint on the gas temperature and density set by this ratio is shown in Figure 4.13 with blue dashed lines. A larger ratio implies a higher temperature. In this case, the integrated optical depth ratio poses a more stringent constraint on the gas properties than the point at which the lines transition from emission to absorption.

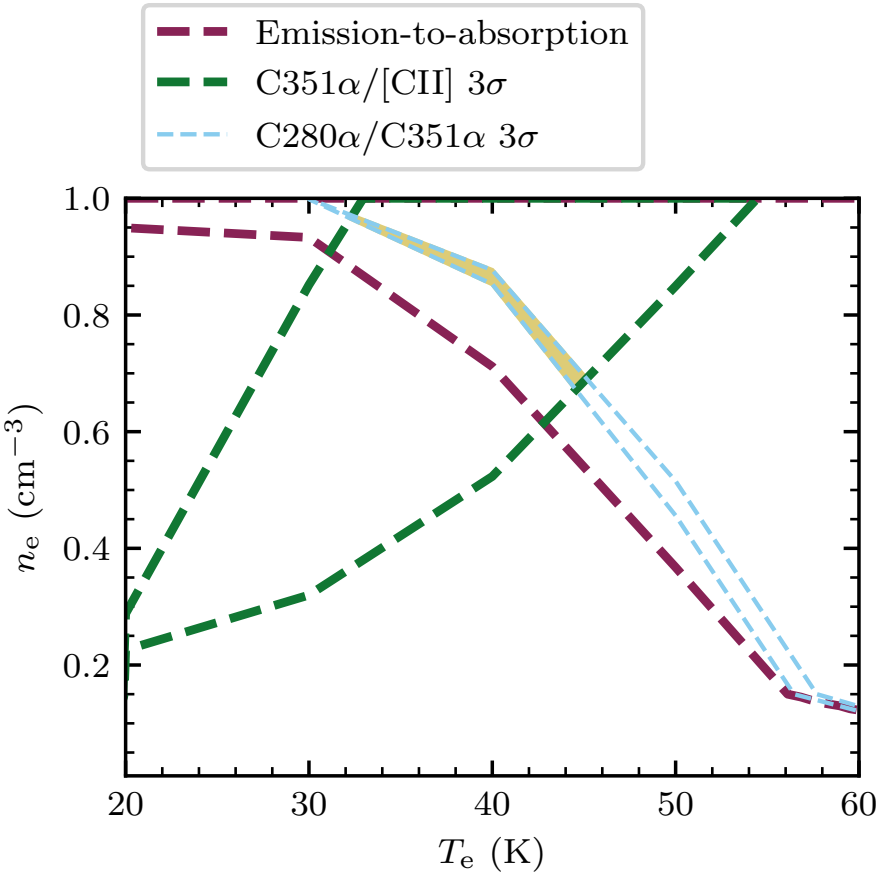

Figure 4.13.: Constraints on the temperature and electron density for gas associated with Orion's Veil. The *dashed lines* show the constraints on the gas properties derived from different observables; the transition of the CRRLs from emission to absorption between $n = 200$ and 279; the ratio of the integrated optical depths of the C280α and C351α lines; the ratio between the C351α velocity integrated optical depth to the 158 μm-[CII] line intensity. All the constraints shown are 3σ ranges. The region where the constraints overlap is shown as a *yellow shaded region*, close to 0.9 cm^{-3} and 40 K.

Table 4.3.: Veil line properties

Line	$v_{\rm lsr}$ (km s^{-1})	$T_{\rm line}$ (K)	Δv(FWHM) (km s^{-1})
	8.98 ± 0.01	17.58 ± 0.07	5.02 ± 0.01
[CII]	3.2 ± 0.1	1.82 ± 0.05	6.6 ± 0.2
	-0.1 ± 0.4	0.70 ± 0.04	17.9 ± 0.5
C280α	0.7 ± 1.0	-0.023 ± 0.003^a	11 ± 1
C351α	2.3 ± 0.8	-0.0061 ± 0.0008^b	10 ± 1

The line properties correspond to the best fit parameters of Gaussian line profiles and the errors quoted are one σ. The fits were performed to the spectra presented in Figure 4.6.
[a] To convert to optical depth we adopted a continuum temperature of 195 ± 6 K.
[b] Optical depth. The flux density of Orion A and M43 measured from the LOFAR continuum image at 149 MHz is 53 ± 3 Jy.

CRRLs and FIR [CII] line

Here we use the latest 158 μm-[CII] line maps of Pabst et al. (2019) to compare with the CRRLs observed in absorption. The cube of Pabst et al. (2019) presents the 158 μm-[CII] line resolved in velocity and samples a region larger than that studied in CRRLs. With this we can perform a direct comparison between the lines over the same regions without making assumptions about their velocity structure. Previous comparisons between CRRLs and the 158 μm-[CII] line have been performed using observations which did not resolve the velocity structure and/or did not sample the same spatial regions (e.g., Natta et al., 1994; Smirnov et al., 1995; Salas et al., 2017).

Here, we compare the C351α line with the 158 μm-[CII] line over the same spatial regions. Since the C351α line is observed in absorption, it will only trace gas which is in front of the continuum source. Then the 158 μm-[CII] line spectrum used to compare with the C351α line should be extracted from a region which encompasses the continuum source. This corresponds to a circular region with a radius of $18'$ centered at $(\alpha, \delta)_{\rm J2000} = (5^{\rm h}35^{\rm m}00^{\rm s}, -5°25^{\rm m}22^{\rm s})$. Though, the absorption spectra will be weighted by the underlying continuum, whereas the 158 μm-[CII] line will not be. Hence, even if we use an aperture that covers most of the continuum emission the lines could trace different portions of the Veil.

The resulting 158 μm-[CII] line spectrum (Figure 4.6) shows the presence of at least three velocity components. We fit three Gaussian components corresponding to the Veil, the dense PDR and the HII region. The best fit parameters of the Gaussian profiles are presented in Table 4.3. Using the values for the component associated with the Veil, at ≈ 3 km s^{-1}, the ratio between the C351α line integrated optical depth and the 158 μm-[CII] line intensity is $(-378 \pm 76) \times 10^3$ Hz erg^{-1} s cm^2 sr^1.

Given that the brightness of the 158 μm-[CII] line is 1.82 ± 0.05 K, and that the hydrogen density in the Veil is $\approx 10^3$ cm^{-3} (Abel et al., 2016), we assume that the line

is effectively optically thin (EOT, Goldsmith et al., 2012). In this case the intensity of the 158 μm-[CII] line is proportional to the column density, hence the ratio with respect to the integrated optical depth of the C351α line is independent of the column density and the line width. The constraints imposed on the gas properties based on the ratio between the 158 μm-[CII] line intensity and the C351α line integrated optical depth are shown in Figure 4.13 with green dashed lines.

Combined constraints: gas temperature and density

The constraints imposed on the gas properties by the integrated optical depth of the C280α and C351α lines and the ratio between the integrated optical depth of the C351α line and the 158 μm-[CII] line intensity intersect (see Figure 4.13). The region where these constraints intersect determines the ranges of temperature and electron density allowed by our analysis. The range of physical properties is then 30 K$\leq T_{\rm e} \leq$ 45 K and 0.65 cm$^{-3} \leq n_{\rm e} \leq$ 0.95 cm^{-3} if we consider the 3σ ranges. These constraints are valid for the Veil at $\approx$ 3 km s^{-1}, under the assumption that the C280α, C351α and 158 μm-[CII] lines trace the same gas. This assumption is appropriate for gas exposed to a radiation field $G_0 \lesssim 10^3$, when the temperature difference between the layers traced by the CRRLs and the 158 μm-[CII] line is lower. Since the gas properties have been derived from line ratios, these do not have a strong dependence on the beam filling factor.

Using the derived gas properties and the observed brightness of the 158 μm-[CII] line we can compute the column density of ionized carbon. The intensity of the 158 μm-[CII] line is 12.7 $\pm$ 0.5 K km s^{-1} over a circular region with a 18$'$ radius. This implies that the beam averaged column density is $N_{\rm CII} = (3.0 \pm 0.4) \times 10^{17}$ cm^{-2}, where the quoted 1σ error considers the 3σ range of possible physical properties.

A closer inspection at the 158 μm-[CII] line cubes at their native spatial resolution of 16$''$ reveals that most of the emission at $v_{\rm lsr} \approx 3$ km s^{-1} comes from the Dark Bay, the Northern streamer (see e.g., Goicoechea et al., 2015), part of M43, and the limb brightened Veil (Pabst et al. 2019, Figure 4.14). These cover an area of roughly 20$' \times$ 5$'$ (Dark Bay plus Northern streamer), 3$'$.5 $\times$ 3$'$.5 (M43) and 10$' \times$ 8$'$ (limb brightened Veil) on the sky. If we correct the column density for the effect of beam dilution we arrive at a value of $(2.3 \pm 0.4) \times 10^{18}$ cm^{-2}, between the value towards the Dark Bay (1.5×10^{18} cm^{-2}; Goicoechea et al., 2015) and the limb brightened Veil (3.5×10^{18}; Pabst et al. 2019).

We use the physical conditions we found to predict the peak antenna temperature of the C157α line. We adopt the 3σ ranges for the gas properties, a full width at half maximum of 6 km s^{-1}, a column density of [CII] of $N_{\rm CII} = (3 \pm 0.4) \times 10^{17}$ cm^{-2} and a continuum temperature of 38 K at 1.68 GHz (over the 36$'$ aperture). The predicted line profile has a peak antenna temperature between 25 mK and 170 mK, consistent with the observed value of 70 mK. The range of predicted values is mainly determined by the gas temperature and density. A variation of a factor of 1.5 in density and in temperature translates to a factor of seven variation in antenna temperature because the departure coefficient $b_n\beta_{nn'}$ is 20% smaller in the high density-low temperature limit, but the exponential factor in the line optical depth (Equation 4.2) is a factor of three

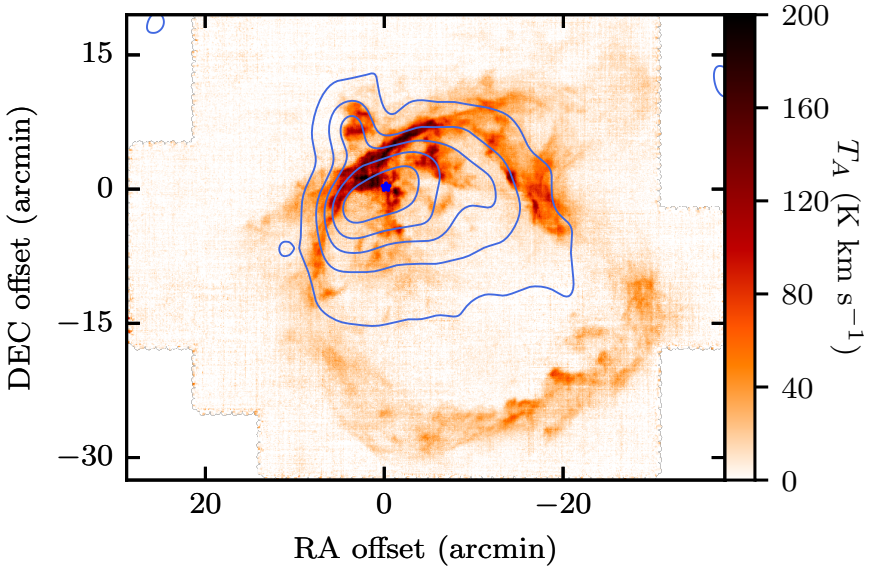

Figure 4.14.: Moment 0 map of the 158 μm-[CII] line associated with the Veil (*colorscale*). The moment 0 map considers emission for velocities between 0 km s^{-1} and 7 km s^{-1}. The *contours* show the radio continuum as observed with LOFAR at 149 MHz. The contours start at 0.2 mJy beam^{-1} and increase in steps of 1 Jy beam^{-1}. The spatial axes are given in offsets with respect to M42, and a *blue star* marks the position of Θ^1 Ori C. The radio continuum partially fills the wind blown bubble.

larger, and the emission measure a factor of three larger.

For a gas temperature between 30 K$\leq T_e \leq$ 45 K and an electron density 0.65 cm$^{-3} \leq n_e \leq$ 0.95 cm^{-3}, the contribution to the antenna temperature due to spontaneous emission is 23%–16%. This implies that most of the C157α line emission associated with the Veil can be explained in terms of stimulated emission. This reflects the importance of stimulated emission at low densities (e.g., Shaver, 1975). For this range of physical conditions, the effects of spontaneous and stimulated emission become comparable at $n \approx 120$.

The Veil has also been studied using other absorption lines; 21 cm-HI, 18 cm-OH and lines in the ultraviolet (UV) (e.g., van der Werf & Goss, 1989; Abel et al., 2004, 2006; van der Werf et al., 2013; Abel et al., 2016; Troland et al., 2016). Using observations of lines in the UV and the 21 cm line of HI, Abel et al. (2016) have derived gas properties for components A and B of the Veil. Their observations only sample the line of sight towards Θ^1 Ori C. They find a gas density of $n_H \approx 10^{2.3}$ and $10^{3.4}$ cm^{-3}, and a temperature of $T_K \approx 50$ and 60 K for components A and B respectively. Here we have used lower spatial resolution data to provide an average of the gas properties of the Veil in front of the HII region. We find temperatures that are a 15% lower than in the work of Abel et al. (2016), which might reflect the fact that CRRLs trace lower temperature regions in a PDR. To compare the density we need to convert from an electron density to an hydrogen density. We assume that all of the electrons come from ionized carbon, $n_e = n_{C^+}$, and that the carbon abundance relative to hydrogen is 1.4×10^{-4} (Sofia et al., 2004). Then, our constraints on the electron density translate to an hydrogen density 2000 cm$^{-3} \leq n_H \leq$ 7000 cm^{-3}, comparable to the ones found by Abel et al. (2016). As the lack of C137α and C145α emission suggests, we do not expect the physical conditions to be uniform across the Veil. This is confirmed by the patchy structure observed in 21 cm-HI absorption (van der Werf & Goss, 1989) and in optical extinction maps (O'Dell & Yusef-Zadeh, 2000). Higher resolution observations of the C280α, or similar n, lines would allow us to study the temperature and density variations across the Veil.

[CII] GAS COOLING AND HEATING EFFICIENCY

We estimate the gas cooling rate per hydrogen atom from the observed 158 μm-[CII] intensity and the column density of hydrogen. We convert the [CII] column density to an hydrogen column density assuming an abundance of carbon relative to hydrogen of $[C/H] = 1.4 \times 10^{-4}$ (Sofia et al., 2004) and that all carbon is ionized. Under these assumptions, the observed intensity of the 158 μm-[CII] line implies a [CII] cooling rate per hydrogen atom of $(4 \pm 0.2) \times 10^{-26}$ erg s^{-1} (H-atom)$^{-1}$. This is similar to the cooling rate found through UV absorption studies towards diffuse clouds (Pottasch et al., 1979; Gry et al., 1992), however the Veil is exposed to a radiation field $\sim$ 100 higher than the average ISRF. Given the geometry of the Veil, a large fraction of the 158 μm-[CII] emission comes from regions which are optically thick towards the observer (Pabst et al. 2019, Figure 4.14). Thus, the cooling rate we derive is likely a lower limit.

In the diffuse ISM most of the gas heating is through the photoelectric effect on polycyclic aromatic hydrocarbons (PAHs) and small dust grains (e.g., Wolfire et al.,

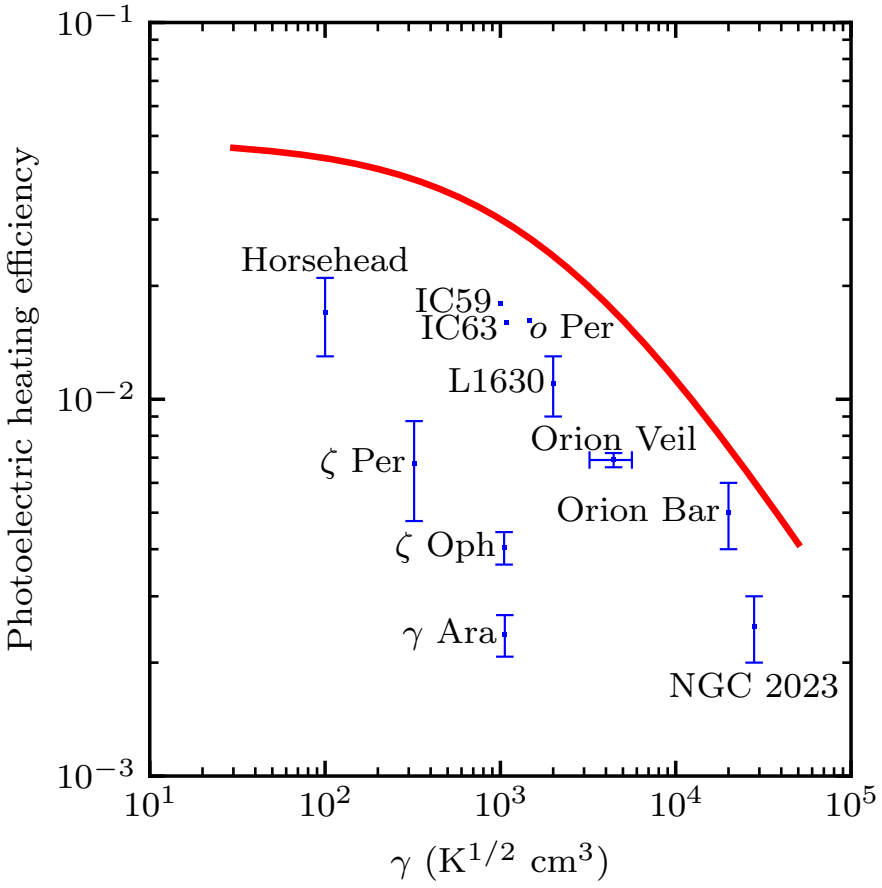

Figure 4.15.: Photoelectric heating efficiency as a function of the ionization parameter γ. The data for the dense PDRs NGC 2023 and the Orion Bar is taken from Hollenbach & Tielens (1999), the data for the Horsehead and L1630 is from Pabst et al. (2017), the data for diffuse PDRs is from Gry et al. (1992) and van Dishoeck & Black (1986), and the data for IC59 and IC63 is from Andrews et al. (2018). The *red line* shows the model of Bakes & Tielens (1994). The error bars for *o* Per, IC59 and IC63 have been omitted for clarity.

1995). In this process, FUV (6 eV to 13.6 eV) photons are absorbed by PAHs and very small dust grains causing them to eject electrons which then heat the gas through collisions. Our understanding of the ISM is intimately related to the efficiency of this process, as it couples the interstellar radiation field to the gas temperature. In general, the gas photoelectric heating efficiency, $\epsilon_{\rm pe}$, is $< 10\%$ (e.g., Bakes & Tielens, 1994; Weingartner & Draine, 2001) and most of the energy absorbed by the dust is re-radiated in the infrared (IR). Its exact value will depend on the charge state of the dust grains, and hence on the ionization parameter $\gamma = G_0 T_{\rm e}^{1/2} n_{\rm e}^{-1}$ (e.g., Hollenbach & Tielens, 1999). The gas heating efficiency through the photoelectric effect can be estimated as ([CII]+[OI])/TIR (e.g., Pabst et al., 2017), where TIR is the total infrared flux and [OI] is the gas cooling through the line of atomic oxygen at 63 μm. Here we ignore the possible contribution from the [OI] line at 63 μm to the gas cooling, since for a gas density of $n_{\rm H} \approx 3 \times 10^3$ cm^{-3} it is estimated to be roughly 5% of the total gas cooling (e.g., Tielens, 2010). As a proxy for TIR we use the Lombardi et al. (2014) maps of dust properties. These present the properties of the dust spectral energy distribution derived from fitting a modified blackbody to continuum data in the wavelength range 100 μm to 3000 μm as observed by Herschel and Planck. From the maps of Lombardi et al. (2014) we can obtain the TIR flux by integrating the modified blackbody between the wavelength range 20 μm to 1000 μm. The median of the TIR flux over the 18′ circle that contains the low-frequency radio continuum is 0.096 erg s^{-1} cm^{-2} sr^{-1}. Then, if we correct for beam dilution, we have $\epsilon_{\rm pe} = (6.9 \pm 0.3) \times 10^{-3}$. For G_0 we use a value of 550, the mean of the values found by Abel et al. (2016) for components A and B of the Veil based on the properties of the Trapezium stars (Ferland et al., 2012) and their relative distances, 2 pc and 4.2 pc. This G_0 value should be valid for most of the gas in the Veil, as this structure is a spherical shell (Pabst et al., 2019). Using this value of G_0 and the derived gas properties we have that $\gamma = (3\text{–}6) \times 10^3$ K$^{1/2}$ cm^3. A comparisson between the heating efficiency as a function of γ measured towards different regions is presented in Figure 4.15. The overall picture is that the theoretical predictions of the heating efficiency overpredict the observed values. This discrepancy might reflect that the heating efficiency is lower, that the PAH abundance is lower, or a bias in the observed values due to the use of TIR as an estimate of the FUV radiation field (e.g., Hollenbach & Tielens, 1999; Okada et al., 2013; Kapala et al., 2017). The present data does not allow us to determine the cause of this discrepancy.

4.4.2. The background molecular cloud; Orion A

Here we use the C30α, C65α, C91α and 158 μm-[CII] lines to study the gas properties in the dense PDR in the envelope of Orion A. Emission from these lines at a velocity of ≈ 9 km s^{-1} is associated with the background molecular cloud.

CRRLs

The C30α cube overlaps with the observations of C65α and C91α of Wyrowski et al. (1997) (see Figure 4.9). Here we use the ratios between the intensities of these lines to constrain the gas properties. Since the lines trace the PDR at the interface between

the HII region and the background molecular cloud, the background continuum will be zero (e.g., Natta et al., 1994).

We focus on a 40″ region to the North of Orion-KL, at $(\alpha, \delta)_{\rm J2000} = (05^{\rm h}35^{\rm m}16.7828^{\rm s}, -05°22^{\rm m}02.7225^{\rm s})$. There, the C30$\alpha$, C65$\alpha$ and C91α cubes overlap, and Wyrowski et al. (1997) provides measurements of the C65α and C91α intensity. We estimate the error on the intensity of the C91α line from the profile shown in Figure 2 of Wyrowski et al. (1997). The root-mean-squared (rms) of the spectrum is close to 0.05 K, and given that the line profile is narrow and shows little contribution from the HeRRL we estimate an error of 0.1 km s^{-1} on the line width. These values imply a 1σ error of 0.2 K km s^{-1} for a 2.9 K km s^{-1} intensity. For the C65α line we adopt an error of 20% of the observed line intensity. The C30α line intensity over this region is 71 ± 13 mK km s^{-1}.

In the studied region, the C30α/C65α line ratio is 0.12 ± 0.02 and the C30α/C91α line ratio 0.038 ± 0.005. The constraints imposed on the gas temperature and density by these ratios are shown in Figure 4.16. The temperature is constrained to values larger than 150 K, but they do not constrain the electron density. The C65α/C91α ratio is 0.30 ± 0.06, and, given the adopted errors, it does not constrain the gas properties.

To fully exploit the power of CRRLs, to provide independent constraints on the gas properties, higher signal-to-noise detections of the observed lines are required. For example, if the error on the intensity of the C65α line was 10% of the observed value and that of the C30α a factor of two lower, then it would be possible to determine the gas temperature and density using only CRRLs. Under this assumption, the gas temperature would be constrained to within 10 K and the electron density within 45 cm^{-3}. Alternatively, we could use CRRLs at lower frequencies. At lower frequencies the frequency separation between adjacent C$n\alpha$ lines decreases, hence it becomes easier to achieve higher signal-to-noise ratios by stacking. Higher resolution observations are also important as with them it is possible to observe the layered structure on higher density PDRs.

CRRLs AND FIR [CII] LINE

When the 158 μm-[CII] line is optically thick its ratio relative to a CRRL depends on the C^+ column density, thus we need an independent measure of the column density to compare them. To determine the C^+ column density we use the [^{13}CII] $F = 2$–1 line. This line has a velocity difference of 11.2 km s^{-1} with respect to the 158 μm-[CII] line. To estimate the column density from 158 μm-[CII] and its isotopologue we follow the analysis of Goicoechea et al. (2015). We adopt the corrected line strengths of Ossenkopf et al. (2013) for the three [^{13}CII] hyperfine structure lines, a [C/^{13}C] abundance ratio of 67 (Langer & Penzias, 1990) and compute the excitation temperature assuming that the 158 μm-[CII] line is optically thick.

For the region studied previously in CRRLs ($(\alpha, \delta)_{\rm J2000} = (05^{\rm h}35^{\rm m}16.7828^{\rm s}, -05°22^{\rm m}02.7225^{\rm s})$), we have peak line temperatures of 177 K and 4 K for [CII] and [^{13}CII] $F = 2$–1, respectively. This translates to an optical depth of 2.3. For a background temperature of 35 K, the excitation temperature of the 158 μm-[CII] line is 230 K. Using the observed full width at half maximum of

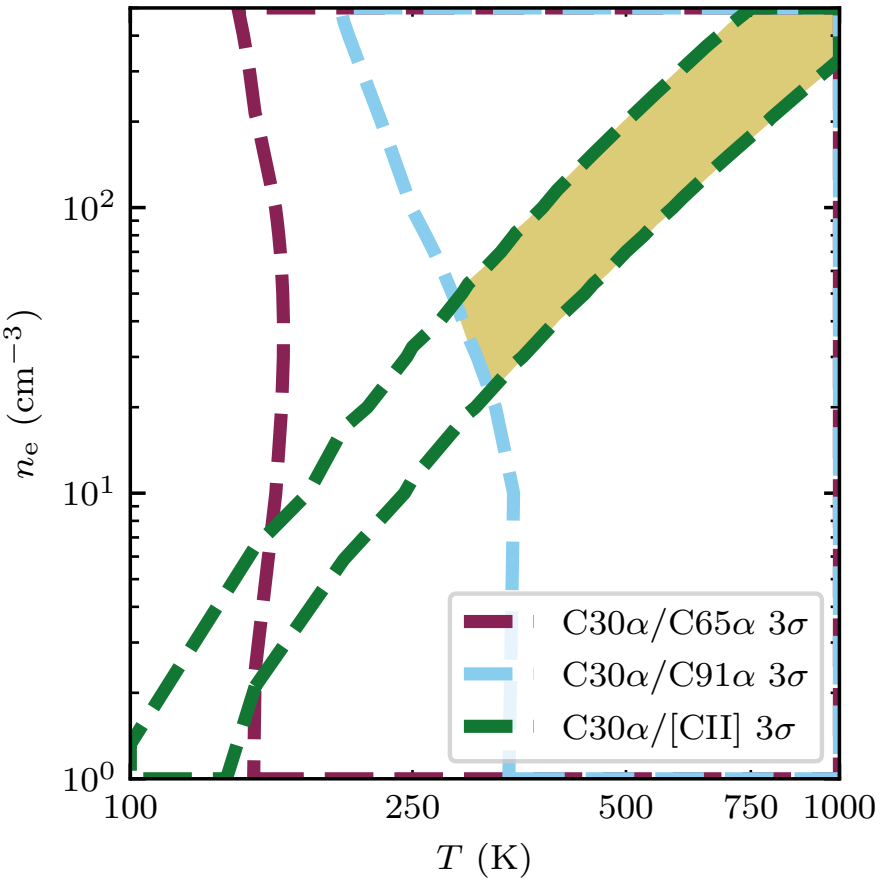

Figure 4.16.: Constraints on the gas temperature and density imposed by the ratios between the C30α, C65α and C91α lines. When the *blue* and *yellow hatched regions* overlap they produce a *gray shaded region*. The *red hatched region* shows the region of parameter space where the column density of C30α is less or equal than that of [CII] (7.3×10^{18} cm^{-2}).

≈ 4 km s^{-1} this corresponds to a [CII] column density of 9.7×10^{18} cm^{-2}.

With an estimate of the [CII] column density we can use the ratio between the 158 μm-[CII] line and the CRRLs to further constrain the gas properties. For the C30α/[CII] ratio we have a value of $(1.4 \pm 0.2) \times 10^{-4}$. The C30$\alpha$/[CII] ratio puts a constraint on the gas properties of the form $n_e \propto T^3$, this is shown in Figure 4.16 with green dashed lines. Using the lower frequency CRRLs or the [^{13}CII] $F = 2$–1 line results in a similar constraint.

COMBINED CONSTRAINTS

As seen in Figure 4.16 the constraints imposed by the CRRL and 158 μm-[CII] line ratios overlap for temperatures larger than 300 K and an electron density larger than 25 cm^{-3}. If we assume that all the free electrons come from the ionization of carbon, and a carbon abundance with respect to hydrogen of 1.4×10^{-4}, this sets a lower limit to the gas thermal pressure of 5×10^7 K cm^{-3}. This is similar to the thermal pressure for the atomic gas layers found by Goicoechea et al. (2016) towards the Orion Bar.

PDR MODELS

Motivated by the resemblance between the observed gas distribution (Figure 4.11) and the structure seen in a PDR (Figure 4.12), we compare the observed line intensities to the predictions of PDR models. In a PDR close to face-on the C^+ column density is determined by the radiation field and gas density, hence we do not need an independent estimate of the column density. The PDR models also take into account the gas density and temperature structure.

We focus on the region previously studied in Sect. 4.4.2, towards the North of Orion-KL. To compare against the PDR model predictions, we need to take into account the geometry, because if the PDRs are not observed face-on, then the column density along the line of sight is not determined by the radiation field and density. For example, the Orion Bar has a length of 0.28 ± 0.06 pc along the line of sight (Salgado et al., 2016), while in the perpendicular direction its extent is ≈ 0.02 pc (e.g., Wyrowski et al., 1997; Goicoechea et al., 2016). To determine the lenght of the PDR along the line of sight we use the intensity of the C30α line, then we use this to scale the rest of the line intensities. Once we have scaled the line intensities, we determine which modeles are able to reproduce the observed line intensities and ratios.

First we compare against constant density PDR models. These models require densities larger than 5×10^5 cm^{-3} to explain the line intensities and ratios. This is equivalent to an electron density larger than 70 cm^{-3}, which is consistent with the values found towards this region (Figure 4.16), however, these models also require radiation fields $G_0 \geq 5 \times 10^5$. In this region, which is a factor of 2.5 closer to the Trapezium than the Orion Bar, the incident radiation field should be a factor of six larger than in the Bar, or $G_0 \approx 1.4 \times 10^5$. This shows that constant density PDR models are not able to explain the observed line properties given reasonable input parameters.

Next we compare against stationary isobaric PDR models. In this case the models require thermal pressures larger than 5×10^7 K cm^{-3}, and a radiation field $G_0 =$

$(0.4–1) \times 10^5$ to explain the observations. The isobaric model which best reproduces the observations has $G_0 = 1 \times 10^5$ and $P_{\rm th} = 5 \times 10^7$ K cm^{-3}. In this case the radiation field and gas thermal pressure are consistent with independent estimates. Stationary isobaric PDR models also provide better results when explaining observations of excited molecular tracers (e.g., Joblin et al., 2018).

Given the best fit isobaric PDR model we assess whether the constraints derived assuming an homogeneous gas slab are reasonable. In this model, the CRRL emission originates mostly from a layer with a gas temperature of 200 K, and a similar excitation temperature for the 158 μm-[CII] line. The gas temperature is 30% lower than that derived under the homogeneous slab model (300 K). The electron density in the isobaric PDR model is 75 cm^{-3} in the layer where the CRRL emission peaks, i.e., roughly 50% larger than in the homogeneous slab model. Therefore, the lower limits from the homogeneous model predict a gas thermal pressure which is 25% to 50% lower than that predicted by a stationary isobaric PDR model. This difference is not significant considering that the isobaric PDR models used only sparsely sample the $P_{\rm th}$–G_0 space.

4.5. SUMMARY

We have presented CRRL observations towards Orion A in the frequency range 230–0.15 GHz, including the first detections of the lines in absorption, with the aim of comparing them with the 158 μm-[CII] line. The CRRLs towards Orion A show the presence of multiple velocity components, similar to what is observed through other tracers of neutral gas (e.g., the 21 cm-HI line or the 158 μm-[CII] line). We identify CRRL emission associated with the Veil and the background molecular cloud.

We find that the Veil is preferentially traced using lines at frequencies $\lesssim$ 2 GHz ($n >$ 150 for C$n\alpha$ lines), similar to the findings of previous studies. This because M42 becomes opaque at these frequencies and its continuum produces significant amplification of the foreground lines. Using C280α/C351α and C350α/[CII] line ratios we are able to constrain the properties of the Veil on 36′ scales (4.3 pc). We find a gas temperature of 30 K$\leq T_{\rm e} \leq$ 45 K and an electron density of 0.65 cm^{-3} $\leq n_{\rm e} \leq$ 0.95 cm^{-3}, where the quoted ranges consider 3σ errors on the line ratios. From these physical conditions we constrain the gas cooling rate through the 158 μm-[CII] line and the efficiency of photoelectric heating. We find a lower limit on the gas cooling rate of $(4 \pm 0.2) \times 10^{-26}$ erg s^{-1} (H-atom)$^{-1}$, and a photoelectric heating efficiency of $\epsilon_{\rm pe} = (6.9 \pm 0.3) \times 10^{-3}$ for $\gamma = (3–6) \times 10^3$ K$^{1/2}$ cm^3. Based on these, the Veil is somewhere in between a diffuse cloud and a dense PDR.

The dense PDR, at the interface between the HII region and Orion A, is traced using CRRLs at frequencies $\gtrsim$ 2 GHz. By comparing the spatial distribution of the C30α and C65α lines to that of the 158 μm-[CII] and ^{12}CO(2–1) lines we find a clump to the South of the Trapezium where we can observe the layered PDR structure. The relative location of the C65α line with respect to the 158 μm-[CII] line indicates that in a dense PDR the radio lines trace colder gas than the FIR line.

Motivated by the observed PDR structure we compared the intensity of the CRRLs and the 158 μm-[CII] line to the predictions of PDR models. We find that stationary

isobaric PDR models are able to reproduce the observations. They imply a thermal gas pressure larger than 5×10^7 K cm^{-3}, and likely a factor of two larger.

This work shows that the combined use of CRRLs and the 158 μm-[CII] line is a powerful tool to study the ISM. They provide an alternative method to determine the gas physical conditions (temperature and electron density). The physical conditions derived this way can be combined with the information provided by the 158 μm-[CII] line to determine the gas heating and cooling.

With new and upgraded telescopes (e.g., SKA, ngVLA, uGMRT, LOFAR2.0), CRRLs will allow us to explore the ISM in our Galaxy and others (Morabito et al., 2014; Emig et al., 2018). In distant galaxies, where spectral tracers of the ISM may be harder to come by, the use of CRRLs and the 158 μm-[CII] line can provide important constraints on the properties of the ISM across cosmic time. Our work shows how these constraints can be obtained by taking into consideration the structure of a PDR.

4.A. Non-linear gain correction

Under ideal circumstances, the relation between the raw counts measured by a radio telescope, P, the source temperature, $T_{\rm sou}$, and the system temperature, $T_{\rm sys}$, will be of the form

$$P^{[\rm CAL]} = G(T_{\rm sou} + T_{\rm sys}^{[\rm CAL]}) + C, \tag{4.3}$$

where, G is the conversion factor between temperature and telescope units (counts) and C a constant offset between the two scales. Here we have adopted the nomenclature of Winkel et al. (2012), in which $T_{\rm sys}^{[\rm CAL]}$ denotes the system temperature, considering the possible contribution from a calibration signal, $T_{\rm cal}$, and $T_{\rm sou}$ is the temperature of the astronomical source of interest which includes both continuum and line, $T_{\rm cont}$ and T_ℓ respectively. In order to determine the conversion between counts and temperature procedures such as those outlined in Winkel et al. (2012) are used.

Given the nature of the signal path on a radio telescope, it is possible that relation 4.3 will break down. This could be due to the amplifiers being driven out of their linear response regime (e.g., if a bright source is observed). This has the effect of changing Equation 4.3 to

$$P^{[\rm CAL]} = G(T_{\rm sou} + T_{\rm sys}^{[\rm CAL]}) + G_{\rm nl}(T_{\rm sou} + T_{\rm sys}^{[\rm CAL]})^2 + C. \tag{4.4}$$

Here $G_{\rm nl}$ represents the non-linear contribution of the amplifier gain.

If Equation 4.3 is no longer valid, and we can represent the conversion between raw counts and temperature using Equation 4.4, then it is possible to calibrate the raw counts if we make some assumptions about $T_{\rm sou}$. To estimate $G_{\rm nl}$ we can use a reference position, $P_{\rm ref}$, ideally devoid of any astronomical signal and a model of $T_{\rm sou}$. Then,

$$G_{\rm nl} = \frac{P_{\rm sou} - P_{\rm ref} - GT_{\rm sou}}{2T_{\rm sys} + T_{\rm sou}^2} \tag{4.5}$$

If we are interested in recovering the temperature of a spectral line, then we can work with the continuum subtracted spectra $P_\ell^{[\rm CAL]} = P^{[\rm CAL]} - P_{\rm cont}^{[\rm CAL]}$. The continuum,

$P_{\rm cont}^{\rm [CAL]}$, can be estimated from line free channels. The line brightness temperature, T_ℓ, is then obtained from

$$T_\ell = P_\ell^{\rm [CAL]} \left[G + G_{\rm nl}(T_\ell + 2T_{\rm cont} + 2T_{\rm sys}^{\rm [CAL]}) \right]^{-1} \tag{4.6}$$

4.B. GAUSSIAN FITS TO RRL SPECTRA

A possible decomposition of the spectra presented in Figure 4.4 into Gaussian components is tabulated in Table 4.4.

Table 4.4.: Best fit Gaussian parameters for RRLs observed towards M42

Region	$v_{\rm lsr}$ (km s^{-1})	$T_{\rm mb}$ (K)	Δv (km s^{-1})
H137α	-6.92 ± 0.05	3.95 ± 0.01	32.9 ± 0.1
H145α	-7.57 ± 0.08	2.98 ± 0.01	34.7 ± 0.2
H151α	-8.5 ± 0.1	4.40 ± 0.03	34.8 ± 0.3
H155α	-8.2 ± 0.1	2.21 ± 0.01	36.0 ± 0.2
H156α	-7.8 ± 0.1	2.85 ± 0.02	36.1 ± 0.3
H164α	-7.9 ± 0.1	2.26 ± 0.02	36.0 ± 0.4
H174α	-8.3 ± 0.2	1.56 ± 0.02	37.0 ± 0.5
H280α	0 ± 2	0.010 ± 0.002	25 ± 5
He137α	-5 ± 1	0.42 ± 0.02	31 ± 2
He145α	-11 ± 2	0.25 ± 0.04	23 ± 3
He151α	-6 ± 1	0.40 ± 0.05	15 ± 4
He155α	-10 ± 3	0.17 ± 0.02	24 ± 5
He156α	-7 ± 5	0.15 ± 0.04	16 ± 10
He164α	-7 ± 3	0.20 ± 0.03	17 ± 6
He174α	-14 ± 2	0.19 ± 0.03	32 ± 4
C137α	7.3 ± 0.6	0.26 ± 0.05	12 ± 2
C145α	6.3 ± 0.7	0.24 ± 0.06	9 ± 2
C151α	5.2 ± 0.8	0.67 ± 0.07	10 ± 1
C155α	4.4 ± 0.4	0.31 ± 0.06	9 ± 1
C156α	6 ± 1	0.5 ± 0.1	10 ± 1
C164α	4.9 ± 0.7	0.54 ± 0.07	10 ± 1
C174α	5.1 ± 0.3	0.47 ± 0.05	6 ± 1
C280α	0.7 ± 0.6	-0.023 ± 0.003	11 ± 1

BIBLIOGRAPHY

Abel, N. P., Brogan, C. L., Ferland, G. J., et al. 2004, ApJ, 609, 247

Abel, N. P., Ferland, G. J., O'Dell, C. R., Shaw, G., & Troland, T. H. 2006, ApJ, 644, 344

Abel, N. P., Ferland, G. J., O'Dell, C. R., & Troland, T. H. 2016, ApJ, 819, 136

Ahmad, I. A. 1976, ApJ, 209, 462

Andrews, H., Peeters, E., Tielens, A. G. G. M., & Okada, Y. 2018, A&A, 619, A170

Baars, J. W. M., Genzel, R., Pauliny-Toth, I. I. K., & Witzel, A. 1977, A&A, 61, 99

Bakes, E. L. O., & Tielens, A. G. G. M. 1994, ApJ, 427, 822

Balick, B., Gammon, R. H., & Doherty, L. H. 1974a, ApJ, 188, 45

Balick, B., Gammon, R. H., & Hjellming, R. M. 1974b, PASP, 86, 616

Bally, J., Ginsburg, A., Arce, H., et al. 2017, ApJ, 837, 60

Bally, J., Langer, W. D., Stark, A. A., & Wilson, R. W. 1987, ApJL, 312, L45

Bernard-Salas, J., Habart, E., Arab, H., et al. 2012, A&A, 538, A37

Berné, O., Marcelino, N., & Cernicharo, J. 2014, ApJ, 795, 13

Boughton, W. L. 1978, ApJ, 222, 517

Briggs, D. S. 1995, in Bulletin of the American Astronomical Society, Vol. 27, American Astronomical Society Meeting Abstracts, 1444

Bussa, S., & VEGAS Development Team. 2012, in American Astronomical Society Meeting Abstracts, Vol. 219, American Astronomical Society Meeting Abstracts #219, 446.10

Cardelli, J. A., Clayton, G. C., & Mathis, J. S. 1989, ApJ, 345, 245

Cartledge, S. I. B., Meyer, D. M., Lauroesch, J. T., & Sofia, U. J. 2001, ApJ, 562, 394

Chaisson, E. J. 1974, ApJ, 191, 411

Chaisson, E. J., & Lada, C. J. 1974, ApJ, 189, 227

Dalgarno, A., & McCray, R. A. 1972, ARA&A, 10, 375

Ducati, J. R., Ribeiro, D., & Rembold, S. B. 2003, ApJ, 588, 344

Dupree, A. K. 1974, ApJ, 187, 25

Emig, K. L., Salas, P., de Gasperin, F., et al. 2018, arXiv e-prints
Ferland, G. J., Henney, W. J., O'Dell, C. R., et al. 2012, ApJ, 757, 79
Field, G. B., Goldsmith, D. W., & Habing, H. J. 1969, ApJL, 155, L149
Fitzpatrick, E. L., & Massa, D. 1988, ApJ, 328, 734
Goicoechea, J. R., Teyssier, D., Etxaluze, M., et al. 2015, ApJ, 812, 75
Goicoechea, J. R., Pety, J., Cuadrado, S., et al. 2016, Nature, 537, 207
Goldsmith, P. F., Langer, W. D., Pineda, J. L., & Velusamy, T. 2012, ApJS, 203, 13
Goldsmith, P. F., Yıldız, U. A., Langer, W. D., & Pineda, J. L. 2015, ApJ, 814, 133
Gordon, M. A., & Sorochenko, R. L., eds. 2009, Astrophysics and Space Science Library, Vol. 282, Radio Recombination Lines
Goudis, C. 1975, Ap&SS, 36, 105
Gry, C., Lequeux, J., & Boulanger, F. 1992, A&A, 266, 457
Heiles, C. 1994, ApJ, 436, 720
Heyminck, S., Graf, U. U., Güsten, R., et al. 2012, A&A, 542, L1
HI4PI Collaboration, Ben Bekhti, N., Flöer, L., et al. 2016, A&A, 594, A116
Hoffleit, D., & Warren, Jr., W. H. 1995, VizieR Online Data Catalog, 5050
Hollenbach, D. J., & Tielens, A. G. G. M. 1999, Reviews of Modern Physics, 71, 173
Jaffe, D. T., & Pankonin, V. 1978, ApJ, 226, 869
Jenkins, E. B., & Tripp, T. M. 2001, ApJS, 137, 297
Joblin, C., Bron, E., Pinto, C., et al. 2018, A&A, 615, A129
Kapala, M. J., Groves, B., Sandstrom, K., et al. 2017, ApJ, 842, 128
Klessen, R. S., & Glover, S. C. O. 2016, Saas-Fee Advanced Course, 43, 85
Langer, W. D., & Penzias, A. A. 1990, ApJ, 357, 477
Large, M. I., Mills, B. Y., Little, A. G., Crawford, D. F., & Sutton, J. M. 1981, MNRAS, 194, 693
Le Petit, F., Nehmé, C., Le Bourlot, J., & Roueff, E. 2006, ApJS, 164, 506
Lockman, F. J., & Brown, R. L. 1975, ApJ, 201, 134
Lombardi, M., Bouy, H., Alves, J., & Lada, C. J. 2014, A&A, 566, A45
Maddalena, R. J., Morris, M., Moscowitz, J., & Thaddeus, P. 1986, ApJ, 303, 375
Mangum, J. G., Emerson, D. T., & Greisen, E. W. 2007, A&A, 474, 679
Mathis, J. S., Mezger, P. G., & Panagia, N. 1983, A&A, 128, 212
Menten, K. M., Reid, M. J., Forbrich, J., & Brunthaler, A. 2007, A&A, 474, 515
Menzel, D. H. 1968, Nature, 218, 756
Morabito, L. K., Oonk, J. B. R., Salgado, F., et al. 2014, ApJL, 795, L33
Napier, P. J., Thompson, A. R., & Ekers, R. D. 1983, IEEE Proceedings, 71, 1295
Natta, A., Walmsley, C. M., & Tielens, A. G. G. M. 1994, ApJ, 428, 209
Noordam, J. E., & Smirnov, O. M. 2010, A&A, 524, A61
O'Dell, C. R. 2001, ARA&A, 39, 99
O'Dell, C. R., & Harris, J. A. 2010, AJ, 140, 985
O'Dell, C. R., Henney, W. J., Abel, N. P., Ferland, G. J., & Arthur, S. J. 2009, AJ, 137, 367
O'Dell, C. R., & Yusef-Zadeh, F. 2000, AJ, 120, 382
Okada, Y., Pilleri, P., Berné, O., et al. 2013, A&A, 553, A2
Oonk, J. B. R., van Weeren, R. J., Salas, P., et al. 2017, MNRAS, 465, 1066
Ossenkopf, V., Röllig, M., Neufeld, D. A., et al. 2013, A&A, 550, A57

Pabst, C., Higgins, R., Goicoechea, J. R., et al. 2019, Nature
Pabst, C. H. M., Goicoechea, J. R., Teyssier, D., et al. 2017, A&A, 606, A29
Payne, H. E., Anantharamaiah, K. R., & Erickson, W. C. 1989, ApJ, 341, 890
—. 1994, ApJ, 430, 690
Pedlar, A., & Hart, L. 1974, MNRAS, 168, 577
Perley, R. A., & Butler, B. J. 2013, ApJS, 204, 19
Pickering, W. H. 1917, Harvard College Observatory Circular, 205, 1
Pineda, J. L., Langer, W. D., Velusamy, T., & Goldsmith, P. F. 2013, A&A, 554, A103
Planck Collaboration, Adam, R., Ade, P. A. R., et al. 2016a, A&A, 594, A1
Planck Collaboration, Aghanim, N., Ashdown, M., et al. 2016b, A&A, 596, A109
Pottasch, S. R., Wesselius, P. R., & van Duinen, R. J. 1979, A&A, 74, L15
Prozesky, A., & Smits, D. P. 2018, MNRAS, 478, 2766
Risacher, C., Güsten, R., Stutzki, J., et al. 2016, A&A, 595, A34
Roshi, D. A., & Kantharia, N. G. 2011, MNRAS, 414, 519
Salas, P., Oonk, J. B. R., van Weeren, R. J., et al. 2018, MNRAS, 475, 2496
—. 2017, MNRAS, 467, 2274
Salgado, F., Berné, O., Adams, J. D., et al. 2016, ApJ, 830, 118
Salgado, F., Morabito, L. K., Oonk, J. B. R., et al. 2017a, ApJ, 837, 141
—. 2017b, ApJ, 837, 142
Sandell, G., Mookerjea, B., Güsten, R., et al. 2015, A&A, 578, A41
Scaife, A. M. M., & Heald, G. H. 2012, MNRAS, 423, L30
Sharpless, S. 1952, ApJ, 116, 251
Shaver, P. A. 1975, Pramana, 5, 1
Shuping, R. Y., & Snow, T. P. 1997, ApJ, 480, 272
Simon, R., Stutzki, J., Sternberg, A., & Winnewisser, G. 1997, A&A, 327, L9
Smirnov, G. T., Sorochenko, R. L., & Walmsley, C. M. 1995, A&A, 300, 923
Sofia, U. J., Lauroesch, J. T., Meyer, D. M., & Cartledge, S. I. B. 2004, ApJ, 605, 272
Subrahmanyan, R., Goss, W. M., & Malin, D. F. 2001, AJ, 121, 399
Tielens, A. G. G. M. 2010, The Physics and Chemistry of the Interstellar Medium
Tielens, A. G. G. M., & Hollenbach, D. 1985, ApJ, 291, 747
Troland, T. H., Goss, W. M., Brogan, C. L., Crutcher, R. M., & Roberts, D. A. 2016, ApJ, 825, 2
van der Werf, P. P., & Goss, W. M. 1989, A&A, 224, 209
van der Werf, P. P., Goss, W. M., & O'Dell, C. R. 2013, ApJ, 762, 101
van Dishoeck, E. F., & Black, J. H. 1986, ApJS, 62, 109
van Haarlem, M. P., Wise, M. W., Gunst, A. W., et al. 2013, A&A, 556, A2
Visser, R., van Dishoeck, E. F., & Black, J. H. 2009, A&A, 503, 323
Walmsley, C. M., & Watson, W. D. 1982, ApJ, 260, 317
Watson, W. D., Western, L. R., & Christensen, R. B. 1980, ApJ, 240, 956
Weingartner, J. C., & Draine, B. T. 2001, ApJS, 134, 263
Wilson, T. L., Bania, T. M., & Balser, D. S. 2015, ApJ, 812, 45
Winkel, B., Kraus, A., & Bach, U. 2012, A&A, 540, A140
Wolfire, M. G., Hollenbach, D., & McKee, C. F. 2010, ApJ, 716, 1191
Wolfire, M. G., Hollenbach, D., McKee, C. F., Tielens, A. G. G. M., & Bakes, E. L. O. 1995, ApJ, 443, 152

Wolfire, M. G., McKee, C. F., Hollenbach, D., & Tielens, A. G. G. M. 2003, ApJ, 587, 278
Wyrowski, F., Schilke, P., Hofner, P., & Walmsley, C. M. 1997, ApJL, 487, L171
Wyrowski, F., Walmsley, C. M., Goss, W. M., & Tielens, A. G. G. M. 2000, ApJ, 543, 245
Young, E. T., Becklin, E. E., Marcum, P. M., et al. 2012, ApJL, 749, L17
Young Owl, R. C., Meixner, M. M., Wolfire, M., Tielens, A. G. G. M., & Tauber, J. 2000, ApJ, 540, 886
Zari, E., Brown, A. G. A., de Bruijne, J., Manara, C. F., & de Zeeuw, P. T. 2017, A&A, 608, A148
Zuckerman, B. 1973, ApJ, 183, 863

V

TIED-ARRAY HOLOGRAPHY WITH LOFAR

5.1. INTRODUCTION

A radio telescope works by combining the signals received by the elements that constitute its aperture (a reflecting surface in the case of a dish, or an array of antennas in the case of a phased array). In order to maximize the sensitivity of the telescope towards a particular direction, the signals arriving from that direction must be combined in phase, i.e., the time difference between the signals received by different aperture elements must be zero. In the case of a dish this is accomplished by shaping the reflecting surface in such a way that all the signals arrive at the receiver at the same time. And in a phased array, by introducing instrumental time delays between its elements to compensate for the time of arrival of the signal at the antennas (e.g., Thompson et al., 2017).

Deviations from a perfect phase alignment when the signals are combined lead to a loss in the efficiency of the telescope (e.g., Ruze, 1952, 1966; D'Addario, 2008). These phase misalignments can be caused by the telescope itself, or they can be produced in the path between the source of the signals and the telescope. An example of the former are phase differences caused by misaligned panels in a reflector (e.g., Baars et al., 2007), or uncorrected cable delays in a phased array.

Different methods to reduce phase misalignments between the elements of an aperture have been developed. These include photogrammetric measurements (e.g., Wiktowy et al., 2003), direct measurement of the aperture distribution (e.g., Chen et al., 1998; Naruse et al., 2009), holographic measurements (e.g., Napier & Bates, 1973; Bennett et al., 1976; Scott & Ryle, 1977; Baars et al., 2007; Hunter et al., 2011) and calibration using astronomical sources (e.g., Fomalont & Perley, 1999; Intema et al., 2009; Thompson et al., 2017; Rioja et al., 2018). This chapter focuses on the holographic measurement of the aperture illumination of a large phased array telescope.

Since the work of Scott & Ryle (1977), holographic measurements have been used to calibrate the dishes of the Very Large Array (VLA, e.g., Kesteven, 1993; Broilo, 1993),

the Atacama Large Millimeter Array (ALMA, e.g., Baars et al., 2007) and the Green Bank Telescope (GBT, e.g., Hunter et al., 2011), to study the primary beam response of the Westerbork radio telescope (WSRT, e.g., Popping & Braun, 2008) and the Allen telescope array dishes (ATA, e.g., Harp et al., 2011), and to characterize the beam and aperture of the Low Frequency Array (LOFAR) stations (Brentjens et al. in prep.). All these measurements have been restricted to the study of apertures $\lesssim 100$ m in diameter.

In the regime of low-frequency and large apertures holographic measurements are particularly challenging. At low-frequencies the ionosphere will introduce additional time delays depending on its total electron content (TEC, e.g., Intema et al., 2009). To accurately measure the intrinsic phase errors between the elements of the phased array without ionospheric distortion, the phased array must be smaller than the diffractive scale of the ionosphere. Night time observations of the ionosphere at 150 MHz show that its diffractive scale is between 30 and 3 km (Mevius et al., 2016).

LOFAR operates at frequencies between 10 MHz and 240 MHz (van Haarlem et al., 2013). This frequency range is covered by two different types of antennas: low band antennas (LBA, 10–90 MHz) and high band antennas (HBA, 120–240 MHz). The HBA antennas are combined in a 4×4 tile with an analog beamformer. The antennas and tiles are grouped into stations, and stations are further combined to form an array. For the core stations of LOFAR, the LBA stations consist of 96 antennas, while the HBA stations have 48 tiles split into two fields. Of the 96 antennas in a core LBA station the available electronics permits only 48 to be actively beamformed. There are 24 stations in the core of LOFAR. The core stations are connected via fiber to a central clock, thus their signals can be added coherently to form a telescope with a maximum baseline of 3.5 km. The stations in the innermost 350 m are known as the *Superterp*.

Each LOFAR LBA dipole observes the entire sky, while the HBA tiles have a field of view (FoV) of 30° at 150 MHz. Since the signals from the antennas and tiles are combined digitally, the stations can point towards multiple directions within their FoV simultaneously (e.g., Barton, 1980; Steyskal, 1987). When the signals from different stations are added together coherently, a phased array (known as a tied-array) is formed. This enables LOFAR to form multiple tied-array beams (TABs) that point towards different directions.

5.2. Method

We want to determine the time delays for the array formed by the stations in LOFAR's core. We will refer to the tied-array formed by these stations as the array under test (AUT). In order to determine the time delays, we start from a map of its complex-valued beam $\boldsymbol{B}$.

The basic procedure used to measure $\boldsymbol{B}$ is the same as that employed by Scott & Ryle (1977), with a difference in its implementation. In their work, a raster scan was used to map the region around the bright unresolved source. Here, we take advantage of LOFAR's multi-beaming capability to map the region around the bright unresolved source. Using multiple TABs the whole region is mapped simultaneously, and there is always a TAB pointing towards the bright unresolved source. Besides speeding up the

process by a factor equal to the number of simultaneous beams, this allows continuous calibration of the AUT as well as the reference stations by always having a TAB at the central calibrator source.

At the frequencies at which LOFAR operates, the Milky Way is bright and it will distort the observed map of $\boldsymbol{B}$. To reduce the contribution from the Milky Way to the measurements, we use a reference station which produces a baseline that resolves out large scale Galactic structure (e.g., Colegate et al., 2015). The contribution from smaller bright sources (e.g., Cassiopeia A or Cygnus A) cannot be completely resolved out, and is reduced by limiting the field of view (FoV) through time and frequency smearing (e.g., Bridle & Schwab, 1999). Moreover, the AUT and the reference station will see different portions of the ionosphere, which will introduce an additional time delay between them. The effects of the different ionosphere seen by the AUT and the reference station are calibrated using the bright point source.

The details behind the calibration method will be presented in Brentjens et al. in prep. Here we summarize the rationale behind the calibration because it is an important aspect of this work. Following the Measurement Equation formalism (Hamaker et al., 1996), we have that the visibility generated by cross-correlating the signals from the AUT and the reference station is

$$V_b = J_{\mathrm{AUT},b} E J^{\dagger}_{\mathrm{ref}}, \tag{5.1}$$

where E represents the coherency matrix formed by the pure sky visibilities, and $J_{\mathrm{AUT},b}$ and J_{ref} are the Jones matrices (Jones, 1941) of the AUT and the reference station respectively. The subscript b represents the TABs formed with the AUT. The $\dagger$ symbol denotes taking the conjugate transpose of the corresponding matrix. The calibration consists of finding the inverse of the visibility of the central beamlet, V_c^{-1}, and right multiplying all the visibilities with it. After doing this, for the central beam $\tilde{V}_{b=c} = V_c V_c^{-1} = 1$, where 1 represents the identity matrix. For the remaining directions $\tilde{V}_i = V_i V_c^{-1} = J_{\mathrm{AUT},i} J^{-1}_{\mathrm{AUT},c}$. That is, the calibrated visibility for the i-eth beam only depends on the Jones matrix of the AUT, and not on the sky brightness distribution. These calibrated visibilities map $\boldsymbol{B}$.

From the observed map of $\boldsymbol{B}$ we determine the amplitude and phase over the aperture of the AUT, A. In the far-field approximation, and for a coplanar array, they are related by (e.g., D'Addario, 1982; Baars et al., 2007; Thompson et al., 2017),

$$B(l,m) \propto \iint A(p,q) e^{2\pi i (pl+qm)\frac{\nu}{c}} dp dq, \tag{5.2}$$

where i denotes the imaginary unit, c is the speed of light, ν is frequency, p and q are orthogonal coordinates in the aperture plane, and l and m are the direction cosines measured with respect to p and q. For LOFAR, the (p,q) coordinate system has its origin at the center of the aperture and it lies in the plane of the station, or in this case, the plane of the superterp stations. The phase of $A(p,q)$ is set by e.g. uncalibrated errors in the clock distribution, cable length, antenna position, and ionospheric phase variations across the aperture.

5.3. OBSERVATIONS

5.3.1. LOFAR HOLOGRAPHY OBSERVATIONS

Table 5.1 summarizes the observations. Each TAB recorded complex voltages in two orthogonal polarizations (X and Y) at 5.12 μs time resolution in ten 195.3125 kHz wide spectral windows. The data were subsequently ingested into the LOFAR long term archive. The calibrator sources are selected to be small compared to the size of the TAB, as well as the fringe spacing of the baselines between the AUT and the reference stations. The former prevents systematic distortions in the measured beam, while the latter guarantees high signal-to-noise ratios (SNR) on the baselines towards the reference stations.

The complex valued beam maps were measured on a regular hexagonal grid, 1.32 and 0.37 deg across for LBA and HBA, respectively. The map size is limited by the number of TABs, spectral windows and stations that the beamformer, COBALT (Broekema et al., 2018), can process simultaneously. Per Fourier relation Equation 5.2 this implies a spatial resolution in the aperture plane of 270 m (HBA at 174 MHz) and 170 m (LBA at 68 MHz), comparable to the diameter of the *Superterp* (350 m). To avoid aliasing in the aperture domain, the separation between TABs was set at λ/D at the highest frequency, and kept constant for lower frequencies.

The required integration time is set by the error on the phase in the aperture plane, $\Delta\phi$, (D'Addario, 1982)

$$\Delta\phi \approx \frac{\pi D}{4\sqrt{2}d\,\mathrm{SNR}_{\mathrm{bm}}}, \tag{5.3}$$

where D is the telescope diameter, d the spatial resolution on the aperture plane and $\mathrm{SNR}_{\mathrm{bm}}$ the signal-to-noise ratio in the complex-valued beam map, i.e., the ratio between the peak response of the array and the root-mean-squared (rms) over the complex-valued beam map, $\mathrm{SNR}_{\mathrm{bm}} = I/\sigma$. σ can be estimated from (e.g., Napier & Crane, 1982)

$$\sigma = \sqrt{(\mathrm{SEFD}_{\mathrm{CS}}/N_{\mathrm{CS}})(\mathrm{SEFD}_{\mathrm{RS}})}/(\sqrt{\Delta\nu\Delta t}), \tag{5.4}$$

where N_{CS} is the number of stations in the AUT, $\mathrm{SEFD}_{\mathrm{CS}}$ and $\mathrm{SEFD}_{\mathrm{RS}}$ are the system equivalent flux density (SEFD) of a core station and a reference station, respectively, $\Delta\nu$ is the bandwdith and Δt the integration time. For the LBA the SEFD of each antenna field is $\approx$ 30 kJy at 60 MHz and for the HBA $\approx$ 3 kJy at 150 MHz (van Haarlem et al., 2013). Thus, for an observation of 3C196 with integration times of 600 s at 60 MHz and 60 s at 150 MHz we can determine the time delays with errors of 1.8 ns and 0.4 ns, respectively.

For a baseline of 52 km, an integration time of 600 s and an observing frequency of 37 MHz, time and bandwidth smearing (e.g., Bridle & Schwab, 1999) will reduce the response to sources at $45'$ from the map center by 5% and 70%, respectively. For the same baseline and an integration time of 60 s these sources will have their apparent fluxes reduced by 23% at 115 MHz.

Table 5.1.: Observations used in this work.[†]

Observation ID[‡]	Antenna	# antenna fields	Start time	Duration (s)	# TABs	TAB spacing (arcmin)	FoV (degrees)	Source
L658168	HBA[b]	46[c]	June 14 13:40:00 UT	60	169	1.6	0.37	3C147
L658158	HBA[b]	46[c]	June 14 13:30:00 UT	60	169	1.6	0.37	3C196
L650445	LBA[d]	24[e]	April 19 09:20:00 UT	600	271	5	1.32	3C48
L645357[a]	LBA[d]	24[e]	March 20 19:45:00 UT	600	271	5	1.32	3C196

[†] The stations used as reference and their distance from the center of the array are; RS210 65 km; RS509 59 km; RS310 52 km; and DE605 226 km.

[‡] For each observation ID the three/four previous odd values contain the observations with the reference stations.

[a] For this observation DE605 was not used as a reference.

[b] Data was recorded for 10 spectral windows centered at; 108.0078125, 114.84375, 125.1953125, 136.9140625, 147.65625, 150.1953125, 154.1015625, 166.6015625, 178.90625 and 189.0625 MHz.

[c] All core stations, except CS024.

[d] Data was recorded for 10 spectral windows centered at; 36.71875, 45.1171875, 50.0, 51.5625, 53.125, 56.0546875, 61.5234375, 65.234375, 67.7734375 MHz.

[e] All core stations.

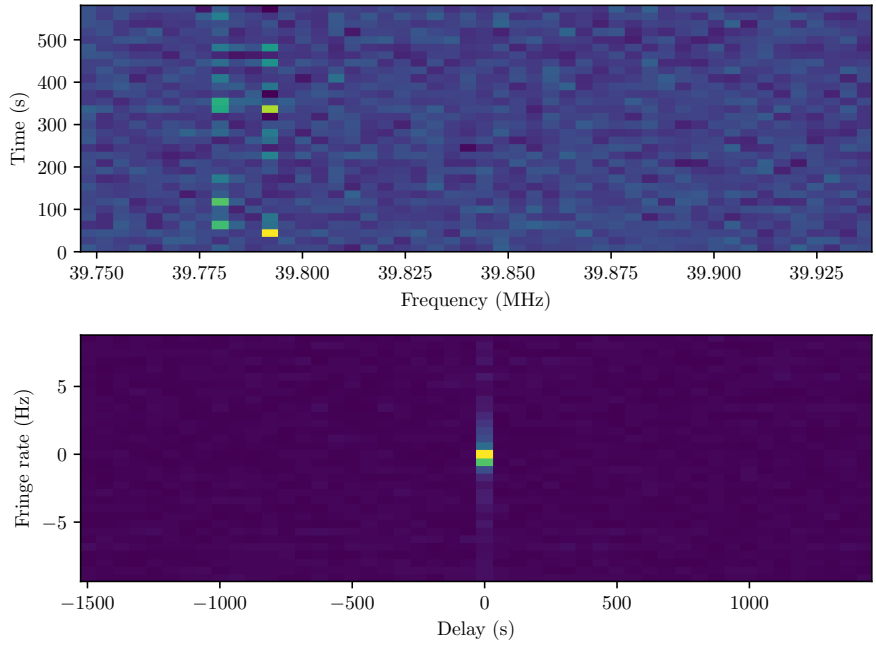

Figure 5.1.: Waterfall plots of the complex visibilities and their Fourier transform. The *top panel* shows the amplitude of the visibilities. RFI can be seen at 39.78 MHz. The *bottom panel* shows the Fourier transform of the visibilities. If the visibilities are dominated by a point source in the array tracking center, then this should be a delta function centered at 0 delay and 0 fringe rate. In this case there is some time variability in the data which produces a spread along the fringe rate.

5.3.2. From raw voltages to beam maps

To obtain a complex-valued map of the array beam we cross-correlate the voltage from the AUT with that of the reference station. This is done using an FX correlator (e.g., Thompson et al., 2017) implemented in *python*. To channelize the time series data from each spectral window we use a polyphase filter bank (PFB, e.g., Price, 2016) with a Hann window to alleviate spectral leakage and scalloping losses. We produce spectra of 64 3 kHz channels, and a time resolution of 327.68 μs. This enables us to, at a later stage, flag narrowband radio frequency interference (RFI) without losing the time sample. In each spectral window we discard 25% of the channels at the edges, leaving a bandwidth of 146.48 kHz per spectral window. The two orthogonal polarizations are combined to produce four cross-correlation products, i.e. XX, XY, YX and YY products.

Before proceeding, we check that the bright unresolved source in the map center dominates the signal. In this case, a time delay versus fringe rate plot will show a peaked response in the center of the diagram. An example of such diagram is presented in Figure 5.1.

After cross-correlation, the visibilities are time averaged to ensure that their SNR is large enough (> 3) for calibration. For the HBA observations we average to a time resolution of 0.4 s, which results in a SNR of 6. For the LBA, which has a lower sensitivity and is more severely affected by the ionosphere (Figure 5.2), the averging times are longer. For L645357 we average to 20 s and for L650445 — 5 s.

After time averaging, we remove visibilities affected by radio frequency interference (RFI) in the frequency-time domain. We use a SumThreshold method (AOFlagger, Offringa, van de Gronde, & Roerdink, 2012) on each TAB, polarization and spectral window independently. For the LBA and HBA observations the fraction of flagged data is $\approx 5\%$. After RFI flagging we average each spectral window in frequency to a single 146.48 kHz channel.

The flagged visibilities are then calibrated by multiplying by the inverse of the Jones matrix of the central beam (Brentjens et al. in prep.). This has the effect of removing most of the undesired systematic effects present in the data, such as the dependence of the observed visibilities on the sky brightness distribution, beam pattern of the reference station, or ionospheric delays between reference station and AUT.

After calibration, we further average the visibilities in time to one time sample with a duration of one minute for the HBA and ten minutes for the LBA (Table 3.1). After averaging in time, we are left with one calibrated complex visibility for each polarization (XX, XY, YX, and YY), spectral window and TAB. These calibrated complex visibilities map the complex-valued beam. Finally, we compute the inverse-variance weighted mean beam maps, averaged over all reference stations.

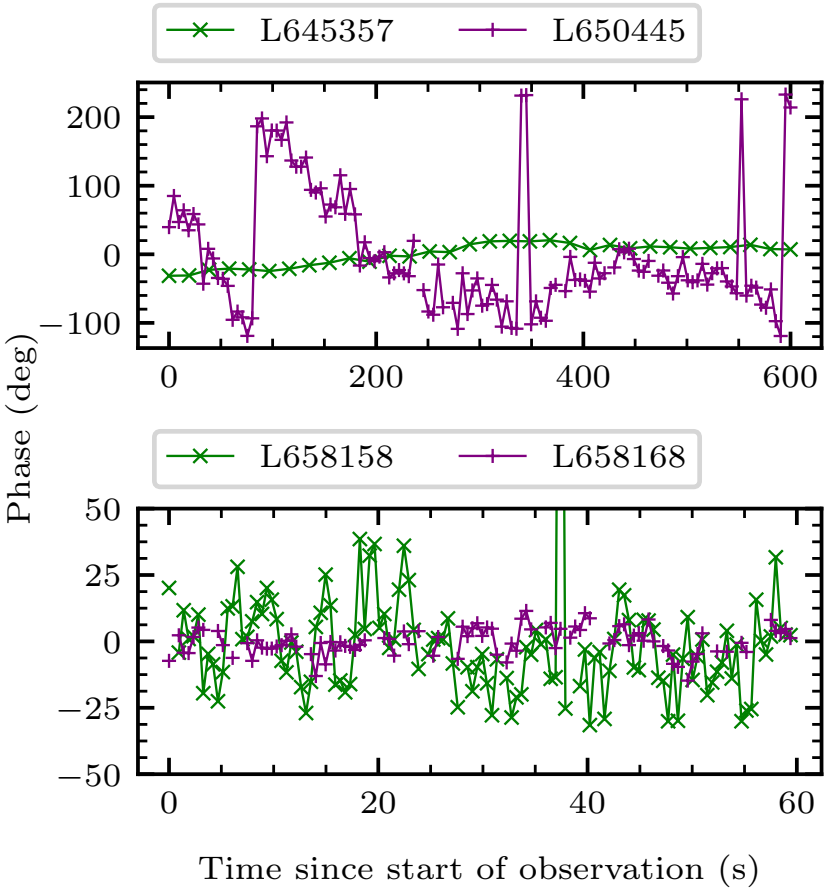

Figure 5.2.: Phase of the visibilities at the map center. The *top* panel shows the observed phase for the LBA observations. The *bottom* panel shows the observed phase for the HBA observations.

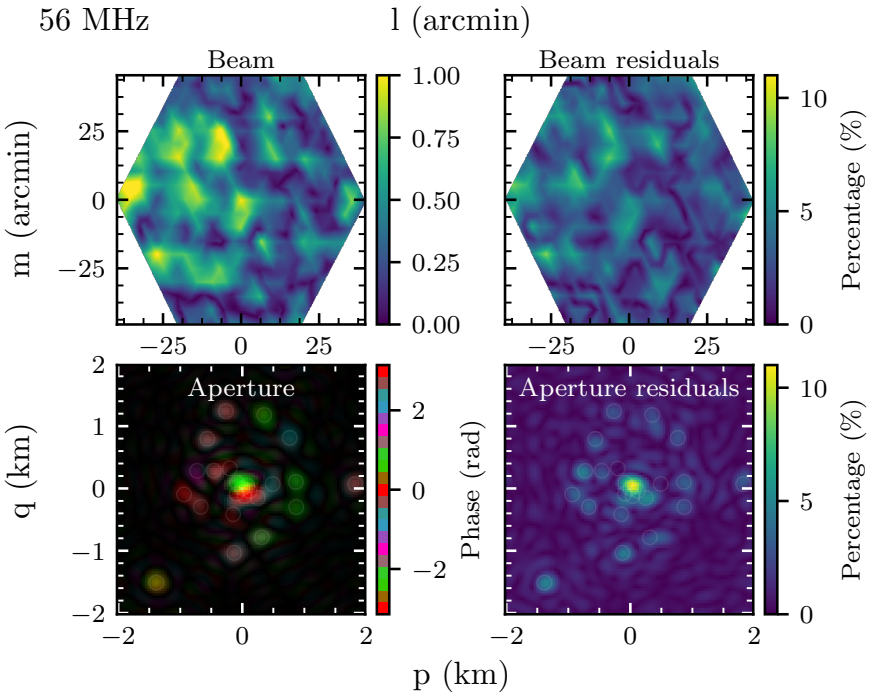

Figure 5.3.: Voltage beam and aperture maps for the LBA at 52 MHz derived from the observation L645357. *Top left*: Amplitude of the voltage beam. *Top right*: Amplitude of the residuals after subtracting the beam model from the observed voltage beam (*top left*). The beam model is generated using the derived phases for the stations in the AUT. *Bottom left*: Aperture map obtained by taking the Fourier transform of the voltage beam (inverse Fourier transform of Equation 5.2). The colorscale represents the phase and the brightness the amplitude at each location in the map. The *white circles* show the location of the stations in the AUT. *Bottom right*: Ampltiude of the Fourier transform of the beam residuals (*top right*).

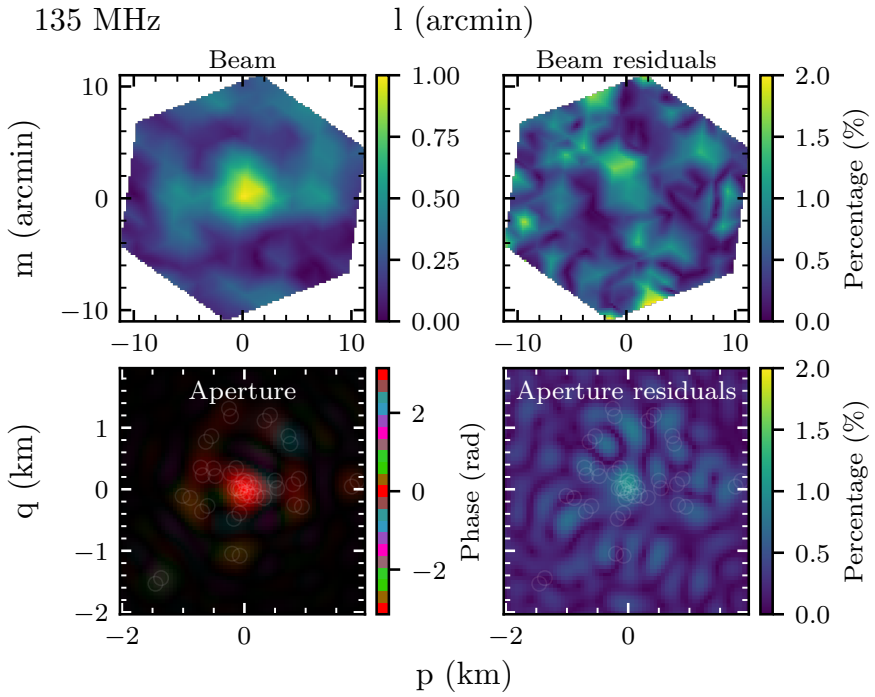

Figure 5.4.: Voltage beam and aperture maps for the HBA at 135 MHz derived from the observation L658168. *Top left*: Amplitude of the voltage beam. *Top right*: Amplitude of the residuals after subtracting the beam model from the observed voltage beam (*top left*). The beam model is generated using the derived phases for the stations in the AUT. *Bottom left*: Aperture map obtained by taking the Fourier transform of the voltage beam (inverse Fourier transform of Equation 5.2). The colorscale represents the phase and the brightness the amplitude at each location in the map. The *white circles* show the location of the stations in the AUT. *Bottom right*: Ampltiude of the Fourier transform of the beam residuals (*top right*).

5.4. Results

5.4.1. Beam and aperture maps

An example of the observed beam of the LBA is presented in the top left panel of Figure 5.3. There, the main lobe of the beam is at the map center, and we can also see that there is a side lobe with a similar amplitude at $(l, m) = (-6, 25)$. This is produced by improperly calibrated time delays between stations. For the HBA (top left panel of Figure 5.4) the side lobes have amplitudes $\approx 30\%$ of the main lobe. The time delays between HBA stations are regularly calibrated using synthesis imaging observations.

The voltage beam is the Fourier transform of the aperture illumination (Eq. 5.2), shown in the bottom left panel of Figures 5.3 and 5.4. There, we can see that the amplitudes are non-zero at the location of the stations in the AUT. The amplitudes are larger in the *Superterp* because there the stations are unresolved and their amplitudes, and phases, overlap.

5.4.2. Time delays and 0 Hz phase offsets

To measure the phase of the stations in the AUT we pose Equation 5.2 as a linear problem. Then, we use least squares parameter estimation to determine the amplitude and phase at the locations of the stations. The phases derived are not meaningful on their own, as an interferometer only measures relative phases (e.g., Jennison, 1958). To remove the arbitrary offset from the phases we reference them with respect to one of the stations in the AUT.

From the referenced phases we can recover the time delay, τ, and the 0-Hz phase offset, ϕ_0, of each station. These are related to the phase, ϕ, by the linear relation $\phi = 2\pi\nu\tau + \phi_0$. An example of the observed phases and their best fit linear relation are presented in Figure 5.5. There we can see that the phases show a linear relation with frequency and that the errorbars on the phases become larger for stations closer to the array center.

Examples of the measured τ and ϕ_0 for the HBA stations derived from the L658168 observations are shown in Figure 5.6. For the *Superterp* stations, CS002 to CS007, the errorbars are a factor of three larger than for the rest of the stations. This is a consequence of the larger phase errors obtained for the *Superterp* stations (see Figure 5.5). This is also reflected in the larger aperture residuals at the *Superterp* (bottom right panel of Figure 5.4). For the stations outside the *Superterp*, the errors on τ have a mean value of 1.4 ± 1.2 ns and 1.2 ± 0.9 ns for the XX and YY polarizations, respectively. For the observation L658158 the same stations have errors on τ with a mean of 3.9 ± 1.7 ns and 3.7 ± 1.7 ns for the XX and YY polarizations, respectively. Since the flux density of 3C196 is a factor of 1.2 larger than that of 3C147, the larger errors on τ for L658158 are produced by the larger phase fluctuations in this observation (Figure 5.2).

The measured time delays and 0-Hz phase offsets for the LBA stations derived from L645357 and L650445 are presented in Figure 5.7. In both observations the derived values of τ and ϕ_0 agree to within 3σ, albeit in L645357 they have a factor of 12 higher SNR. This is because for the L645357 observations the ionosphere over the array

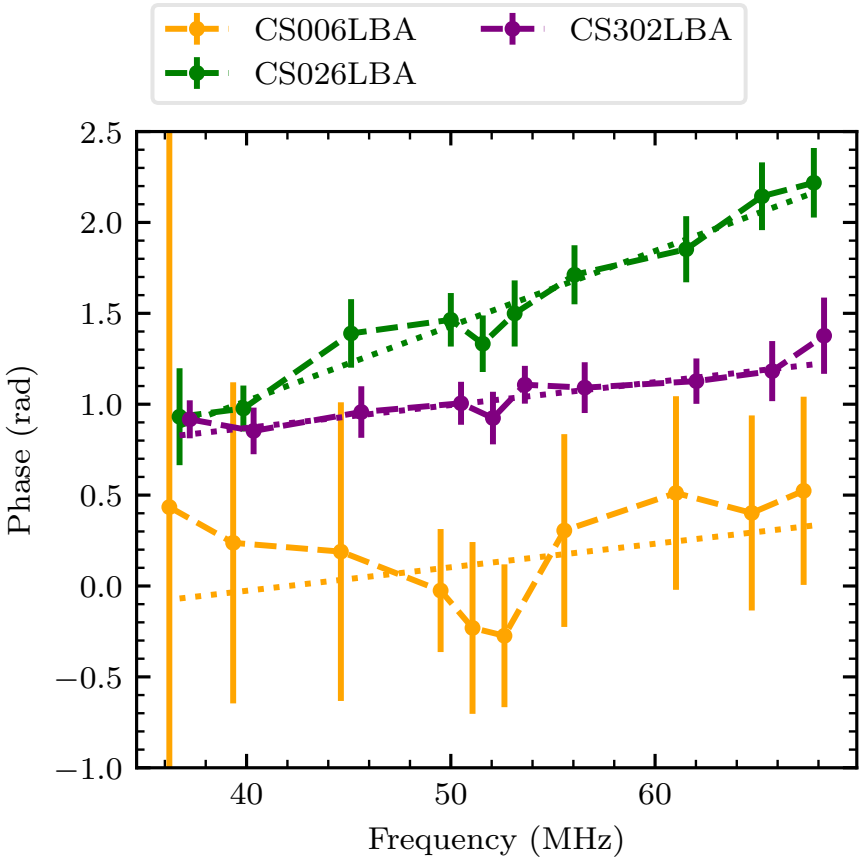

Figure 5.5.: Example of the measured phases as a function of frequency for three LBA stations. The measured phases are shown with *dashed lines* and *error bars*, while the best fit lines are shown with *dotted lines*. CS302LBA is at a distance of two km from the array center, CS026LBA at 870 m and CS006LBA 126 m, part of the *superterp*. These correspond to values derived from observation L645357.

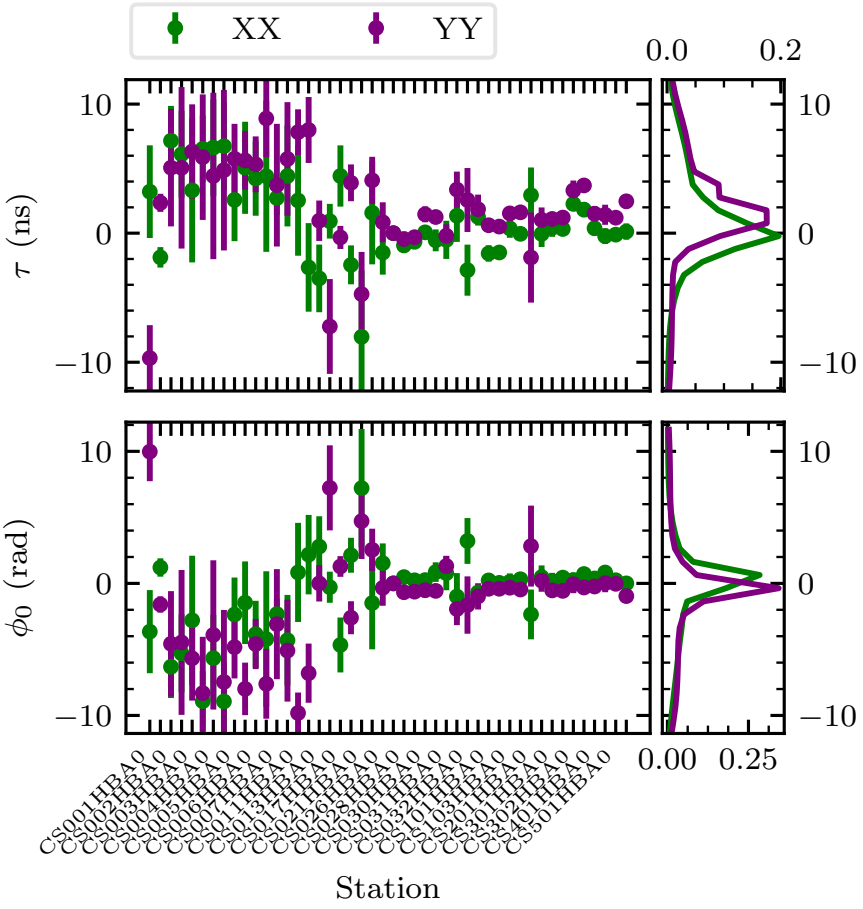

Figure 5.6.: Time delay and 0-Hz phase offsets for the HBA stations derived from observation L658168. The *top panel* shows the derived time delay τ for each station in the AUT. The time delay for CS026HBA1 is 0 because this station was used to reference the phases. The *bottom panel* shows the 0-Hz phase offset. It can be seen that the time delays and 0-Hz phase offsets are consistent between the two polarizations. For the innermost stations, CS002 to CS007, the scatter is larger because the stations are unresolved.

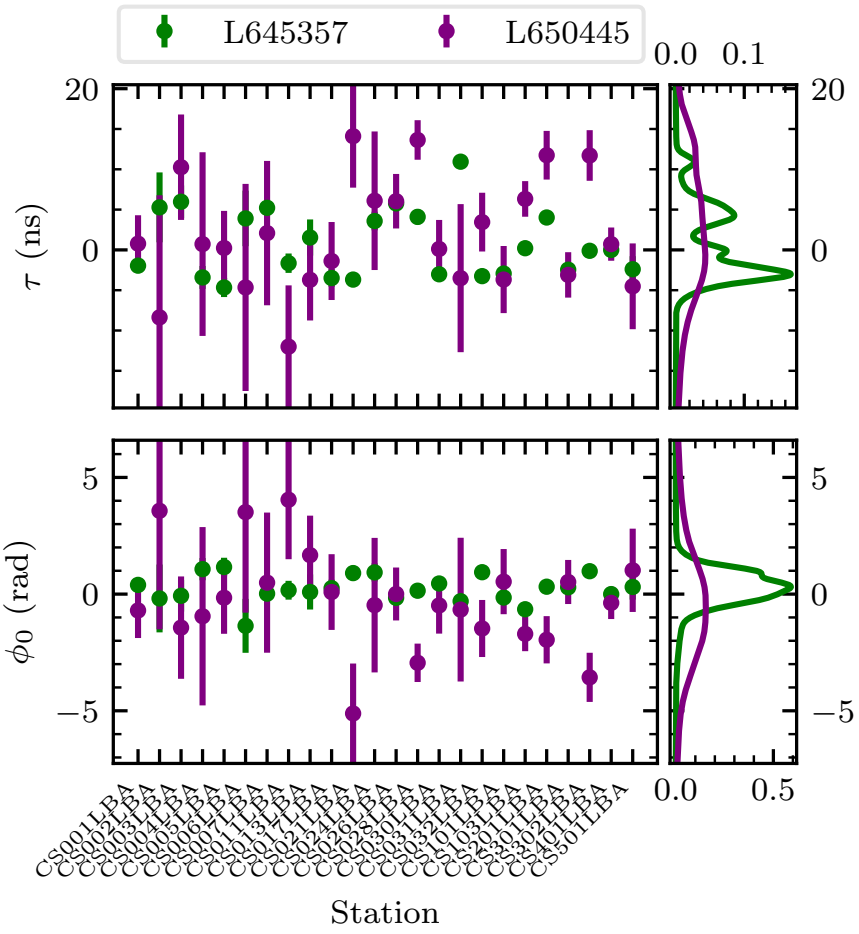

Figure 5.7.: Time delays and 0-Hz phase offsets for the LBA stations derived from holography observations. The time delays and 0-Hz phase offsets correspond to those of the XX polarization for two observations (L645357 and L650445). The *top panel* shows the derived time delay τ for each station in the AUT. The time delay for CS028 is 0 because this station was used to reference the phases. The *bottom panel* shows the 0-Hz phase offset. It can be seen that the time delays and 0-Hz phase offsets are consistent between the two observations. For the innermost stations, CS002 to CS007, the scatter is larger because the stations are unresolved.

produces a smooth slow time-varying phase rotation, while for L650445 the changes are faster and more pronounced (Figure 5.2). The time delays for the *Superterp* stations have errors a factor of four larger than for the rest of the stations.

For both HBA and LBA (Figures 5.6 and 5.7), the 0-Hz phase offsets are consistent with being zero at the 5σ level. Motivated by this, we fit a linear relation to the phases with $\phi_0 = 0$. The values of τ for the LBA stations under this assumption are presented in Figure 5.8. We can see that the derived time delays are consistent with those presented in Figure 5.7, but in this case the errorbars are smaller because there is one free parameter less and setting $\phi_0 = 0$ is a strong constraint. Using $\phi_0 = 0$ the mean value of the error of the derived time delays is 0.26 ± 0.16 ns and 0.17 ± 0.10 ns for the HBA and LBA, respectively.

In Figure 5.8 we also show the time delays for the LBA stations derived from imaging observations. In these, phase solutions for each station are derived from observations of a bright calibrator source and a model of the sky brightness distribution (e.g., Fomalont & Perley, 1999). Then, the contribution to the phase from the station delays and the ionosphere are separated (e.g., van Weeren et al., 2016; de Gasperin et al., 2018). We see that the time delays derived using holography and imaging observations agree to within 3σ for 20 out of the 23 stations present in both observations. This shows that the time delays derived here, where no model of the sky brightness distribution is used, are indistinguishable from those derived in imaging observations. The interferometric time delays have smaller errorbars because they are the average of 4 hours of data.

We check that the derived time delays and 0-Hz phase offsets capture the status of the AUT by using them to simulate the array beam and comparing it with the observed one. To simulate the array beam we use the time delays and 0-Hz phase offsets shown in Figures 5.6 and 5.7 for the HBA and LBA stations, respectively. These are used to evaluate the phase of each station at a particular frequency, producing a complex valued map of the AUT. The Fourier transform of the AUT simulates the array beam. The residuals between the observed and simulated array beams are presented in the top right panel of Figures 5.3 and 5.4. The residuals in the image plane have no obvious structure and show amplitudes of $\lesssim 10\%$. This shows that we can reproduce the array beam using the derived time delays and 0-Hz phase offsets. However, the Fourier transform of the beam residuals reveals that there is significant structure in the aperture plane (bottom right panel of Figures 5.3 and 5.4). This can be noticed as a larger amplitude (11% for the LBA) at the location of the *Superterp*, for which we are not capturing the phase behavior as accurately as for the stations away from it (see also Figure 5.5).

5.5. Discussion

5.5.1. Corrected time delays

We use the derived time delays (Figure 5.8) to update the instrumental time delays in LOFAR's beamformer. To test the effect of updating the instrumental time delays in the beamformer we observed Cygnus A with the core stations of LOFAR. The observation was one minute long using the imaging mode, where the signals of different stations

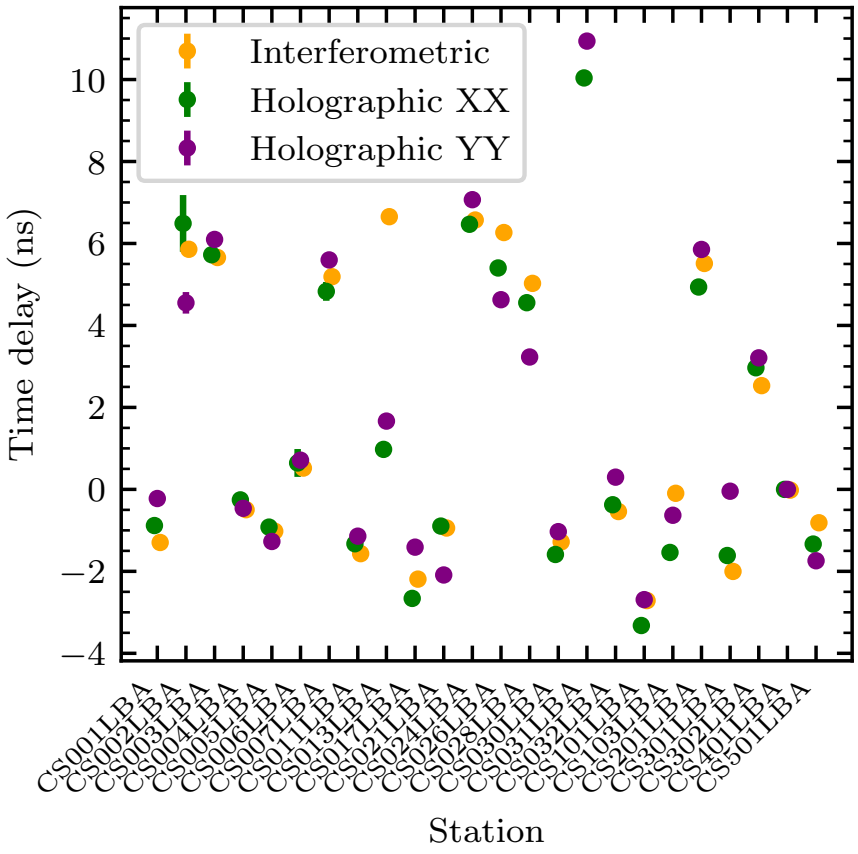

Figure 5.8.: Time delays for the LBA stations assuming that $\phi_0 = 0$. The time delays obtained from holography observations are shown for two orthogonal polarizations (XX and YY). We also show the time delays derived from imaging observations for Stokes I. The time delay for CS401LBA is 0 because this station was used to reference the phases. Station CS031LBA is missing in the imaging data because it was completely flagged.

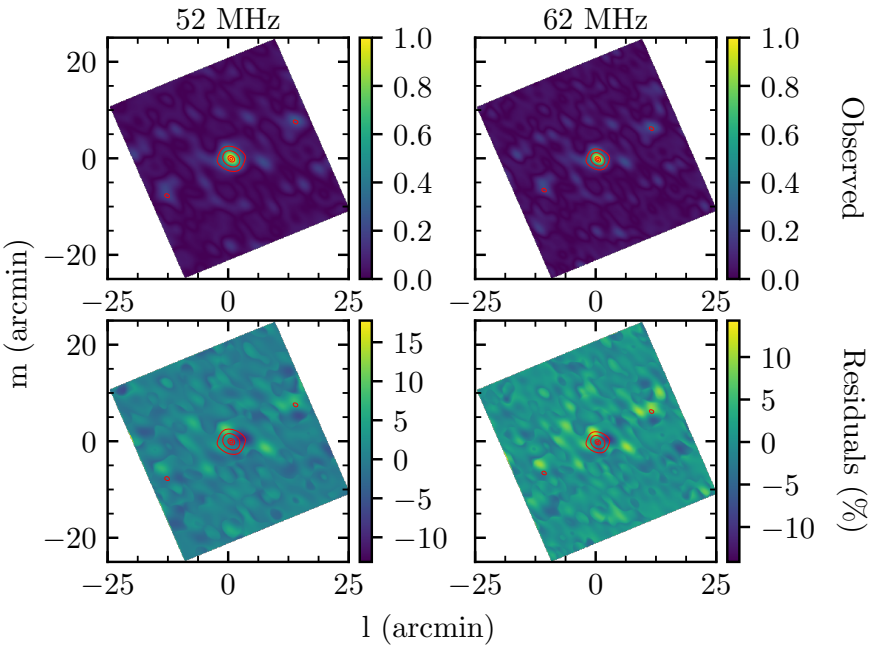

Figure 5.9.: Observed beam for the LBA. The *top row* shows the observed beam after updating the instrumental time delays in the beamformer (*colorscale*). The *red contours* show the amplitude of a beam model generated from the position of the stations with no additional time delays. They are at the 20%, 50%, 90% and 98% level with respect to the peak response. The *bottom row* shows the residuals after subtracting the beam model from the observed beam (*colorscale*). The *red contours* are the same as in the top row.

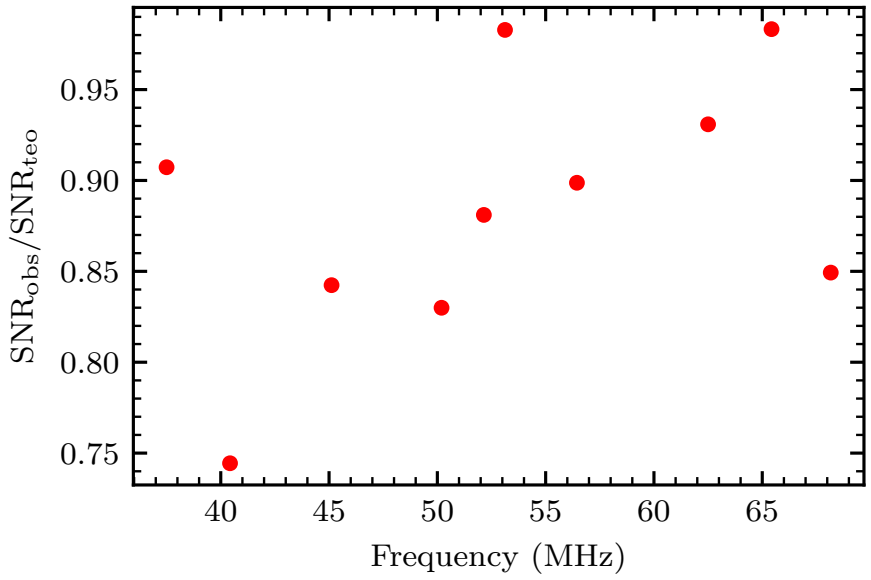

Figure 5.10.: Ratio between the observed SNR and the theoretical value.

are cross-correlated instead of added. Since the signal path between stations and the beamformer is the same in tied-array and imaging modes, these observations have a beam equivalent to the one observed using holography. Cygnus A has a size of $\approx 1'$ (e.g., McKean et al., 2016), so it will be unresolved by the LOFAR core at LBA frequencies (at 90 MHz the spatial resolution of the core is $3\farcm3$). Hence, a dirty image obtained from this observation will show the array beam.

A comparison between the LBA beam after the update and a model of the beam is presented in Figure 5.9. In the beam model the phase of each station is given by its location with no additional time delays. We see that the sidelobes in the observed beam are similar to those of the beam model. After subtracting the beam model the residuals are $\lesssim 20\%$.

We compare the SNR of the observations of Cygnus A with the theoretical SNR in Figure 5.10. The ratio between the observed SNR and its theoretical value has a mean of 0.88 ± 0.06. These results show that after updating the time delays in the beamformer the array beam is close to the ideal case. The remaining differences are produced by propagation delays introduced by the ionosphere and any remaining errors in the instrumental time delays.

When using an unpolarized bright unresolved source to determine the time delays, there will be an arbitrary offset between the X and Y polarizations. When these time delays are applied to the beamformer, the offset will produce a rotation of Stokes U into Stokes V. In order to find this offset we need to observe a linearly polarized source for which the sign of the rotation measure is known. From this observation the offset

is determined from the angle between the apparent Stokes U and V (e.g., Brentjens, 2008). This step has not been performed yet.

5.5.2. Improvements to holographic measurements with LOFAR

One of the main limitations of the holographic measurements presented is the spatial resolution over the telescope aperture. For a constant number of TABs, this is can be improved by observing a larger portion of the beam using a mosaic while keeping a TAB at the calibrator source. Additionally, the separation between TABs could be made smaller, reducing aliasing artifacts in the aperture plane.

For the experiments presented in this work we have used only four reference stations. Outside its core, LOFAR has 14 stations within the Netherlands and 13 stations distributed all over Europe. Any of these stations can be used as reference station, as long as the baseline formed with the AUT does not resolve the source used to map the beam. This means that the improvement in the SNR of the complex-valued beam map can be up to a factor of four using the same sources. With an improvement a factor of four in the maps of the complex-valued beam the integration times could be made shorter, or more precise time delays could be derived.

The time delays derived from holographic measurements can be used to update the instrumental time delays prior to an observation with the tied-array (e.g., of a pulsar). Moreover, if the integration time required to reach ns precision can be made shorter, and the post-processing of the holographic measurements made in real time, then it would be possible to interleave holographic observations during the tied-array observations. This could be a way towards semi-real-time beam calibration for the Square Kilometer Array (SKA). Implementing a dedicated holography mode in the supercomputer that processes the raw LOFAR data is one of the next steps towards this goal.

5.6. Summary

In this work we have used radio holography along with a new calibration method to characterize the time delays between LOFAR's core stations. This new calibration method consists on calibrating the measured complex-valued beam map by right multiplying by the matrix inverse of the map center. This calibration makes the observed complex-valued reception pattern independent of the sky brightness distribution.

Four (HBA) and three (LBA) reference stations were used simultaneously to produce maps of the tied array voltage beam. Using 60 s (HBA) and 600 s (LBA) long observations of 3C196, 3C147 and 3C48 we derived time delays with an error < 1 ns. We find that the main limitations in reaching nanosecond precision in the measured time delays are the condition of the ionosphere over the array and the ability to spatially resolve the array elements. LOFAR now uses the derived time delays operationally.

BIBLIOGRAPHY

Baars, J. W. M., Lucas, R., Mangum, J. G., & Lopez-Perez, J. A. 2007, IEEE Antennas and Propagation Magazine, 49

Barton, P. 1980, IEE Proceedings F (Communications, Radar and Signal Processing), 127, 266

Bennett, J. C., Anderson, A. P., McInnes, P. A., & Whitaker, A. J. T. 1976, IEEE Transactions on Antennas and Propagation, 24, 295

Brentjens, M. A. 2008, A&A, 489, 69

Bridle, A. H., & Schwab, F. R. 1999, in Astronomical Society of the Pacific Conference Series, Vol. 180, Synthesis Imaging in Radio Astronomy II, ed. G. B. Taylor, C. L. Carilli, & R. A. Perley, 371

Broekema, P. C., Mol, J. J. D., Nijboer, R., et al. 2018, Astronomy and Computing, 23, 180

Broilo, B. 1993, Holographic Directed Adjustments of the VLA-VLBA Antennas

Chen, M.-T., Tong, C.-Y. E., Blundell, R., Papa, D. C., & Paine, S. N. 1998, in Proc. SPIE, Vol. 3357, Advanced Technology MMW, Radio, and Terahertz Telescopes, ed. T. G. Phillips, 106–113

Colegate, T. M., Sutinjo, A. T., Hall, P. J., et al. 2015, ArXiv e-prints

D'Addario, L. R. 1982, Holographic Antenna Measurements: Further Technical Considerations

—. 2008, Interplanetary Network Progress Report, 175, 1

de Gasperin, F., Mevius, M., Rafferty, D. A., Intema, H. T., & Fallows, R. A. 2018, A&A, 615, A179

Fomalont, E. B., & Perley, R. A. 1999, in Astronomical Society of the Pacific Conference Series, Vol. 180, Synthesis Imaging in Radio Astronomy II, ed. G. B. Taylor, C. L. Carilli, & R. A. Perley, 79

Hamaker, J. P., Bregman, J. D., & Sault, R. J. 1996, A&AS, 117, 137

Harp, G. R., Ackermann, R. F., Nadler, Z. J., et al. 2011, IEEE Transactions on Antennas and Propagation, 59, 2004
Hunter, T. R., Schwab, F. R., White, S. D., et al. 2011, Publications of the Astronomical Society of the Pacific, 123, 1087
Intema, H. T., van der Tol, S., Cotton, W. D., et al. 2009, A&A, 501, 1185
Jennison, R. C. 1958, MNRAS, 118, 276
Jones, R. C. 1941, Journal of the Optical Society of America (1917-1983), 31, 488
Kesteven, M. 1993, VLA Holography
McKean, J. P., Godfrey, L. E. H., Vegetti, S., et al. 2016, MNRAS, 463, 3143
Mevius, M., van der Tol, S., Pandey, V. N., et al. 2016, Radio Science, 51, 927
Napier, P. J., & Bates, R. H. T. 1973, Institution of Electrical Engineers Proceedings, 120, 30
Napier, P. J., & Crane, P. C. 1982, in Synthesis Mapping, ed. A. R. Thompson & L. R. D'Addario
Naruse, M., Ito, T., Sekimoto, Y., et al. 2009, Experimental Astronomy, 24, 89
Offringa, A. R., van de Gronde, J. J., & Roerdink, J. B. T. M. 2012, A&A, 539
Popping, A., & Braun, R. 2008, A&A, 479, 903
Price, D. C. 2016, arXiv e-prints, arXiv:1607.03579
Rioja, M. J., Dodson, R., & Franzen, T. M. O. 2018, MNRAS, 478, 2337
Ruze, J. 1952, Il Nuovo Cimento, 9, 364
—. 1966, IEEE Proceedings, 54
Scott, P. F., & Ryle, M. 1977, MNRAS, 178, 539
Steyskal, H. 1987, Microwave Journal, 30, 107
Thompson, A. R., Moran, J. M., & Swenson, Jr., G. W. 2017, Interferometry and Synthesis in Radio Astronomy, 3rd Edition
van Haarlem, M. P., Wise, M. W., Gunst, A. W., et al. 2013, A&A, 556, A2
van Weeren, R. J., Williams, W. L., Hardcastle, M. J., et al. 2016, ApJS, 223, 2
Wiktowy, M., O'Grady, M., Atkins, G., & Singhal, R. 2003, Canadian Aeronautics and Space Journal, 49, 65

VI

SAMENVATTING

6.1. INTRODUCTIE

De ruimte is, zoals de naam suggereert, vooral een lege ruimte. Maar, iedereen die weleens een heldere nacht heeft meegemaakt, kan je vertellen dat de ruimte vol is met sterren. Als je nauwkeuriger gaat kijken, zul je zien dat deze sterren zich voornamelijk bevinden in een band over de hemel. Met een beetje verbeeldingskracht lijkt deze band wel een beetje op een rivier van gemorste melk. Dit is het sterrenstelsel waar ook de Aarde zich in bevindt, de Melkweg. Wij zien de Melkweg dus ook van binnen, als een dunne streep aan de hemel. Dit komt omdat de Melkweg zo dun is als een pannenkoek. (Bekijk de volgende keer wanneer je pannenkoeken eet je pannenkoek maar van de zijkant. Hartstikke dun!)

De Melkweg is niet het enige sterrenstelsel in het universum, het zit er vol mee. Jonge stelsels, oude stelsels, stelsels in de vormen van pannenkoeken, rugbyballen en nog veel meer en vaak ook met allemaal verschillende kleuren. Je ziet heel duidelijk alle sterren schijnen, maar naast deze sterren is er nog veel meer te vinden in een sterrenstelsel. Tussen de sterren zit stof en gas. Heb je op een zonnige dag wel eens over een stoffig oppervlak gekeken en het stof de lucht in geblazen? En heb je ook gezien dat dit stof zonlicht tegenhoudt of weerkaatst? Het stof in de ruimte heeft ook veel van dat soort eigenschappen. En het gas in de ruimte is erg te vergelijken met de wolken in de lucht, en het stof lijkt op de dampen die uit een schoorsteen komen. Ook al zijn het stof in huis en het gas uit de uitlaat misschien vervelend voor ons, het gas en stof in de ruimte spelen een belangrijke rol in het leven van een sterrenstelsel.

Heb je je bijvoorbeeld ooit afgevraagd waar de Zon vandaan komt? De zon is een ster, net als de stipjes aan de nachtelijke hemel. Het is een relatief kleine ster, maar sterren zoals de zon komen veel voor in de Melkweg. Alle biljoenen sterren in ons universum worden op eenzelfde manier geboren, uiteraard allemaal op verschillende momenten en verschillende plaatsen, maar allemaal begonnen ze als stof en gas. Veel stof en gas kan samenkomen tot structuren die lijken op wolken, zoals de wolken die waarschijnlijk op

Figure 6.1.: De Melkweg bij heldere hemel boven Paranal, Chili. De meeste stipjes die je hier ziet zijn sterren. Je ziet dat sommige gebieden bijna "wit" zijn, hier zien we heel veel sterren bij elkaar. Je ziet ook donkere gebieden, dit zijn wolken van stof die licht van de sterren voor ons verbergen. Image credit: B. Fugate (FASORtronics)/ESO

dit moment in de lucht boven je hangen, maar dan veel groter dan onze wolken. Deze interstellaire wolken, tussen de sterren, kunnen zelfs vele malen groter worden dan ons zonnestelsel, waar de aarde maar een hele kleine fractie van is. Groter betekend natuurlijk ook zwaarder, sommige wegen meer dan een millioen keer onze Zon. Op een gegeven moment is zo'n wolk zo zwaar dat het geen wolk kan blijven, maar alleen nog maar ineen kan vallen. Net als wanneer je een tas probeert te dragen die te zwaar is, je kunt niks anders dan hem weer neerleggen. Wanneer deze grote wolken ineenvallen, kunnen sterren zich vormen, maar de temperatuur van de wolk moet wel laag genoeg zijn. Een andere manier om hier over na te denken is met regendruppels in een wolk. Wanneer het gasvormige water in de wolk afkoelt, condenseert het tot waterdruppels. Het stervormingsproces kan vele duizenden keren plaatsvinden in een sterrenstelsel. En elke keer wordt niet al het gas en stof omgezet tot ster, maar blijft er een beetje van de wolk over.

Betekend dit dat al het gas en stof in een keer opgebruikt wordt? Niet helemaal, sterrenstelsels zijn namelijk erg goed in het hergebruiken van materiaal. In de loop der tijd worden de sterren ouder. Op een gegeven moment kan een ster niet meer schijnen, wanneer dit bijna zo is geeft de ster een deel van zijn gas en stof af aan zijn omgeving. Sterren zoals de Zon doen dit langzaam, ze niezen beetje bij beetje wat van hun gas en stof de ruimte in. Sterren die groter zijn dan de Zon "niezen" heel vaak voor ze uitdoven, maar deze sterren hebben ook een laatste hele grote nies. Ze zeggen "boem" in iets dat

een supernova heet. Of de ster een supernova wordt of niet, een deel van het stof en gas wordt altijd terug gegeven aan het sterrenstelsel. Dit betekent dat weer nieuwe sterren gevormd kunnen worden uit dit gerecyclede materiaal, net zoals je dat zelf met een deel van je afval ook kunt doen. Dit was het laatste stapje in de beschrijving van de werking van een sterrenstelsel.

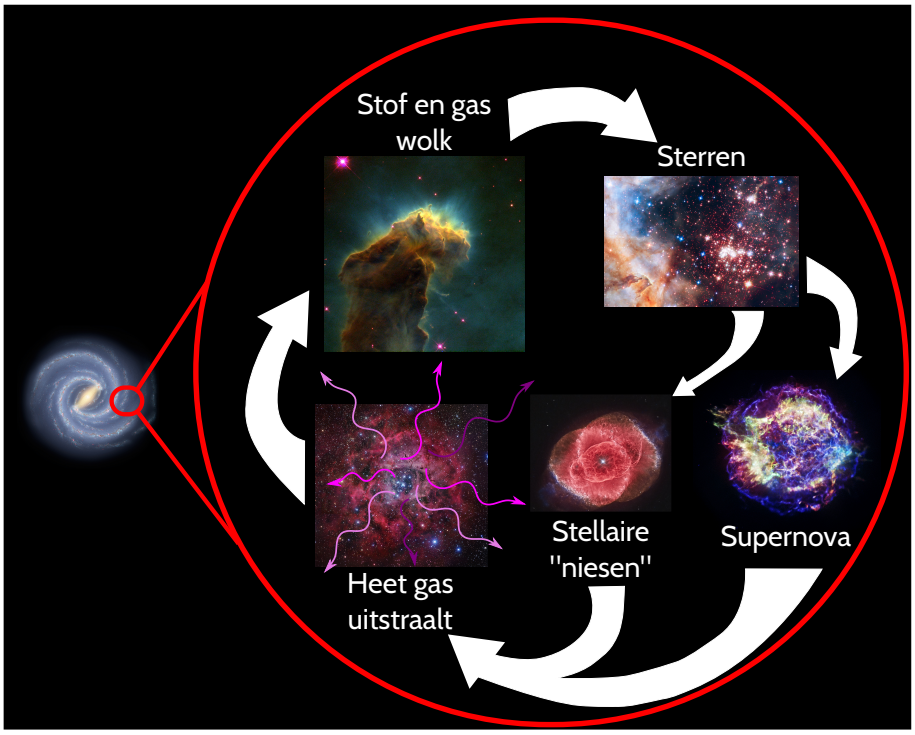

Figure 6.2.: Het ecosysteem van een sterrenstelsel is net een levenscyclus. In een stelsel als de Melkweg worden continue sterren geboren uit wolken van gas en stof. Op hun beurt geven sterren dit terug aan het stelsel wanneer ze uit gaan. Het afkoelende gas en stof van deze sterren is spectaculair om te zien. Wanneer het ver genoeg is afgekoeld kan het weer gebruikt worden om sterren te vormen. Image credit: NASA/ESA/Hubble/HLA/Robert Gendler/Raul Villaverde

Zoals je misschien wel kunt raden is al het materiaal dat de ster heeft uitgeniest nog erg warm. Hoe koelt dit nou weer voldoende af dat er sterren gevormd kunnen worden? Zelfs met al het gas en stof en alle sterren is de ruimte nog steeds erg leeg. Onder deze omstandigheden straalt het hete materiaal al zijn hitte de ruimte in. Je kunt het vergelijken met een warme zonnige dag, de meeste warmte komt dan van de straling die we opvangen van de Zon. Het gas tussen de sterren straalt ook, net als de Zon, en koelt daarmee af (De Zon koelt niet af omdat het continue bezig is materie om te zetten in energie. Warmte is gewoon een andere vorm van energie). Het uitstralen van de warmte door de hete materie zorgt voor de afkoeling die nodig is om weer nieuwe sterren te kunnen vormen.

Dit is het Galactische ecosysteem, een cyclus. In sterrenstelsels, verzamelingen sterren, stof en gas worden aan de lopende band sterren gevormd. In dit proces recyclen de sterren een deel van het stof en gas dat zijn oorsprong has in niesbuien van sterren. Het gerecyclede materiaal koelt af en kan dan weer gebruikt worden voor de bouw van nieuwe sterren. Deze cyclus is een van de belangrijkste aspecten van de evolutie van sterrenstelsels.

6.2. DIT PROEFSCHRIFT

In dit proefschrift concentreren we ons op de studie van koud gas in de Melkweg, in het bijzonder de grote gasreservoirs van atomair waterstof. Waterstof is het meest voorkomende element in het universum en het interstellaire medium (ISM). In het ISM wordt atomair waterstof gevonden in gigantische wolken, HI-wolken. Deze wolken kunnen worden bestudeerd op radiogolflengten met behulp van de 21 cm-lijn van atomair waterstof. En hoewel deze lijn astronomen heeft geholpen om de eigenschappen van HI-wolken te begrijpen, zijn er veel open vragen, omdat deze 21 cm-lijn weinig informatie biedt over het gas. We weten bijvoorbeeld niet zo goed wat de druk is in HI-wolken. Het is belangrijk om dit te weten als we de levenscyclus van sterrenstelsels willen begrijpen, omdat waterstof het grootste reservoir van materiaal is waaruit sterren zich vormen, en afhankelijk van zijn druk zal het kunnen afkoelen en sterren vormen of het zal nog een langere tijd een gaswolk blijven.

Een alternatief dat we kunnen waarnemen om HI-wolken te bestuderen, zijn koolstof radio-recombinatielijnen. Deze lijnen worden uitgestraald door koolstofatomen die zo groot kunnen zijn als de diameter van een mensenhaar! En hoewel ze veel zwakker zijn dan de 21 cm-lijn, bieden ze de aanvullende informatie die nodig is om HI-wolken te begrijpen.

Omdat lijnen voor koolstofradio-recombinatie lijnen zwakker zijn dan de lijn van 21 cm, hebben we grotere telescopen nodig om ze te observeren. Een voorbeeld van een telescoop die recombinatielijnen kan detecteren, is de Low Frequency Array (LOFAR). LOFAR is een radio-interferometer, dit betekend dat het de signalen van vele antennes combineert om beelden van de sterrenhemel te maken. De antennes bevinden zich overal in Europa. De meesten van hen zijn in Nederland, maar er zijn antennes in Ierland, Polen, Zweden, Frankrijk, Verenigd Koninkrijk, Duitsland en in de toekomst ook in Italië. De signalen van deze antennes worden over een high-speed glasvezelnetwerk naar Groningen vervoerd, waar ze worden gecombineerd en later door astronomen worden verwerkt om beelden van onze Melkweg en andere sterrenstelsels te maken. Bij het combineren van de signalen van deze antennes, is het erg belangrijk om heel precies te weten hoe laat het signaal bij elke antenne arriveert. Hoofdstuk 5 van dit proefschrift presenteert de implementatie van een methode waarmee astronomen het tijdstip van aankomst van een signaal vanuit de ruimte naar de antennes kunnen bepalen.

Dankzij LOFAR kunnen we koolstofradio-recombinatielijnen uit onze Melkweg waarnemen en voor de eerste keer individuele HI-wolken identificeren via deze lijnen. Dit is een grote stap in ons begrip van het ISM, omdat het nu mogelijk is om gedetailleerde kaarten te maken, niet alleen van de gasdistributie, maar ook van de druk.

Hoofdstuk 3 van dit proefschrift presenteert de eerste kaarten van de gasdruk in onze Melkweg. Hoofdstuk 2 van dit proefschrift laat zien hoe we met LOFAR koolstofradio-recombinatielijnen kunnen detecteren op de laagste frequenties die we vanaf de aarde waarnemen (de atmosfeer wordt ondoorzichtig voor radiogolven op lagere frequenties) en wat we daarover van het ISM kunnen leren. Hoofdstuk 4 past de lessen die zijn geleerd uit de hoofdstukken 2 en 3 toe op de emblematische Orion-nevel (gelegen op de punt van het zwaard van Orion) en maakt ook gebruik van koolstofradio-recombinatielijnen op hogere frequenties (zoals degene die kunnen worden waargenomen door ALMA) om de druk te bepalen in een stervormingsgebied.

In de toekomst zal het dankzij LOFAR en andere radiotelescopen mogelijk zijn om de druk in de HI-wolken in onze Melkweg met grote precisie te bepalen. Dit zal astronomen helpen te begrijpen wat de rol is van deze gigantische gasreservoirs in de levenscyclus van sterrenstelsels in de kosmische tijdschalen.

ACKNOWLEDGEMENTS

After 4.5 years in Leiden remembering the names of all the people that contributed, in their own way, to this thesis is a difficult task, but at the same time it is gratifying to dig in my memory and find the moments and names that made my stay what it was. Days of hard work, foggy nights out, running and sweets, are some of the things this time has been about.

I would like to start by thanking the people most closely related to this thesis, the radio recombination line group at Leiden. Raymond, Carmen, Leah, Francisco, Kim, Huub and Xander, thanks for your time and support during this process. Many thanks as well to the people in the LOFAR group, Reinout, Huib, Jit, Aayush, Frits, Gabi, Edwin, Duy and Tim. You brought me a bit closer to radio astronomy. Thanks to the interstellar medium group, the X-people, Liz, Alessandra, Dario, Michal, Cornelia, Jordy, Héctor, Sascha, Andrew, Ainil, Isabel, Marcelo, Annemieke, Suklima, Sebastiaan and Kirstin. You taught me a lot about laboratory astrophysics and it was a pleasure to share pizza with you. To the LOFAR Galactic working group, Irene, Maria and Glenn. Thanks for the moments we shared and for showing that LOFAR can do galactic science. To other enthusiasts of the interstellar medium, Yanett and Alvaro. A special thanks to Bram for making our office a greener place, Marin for bringing joy into it and Madusha for making it a mellow place. The people at ASTRON, thanks for your help in making this thesis possible, and specially to Michiel for his guidance and for sharing his knowledge of radio astronomy. To Juan and Rolando for keeping me up to date with the latest developments on low-frequency radioastronomy in Chile. To Franz for helping me take the first steps to get here. And to the best office mate, one so good I could not have wished for a better one. Kim, thanks a lot for sharing this last year with me, in the office, running or dancing. You taught me a lot about science, people and life, and I know you will continue to do so. Thanks for being such an awesome person.

The scientific part of a PhD is a large part of it, but without good friends and family it would not have been able to pull this out. Pablo, Carlos and Emanuele, thanks a lot

for all those breaks and beers we shared. I look forward to that infamous *ultima cerveza* that never arrives. Nikita and Anne, thanks for sharing your love for music. Stefano, thanks a lot for making me feel at home in oude rijn. Vicente, Manuela, Matthieu, Maren, Claudio and James, I will keep on practicing *vicentology* wherever I end. Paula, thanks for teaching me those first salsa steps. Lina, Marta and Jorge, I cannot remember all the fun we had. Heather, Fran and Cristi, thanks for keeping the chilean spirit alive for those that surround you. Santi, Claudio, Max, Seba, Rodrigo, Chero, what a good team we made. Maria Cristina, Valeria, Eleonora, Tommaso, Fraser, Turgay, thanks for being yourselves. Seba, I am happy our paths crossed. Pelao, Christian, Manuel, Rosita and Carla, for bringing with you the grass fields from PUC. Choco, Vicky, Jaca and Pipe, for opening up my worldview. Gero, thanks for introducing me to the speaker. Shalos! *tantos años pelando el cable y aun amigos. Son una bendición!* Mary, Rorri, Sofia, Yasna and Ariel, because *Wooooaaaa!* Isa, *vida!* Keegan and Susie, we finally are at a safe distance!

To my family, thanks a lot for being there for me, always, with your words, arms and ears, for helping me become who I am. Be it in the Alps, the streets of Spain or a hot summer day, you are always there with me.